



Title	Studies on Photofunctional Ruthenium(II)-Complexes for Hole-Mediator-Functionalized Photodriven Oxygen Evolution System
Author(s)	大塚, 滉喜
Citation	北海道大学. 博士(理学) 甲第14896号
Issue Date	2022-03-24
DOI	10.14943/doctoral.k14896
Doc URL	http://hdl.handle.net/2115/88669
Type	theses (doctoral)
File Information	OTSUKA_Hiroki.pdf



[Instructions for use](#)

Studies on Photofunctional
Ruthenium(II)-Complexes for
Hole-Mediator-Functionalized
Photodriven Oxygen Evolution System

(正孔輸送部を修飾した光駆動酸素発生システムのための
光機能性ルテニウム(II)錯体に関する研究)

Hiroki Otsuka

Graduate School of Chemical Sciences and Engineering
Hokkaido University

2022

Contents

Chapter 1. General Introduction

1-1 Artificial photosynthesis	- 2 -
1-2 Oxygen evolution reaction (OER)	- 3 -
1-3 Molecular-based photo(electro)chemical OER system	- 4 -
1-4 Hole-mediator materials (HM)	- 9 -
1-5 Photosensitizers for HM-functionalized photoanodes	-12-
1-6 Purpose of this thesis	-13-
1-7 Outline of this thesis	-15-
1-8 References	-16-

Chapter 2. Construction of Prussian-White Hole-Mediator-Integrated Photoanodes

2-1 Introduction	-24-
2-2 Experimental	-26-
2-3 Results and discussion	-30-
2-4 Conclusion	-44-
2-5 References	-45-

Chapter 3. Oxygen Evolution Reaction by Carbazole-Functionalized Ru(II) Molecular Catalysts

3-1 Introduction	-48-
3-2 Experimental	-50-
3-3 Results and discussion	-56-
3-4 Conclusion	-87-
3-5 References	-88-

Chapter 4. Photochemical Oxygen Evolution Reaction with Pyridyl-Anchor Modified Ru(II) Photosensitizers and Sensitizer-Loaded Nanoparticles

4-1 Introduction	-92-
4-2 Experimental	-94-
4-3 Results and discussion	-98-
4-4 Conclusion	-112-
4-5 References	-113-

Chapter 5. Synthesis and Properties of Pyridyl-Anchor and Carbazole Modified Ru(II) Complexes	
5-1 Introduction	-116-
5-2 Experimental	-118-
5-3 Results and discussion	-124-
5-4 Conclusion	-143-
5-5 References	-144-
Chapter 6. General Conclusion	-147-
Appendix	-151-
Acknowledgement	-168-

Chapter 1

General introduction

1-1. Artificial photosynthesis

As a promising approach that addresses the global energy issue, the artificial photosynthesis has attracted considerable attention because it enables the storage of the sunlight energy into chemical bonds, such as dihydrogen (H_2)¹, CO_2 reduced species (CO , HCOOH , etc.)² and so on. Since the pioneering work on the water splitting on TiO_2 by Honda and Fujishima (Fig. 1)³, extensive efforts have been devoted over several decades to the development of solar small-molecule conversion systems ranging from semiconductor materials⁴ to molecular materials.^{5, 6}

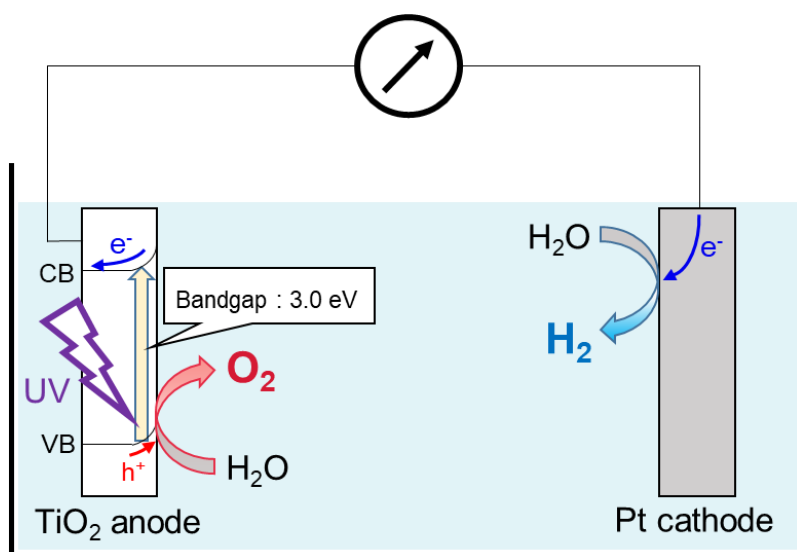
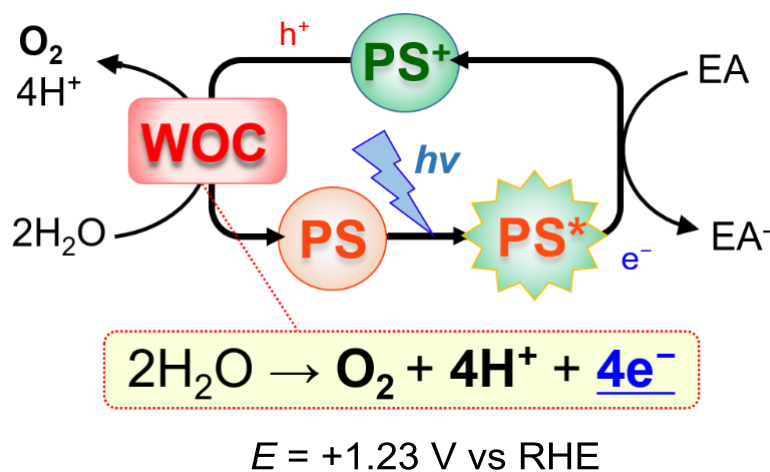


Figure 1. Light-driven water splitting by TiO_2 (Honda-Fujishima effect).

As the oxidative half reaction process of these artificial photosynthesis, water oxidation process, including the oxygen evolution reaction (OER; $2\text{H}_2\text{O} \rightarrow \text{O}_2 + 4\text{H}^+ + 4\text{e}^-$) plays key roles to deliver electrons and protons to reduction system, same as natural photosynthesis systems.⁷

1-2. Oxygen evolution reaction (OER)

Water oxidation process is advantageous with a view to the utilization of earth-abundant water as electrons and protons source.⁸ Especially OER is attracted because of its lower redox potential (+1.23 V vs RHE) than the other water oxidation reactions like hydrogen peroxide generation (+1.77 V vs RHE).⁷ However, this reaction is considered to be one of the bottlenecks especially in water splitting reactions, because it requires photoinduced four-electron and four-proton transfers (Scheme 1).⁹ In order to achieve the highly-active OER driven by visible-light, hole accumulation on water oxidation catalysts (WOCs) by improving the electron transfer efficiency between WOCs and photosensitizers (PSs) is required. From this viewpoint, efficient combination methods with WOCs and photosensitizing systems for good electron-communication are intensively being explored as described in the following section, no less than the development of highly-active photo- and/or electrochemical WOCs using molecular materials,¹⁰ semiconductor and metal-oxide-based materials¹¹ and polymers¹².



Scheme 1. Photochemical oxygen evolution reaction (OER). Water oxidation catalyst, photosensitizer and electron acceptor are denoted as WOC, PS and EA, respectively.

RHE: Reversible hydrogen electrode.

1-3. Molecular-based photo(electro)chemical OER systems

Intensive efforts to improve electron transfer processes between WOC and PS have been dedicated to molecular components based photocatalytic systems. Although their activities and durabilities are still inferior to semiconductor-based heterogeneous OER photocatalysts, these molecular approaches are advantageous on account of their tunability and variable methods for assembly and integration. The four typical approaches are briefly described in the following sections.

1-3-1. Integration of catalyst and sensitizer units

A direct linkage with WOCs and PSs is an intuitive approach to induce through-bond electron transfer, also well-known on the donor-acceptor connected charge separation,¹³ photochemical hydrogen evolution,¹⁴ and CO₂ reduction systems¹⁵. Sun et al.^{16a} and Hammarström et al.^{16b} reported photochemical OER by Ru(II) WOC and Ru(II) PS directly connected assemblies, which exhibited better electron-communication and higher OER activity than non-connected system. (Fig. 2)

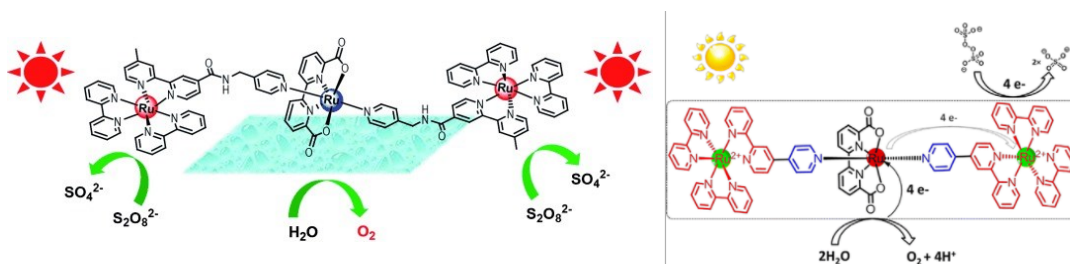


Figure 2. Dye-catalyst directly connected molecules for photochemical OER.¹⁶

However, a generic application and design of such molecules for homogeneous catalysis is restricted by complicated design or synthesis for the extension to water splitting system and controlling the WOC/PS ratio in one assembled molecule, with sufficient solubility.

1-3-2. Combination of semiconductors and functional molecules

In relation to above-mentioned viewpoints, in order to connect with reduction system and an expansion of applicability, the combination with molecular components and semiconductors is attracted as a promising strategy. The surface modification of semiconductor electrode is useful and facile method to place catalysts and PSs in close proximity. Furthermore, an efficient charge-separation by the electron injection from surface-modified molecules to a conduction band (CB) of a semiconductor is also significant. Sakata et al. reported that [Ru(bpy)₃]²⁺ (bpy = 2,2'-bipyridyl) molecules adsorbed on TiO₂ surface rapidly inject electrons after photoexcitation.¹⁷ Especially, strongly-adsorbed [Ru(bpy)₃]²⁺ molecules exhibited shorter

excited lifetime (12-20 ns), which means faster electron injection than that of weakly-adsorbed ones (40-3500 ns), suggesting that a strong adsorption of PS on the semiconductor surface provide a rapid electron injection and efficient charge separation. Since then, an immobilization of molecules via anchor parts were intensively investigated.¹⁸ Meyer et al. reported that phosphate-anchor modified $[\text{Ru}(\text{bpy})_3]^{2+}$ shows electron injection processes with $\sim 10^{13} \text{ s}^{-1}$ order from $^1\text{MLCT}$ state and $\sim 10^{11} \text{ s}^{-1}$ order from $^3\text{MLCT}$ state.^{18a} Therefore, photoexcitation of the Ru(II) complex immobilized on the TiO_2 surface leads to a rapid and efficient electron injection from the MLCT excited state to the TiO_2 conduction band, resulting in a spatial separation of electrons and holes. Such an electron injection ability enables the molecules- TiO_2 interface to be used not only for placing several components in close proximity but also as a functional interface to promote photoinduced charge separation. In this context, recently it has been vigorously pursued that the application to molecular-based photovoltaic devices such as a dye-sensitized solar cell¹⁹, and photochemical reaction systems such as dye-sensitized photoelectrochemical cell (DSPEC)²⁰⁻²⁴ and dye-sensitized photocatalysts (DSP).²⁵⁻²⁸

1-3-3. Dye-sensitized photoelectrochemical cells (DSPEC)

Around the 2010s, the studies about the molecular-based DSPEC consisted of both catalyst- and dye-loaded semiconductor electrodes began to be reported.²⁰ Especially, intensive efforts have been devoted on the WOC-PS integrated photoanodes. Several types of fabrication methods have been developed for OER photoanode to improve electron-transfer (Fig. 3);²¹ coadsorption,²² loading WOC-embedded Nafion© membrane,^{20b, c} modification of dyads,²³ step-growth connection via bridging metal anion^{24a-c} or metal oxide layer^{24d, e}, and electrochemical polymerization^{24f, g} and so on. These methods can provide the good electron-communication between WOC and PS. And additionally, step-growth modification methods by bridging metal (oxide) and electropolymerization can expand the range of applicability by simplifying the synthesis, increase the loading amount of WOC and/or PS, and improve durability, too.²⁴ These DSPECs are advantageous on the connection with reduction-reaction system and facile approaches to investigate mechanisms by photo/electrochemical analyses are available.

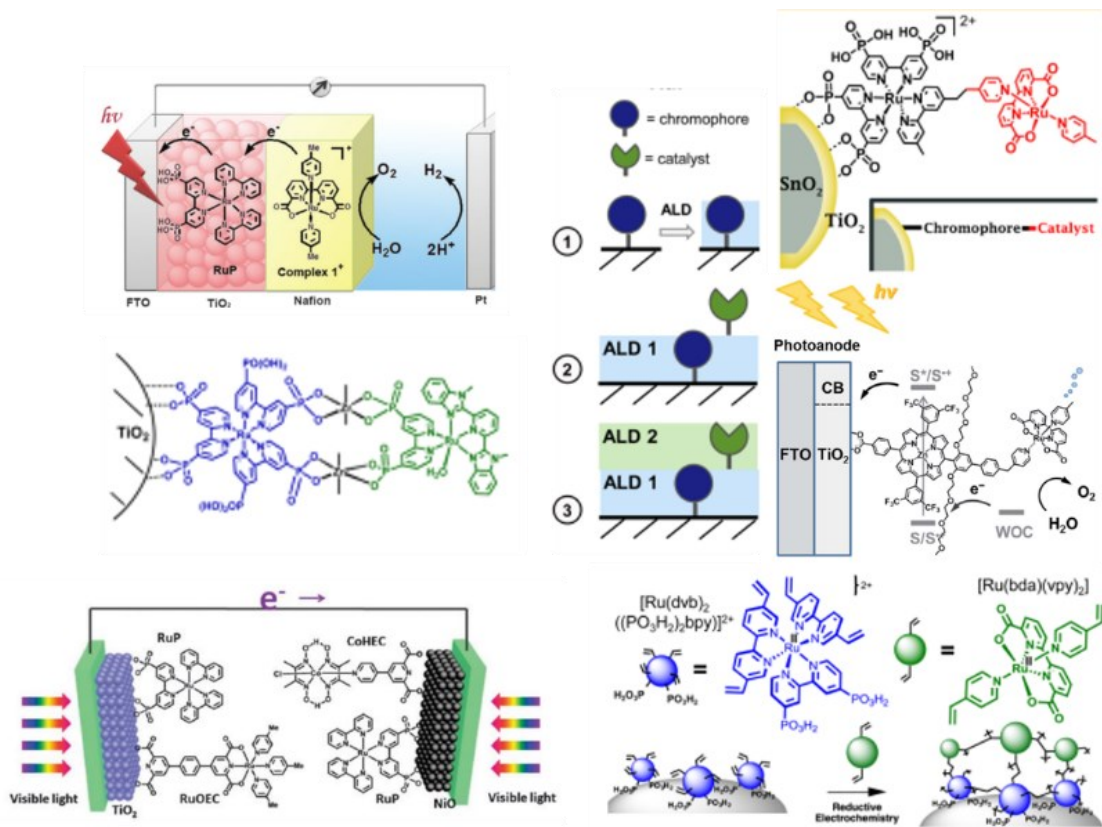


Figure 3. Several types of reported DSPEC for photoelectrochemical OER.²⁰⁻²⁴

1-3-4. Dye-sensitized photocatalysts (DSP)

Dye-sensitized photocatalysts (DSP) composed of surface-immobilized dye molecules and semiconductor particles, have been investigated as a promising method for the application of charge-separation toward the dispersion reaction system and controlling proximity between dyes and catalysts. Lots of studies on DSPs for water oxidation,²⁵ hydrogen evolution reaction,^{25b, 26} water splitting²⁷ and CO₂ reduction²⁸ have been reported so far. Especially, on photochemical OER, Kobayashi et al. conducted to fabricate photosensitized nanoparticles with phosphonic acid group-modified Ru(II) complex dye immobilized on TiO₂ nanoparticles (Fig. 4). The photochemical OER activity was reported to be higher than that of the unimmobilized Ru(II) complex.^{25a}

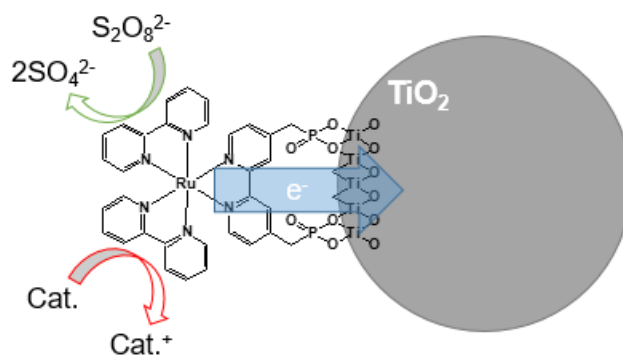


Figure 4. Ru(II)-dye loaded TiO₂ nanoparticles. ^{25a}

Although these approaches mentioned from § 1-3-1 to this section provide the rapid electron transfer from WOC and long-lived charge-separated state, the photocatalytic activity of molecular-based systems are still low. As one of the remained problems for such systems, back-electron transfer to WOC is one of the problems required to overcome.

1-3-5. Back electron transfer process

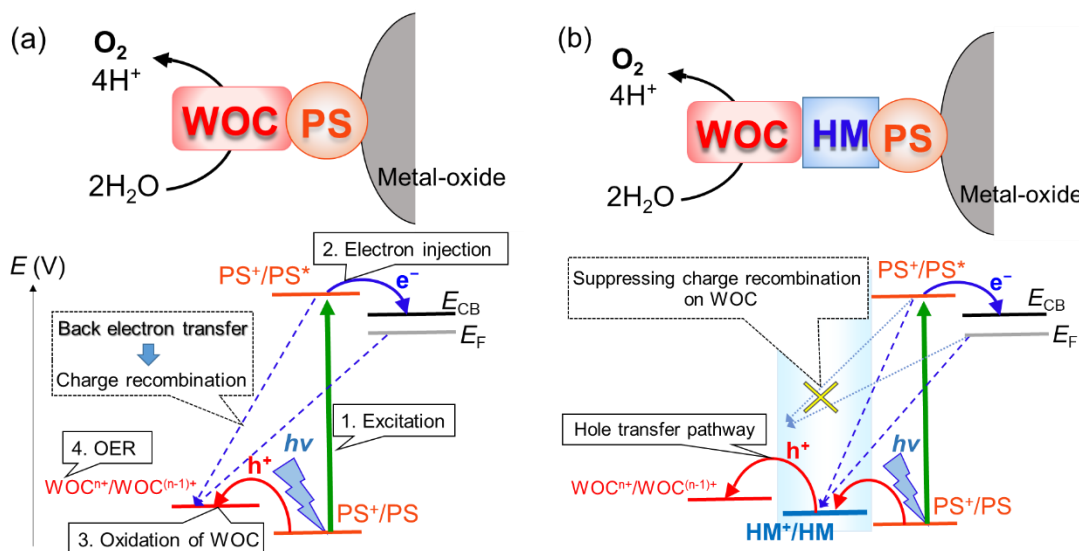
Generally, the photochemical OER on DSPEC and DSP composed of n-type semiconductor substrate like TiO₂ proceeds as follows (Scheme 2a).

- | | |
|--|--|
| 1: Photoexcitation of PS | $PS + h\nu \rightarrow PS^*$ |
| 2: Electron injection from PS* to TiO ₂ | $PS^* + TiO_2 \rightarrow PS^+ + TiO_2(e^-)$ |
| 3: Hole transfer to WOC to regenerate PS | $PS^+ + WOC \rightarrow PS + WOC^{(+)}$ |
| 4: Water oxidation by WOC | |

However, there're subprocesses, back-electron-transfer from PS* or electrode surface, which induces charge-recombination process on the WOC and lowering the catalytic activity.

Considering OER process is followed by light-induced four electron transfer and hole accumulation on the WOC, back-electron transfer is required to suppress for efficient catalysis.

In order to suppress such a back-electron transfer process and achieve efficient hole accumulation on WOC, hole-transporting materials was attracted considerable attention.



Scheme 2. Electron transfer process on photoinduced OER process on (a) WOC-PS directly connected system and (b) HM-inserted system.

1-4 Hole-mediator materials (HM)

Inserting hole-mediator (HM) materials between a WOC part and a PS part is regarded as a promising method for one-directional electron transfer from WOC to PS. There are several requirements for the HM materials on photo/electrochemical OER as follows; high electron mobility, suitable redox potential to provide holes to WOC, and permeability for visible-light. If the materials satisfying above requirements are introduced as HM, back-electron transfer is expected to be blocked up to HM (Scheme 2b) and charge recombination on WOC can be suppressed, with keeping forward-electron transfer as possible.

Similar mechanism exists in the natural photosynthesis system, PSII. Photochemically-generated holes on the photosensitizing P680 dimer passed through tyrosine (Yz) as the hole mediator²⁹ and then finally transferred to WOC Mn_4CaO_5 cluster.³¹ (Fig. 5)

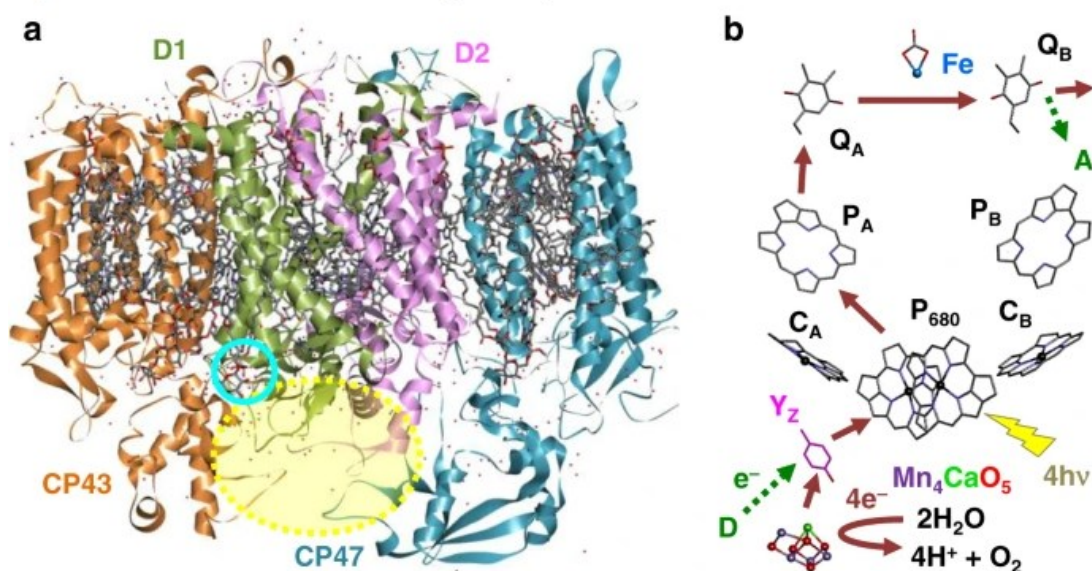


Figure 5. (a) Structure of PSII and (b) electron transfer process including the pathway around tyrosine mediator (Y_z).^{29d}

Such hole-mediating methods have also been utilized for organic light-emitting diodes (OLED) and solar cells in order to improve a hole transfer efficiency, and an exploitation of HM materials has been progressed from this viewpoint.³²

1-4-1 Application of HMs for photo/electrochemical OER system

Recently, HM-inserted photoelectrochemical cells has investigated on molecular-linked systems³³ (Fig. 6) not only on the hetero-junction type metal-oxide-based photoanodes.^{4b, 34} These photoanodes was reported to exhibit higher photoelectrochemical OER activity with suppressing back-electron transfer by the various method such as WOC-HM-PS linkage (Fig. 6a)^{33a}, co-adsorption of HM-modified WOC colloid (Fig. 6b),^{33b} and WOC/HM co-linked PS (Fig. 6c)^{33c}. Especially, WOC-PS connected system via Fe(II) HM achieved achieved further increase of photocurrent and remarkably slow back-electron transfer ($\sim 6\text{ s}^{-1}$) by combination with a viologen-type electron-mediator.^{33a} Meanwhile, these molecular-based attempts are now in trial and error mainly because of the restriction of redox potential. For instance, in the cases on Ru(II)(4, 4'-bipyridyl-6, 6'-dicarboxylato) derivatives (Ru-bda) WOCs, which are popular on molecular-based photoanodes or photocatalysis,³⁵ the redox potential to generate the active species, $\text{Ru}^{\text{IV}}\text{ORu}^{\text{IV}}$ μ -oxo dimer, is reported to be $\sim 1.2\text{ V}$ vs NHE.^{33, 36} However, the redox potentials of commonly-used HM materials like triphenylamine and $[\text{Fe}^{\text{II}}(\text{terpyridyl})_2]^{2+}$ are less than $+1.2\text{ V}$ ³³ that are not enough positive to oxidize WOC. In addition to the lack of oxidizing power of HM, compatibility with the decorating connection part to WOC and/or PS and low photo-silency of HM themselves are difficult. From these background, the rational design for HM-modified photochemical OER system is still explored. Furthermore, the effect on the catalytic activity by modification of HM to WOC from the aspect of molecular chemistry in homogeneous reaction has not investigated yet, while the spectroscopic studies of HM-PS connected systems are intensively examined.³⁷

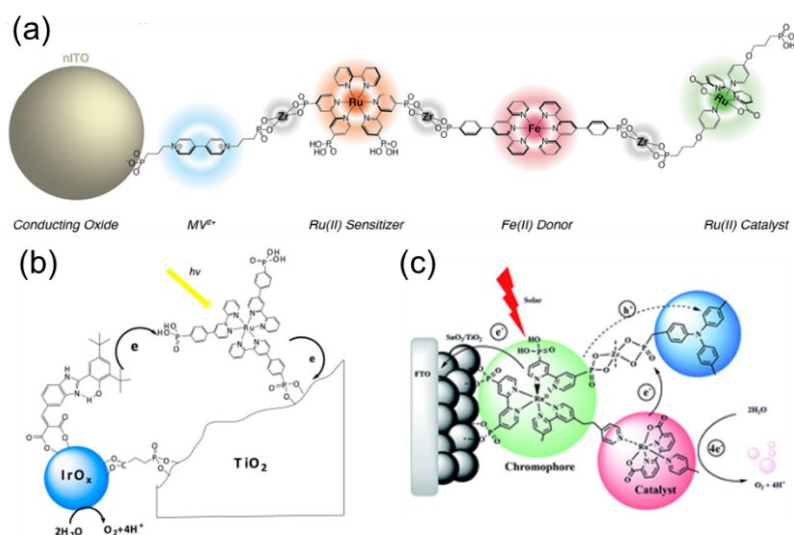


Figure 6. Reported HM-inserted DSPEC for OER on molecular-based systems by (a) WOC-HM-PS-electron mediator connection^{33a}, (b) Co-adsorption of HM-tethered WOC colloid^{33b} and (c) WOC and HM co-linked PS.^{33c}

1-4-2 HMs with positive redox potential

Materials that have positive redox potential and applicable for HM were recently reported. For example, p-doped 2,2', 7,7'-tetrakis(N,N-di-*p*-methoxyphenylamine)-9,9'-spirobifluorene (spiro-OMeTAD) derivatives³⁸ and spiro[fluorene-9,9'-xanthene] (SFX) series³⁹ have been investigated as HM on solar cells with exhibiting high redox potential (>1.25 V). However, the application of these materials for photochemical OER system is still restricted by the difficulty on the connection between PS and WOC. On the other hand, Kobayashi et al. were reported K₂Cd[Ru(CN)₆] Prussian-white analogue, (CdRu-PWA, Fig. 7) which can work as a HM for hydrogen evolution reaction with highly-positive redox potential (~1.42 V).⁴⁰ Such a Prussian-white analogue can be modified to WOC or PS by layer-by-layer method and expected as a promising HM material to integrate to coordination polymer WOC such as Prussian-blue analogues.^{12c, d}

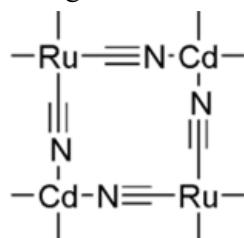


Figure 7. The schematic structure of CdRu-PWA

Carbazole (cbz) derivatives and polycarbazole are also promising HM materials because of their high hole-transporting ability⁴¹ and positive redox potential (cbz : ~1.6 V⁴², polycarbazole : > 1.2 V^{43a}). Especially, polycarbazole was used as a connector to the electrodes or HM materials on electrochemical OER,⁴³ (Fig. 7) and is regarded as attractive materials taking into account its electropolymerization ability. However, a utilization of these HM materials for photochemical OER, especially connection with WOC has been hardly studied yet.

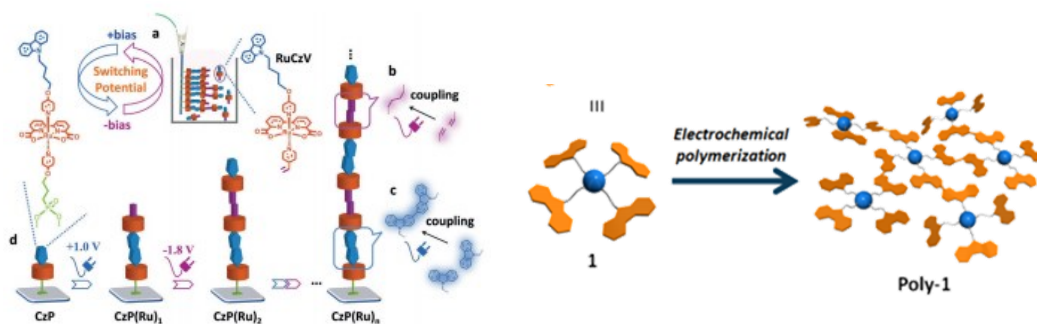
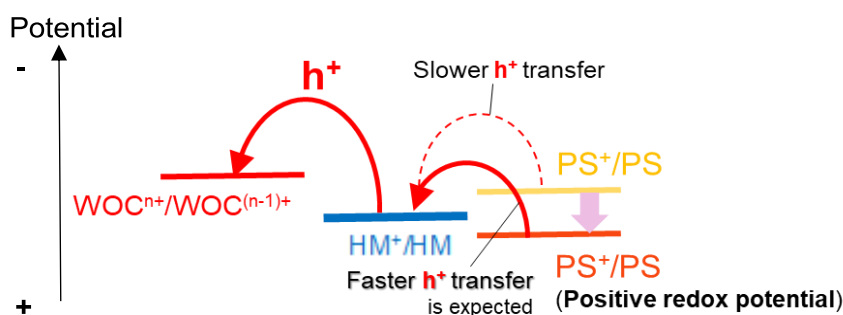


Figure 7 Electrochemical OER photoanodes fabricated by electropolymerization of carbazole-tethered WOCs.⁴³

1-5 Photosensitizers for HM-functionalized photoanodes

PSs with high-oxidation potential are also required for HM-functionalized photoanodes to guarantee the sufficient electron transfer from WOC even through the HM part. The redox potential of PS should be more positive than that of HM to achieve faster hole transfer to WOC. (Scheme 3)



Scheme 3. PSs with positive oxidation potential for HM-integrated photodriven OER system.

For increasing oxidation potential of PSs, an introduction of electron-withdrawing substituents such as trifluoromethyl group is one of the popular methods.⁴⁴ On PSs for the application to photoanodes, anchor groups for modification on metal-oxide surfaces is needed for an efficient electron transfer (§ 1-3-2). As anchor groups, carboxylate or phosphonate⁴⁵ groups are often used and their redox potentials are relatively high. (On $[\text{Ru}(\text{bpy})_3]^{2+}$ derivatives : ~ 1.4 V) However, to expand the scope of an applicability of HM, PSs with more positive redox potential are to be required. Additionally, it is also reported that these anchors can easily desorb into aqueous media due to hydrolysis of the linkages.⁴⁶ From such viewpoints, pyridyl-group⁴⁷ is one remarkable anchor, because of its electron withdrawing ability (Hammett constant = 0.94⁴⁸, higher than that of carboxylate and phosphonate, 0.45 and 0.48).⁴⁹ Furthermore, pyridyl-anchor is reported to have high durability against hydrolysis and following desorption from TiO_2 electrode in the aqueous mixture.^{22g, 47c-f} (Fig. 9).^{47c} From such features, PSs with pyridyl-anchors are promising for HM-inserted photoanodes.

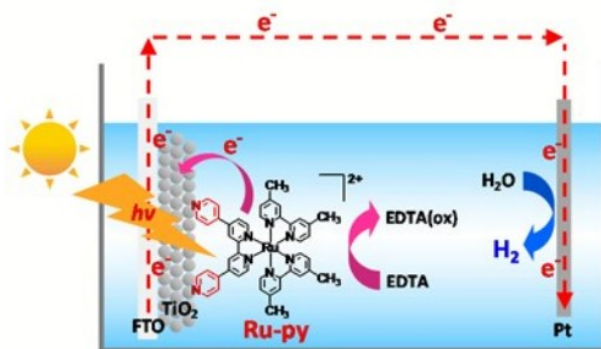


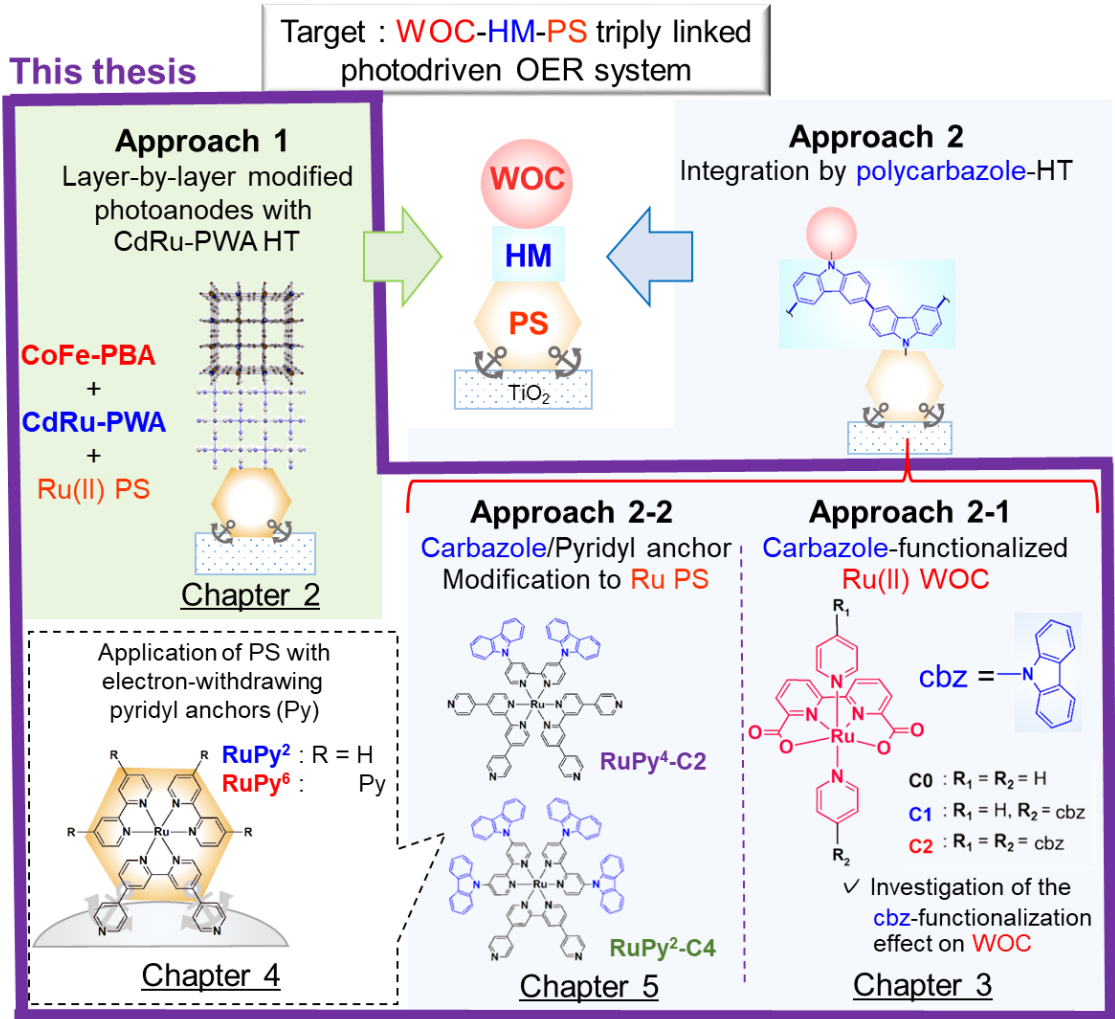
Fig. 9 Hydrogen-evolution DSPEC with pyridyl-anchor modified Ru(II) PS.^{47c}

1-6 Purpose of this thesis

In this thesis, aiming to construct HM-functionalized photochemical OER system, HMs and PSs with highly positive redox potential are focused. The outline of this thesis is shown in Scheme 4.

As HM, CdRu-PWA or cbzs were investigated because of their suitable redox property, facile modification, permeability for visible light and electrical conductivity. The former HM was utilized for layer-by-layer modification of WOC and HM, and the latter was directed to apply for WOC-PS connection via HM polymers by electropolymerization method. The effect by introduction of cbz groups on WOC and PS was studied for the utilization on the electrodes. Pyridyl-anchor modified $[\text{Ru}(\text{bpy})_3]^{2+}$ derivatives are promising as the PS from the viewpoint of their highly positive oxidation potential, immobilization ability and WOC-capturing ability. Although pyridyl-anchored complexes were often used for photochemical hydrogen-evolution reaction,^{47c, e, 49} the applicability for photochemical OER hadn't been reported yet at the beginning of this research. Thus, their applicability for photochemical OER was investigated with applying $[\text{Ru}(\text{bpy})_3]^{2+}$ derivatives two- or six-pyridyl groups, $[\text{Ru}(\text{bpy})_2(\text{qpy})]^{2+}$ and $[\text{Ru}(\text{qpy})_3]^{2+}$ (bpy : 2,2'-bipyridine, qpy : 2,2'-4,4''-4',4'''-quaterpyridine), denoted as **RuPy²** and **RuPy⁶**.

Aiming to apply for above-mentioned HM-polymer integrated photoanodes, cbz-connected Ru(II) molecular WOCs, $[\text{Ru}(\text{bda})(\text{cbz-py})(\text{pyridine})]$ and $[\text{Ru}(\text{bda})(\text{cbz-py})_2]$ (**C1** and **C2**, cbz-py = 9-(pyridin-4-yl)-9*H*-carbazole) and Ru(II) dyes; $[\text{Ru}(\text{dcbzbpy})_2(\text{qpy})]^{2+}$ and $[\text{Ru}(\text{dcbzbpy})(\text{qpy})_2]^{2+}$ (**RuPy²-C4** and **RuPy⁴-C2**, dcbzbpy = 4,4'-di(9*H*-carbazol-9-yl)-2,2'-bipyridine), were synthesized, and investigated their catalytic activity or photochemical property.



Scheme 4. Outline of this thesis.

1-7 Outline of this thesis

This thesis consists of six chapters as follows.

The general background and the purpose of this thesis are described in chapter 1.

In chapter 2, as an exploitation of HM materials for photoelectrochemical OER, $K_2Cd[Ru(CN)_6]$ (CdRu-PWA) was in focus. CdRu-PWA and $K_{2x}Co_{(3-x)}[Fe(CN)_6]_2 \cdot nH_2O$ Prussian-blue analogue (PBA) WOC were modified on the Ru(II) PS-modified TiO_2 electrode by layer-by-layer method. Modification of both CoFe-PBA and CdRu-PWA were successfully achieved. Electrochemical OER and photoelectrochemical response of these obtained multilayered anodes were also observed.

In chapter 3, the author focused on the application of carbazole (cbz) as HM precursor from the viewpoint of the suitable redox potential, polymerization ability and electrical conductivity. In order to elucidate the effect of cbz-functionalization on WOC, the $[Ru(bda)(pyridine)_2]$ -type ³⁵ WOCs modified 1 or 2 eq. of cbz substituents, denoted as **C1** and **C2**, were synthesized and compared their photo/electro-chemical properties and chemical or photochemical OER catalytic activity with non-substituted $[Ru(bda)(pyridine)_2]$. **C1** and **C2** maintained the catalytic processes of original $[Ru(bda)(pyridine)_2]$ -type WOCs and exhibited higher catalytic activity mainly due to the electron-withdrawing ability of cbz groups. In addition, specific redox and OER behaviors related to the oxidation process of cbz groups are also discussed.

In chapter 4, pyridyl-anchor-modified Ru(II) PSs, $[Ru(bpy)_2(qpy)]^{2+}$ (**RuPy²**) and $[Ru(qpy)_3]^{2+}$ (**RuPy²**; bpy = 2, 2'-bipyridyl, qpy = 2,2'-4,4''-4',4'''-quaterpyridine) are highlighted as the PSs with anchor parts and a positive oxidation potential. The applicability of these complexes and photosensitizing- TiO_2 nanoparticles loaded them to OER was investigated. In the solution reaction with a sacrificial oxidant, these complexes showed lower reactivity with the oxidant and OER photocatalytic activity. In contrast, those of **RuPy²** were improved by immobilization on TiO_2 nanoparticle. These results exhibited the ability as PS for OER of these complexes were mainly restricted by low reactivity by introduced pyridyl groups and such an affect can mitigate by immobilization. In addition, the effect of exposing the pyridyl group on the surface on catalytic adsorption was also examined.

In chapter 5, The syntheses of both pyridyl- and carbazoles-modified Ru(II) complexes, **RuPy⁴-C2** and **RuPy²-C4**, aiming to apply the polycarbazole-inserted OER photoanodes (**RuPy⁴-C2** : $[Ru(dcbzbpy)(qpy)_2]^{2+}$, **RuPy²-C4** : $[Ru(dcbzbpy)_2(qpy)]^{2+}$ and dcbzbpy : 4,4'-di(9*H*-carbazol-9-yl)-2,2'-bipyridine). Their photochemical property was investigated with using theoretical calculations. Obtained complexes exhibited high-molar absorptivity, long lifetime and polymerization behavior, suggesting the applicability for electropolymerization to connect PS and WOC.

Finally, the general conclusion and future perspective of this thesis are described in chapter 6.

1-8 References

- 1 (a) A. J. Esswein, D. G. Nocera, *Chem. Rev.*, 2007, **107**, 4022.(b) T. R. Cook, D. K. Dogutan, S. Y. Reece, Y. Surendranath, T. S. Teets, D. G. Nocera, *Chem. Rev.* 2010, **110**, 6474.(c) M.G. Walter, E.L. Warren, J.R. McKone, S.W. Boettcher, Q. Mi, E.A. Santori, N.S. Lewis, *Chem. Rev.*, 2010, **110**, 6446.
- 2 (a) Ž. Kovačič, B. Likozar, M. Huš, *ACS Catal.* 2020, **10**, 14984. (b) T. Kong, Y. Jiang, Y. Xiong, *Chem. Soc. Rev.*, 2020, **49**, 6579.
- 3 A. Fujishima, K. Honda, *Nature* 1972, **238**, 37.
- 4 (a) A. Kudo, Y. Miseki, *Chem. Soc. Rev.* 2009, **38**, 253.(b) D.G. Nocera, *Acc. Chem. Res.* 2012, **45**, 767.(c) Q. Wang, T. Hisatomi, Q. Jia, H. Tokudome, M. Zhong, C. Wang, Z. Pan, T. Takata, M. Nakabayashi, N. Shibata, Y. Li, I. D. Sharp, A. Kudo, T. Yamada, K. Domen, *Nat. Mater.* 2016, **15**, 611.
- 5 (c) D. Wang, J. Hu, B. D. Sherman, M. V. Sheridan, L. Yan, C. J. Dares, Y. Zhu, F. Li, Qing Huang, Wei You, Thomas J. Meyer, *Proc. Natl. Acad. Sci, USA*, 2020, **117**, 13256.
- 6 (a) S. Sato, T. Arai, T. Morikawa, K. Uemura, T. M. Suzuki, H. Tanaka, T. Kajino, *J. Am. Chem. Soc.*, 2011, **133**, 15240. (b) Q. Wang, J. Warnan, S. Rodríguez-Jimenez, J. J. Leung, S. Kalathil, V. Andrei, K. Domen, E. Reisner, *Nat. Energy*, 2020, **5**, 703.(c) A. Nakada, H. Kumagai, M. Robert, O. Ishitani, K. Maeda, *Acc. Mater. Res.*, 2021, **2**, 458. (d) F. Kuttassery, H. Kumagai, R. Kamata, Y. Ebato, M. Higashi, H. Suzuki, R. Abe, O. Ishitani, *Chem. Sci.*, 2021, **12**, 13216.
- 7 (a) F. A. Armstrong, *Philos. Trans. R. Soc., B*, 2007, **363**, 1263. (b) N. Cox, D. A. Pantazis, F. Neese, W. Lubitz, *Acc. Chem. Res.* 2013, **46**, 1588.(c) D. J. Vinyard, G. M. Ananyev, G. C. Dismukes, *Annu. Rev. Biochem.* 2013, **82**, 577. (d) J. Yano, V. Yachandra, *Chem. Rev.* 2014, **114**, 4175. (e) J. Barber, *Biochemistry* 2016, **55**, 5901.
- 8 K. Maeda, *Adv. Mater.*, 2019, **31**, 1808205.
- 9 H. Inoue, T. Shimada, Y. Kou, Y. Nabetani, D. Masui, S. Takagi and H. Tachibana, *ChemSusChem.*, 2011, **4**, 173.
- 10 (a) M. D. Kärkäs, E. V. Johnston, O. Verho and B. Åkermark, *Acc. Chem. Res.*, 2014, **47**, 100. (b) M. D. Kärkäs, O. Verho, E. V. Johnston and B. Åkermark, *Chem. Rev.*, 2014, **114**, 11863. (c) J. D. Blakemore, R. H. Crabtree and G. W. Brudvig, *Chem. Rev.*, 2015, **115**, 12974.(d) R. Matheu, P. Garrido-Barros, M. Gil-Sepulcre, M. Z. Ertem, X. Sala, C. Gimbert-Suriñach and A. Llobet, *Nat. Rev. Chem.*, 2019, **3**, 331. (e) M. Kondo, H. Tatewaki and S. Masaoka, *Chem. Soc. Rev.*, 2021, **50**, 6790.
- 11 (a) L. Yang, H. Zhou, T. Fan, D. Zhang, *Phys. Chem. Chem. Phys.*, 2014,**16**, 6810. (b) K. Sivula, R. van de Krol, *Nat. Rev. Mater.* 2016, **1**, 15010. (c) Z. N. Zahran, E. A. Mohamed, Y.

- Tsubonouchi, M. Ishizaki, T. Togashi, M. Kurihara, K. Saito, T. Yui, M. Yagi, *Energy Environ. Sci.*, 2021, **14**, 5358.
- 12 (a) H. Cho, L. Yao, J. H. Yum, Y. Liu, F. Boudoire, R. A. Wells, N. Guijarro, A. Sekar, K. Sivula, *Nat. Catal.*, 2021, **4**, 431. (b) H. Hu, Z. Wang, L. Cao, L. Zeng, C. Zhang, W. Lin, C. Wang, *Nat. Chem.* 2021, **13**, 358. (c) S. Goberna-Ferrón, W. Y. Hernández, B. Rodríguez-García, J. R. Galán-Mascarós, *ACS Catal.* 2014, **4**, 1637. (d) S. Pintado, S. Goberna-Ferrón, E. C. Escudero-Adán, J. R. Galán-Mascarós, *J. Am. Chem. Soc.*, 2013, **135**, 13270. (e) C. Wang, J. Wang, W. Lin, *J. Am. Chem. Soc.*, 2012, **134**, 19895. (f) W. Li, S. Watzele, H. A. El-Sayed, Y. Liang, G. Kieslich, A. S. Bandarenka, K. Rodewald, B. Rieger, R. A. Fischer, *J. Am. Chem. Soc.*, 2019, **141**, 5926.
- 13 (a) S. Fukuzumi, K. Ohkubo, H. Imahori, J. Shao, Z. Ou, G. Zheng, Y. Chen, R. K. Pandey, M. Fujitsuka, O. Ito, K. M. Kadish, *J. Am. Chem. Soc.*, 2001, **123**, 10676. (b) H. Imahori, D. M. Guldi, K. Tamaki, Y. Yoshida, C. Luo, Y. Sakata, S. Fukuzumi, *J. Am. Chem. Soc.*, 2001, **123**, 6617. (c) H. Imahori, Y. Sekiguchi, Y. Kashiwagi, T. Sato, Y. Araki, O. Ito, H. Yamada, S. Fukuzumi, *Chem-Eur. J.*, 2004, **10**, 3184.
- 14 (a) H. Ozawa, M. Haga, K. Sakai, *J. Am. Chem. Soc.*, 2006, **128**, 4926. (b) G. F. Manbeck, E. Fujita, K. J. Brewer, *J. Am. Chem. Soc.* 2017, **139**, 7843.
- 15 (a) B. Gholamkhash, H. Mametsuka, K. Koike, T. Tanabe, M. Furue, O. Ishitani, *Inorg. Chem.*, 2005, **44**, 2326. (b) Y. Tamaki, K. Koike, T. Morimoto, Y. Yamazaki, O. Ishitani, *Inorg. Chem.*, 2013, **52**, 11902. (c) Y. Kuramochi, O. Ishitani, *Inorg. Chem.*, 2016, **55**, 5702. Y. Tamaki, O. Ishitani, *ACS Catal.*, 2017, **7**, 3394.
- 16 (a) F. Li, Y. Jiang, B. Zhang, F. Huang and Y. Gao, L. Sun, *Angew. Chem. Int. Ed.*, 2012, **51**, 2417. (b) L. Wang, M. Mirmohades, A. Brown, L. Duan, F. Li, Q. Daniel, R. Lomoth, L. Sun and L. Hammarström, *Inorg. Chem.*, 2015, **54**, 2742.
- 17 T. Kajiwara, K. Hashimoto, T. Kawai, T. Sakata, *J. Phys. Chem.*, 1982, **86**, 4516.
- 18 (a) K. Hanson, M. K. Brennaman, A. Ito, H. Luo, W. Song, K. A. Parker, R. Ghosh, M. R. Norris, C. R. K. Glasson, J. J. Concepcion, R. Lopez, T. J. Meyer, *J. Phys. Chem. C*, 2012, **116**, 14837. (b) M. Abrahamsson, P. G. Johansson, S. Ardo, A. Kopecky, E. Galoppini, G. J. Meyer, *J. Phys. Chem. Lett.* 2010, **1**, 1725. (c) S. Ardo, G. J. Meyer, *Chem. Soc. Rev.* 2009, **38**, 115. (d) P. G. Giokas, S. A. Miller, K. Hanson, M. R. Norris, C. R. K. Glasson, J. J. Concepcion, S. E. Bettis, T. J. Meyer, A. M. Moran, *J. Phys. Chem. C*, 2013, **117**, 812.
- 19 (a) A. Hagfeldt, G. Boschloo, L. Sun, L. Kloo, H. Pettersson, *Chem. Rev.* 2010, **110**, 6595. (b) K. Kalyanasundaram, M. Grätzel, *Coord. Chem. Rev.*, 1998, **77**, 347.
- 20 (a) W. J. Youngblood, S. H. A. Lee, Y. Kobayashi, E. A. Hernandez-Pagan, P. G. Hoertz, T. A. Moore, A. L. Moore, D. Gust, T. E. Mallouk, *J. Am. Chem. Soc.*, 2009, **131**, 926. (b) R. Brimblecombe, A. Koo, G. C. Dismukes, G. F. Swiegers, L. Spiccia, *J. Am. Chem. Soc.*,

- 2010, **132**, 2892. (c) L. Li, L. Duan, Y. Xu, M.I. Gorlov, A. Hagfeldt, L. Sun, *Chem. Commun.*, 2010, **46**, 7307.
- 21 (a) D. L. Ashford, M.K. Gish, A.K. Vannucci, M.K. Brennaman, J. L. Templeton, J. M. Papanikolas, *Chem. Rev.* 2015, **115**, 13006. (b) M. K. Brennaman, R. J. Dillon, L. Alibabaei, M. K. Gish, C. J. Dares, D. L. Ashford, R. L. House, G. J. Meyer, J. M. Papanikolas, T. J. Meyer, *J. Am. Chem. Soc.* 2016, **138**, 13085. (c) X. Fang, S. Kalathil, E. Reisner, *Chem. Soc. Rev.*, 2020, **49**, 4926. (d) X. Liang, X. Cao, W. Sun, Y. Ding, *ChemCatChem*, 2019, **11**, 6190. (e) F. Niu, D. Wang, F. Li, Y. Liu, S. Shen, T. J. Meyer, *Adv. Energy Mater.*, 2020, **10**, 1900399.
- 22 (a) K. Fan, F. Li, L. Wang, Q. Daniel, E. Gabrielsson, L. Sun, *Phys. Chem. Chem. Phys.*, 2014, **16**, 25234. (b) F. Li, K. Fan, B. Xu, E. Gabrielsson, Q. Daniel, L. Li, L. Sun, *J. Am. Chem. Soc.*, 2015, **137**, 9153. (c) T. E. Rosser, M. A. Gross, Y.H. Lai, E. Reisner, *Chem. Sci.*, 2016, **7**, 4024. (d) K.-R. Wee, B. D. Sherman, M. K. Brennaman, M. V. Sheridan, A. Nayak, L. Alibabaei, T. J. Meyer, *J. Mater. Chem. A* 2016, **4**, 2969. (e) M. Yamamoto, Y. Nishizawa, P. Chábera, F. Li, T. Pascher, V. Sundström, L. Sun, H. Imahori, *Chem Commun.*, 2016, **52**, 13702. (f) Y. K. Eom, L. Nhon, G. Leem, B. D. Sherman, D. Wang, L. Troian-Gautier, S. Kim, J. Kim, T. J. Meyer, J. R. Reynolds, K. S. Schanze, *ACS Energy Lett.* 2018, **3**, 2114. (g) Y. Zhu, D. Wang, Q. Huang, J. Du, L. Sun, F. Li, T. J. Meyer, *Nat. Commun.* 2020, **11**, 4610. (h) M. V. Sheridan, D. J. Hill, B. D. Sherman, D. Wang, S. L. Marquard, K. -R. Wee, J. F. Cahoon, T. J. Meyer, *Nano Lett.* 2017, **17**, 2440.
- 23 (a) J. J. Concepcion, J. W. Jurss, P. G. Hoertz and T. J. Meyer, *Angew. Chem. Int. Ed.* 2009, **48**, 9473. (b) L. Alibabaei, B. D. Sherman, M. R. Norris, M. K. Brennaman, T. J. Meyer, *Proc. Natl. Acad. Sci. U. S. A.* 2015, **112**, 5899. (c) B. D. Sherman, Y. Xie, M. V. Sheridan, D. Wang, D. W. Shaffer, T. J. Meyer and J. J. Concepcion, *ACS Energy Lett.*, 2017, **2**, 124. (d) M. K. Brennaman, M. K. Gish, L. Alibabaei, M. R. Norris, R. A. Binstead, A. Nayak, A. M. Lapides, W. Song, R. J. Brown, J. J. Concepcion, J. L. Templeton, J. M. Papanikolas, T. J. Meyer, *J. Phys. Chem. C* 2018, **122**, 13017. (e) M. Yamamoto, L. Wang, F. Li, T. Fukushima, K. Tanaka, L. Sun and H. Imahori, *Chem. Sci.*, 2016, **7**, 1430. (f) D. Antón-García, J. Warnan and E. Reisner, *Chem. Sci.*, 2020, **11**, 12769.
- 24 (a) M. V. Sheridan, B. D. Sherman, R. L. Coppo, D. Wang, S. L. Marquard, K. -R. Wee, N. Y. Murakami Iha, T. J. Meyer, *ACS Energy Lett.* 2016, **1**, 231. (b) B. Shan, M. K. Brennaman, L. Troian-Gautier, Y. Liu, A. Nayak, C. M. Klug, T. -T. Li, R. M. Bullock, T. J. Meyer, *J. Am. Chem. Soc.* 2019, **141**, 10390. (c) K. Hanson, D. A. Torelli, A. K. Vannucci, M. K. Brennaman, H. Luo, L. Alibabaei, W. Song, D. L. Ashford, M. R. Norris, C. R. K. Glasson, J. J. Concepcion, T. J. Meyer, *Angew. Chem. Int. Ed.*, 2012, **51**, 12782. (d) D. Wang, F. Niu, M. J. Mortelliti, M. V. Sheridan, B. D. Sherman, Y. Zhu, J. R. McBride, J. L. Dempsey, S. Shen,

- C. J. Dares, F. Li, T. J. Meyer, *Proc. Natl. Acad. Sci.* 2020, **117**, 12564. (e) A. M. Lapidés, B. D. Sherman, M. K. Brennaman, C. J. Dares, K. R. Skinner, J. L. Templeton, T. J. Meyer, *Chem. Sci.* 2015, **6**, 6398. (f) D. L. Ashford, A. M. Lapidés, A. K. Vannucci, K. Hanson, D. A. Torelli, D. P. Harrison, J. L. Templeton, T. J. Meyer, *J. Am. Chem. Soc.* 2014, **136**, 6578. (g) D. L. Ashford, B. D. Sherman, R. A. Binstead, J. L. Templeton, T. J. Meyer, *Angew. Chem. Int. Ed.* 2015, **54**, 4778.
- 25 (a) A. Kobayashi, S. Furugori, M. Yoshida, M. Kato, *Chem. Lett.*, 2016, **45**, 619. (b) S. Furugori, A. Kobayashi, A. Watanabe, M. Yoshida, M. Kato, *ACS Omega*, 2017, **2**, 3902.
- 26 (a) F. Lakadamyali, E. Reisner, *Chem. Commun.*, 2011, **47**, 1695. (b) J. Willkomm, K. L. Orchard, A. Reynal, E. Pastor, J. R. Durrant, E. Reisner, *Chem. Soc. Rev.*, 2016, **45**, 9. (c) Z. Youssef, L. Colombeau, N. Yesmurzayeva, F. Baros, R. Vanderesse, T. Hamieh, J. Toufaily, C. Frochot, T. Roques-Carmes, S. Acherar, *Dyes and Pigments*, 2018, **159**, 49. (d) A. Kobayashi, S. Watanabe, M. Yoshida, M. Kato, *ACS Appl. Energy Mater.*, 2018, **1**, 2882. (e) N. Yoshimura, A. Kobayashi, M. Yoshida, M. Kato, *Bull. Chem. Soc. Jpn.* 2019, **92**, 1793. (f) N. Yoshimura, A. Kobayashi, W. Genno, T. Okubo, M. Yoshida, M. Kato, *SusEneFuels* 2020, **4**, 3450. (g) N. Yoshimura, A. Kobayashi, M. Yoshida, M. Kato, *Chem-Eur. J.* 2020, **26**, 16939. (h) A. Kobayashi, E. Muramatsu, M. Yoshida, M. Kato, *Energies* 2021, **14**, 2425. (i) L. Zani, M. Melchionna, T. Montini, P. Fornasiero, *J. Phys. Energy*, 2021, **3**, 31001
- 27 (a) T. Oshima, S. Nishioka, Y. Kikuchi, S. Hirai, K. Yanagisawa, M. Eguchi, Y. Miseki, T. Yokoi, T. Yui, K. Kimoto, K. Sayama, O. Ishitani, T. Mallouk, K. Maeda, *J. Am. Chem. Soc.*, 2020, **142**, 8412. (b) F. Kuttassery, S. Sagawa, S. Mathew, Y. Nabetani, A. Iwase, A. Kudo, H. Tachibana, H. Inoue, *ACS Applied Energy Mater.* 2019, **2**, 8045.
- 28 D. Saito, Y. Yamazaki, Y. Tamaki, O. Ishitani, *J. Am. Chem. Soc.*, 2020, **142**, 19249.
- 29 (a) L. Hammarström, S. Styring, *Energy Environ. Sci.* 2011, **4**, 2379. (b) J. P. McEvoy, G. W. Brudvig, *Chem. Rev.* 2006, **106**, 4455. (c) K. Saito, A. W. Rutherford, H. Ishikita, *Proc. Natl. Acad. Sci. USA*, 2013, **110**, 7690. (d) P. Chernev, S. Fischer, J. Hoffmann, N. Oliver, R. Assunção, B. Yu, R. L. Burnap, I. Zaharieva, D. J. Nürnberg, M. Haumann H. Dau, *Nat. Commun.*, 2020, **11**, 6110
- 30 Y. Umena, K. Kawakami, J. R. Shen, N. Kamiya, *Nature*, 2011, **473**, 55.
- 31 T. J. Meyer, M. H. V. Huynh, H. H. Thorp, *Angew. Chem., Int. Ed.* 2007, **46**, 5284.
- 32 (a) Z. Yu, A. Hagfeldt, L. Sun, *Coord. Chem. Rev.*, 2020, **406**, 213143. (b) Shahnawaz, S. S. Swayamprabha, M. R. Nagar, R. A. K. Yadav, S. Gull, D. K. Dubey, J. –H. Jou, *J. Mater. Chem. C*, 2019, **7**, 7144.
- 33 (a) D. Wang, R. N. Sampaio, L. Troian-Gautier, S. L. Marquard, B. H. Farnum, B. D. Sherman, M. V. Sheridan, C. J. Dares, G. J. Meyer and T. J. Meyer, *J. Am. Chem. Soc.*, 2019, **141**, 7926.

- (b) Y. Zhao, J. R. Swierk, J. D. Megiatto, B. Sherman, W. J. Youngblood, D. Qin, D. M. Lentz, A. L. Moore, T. A. Moore, D. Gust, T. E. Mallouk, *Proc. Natl. Acad. Sci. U. S. A.* 2012, **109**, 15612. (c) D. Wang, Z. Xu, M. V. Sheridan, J. J. Concepcion, F. Li, T. Lian, T. J. Meyer, *Chem. Sci.*, 2021, **12**, 14441.
- 34 (a) X. Ning, B. Lu, Z. Zhang, P. Du, H. Ren, D. Shan, J. Chen, Y. Gao, X. Lu, *Angew. Chem. Int. Ed.* 2019, **58**, 16800. (b) G. Yang, S. Li, X. Wang, B. Ding, Y. Li, H. Lin, D. Tang, X. Ren, Q. Wang, S. Luo, J. Ye, *Appl. Catal. B: Environmental* 2021, **297**, 120268.
- 35 B. Zhang and L. Sun, *J. Am. Chem. Soc.* 2019, **141**, 5565.
- 36 J. J. Concepcion, D. K. Zhong, D. J. Szalda, J. T. Muckerman, E. Fujita, *Chem. Commun.* 2015, **51**, 4105.
- 37 K. Hu, R. N. Sampaio, J. Schneider, L. Troian-Gautier, G. J. Meyer, *J. Am. Chem. Soc.* 2020, **142**, 16099.
- 38 (a) M. K. Teck, S. Dharani, H. Li, R. P. Rajiv, N. Mathews, C. G. Andrew, G. M. Subodh, *ChemSusChem* 2014, **7**, 1909. (b) J. Lu, A.D. Scully, J. Sun, B. Tan, A.S.R. Chesman, S. Ruiz Raga, L. Jiang, X. Lin, N. Pai, W. Huang, Y.-B. Cheng, U. Bach, A.N. Simonov, *J. Phys. Chem. Lett.* 2019, 4675. (c) Y. Saygili, S.-H. Turren-Cruz, S. Olthof, H. Saes Bartholomeus Wilhelmus, B. P. Ilknur, M. Saliba, K. Meerholz, T. Edvinsson, S. M. Zakeeruddin, M. Grätzel, J.-P. Correa-Baena, A. Hagfeldt, M. Freitag, W. Tress, *ChemPhysChem* 2018, **19**, 1363.
- 39 M. Maciejczyk, A. Ivaturia, N. Robertson, *J. Mater. Chem. A*, 2016, **4**, 4855.
- 40 H. Kitano, A. Kobayashi, M. Yoshida, M. Kato, *Sustainable Energy Fuels*, 2018, **2**, 2609.
- 41 (a) K. Karon and M. Lapkowski, *J. Solid State Electrochem.*, 2015, **19**, 2601. (b) L. Kortekaas, F. Lancia, J. D. Steen and W. R. Browne, *J. Phys. Chem. C*, 2017, **121**, 14688. (c) M. Li, *Chem. - A Eur. J.*, 2019, **25**, 1142.
- 42 (a) Z. Singh, P. R. Donnarumma and M. B. Majewski, *Inorg. Chem.*, 2020, **59**, 12994. (b) S. O. Furer, B. Bozic-Weber, M. Neuburger, E. C. Constable, C. E. Housecroft, *RSC Adv.*, 2015, **5**, 69430.
- 43 (a) J. Zhang, J. Du, J. Wang, Y. Wang, C. Wei, M. Li, *Angew. Chem. Int. Ed.*, 2018, **57**, 16698. (b) H. Iwami, M. Okamura, M. Kondo, S. Masaoka, *Angew. Chem. Int. Ed.*, 2021, **60**, 5965.
- 44 (a) L. Wang, D. W. Shaffer, G. F. Manbeck, D. E. Polyansky, J. J. Concepcion, *ACS Catal.*, 2020, **10**, 580. (b) R. M. O'Donnell, R. N. Sampaio, G. Li, P. G. Johansson, C. L. Ward, G. J. Meyer, *J. Am. Chem. Soc.* 2016, **138**, 3891.
- 45 (a) P. Pechy, F. P. Rotzinger, M. K. Nazeeruddin, O. Kohle, S. M. Zakeeruddin, R. Humphry-Baker, M. Gratzel, *J. Chem. Soc., Chem. Commun.*, 1995, **65**. (b) K. A. Mauritz, R. B. Moore, *Chem. Rev.*, 2004, **104**, 4535. (c) M. Yagi, K. Nagoshi, M. Kaneko, *J. Phys. Chem. B*, 1997, **101**, 5143. (d) R. Brimblecombe, D. R. J. Kolling, A. M. Bond, G. C. Dismukes, G. F.

- Swiegers, L. Spiccia, *Inorg. Chem.*, 2009, **48**, 7269. (e) L. Zhang, J. M. Cole, *ACS Appl. Mater. Interfaces*, 2015, **7**, 3427.
- 46 (a) B. J. Brennan, A. E. Keirstead, P. A. Liddell, S. A. Vail, T. A. Moore, A. L. Moore, D. Gust, *Nanotechnology*, 2009, **20**, 505203. (b) B. J. Brennan, M. J. L. Portolos, P. A. Liddell, T. A. Moore, A. L. Moore, D. Gust, *Phys. Chem. Chem. Phys.*, 2003, **15**, 16605.
- 47 (a) Y. Ooyama, S. Inoue, T. Nagano, K. Kushimoto, J. Ohshita, I. Imae, K. Komaguchi, Y. Harima, *Angew. Chem. Int. Ed.*, 2011, **50**, 7429. (b) C. -L. Mai, T. Moehl, C. -H. Hsieh, J. -D. Décoppet, S. M. Zakeeruddin, M. Grätzel, C. -Y. Yeh, *ACS Appl. Mater. Interfaces*, 2015, **7**, 14975 (c) K. Takijiri, K. Morita, T. Nakazono, K. Sakai, H. Ozawa, *Chem. Commun.*, 2017, **53**, 3042. (d) K. Morita, K. Takijiri, K. Sakai, H. Ozawa, *Dalton Trans.*, 2017, **46**, 15181. (e) K. Morita, K. Sakai, H. Ozawa, *ACS Appl. Energy Mater.* 2019, **2**, 987. (f) K. Akamine, K. Morita, K. Sakai, H. Ozawa, *ACS Appl. Energy Mater.* 2020, **3**, 4860.
- 48 J. H. Blanch, *J. Chem. Soc. B*, 1966, **937**.
- 49 C. Hansch, A. Leo, R.W. Taft, *Chem. Rev.* 1991, **91**, 165
- 50 (a) E. Rousset, D. Chartrand, I. Ciofini, V. Marvaud, G.S. Hanan, *Inorg. Chem.* 2017, **56**, 9515. (b) E. Rousset, D. Chartrand, I. Ciofini, V. Marvaud, G.S. Hanan, *Chem. Commun.* 2015, **51**, 9261.

Chapter 2

**Construction of Prussian-White
Hole-Mediator-Integrated Photoanodes**

1 Introduction

As mentioned in Chapter 1, a Prussian-white analogue composed by cyanide bridges of Cd(II) and Ru(II), $K_2Cd^{II}[Ru^{II}(CN)_6]$ (**CdRu-PWA**, Fig. 1), is expected as a hole-mediator (HM) material because of the suitable redox property and transparent nature for visible light.¹ As one of the methods to apply such coordination polymers for (photo)electrodes, stepwise growth on a substrate by layer-by-layer (LbL) method to form a surface-mounted metal–organic framework (SURMOF) has attracted considerable attention.² General procedures for fabricating such SURMOFs are as follows (Scheme 1a); 1. Modification of self-assembled monolayer (SAM) on a substrate as the scaffold for construction of framework, 2. Stepwise growth of MOF by repeating alternate immersions to metal precursor solution and (metallo)ligand solution. In this context, this LbL method for SURMOF formation could be applicable to fabricate photoanodes comprising the three components, PS, HM and WOC. An anchor-modified dye modification to semiconductor was studied intensively as mentioned in the sections 1-3 and 1-5 in Chapter 1. By utilizing PS molecules immobilized on an electrode surface as the SAM, the HM-integrated OER photoelectrode is expected to construct by further formation of **CdRu-PWA** HM layer and **CoFe-PBA** WOC layer by the LbL method. In fact, Haga et al. reported the growth of Prussian-blue film on a Ru(II) complex modified ITO electrode.³

In this chapter, HM-integrated OER photoanodes were fabricated by the following LbL method (Scheme 1b); 1. phosphonate anchor-substituted Ru(II) photosensitizer, **RuP⁶** ($[Ru(dpbbpy)_3]^{2+}$, $dpbbpy = 4, 4'$ -diphosphonate-2, 2'-bipyridyl, Fig. 1), was immobilized on TiO₂-annealed FTO (fluorine-doped tin oxide) electrode, 2. **CdRu-PWA** was formed on the upper surface of **RuP⁶** dye layer scaffold, 3. $K_{2x}Co^{III}_{(3-x)}[Fe^{II}(CN)_6]_2 \cdot nH_2O$ (**CoFe-PBA**, Fig. 1), was formed on the upper surface of **CdRu-PWA** as a coordination-polymer WOC with low overpotential (~305 mV).⁴ By altering the number of LbL process for **CoFe-PBA** (denoted as **x**) and **CdRu-PWA** (**y**) formations, several photoanodes **B^xW^yRu** with different layer thickness of WOC (**x** = 1, 3) and HM (**y** = 1, 3) were prepared (Scheme 2). Obtained **B^xW^yRu** photoanodes exhibited electrochemical OER activity, and such response was indicated to occur after the electron transfer through **CdRu-PWA**. These photoelectrochemical responses were also investigated.

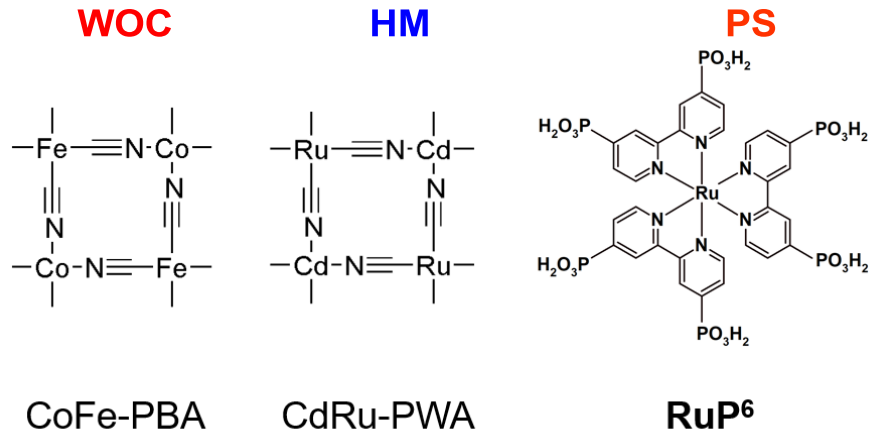
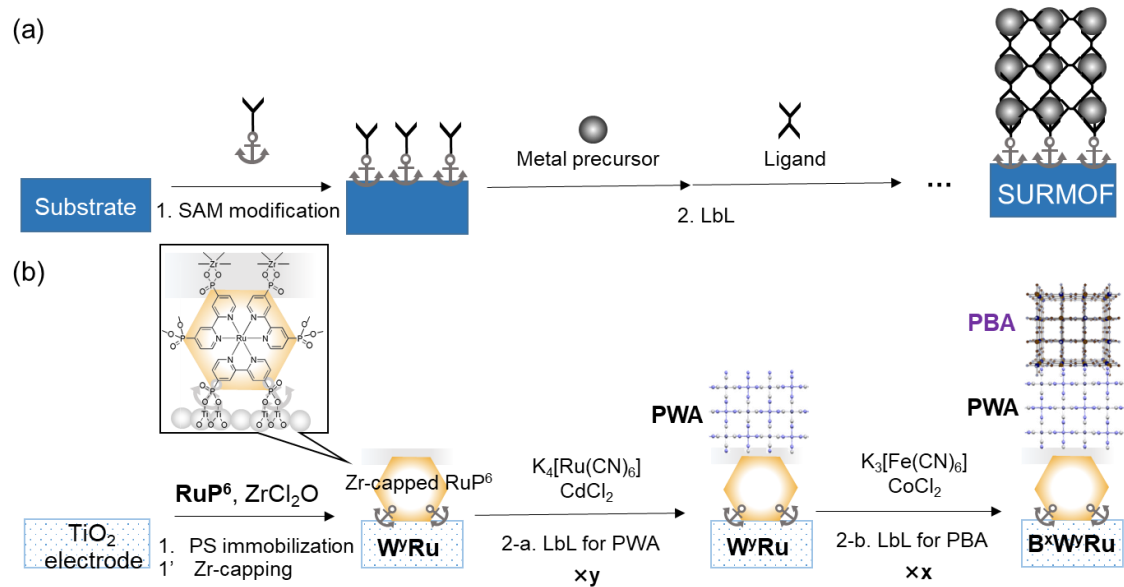
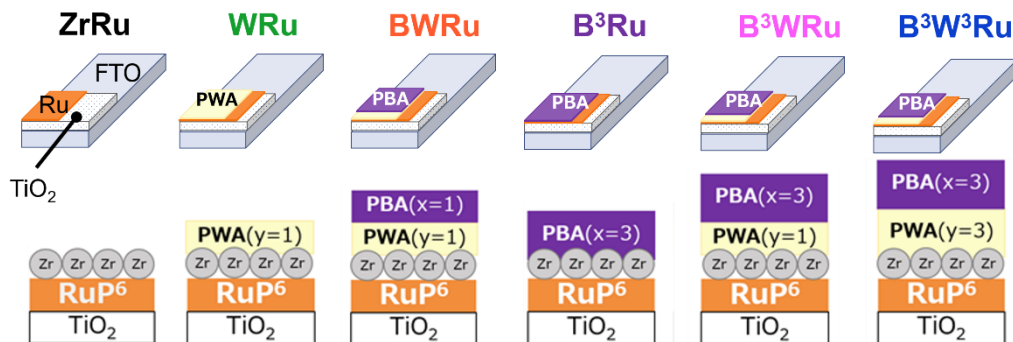


Figure 1. The framework of **CoFe-PBA** WOC and **CdRu-PWA** HM, and the chemical structure of fully-protonated **RuP⁶** PS.



Scheme 1. Procedures of (a) SURMOF formation by LbL method and (b) fabrication of the multilayered OER photoelectrodes used in this work.



Scheme 2. Schematic representation of **B^xW^yRu** photoanodes.

2-2 Experimental

2-2-1 Measurements

¹H NMR spectra were recorded using a JEOL ECZ-400S instrument. IR spectra were recorded on a JASCO FT-IR 4100 spectrophotometer equipped diamond ATR crystal unit. X-ray fluorescence (XRF) analyses were carried out on a Bruker S2 PUMA energy-dispersive X-ray fluorescence spectrometer. UV-vis absorption spectra and diffuse-reflectance spectra were recorded on a Shimadzu UV-2400PC spectrophotometer. The obtained reflectance spectra were converted to absorption spectra using the Kubelka-Munk function $F(R_{\infty})$. Electrochemical measurements were recorded using a HOKUTO DENKO HZ-3000 three-electrode electrochemical measurement system equipped with a modified TiO₂ electrode, Pt wire, and Ag/AgCl (aqueous mixture) electrodes as the working, counter, and reference electrodes, respectively. Aqueous solution of phosphate buffer (pH = 6.0, 100 mM) containing 0.5 M sodium perchlorate (NaClO₄) as the supporting electrolyte were used in the electrochemical measurements. All solutions were deaerated by N₂ bubbling for more than 15 min before measurement. Cyclic voltammetry measurements were carried out in the one-compartment cell with 8 mL of solution and the other electrochemical measurements were carried out on the condition described in § 2-2-2 to monitor the amount of evolved oxygen or light irradiation.

2-2-2 Electrochemical water oxidation

In an H-shaped two-compartments cell (EC frontier VB12) separated by a membrane, 15 mL of aqueous solution of phosphate buffer (pH = 6.0, 100 mM) containing 0.5 M sodium perchlorate (NaClO₄) was placed to both compartments. Gaseous phase is ca. 21 mL in each compartment. A working and an Ag/AgCl reference electrode were inserted to an anodic compartment and a Pt coil counter electrode was inserted to a cathodic one. Solutions in both of compartments were deaerated by Ar bubbling for ~30 min before injection. The amount of evolved oxygen was monitored using a FireSting oxygen monitor (PyroScience GmbH). The Faradaic efficiency (FE) was estimated using the eq. (1) and (2) from the amount of evolved O₂ (n_{O_2}), the generated current I (A) and passed electron (n_e):

$$n_e \text{ (mol)} = \text{Charge (C)} / 96500 \text{ (Cmol}^{-1}\text{)} = \sum_t (s) I \text{ (A)} / 96500 \text{ (Cmol}^{-1}\text{)} \quad (1)$$

$$\text{FE(\%)} = n_{O_2} \text{ (mol)} / (1/4 n_e) \times 100 \quad (2)$$

In order to eliminate the contribution of the large current in initial several minutes attributed to charge collection state, the values until 10 minutes after the bias application were omitted for these estimations.

2-2-3 Photoelectrochemical measurement

In the dark, the experimental setup was carried out with the same manner as the electrochemical water oxidation described in the § 2-2-2. The solution was deoxygenated by bubbling with Ar gas for 30 min. The amount of evolved oxygen was monitored using a FireSting oxygen monitor (PyroScience GmbH). The cell was irradiated by a 300 W Xe lamp (Asahi spectra, MAX-303) through cutoff (Asahi spectra Y-42) and cold filters. ($420 \text{ nm} < \lambda < 800 \text{ nm}$, 40 mW cm^{-2})

2-2-6 Materials

4,4'-bis(diethylphosphonate)-2,2'-bipyridine,⁵ [Ru(4,4'-bisphosphonate-2,2'-bpy)₃]Cl₂ (**RuP⁶**)^{5, 6}, **CoFe-PBA**^{4a} and **CdRu-PWA**⁷ were synthesized according to literature methods. TiO₂ nanoparticles (SSP-M, $\sim\phi = 15$ nm) were purchased from the Sakai Chemical Industry Co. Ltd. Fluorine-doped tin oxide coated electrode (8 Ω /sq., Thickness ~ 3.0 mm 735183-5EA, Aldrich) was purchased from Sigma-Aldrich. High-purity water was obtained by passing house-distilled water through a Millipore Milli-Q Simplicity® UV system. All other reagents and solvents were purchased from commercial sources and used as received.

2-2-7 Mesoporous TiO₂ thin film on FTO glasses substrate (TiO₂/FTO)

Mesoporous TiO₂ thin film on FTO glasses substrate (FTO/TiO₂ electrode) were fabricated by squeegee method followed by sintering process. TiO₂ paste was prepared by mixing and sonication of SSP-M (1.6 g), acetic acid (2 mL), Milli-Q (4 mL) and PEG-1000 (0.8 g).⁸ TiO₂ paste-applied FTO electrodes were dried in the air and then annealed at 520°C for 30 min.⁹ Before the dye-immobilization process, these electrodes were re-annealed at 520°C for 30 min for elimination of surface-coordinated water molecules. The apparent area of the TiO₂ film was 1.0 cm².

2-2-8 Preparation of RuPy⁶ modified TiO₂ electrodes (RuP⁶@TiO₂/FTO)

Modification of **RuP⁶** to pristine TiO₂/FTO electrodes were carried out by an immersion to 200 μ M, 2 mL of **RuP⁶** solution (100 mM HClO₄ aq.) for 24 hours at r.t..¹⁰ After the immersion process, electrodes were rinsed by HClO₄ aq., water and methanol, and dried in the air at room temperature. The amount of **RuP⁶** adsorbed on the TiO₂ surfaces was estimated to be 226 nmolcm⁻² by the absorbance change at 463 nm in the immersion solution. (Fig. 2)

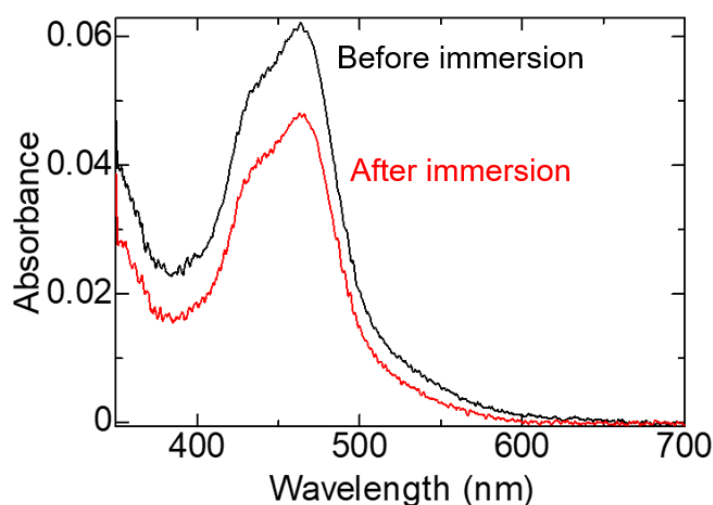


Figure 2. UV-Vis absorption spectra of the immersion solutions before/after immobilization of **RuP⁶**. Solutions were diluted 50 times by the solvent of each reaction.

2-2-9 Preparation of Zr-capped RuPy⁶ modified electrodes (ZrRu)

RuP⁶@TiO₂/FTO was immersed to 5 mM of ZrCl₂O solution in methanol for 1 h¹¹, and then washed with methanol and dried in the air at room temperature. Electrodes were stored in the dark except when the measurement.

2-2-10 Preparation of CdRu-PWA modified electrodes (W^yRu)^{1, 7}

ZrRu was immersed to 20 mM of K₄[Ru(CN)₆] aqueous solution for 30 min. After washing with water, the electrode was immersed to 20 mM of CdCl₂ aqueous solution for 30 min to form **CdRu-PWA** and then washed and dried in the air to afford **W¹Ru** photoanode. By repeating this process (e.g. immersion to K₄[Ru(CN)₆] solution → washing → CdCl₂ solution → washing) for **y** times to afford **W^yRu** photoanodes.

2-2-11 Preparation of CoFe-PBA modified electrodes (B^xW^yRu)

B^x(W^y)Ru were fabricated by the similar LbL method described in § 2-2-10 by using 20 mM of K₃[Fe(CN)₆] aqueous solution and 40 mM of CoCl₂ aqueous solution as precursors of **CoFe-PBA** WOC. **ZrRu** without CdRu-PWA layer or **W^yRu** photoanodes were used for fabrication of **B^xRu** or **B^xW^yRu** photoanodes, respectively.

2-3. Results and Discussion

2-3-1 Fabrication and Characterization

Modification of CdRu-PWA and CoFe-PBA

The amount of immobilized **RuP⁶** was estimated as 226 nmolcm⁻² from the UV-vis absorption spectra of the dye solutions before and after immersion (Figure 2). Zr(IV)-capping was followed to suppress the desorption of **RuP⁶** during the LbL process and in the measurement. After the LbL modification, **B^xW^yRu**s was obtained.

XRF measurement was also carried out. Fig. 3 and Table 1 showed the XRF spectra of each anode and estimated atomic ratio, respectively. Ru K α radiation at 19.0-19.6 keV and Zr K α radiation at 15.4-16.0 keV were detected on all the electrodes (Fig. 3b), indicating the successful immobilization of **RuP⁶** on TiO₂ surface and the binding of Zr capping metal anions to the phosphonate groups of **RuP⁶**. Cd K α radiation was detected on PWA-modified electrodes, **WRu**, **BWRu**, **B³WRu** and **B³W³Ru** while it was hardly observed for **B³Ru** and **ZrRu** photoanodes without **CdRu-PWA** layer (Fig. 3c). Thus, the **CdRu-PWA** layer was successfully formed on the upper surface of ZrRu electrode (Fig. 3c and Table 1). In addition to the Cd radiation, peaks of Fe and Co (K α and K β) were observed on **BWRu**. These peaks suggest **CoFe-PBA** layer were also modified on **BWRu**. Larger peaks of Fe and Co K radiations around 6-8 keV were observed on **B³**-type electrodes than the others, (Fig. 3a) which indicates the presence of larger amount of **CoFe-PBA** on the **B³**-type electrode than the others. These results suggest that the larger amount of **CoFe-PBA** grow by the increasing number of LbL process. Notably, the loading amount of **CoFe-PBA** of **B³Ru** was estimated to be higher (1.6-1.7 times on Co atom as a catalytic center^{4, 12}) than that of the other **B³**-types anodes, **B³WRu** and **B³W³Ru**. These lower loading amounts of **CoFe-PBA** on the **CdRu-PWA**-modified anodes may be due to the lattice mismatch between **CoFe-PBA** and **CdRu-PWA**.

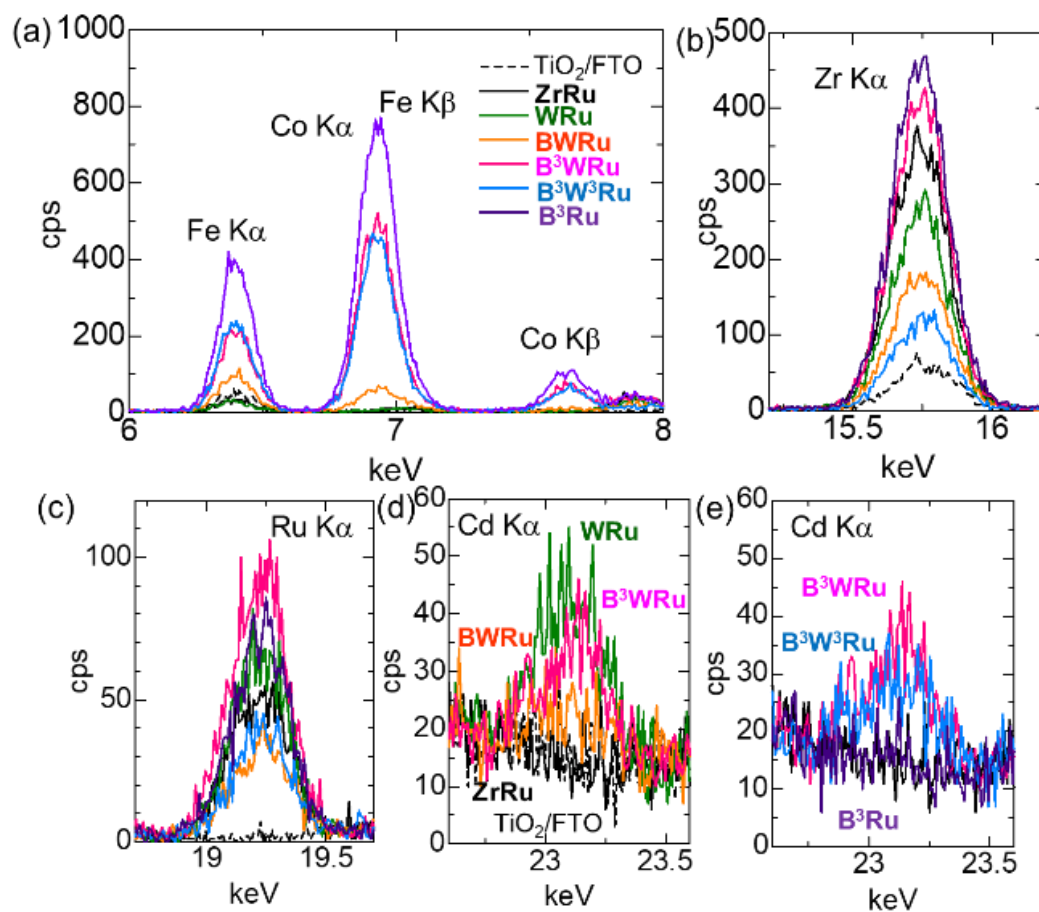


Figure 3. XRF spectra on (a) Co and Fe K region (tube voltage: 40 kV), (b) Zr K α , (c) Ru K α and (d)(e) Cd K α region (tube voltage: 50 kV) of **B³Ru** (purple dashed line), **B³WRu** (pink), **B³W³Ru** (blue), **BWRu** (orange), **WRu** (green), **ZrRu** (black) and TiO₂/FTO (black dashed line) electrodes.

Table 1. Atomic ratio of each electrode.

Anode	Atomic ratio (mol/100 mol TiO ₂)				
	Fe	Co	Zr	Ru	Cd
B³Ru	0.475	0.633	0.318	0.0292	n.d.
B³WRu	0.270	0.424	0.119	0.0375	9.32×10 ⁻³
B³W³Ru	0.291	0.379	0.277	0.0145	7.01×10 ⁻³
BWRu	0.113	0.0516	0.0780	0.0127	3.63×10 ⁻³
WRu	0.0361 ^a	4.08×10 ^{-3a}	0.173	0.0253	0.0145
ZrRu	0.0416 ^a	3.67×10 ^{-3a}	0.244	0.0211	n.d.
TiO ₂ /FTO	0.0562 ^a	2.71×10 ^{-3a}	0.0358	2.37×10 ⁻⁴	n.d.

^a Residual peaks of FTO electrodes.

ATR-IR spectrum of each electrode is shown in Fig. 4a. **B³Ru** exhibited a strong peak at 2161 cm⁻¹ that is assignable to the C≡N stretching mode of **CoFe-PBA** (Fig. 4b),^{4a, 12} indicating that the **CoFe-PBA** WOC layer was successfully formed on the surface of **ZrRu** electrode. Additionally, a broad peak assigned as C≡N stretching mode of K_{2x}Co^{II}_(2-x)[Fe^{II}(CN)₆]₂ that is a Co-reduced Prussian-white species (**CoFe-PWA**) was observed at 2094 cm⁻¹,^{4a, 12} similar as **CoFe-PBA** powder (Fig. 4b). On the other hand, on **WRu**, a broad peak at 2084 cm⁻¹, assigned as the C≡N stretching mode of **CdRu-PWA**, was observed. This peak was shifted higher wavenumber than that of **CdRu-PWA** powder (2064 cm⁻¹, Fig. 4b). Considering the position of the C≡N stretching mode reflects the electron deficiency of coordinated metals, this peak shift is possibly due to the growth of **CdRu-PWA** layer on the higher-valent Zr(IV) scaffold. Similar peaks at 2072 cm⁻¹, 2105 cm⁻¹ and 2161 cm⁻¹ were observed on both **B³W³Ru** and **B³WRu**. These peaks were assigned as C≡N stretching mode of **CdRu-PWA**, **CoFe-PWA** and **CoFe-PBA**, respectively. This assignment is in agreement to the electron density of coordinated metals. The intensity of the peak at 2161 cm⁻¹ of each anode was smaller than that of **B³Ru**. This result suggests that smaller amount of **CoFe-PBA** was modified on the PWA-functionalized electrodes. On the other hand, the CN stretching peak of **CoFe-PBA** was hardly observed for **BWRu** while the peak assignable to that of **CoFe-PWA** was obviously observed at 2074 and 2087 cm⁻¹, suggesting that the CoFe species are existed as the Co-reduced PWA on the electrode. These two mostly overlapped peaks are assignable to the CN stretching mode of **CdRu-PWA**, and **CoFe-PWA** species respectively, because of the high-electron density nature of **CdRu-PWA** than **CoFe-PWA**.

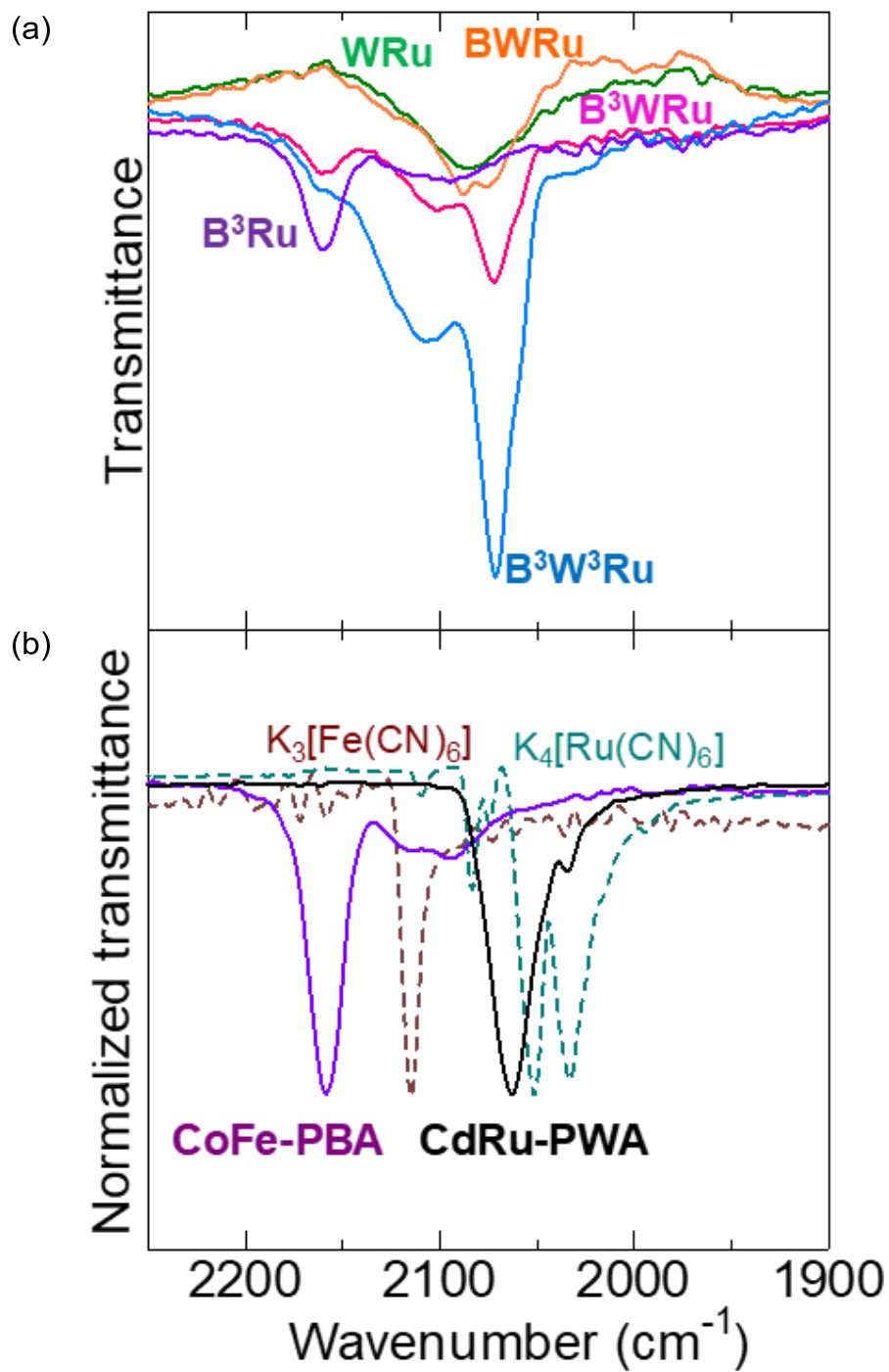


Fig. 4 (a) ATR-IR spectra of B^3W^3Ru photoanodes. (b) IR spectra of bulk CoFe-PBA (purple solid line), CdRu-PWA (black solid line), $K_3[Fe(CN)_6]$ (brown dashed line) and $K_4[Ru(CN)_6]$ (green dashed line) by KBr method.

2-3-2 Photochemical property

Diffuse reflectance spectra of all $\mathbf{B^xW^yRu}$ photoelectrodes are shown in Fig. 5 in comparison with TiO_2/FTO substrate. All photoanodes except for TiO_2/FTO substrate exhibited the absorption band at around 460 nm assignable to the $^1\text{MLCT}$ band of RuP^6 (Fig. 5), indicating that RuP^6 was successfully immobilized on TiO_2 surface. Notably, the absorption band edge of $\mathbf{B^3W^yRu}$ photoanodes was commonly shifted to longer wavelength up to 700 nm, while that of the other photoanodes with thinner (\mathbf{BWRu}) or without CoFe-PBA layer (\mathbf{WRu}) were observed at around 620 nm. Considering the absorption edge of $\mathbf{CoFe-PBA}$ was observed at around 700 nm (Fig. 5b), the longer wavelength shift of the absorption band edge suggests the successful formation of $\mathbf{CoFe-PBA}$ layer on the electrode surface.

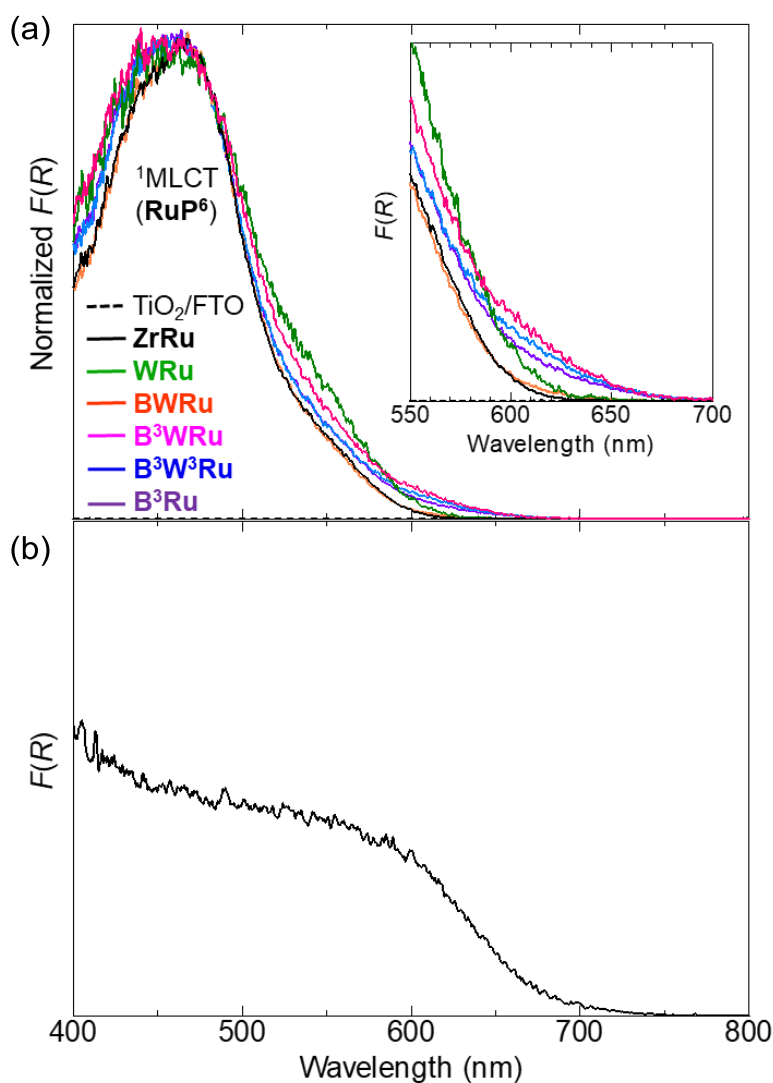


Figure 5. (a) Diffuse reflection spectra of $\mathbf{B^xW^yRu}$. (The absorbance was normalized by the values at 460 nm.) (b) Diffuse reflection spectra of $\mathbf{CoFe-PBA}$.

2-3-3 Electrochemical measurement

Cyclic voltammograms of anodes in neutral media (pH = 6.0) are shown in Fig. 6. **ZrRu** and **WRu** photoanodes exhibited a quasi-reversible redox couple at 1.24 V (vs NHE) that is assigned as the Ru(III/II) process of the surface-immobilized **RuP⁶**. The Ru(III/II) redox potential of these photoanodes were almost comparable, indicating that the formation of **CdRu-PWA** layer on the surface of **ZrRu** electrode hardly affected on the redox behavior of **RuP⁶**. Since the catalytic current assignable to OER was hardly observed for **ZrRu** and **WRu**, neither **RuP⁶** nor **CdRu-PWA** has OER catalytic activity. On the other hand, **CoFe-PBA** loaded photoanodes, **BWRu** and **B³WRu**, exhibited large current above 1.3 V, assignable as the catalytic current of OER. These results are consistent to the literatures showing that **CoFe-PBA** can act as the WOC. The catalytic current increased by increasing the number of LbL processes for **CoFe-PBA** (**B³WRu** > **BWRu**) probably because of the larger loading amount of **CoFe-PBA** WOC.

To elucidate the loading effect of **CdRu-PWA** as the HM layer, the cyclic voltammograms of **B³**-type photoanodes, **B³Ru**, **B³WRu** and **B³W³Ru**, were compared in Fig. 7. The catalytic current of OER obviously decreased by increasing the thickness of **CdRu-PWA** HM layer (Table 2, **B³Ru** > **B³WRu** > **B³W³Ru**). One of the plausible origins of the catalytic current decrease is the lower loading amount of **CoFe-PBA** WOC as discussed in section 2-3-1. Notably, the catalytic current of **B³W³Ru** was much lower than that of **B³WRu** whereas XRF analysis suggested that the amount of Co atom in **CoFe-PBA** WOC of **B³WRu** was almost comparable to that of **B³W³Ru** (Table 1). These results suggest that the **CdRu-PWA** HM layer may act as the insulator between **CoFe-PBA** WOC and **RuP⁶** photosensitizer.

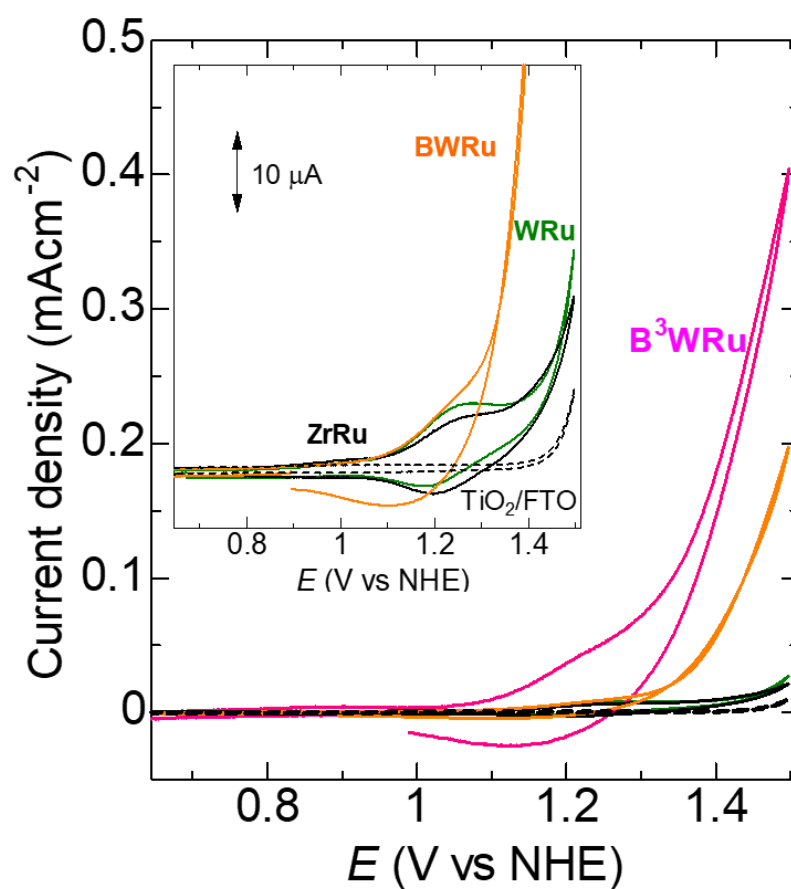


Fig. 6. Cyclic voltammograms of **B^xWRu** (x = 0, 1, 3) and **ZrRu**.

In aqueous solution of phosphate buffer (pH = 6.0, 100 mM) containing 0.5 M NaClO₄.

Counter electrode: Pt wire, Reference electrode: Ag/AgCl (aqueous mixture).

Scan rate: 10 mVs⁻¹. Inset is enlarged figure of the voltammograms on 0.9-1.5 V vs NHE.

Inset: enlarged voltammograms around the Ru(III/II) redox wave of **RuP⁶**.

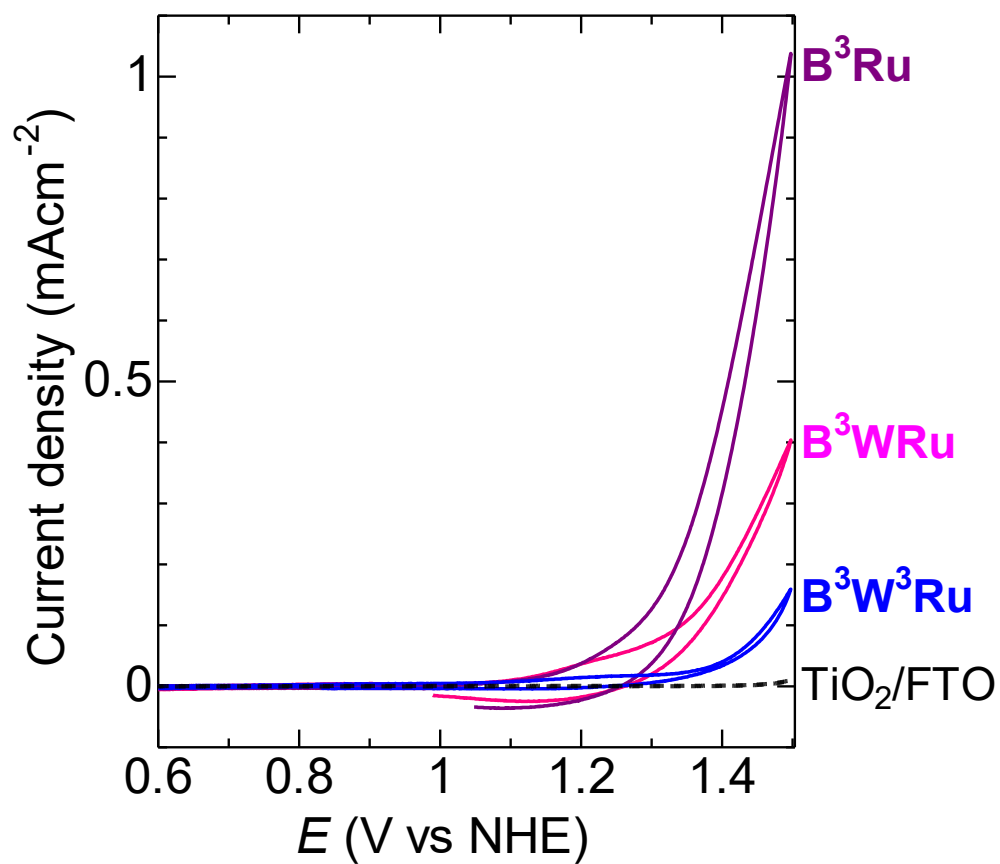


Figure 7. Cyclic voltammograms of $\text{B}^3\text{W}^y\text{Ru}$. Each measurement was carried out under the same condition noted in the caption of Fig. 7.

Table 2. The values of current density at 1.5 V vs NHE.

	Current density ($\mu\text{A cm}^{-2}$)
B^3Ru	1038
B^3WRu	404
$\text{B}^3\text{W}^3\text{Ru}$	159
BWRu	197
WRu	27.2
ZrRu	21.5

2-3-4 Electrochemical water oxidation

The electrochemical OER activity of each photoanode was evaluated by chronoamperometry with monitoring the O_2 concentration in the anodic compartment of reaction cell. Time-profiles of the anodic current under application of external bias (+1.5 V vs NHE) and plots of OER were shown in Fig. 8a and 8b, respectively. The large current due to charge-collection state was observed in the initial few minutes and followed by constant current that depended on the photoanode. The total charge of each anode in 10-60 min is listed in Table 3. The similar trend to the CV measurement was observed in this experiment; the current density decreased in the following order ($B^3Ru > B^3WRu > BWRu > WRu \cong ZrRu \cong 0$). In this electrolysis, O_2 amount was continuously increased on PBA-loaded photoanodes, showing the electrocatalytic OER. Faradaic efficiency (FE) of each photoanode was estimated from these OER plots and total charge estimated by eq. (1). Comparison of the ideal amount of O_2 evolution with 100% FE and experimentally detected O_2 amount is shown in Figure 10 and summarized in Table 3. Estimated FE of all the three PBA-modified anodes, B^3Ru , B^3WRu and $BWRu$ were in the range from 50 to 58%, suggesting the integration of $CdRu$ -PWA hardly give a negative effect on FE. However, these FE are about half to the literature value for $CoFe$ -PBA modified FTO electrode (~100%).^{4b} The reason of low FE of these anodes is still unclear, it might be due to H_2O_2 generation and/or oxidative dissolution the surface immobilized $CoFe$ -PBA on the $CdRu$ -PWA that could be promoted by the lattice mismatch between these two layers.

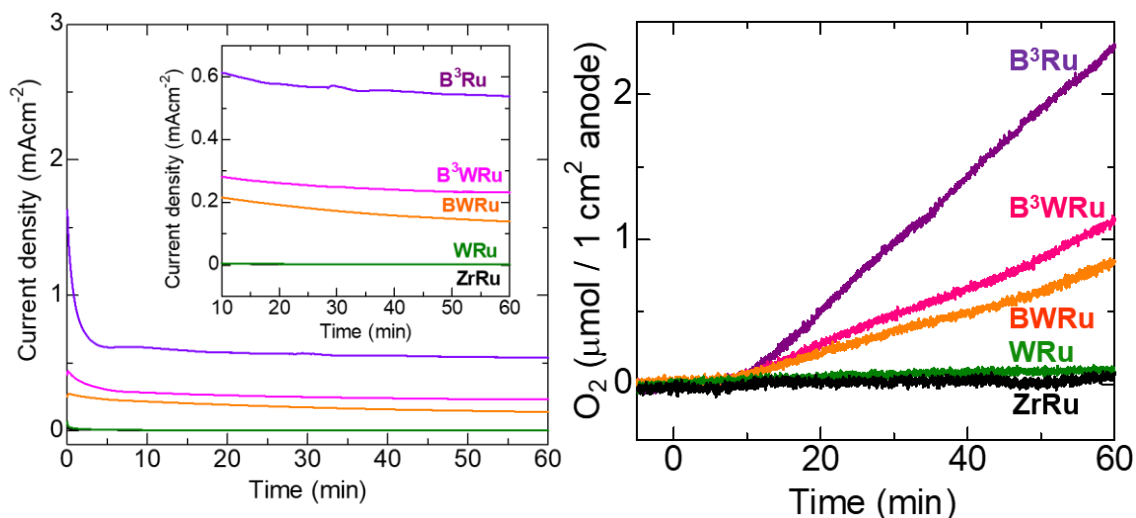


Figure 8. (a) Time profile of the current on the chronoamperometry of anodes (pH = 6.0) with applying 1.5 V vs NHE. Inset is enlarged plots in 10~60 min. (b) Electrochemical OER plots of each anode in the chronoamperometry.

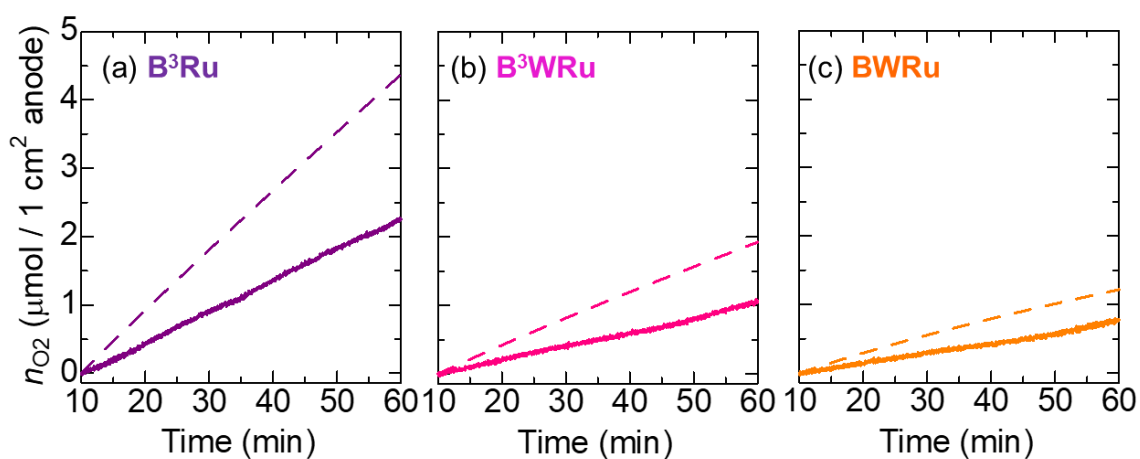


Figure 9. Electrochemical OER plots (solid line) at 10-60 min after starting application of 1.5 V of external bias and the ideal (FE=100%) amount of O₂ production estimated from the current values in Fig. 8 (dashed line) of (a) **B³Ru**, (b) **B³WRu**, and (c) **BWRu**. The amount of generated oxygen (n_{O_2}) were estimated as the difference of the actual O₂ amount and the amount at 10 min.

Table 3. The values of n_{O_2} , total charge, and FE in 10-60 min.

	n_{O_2} (μmol)	Ideal n_{O_2} (μmol) ^a	Total charge (mC)	FE(%)
B³Ru	2.17	4.37	1686	50
B³WRu	1.00	1.92	741	52
BWRu	0.71	1.22	471	58
WRu	< 0.1		8.9	-

^a Estimated as FE = 100%.

2-3-5 Photoelectrochemical measurement

The photoelectrochemical responses of these photoanodes were evaluated by linear sweep voltammetry (LSV) under chopped visible light irradiation ($\lambda > 420$ nm). Observed photocurrent responses of **ZrRu** and **WRu** are shown in Figure 10. Obvious photocurrent was observed under light irradiation while such a response hardly observed for the pristine TiO_2/FTO electrode. Considering the Ru(III/II) redox potential of **RuP⁶** (+1.24 V vs NHE, § 2-3-3) and E_{00} energy (1.91 eV¹⁰), the redox potential at ³MLCT excited state Ru(III/II*) is estimated as -0.67 V that is more negative than conduction band edge of TiO_2 (~ -0.5 V¹³). This simple estimation clearly indicates the photocurrent observed for **ZrRu** and **WRu** is assignable to the electron injection from the photoexcited **RuP^{6*}** to the TiO_2 substrate. The photocurrents of these photoanodes were comparable, suggesting that the surface modification of **ZrRu** by CdRu-PWA HM layer hardly gave a negative effect on the electron injection process.

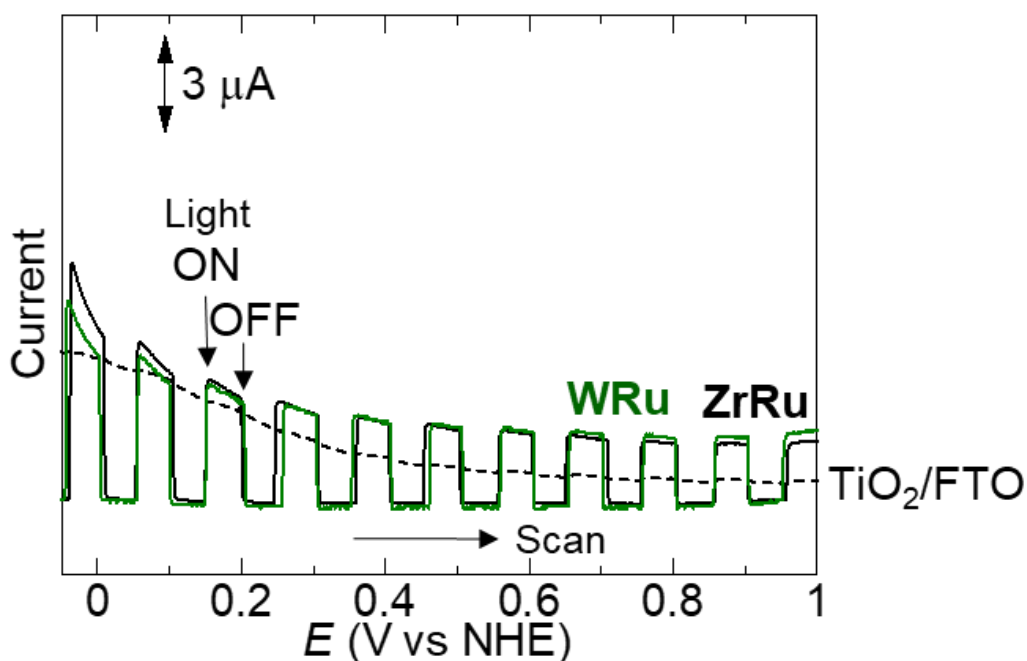


Figure 10. LSV scans of **ZrRu** and **WRu** under chopped light irradiation (every 50 mV, in pH = 6.0) Measurement was carried out under the condition described in § 2-2-2. Scan rate = 10 mVs⁻¹.

The results of LSV scans of **B³W^yRu** photoanodes under chopped light irradiation are shown in Fig. 11 in comparison with **WRu** without modification of **CoFe-PBA** WOC. All the three PBA-modified electrodes, **B³Ru**, **B³WRu** and **BWRu** showed larger photocurrent than **WRu**, especially on the **B³**-type anodes that exhibited more than twice larger photocurrent than **WRu** in whole region examined in the measurement. The photocurrent peak height of each anode was moderately agreed with the

current difference observed in the LSV scans under light irradiation and the dark condition in the range at $-0.05 \sim 0.5$ V. (Fig. 12), suggesting that the photocurrent observed in these experiments are not due to the charge correction state at the solid-solution interface but to the redox reaction of the photoanodes. At $0.6 \sim 1.0$ V, the peak assigned as Co(III/II) redox of **CoFe-PBA** was observed. Considering the Ru(III/II) redox potential of **RuP⁶** ($+1.24$ V) is located at more positive than both the Co(III/II) redox potential ($+0.96$ V) and the threshold potential for OER of **CoFe-PBA WOC** (~ 1.10 V),^{4b} the Ru(III) species generated after the electron injection to TiO₂ could oxidize the Co(II) centers to regenerate the original Ru(II) species. Thus, the larger photocurrent observed for **B³**-type photoanodes could be assigned to the oxidation of Co(II) centers of **CoFe-PBA WOC** and possibly followed by OER. Notably, the photocurrent observed for **B³WRu** was comparable to that of **B³Ru** whereas the loading amount of CoFe-PBA WOC of **B³WRu** was smaller by about 70% than that of **B³Ru** as discussed in § 2-3-1.

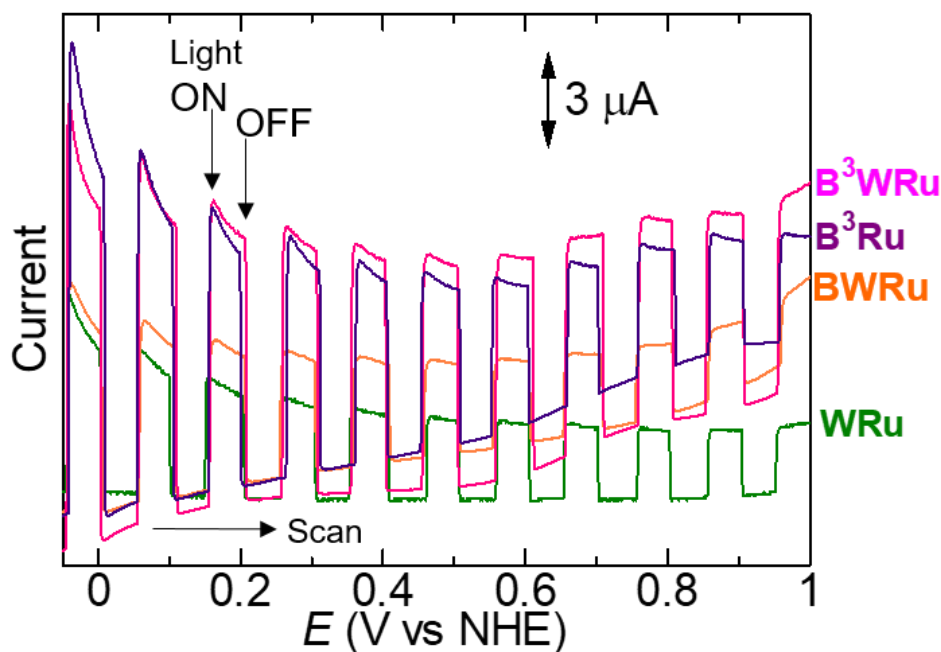


Figure 11. LSV scans of **B³W³Ru** under chopped light irradiation (every 50 mV, pH = 6.0). Measurement was carried out under the condition described in § 2-2-2. Scan rate = 10 mVs^{-1} .

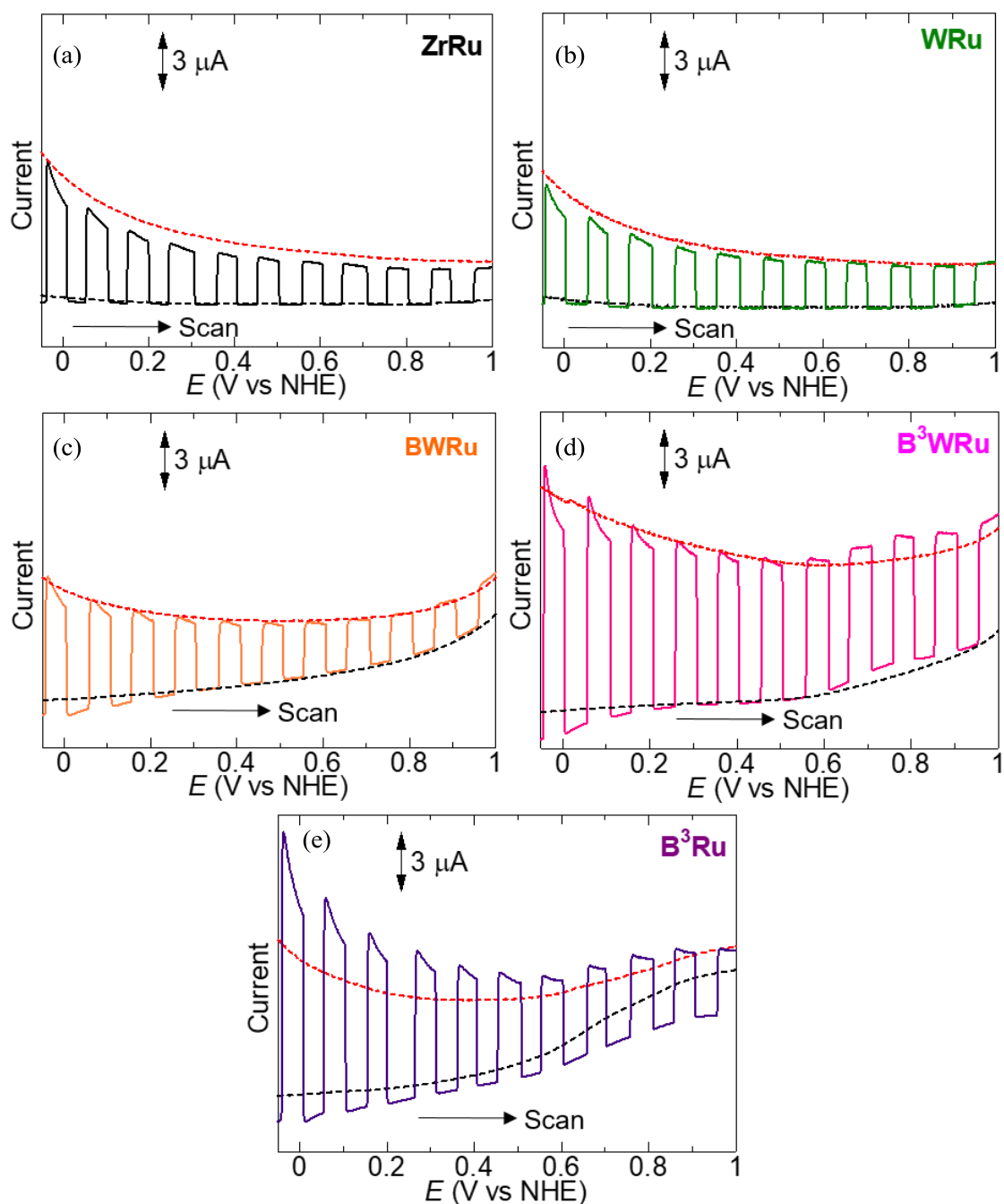
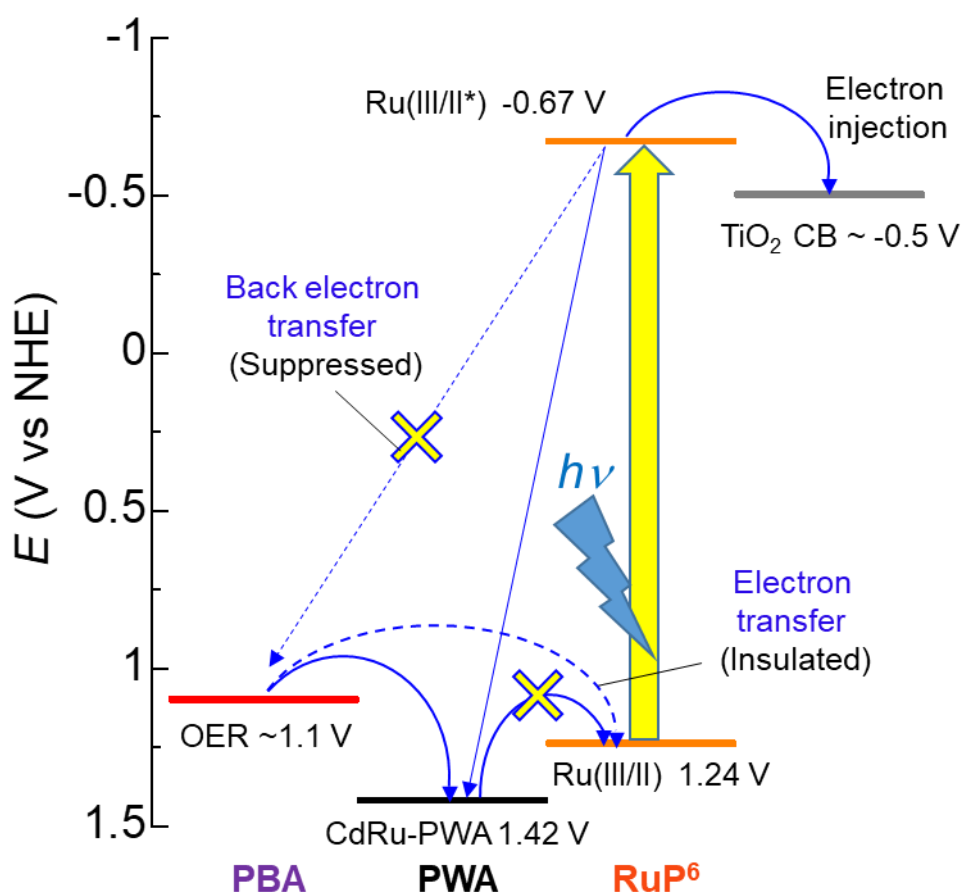


Figure 12. LSV plots in the dark (black dashed line) and under the light ($420 \text{ nm} < \lambda < 800 \text{ nm}$) irradiation (red dashed line) of (a) **ZrRu**, (b) **WRu**, (c) **BWRu**, (d) **B³WRu** and (e) **B³Ru** in comparison with the scan under chopped light irradiation (pH = 6.0). Measurement was carried out under the condition described in section 2-2-2. Scan rate = 10 mVs^{-1} .

Unfortunately, the Ru(III/II) redox potential of **RuP⁶** is negative than that of **CdRu-PWA**, resulting in the thermodynamically unfavorable hole transfer from PS to HM (Scheme 3). Although such the negative effect was suggested, the comparable photocurrent with **B³Ru** was observed on **B³WRu**. This behavior possibly reflected two different contributions of **CdRu-PWA**; the positive contribution is to block the back electron transfer from the photoexcited **RuP^{6*}** to CoFe-PBA WOC, and another negative one is the barrier for forward electron transfer from WOC to the one-electron oxidized PS. However, their photocurrent values are very small ($\sim 10 \mu\text{A}$) and the amount of oxygen which can generate is less than $0.1 \mu\text{mol/h}$, too small to evaluate. Some reasons of this small photocurrent are suggested; low conductivity, deactivation process by energy transfer from **RuP⁶** to **CoFe-PBA**, or stoichiometry of PBA. To evaluate the effect of HM, high-electron conductivity and tuning of redox potential on PS is to be required.



Scheme 3. Expected scheme of electron transfer in **B³WRu**. The water oxidation potential,⁴ redox potential of **CdRu-PWA**,¹ E_{00} of **RuP⁶** ($= 1.91 \text{ eV}^{10}$) and conduction band edge of TiO_2 ¹³ was noted reported values.

2-4. Conclusions

In this work, multilayered photoanodes consisted of **CoFe-PBA** water-oxidation catalyst (WOC), **CdRu-PWA** hole-transporter (HM) and **RuP⁶** photosensitizer (PS) on TiO₂/FTO electrode were fabricated. The stepwise growth of **CoFe-PBA** and **CdRu-PWA** was succeeded by repeating the layer-by-layer (LbL) process. Obtained photoanodes **B^xW^yRu** exhibited electrochemical OER behavior in the order of **B³Ru** > **B³WRu** > **BWRu** > **WRu** \cong **ZrRu** \cong 0. The lower catalytic activity of **CdRu-PWA**-loaded photoanodes than **B³Ru** is possibly due to the lower loading amount of **CoFe-PBA** WOC and/or the low electrical conductivity of **CdRu-PWA** HM layer. On the other hand, the comparable photocurrent was observed on **B³Ru** without CdRu-PWA HM layer and **B³WRu**, suggesting that the photochemical electron transfer processes between **RuP⁶** and **CoFe-PBA** was negligibly affected by **CdRu-PWA** HM layer. However, photocurrents of these anodes were too small to quantitatively elucidate the effect of HM on photoelectrochemical OER. An improvement of electrical conductivity, surface uniformity and tuning redox potential of PS are to be required.

2-5 References

- 1 H. Kitano, A. Kobayashi, M. Yoshida, M. Kato, *SusEneFuels*, 2018, **2**, 2609.
- 2 (a) L. Heinke, C. Wöll, *Adv. Mater.* 2019, **31**, 1806324. (b) Y. –H. Xiao, Z. –G. Gu, J. Zhang, *Nanoscale*, 2020, **12**, 12712. (c) A. L. Semrau, Z. Zhou, S. Mukherjee, M. Tu, W. Li, R. A. Fischer, *Langmuir* 2021, **37**, 6847.
- 3 (a) H. Sato, M. Ide, R. Saito, T. Togashi, K. Kanaizuka, M. Kurihara, H. Nishihara, H. Ozawa, M. Haga, *J. Mater. Chem. C*, 2019, **7**, 12491. (b) M. Ide, H. Sato, H. Ozawa M. Haga, *ACS Appl. Electron. Mater.*, 2021, **3**, 3962.
- 4 (a) S. Goberna-Ferrón, W. Y. Hernández, B. Rodríguez-García, J. R. Galán-Mascarós, *ACS Catal.* 2014, **4**, 1637. (b) S. Pintado, S. Goberna-Ferrón, E. C. Escudero-Adán, J. R. Galán-Mascarós, *J. Am. Chem. Soc.*, 2013, **135**, 13270.
- 5 M. R. Norris, J. J. Concepcion, C. R. K. Glasson, Z. Fang, A. M. Lapidés, D. L. Ashford, J. L. Templeton, T. J. Meyer, *Inorg. Chem.*, 2013, **52**, 12492
- 6 I. Gillaizeau-Gauthier, F. Odobel, M. Alebbi, R. Argazzi, E. Costa, C. A. Bignozzi, P. Qu, G. J. Meyer, *Inorg. Chem.*, 2001, **40**, 6073
- 7 K. Itaya, T. Ataka, S. Toshima, *J. Am. Chem. Soc.* 1982, **104**, 4767.
- 8 S. Ito, P. Chen, P. Comte, M. K. Nazeeruddin, P. Liska, P. Péchy, M. Grätzel, *Progress in Photovoltaics: Research and Applications* 2007, **15**, 603.
- 9 (a) K. Morita, K. Sakai, H. Ozawa, *ACS Appl. Energy Mater.* 2019, **2**, 987. (b) K. Takijiri, K. Morita, T. Nakazono, K. Sakai, H. Ozawa, *Chem. Commun.*, 2017, **53**, 3042.
- 10 K. Hanson, D. A. Torelli, A. K. Vannucci, M. K. Brennaman, H. Luo, L. Alibabaei, W. Song, D. L. Ashford, M. R. Norris, C. R. K. Glasson, J. J. Concepcion, T. J. Meyer, *Angew. Chem. Int. Ed.*, 2012, **51**, 12782.
- 11 (a) S. Furugori, A. Kobayashi, A. Watanabe, M. Yoshida, M. Kato, *ACS Omega*, 2017, **2**, 3902. (b) N. Yoshimura, A. Kobayashi, W. Genno, T. Okubo, M. Yoshida, M. Kato, *SusEneFuels* 2020, **4**, 3450.
- 12 E. P. Alsaç, E. Ülker, S. V. K. Nune, Y. Dede, F. Karadas, *Chem. Eur. J.*, 2018, **24**, 4856.
- 13 G. Rothenberger, D. Fitzmaurice, M. Grätzel, *J. Phys. Chem.* 1992, **96**, 5983.

Chapter 3
Oxygen Evolution Reaction by
Carbazole-Functionalized
Ru(II) Molecular Catalysts

3-1 Introduction

As mentioned in general introduction, an introduction of hole mediator (HM) unit between the photosensitizer and oxygen evolution catalyst is expected as one of the promising approaches for OER systems to improve the charge separation efficiency. Carbazole (cbz) derivatives with high electron mobility and positive redox potentials¹ are promising candidates as hole mediators. Cbz derivatives HMs are also attracted on (photo)electrochemical OER systems. One example is the application of Cu(I) PS with cbz as an electron donor moiety for an OER photoanode (Fig. 1a)² and electrochemical OER anodes with polycarbazole as hole-transporters.^{3a} In particular, several studies have suggested that the OER catalytic activity was improved by modification of polycarbazole-functionalized WOCs by electropolymerization on the electrode surface. (Fig. 1b)³ Furthermore, polycarbazole systems can provide a facile method for connecting functional molecules by oxidative electropolymerization⁴, including the conjugation with WOCs and PSs. If such a WOC-PS integration via polycarbazole hole-mediator can be achieved, this method can be a versatile and effective approach for photochemical OER system.

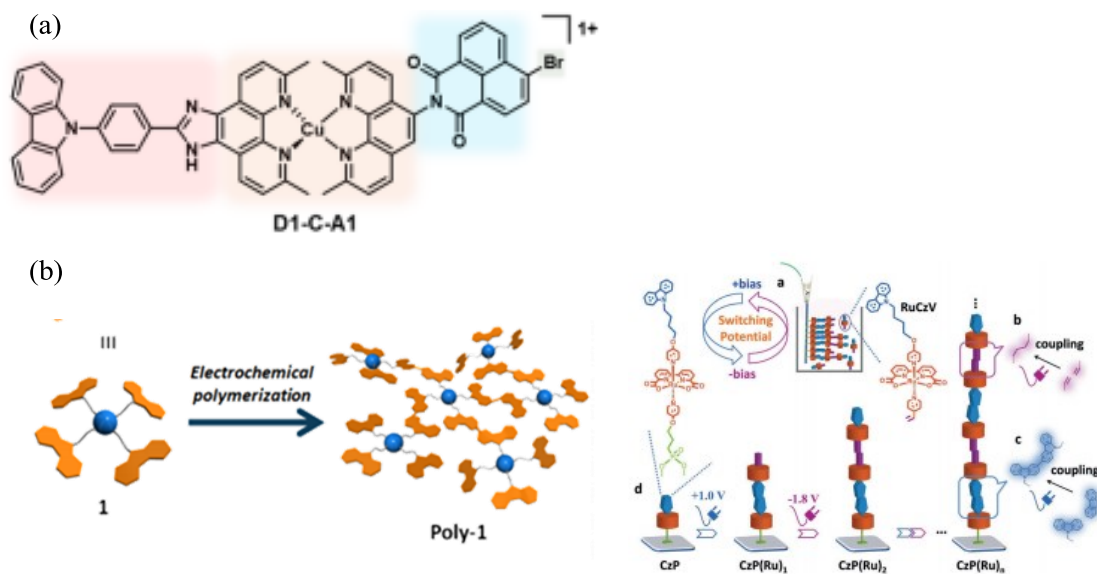
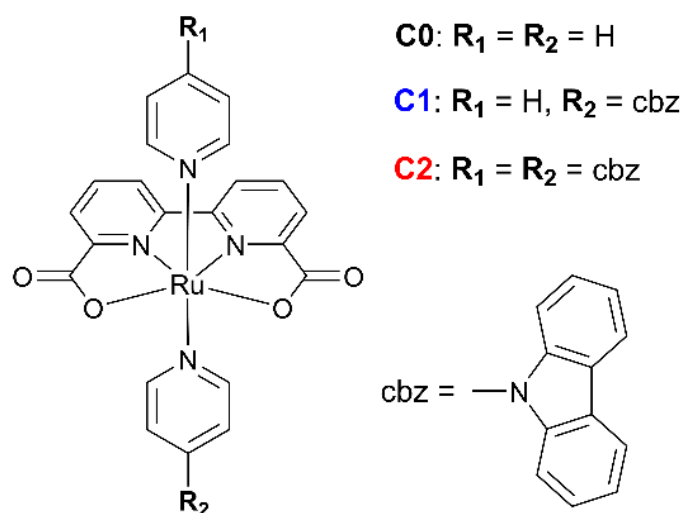


Figure 1 The examples of (a) cbz-modified Cu(I) chromophore for OER photoanodes² and (b) polycarbazole-functionalized WOCs.³

However, the effect of cbz modification on the OER catalytic activity of molecular WOC homogeneous systems have been hardly elucidated so far. The redox mediating cbz group attached on the axial py ligand may adversely affect the catalysis through electrostatic interactions on WOCs with bimolecular O-O coupling process, including Ru-bda complexes, which is one of the most popular molecular WOCs in photo- and/or electrochemical OERs, owing to its high catalytic activity, stability, and ligand tunability.⁵ In this study, in order to elucidate the effect of cbz functionalization on the OER, two complexes [Ru(bda)(cbz-py)(py)] and [Ru(bda)(cbz-py)₂] (Scheme. 1, denoted as **C1** and **C2**, cbz-py = 9-(pyridyn-4-yl)-9*H*-carbazole, py = pyridine) were newly synthesized, comprising a Ru-bda (bdaH₂ = 2, 2'-bipyridyl-6, 6'-dicarboxylic acid) complex backbone modified with one or two cbz-py moieties, respectively. This work revealed that the introduced cbz group(s) acted as the electron-withdrawing group(s) to improve the OER activity during the early stage of the reaction. Furthermore, the effect of cbz oxidation on chemical and photochemical oxygen evolution catalysis was investigated in detail.



Scheme 1. Molecular structure of the complexes **C0**, **C1**, and **C2**.

3-2 Experimental

3-2-1 Measurements

¹H NMR spectra were recorded using a JEOL ECZ-400S instrument. Elemental analysis was conducted at the analysis centre of Hokkaido University. MALDI-TOFMS measurements were carried out using a Bruker Autoflex Speed instrument, with α -cyano-4-hydroxycinnamic acid as the matrix. IR spectra were recorded on a JASCO FT-IR 4100 spectrophotometer using KBr pellets. UV-vis absorption spectra were recorded on Shimadzu UV-2400PC or Hitachi U-3000 spectrophotometers. Electrochemical measurements (CV and DPV) were recorded using a HOKUTO DENKO HZ-3000 electrochemical measurement system equipped with glassy carbon, Pt wire, and Ag/AgCl (aqueous mixture) or Ag/Ag⁺ (organic solvents) electrodes as the working, counter, and reference electrodes, respectively. Solutions of aqueous mixture (pH = 1.0–8.0, pH adjusted by HClO₄/40 mM of Britton-Robinson buffer/NaOH)/2,2,2-trifluoroethanol(TFE) /acetonitrile (v/v/v = 1/2/1 for CV or 3/2/1 for the other measurements) containing 0.1 M sodium perchlorate (NaClO₄) or dichloromethane/TFE (v/v = 9/1) containing 0.1 M tetrabutylammonium hexafluorophosphate (TBAPF₆) as the supporting electrolyte were used in the electrochemical measurements. Ferrocene was used as an internal reference. All solutions were deaerated by N₂ bubbling for 15 min before measurement.

3-2-2 Chemical OER

A solution of (NH₄)₂[Ce(NO₃)₆] (CAN, 240 mM) in HClO₄ aqueous solution (2.5 mL, pH = 1.0) was placed in a glass vessel (volume ~87.8 mL) with vigorous stirring (296 ± 1 K). A solution of the ruthenium catalyst (0–200 μ M) in TFE/acetonitrile (v/v = 2/1, 2.5 mL) was injected into the CAN solution; these solutions were deaerated by Ar bubbling for ~30 min before injection. The amount of evolved oxygen was monitored using a FireSting oxygen monitor (PyroScience GmbH). The OER rate and TOF were estimated using the following formulae from the amount of evolved O₂:

$$\text{OER rate (mMs}^{-1}\text{)} = \text{evolved O}_2 \text{ (}\mu\text{mol)} / 5 \text{ mL} \times \text{time (s)}$$

$$\text{TOF (s}^{-1}\text{)} = 1000 \times \text{OER rate} / [\text{Cat.}] \text{ (}\mu\text{M)}$$

3-2-3 Photochemical OER

In the dark, aqueous borate buffer/TFE/acetonitrile (v/v/v = 3/2/1) solution (10 mM, pH = 8.0^{6,7}) containing [Ru(bpy)₃](SO₄) photosensitizer (200 μ M), water oxidation catalyst (10 μ M), and Na₂S₂O₈ (5 mM) was placed in a Pyrex vial (volume ~21.2 mL) with a small magnetic stirring bar and covered with a rubber septum. The resultant solution (total 5 mL) was deoxygenated by bubbling with Ar gas for 30 min. The amount of evolved oxygen was monitored using a FireSting oxygen monitor (PyroScience GmbH). The vials were irradiated

with a blue LED lamp ($\lambda = 470 \pm 10$ nm; 30 mW; OptoDevice Lab. Ltd., OP6-4710HP2). The temperature was controlled at 296 ± 1 K using an in-house aluminum water-cooling jacket with a water-circulating temperature controller (EYELA CCA-1111).

3-2-4 Single crystal X-ray diffraction measurement

Single-crystal X-ray diffraction data were collected using a Rigaku XtaLAB Synergy diffractometer equipped with Cu K α radiation (PhotonJet (Cu)). Each crystal was mounted on a MicroMount using paraffin oil. The crystal was then cooled using a N₂-flow-type temperature controller. The diffraction data were processed using CrysAlisPRO software.⁸ The structures were solved by direct methods using SHELXT⁹ and refined by full-matrix least-squares refinement using SHELXL.¹⁰ Non-hydrogen atoms were refined anisotropically, while the hydrogen atoms were refined using the riding model. All calculations were performed using the Olex2 software package.¹¹

3-2-5 Theoretical calculation

Calculations were performed using the Gaussian 09 software package.¹² For **C2**, the molecular structure was determined by X-ray structure analysis, and the obtained structure was used as the initial structure for the calculation. Geometry optimizations and TD-DFT calculation were performed in the ground state using the B3LYP functional¹³ together with the 6-31G basis set¹⁴ on C, H, N, and O atoms. The LANL2DZ effective core potentials and associated basis set were used on the Ru atom.¹⁵ Although the results of **C0** calculated under the same basis/functional set with Gaussian 03 have already been reported,⁷ re-calculations using Gaussian 09 was conducted for a more precise comparison with the values of **C1** and **C2**. The difference in the frontier orbital energy values was negligible (<0.001 eV).

3-2-6 Materials

2, 2'-Bipyridyl-6, 6'-dicarboxylic acid (bdaH₂),¹⁶ 9-(pyridin-4-yl)-9*H*-carbazole (cbz-py),¹⁷ [Ru(bda)(py)₂] (**C0**),¹⁸ [RuCl₂(DMSO)₄],¹⁹ [Ru(bda)(DMSO)₂],²⁰ [Ru(bda)(4-bromopyridine)₂] (**C0-Br**),^{18a} and [Ru(bpy)₃](SO₄)²¹ were synthesized according to previously reported methods. **C0**, **C0-Br**, **C1**, and **C2** were stored in a nitrogen-filled glovebox^{18a, 22, 23} until use. High-purity water was obtained by passing house-distilled water through a Millipore Milli-Q Simplicity® UV system. All other reagents and solvents were purchased from commercial sources and used as received.

2-2-7 Synthesis

Synthesis of [Ru(bda)(cbz-py)(pyridine)] (**C1**).

[Ru(bda)(DMSO)₂] (203.8 mg, 0.41 mmol, 1 eq.), pyridine (33 μL, 0.40 mmol, 1 eq.), and methanol (10 mL) were added to a two-necked round-bottom flask and bubbled with N₂ for 10 min. The resultant dark-red solution was stirred at 313 K under N₂ for 5 min, after which cbz-py (101.2 mg, 0.41 mmol, 1 eq.) was added under N₂ flow. The reaction mixture was then refluxed under N₂ for 4 h. After cooling to 293 K, the solvent was removed using a rotary evaporator, and the obtained dark-red crude powder was subjected to silica-gel column chromatography. (Eluent: CH₂Cl₂/methanol = 10/1). The second red band (*R_f* = 0.16) was collected, and the solvent removed. Finally, the product was recrystallized by the gas-liquid diffusion method with CH₂Cl₂/methanol-diethyl ether and dried in vacuo to afford dark-red needle-like crystals. Yield: 106.1 mg (0.16 mmol, 39%). ¹H NMR (Fig. 2, 400 MHz, CD₂Cl₂/methanol-*d*₄ with a small amount of L-ascorbic acid): δ = 8.46 (d, *J* = 8.0 Hz, 2H), 8.13–8.08 (m, 4H), 8.03 (d, *J* = 6.6 Hz, 2H), 7.92–7.86 (m, 4H), 7.84 (t, *J* = 7.8 Hz, 1H), 7.54–7.50 (m, 4H), 7.40 (td, 2H, *J* = 1.4, 7.3 Hz), 7.32 (2H, t, *J* = 7.7 Hz), 7.18 (2H, t, *J* = 1.4, 7.2 Hz). MALDI-TOF MS (positive mode, CH₂Cl₂/methanol) *m/z*⁺ = 667.08. (**C1**+H⁺) calcd. 667.65. Elemental analysis calcd. for C_{34.4}Cl_{0.8}H_{23.8}N₅O₄Ru ([**C1**]·0.4CH₂Cl₂): C, 58.97; H, 3.42; N, 10.00. Found: C, 59.09; H, 3.39; N, 9.85. IR (KBr pellets, cm⁻¹): 3059, 1651, 1631, 1609, 1509, 1477, 1449, 1368, 1336, 1287, 1220, 834, 778, 756.

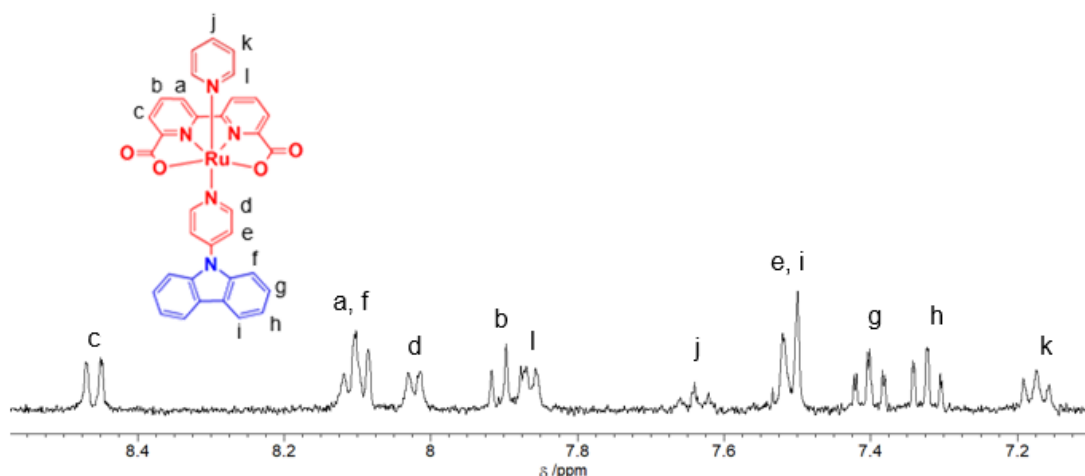


Figure 2. The aromatic region of ^1H NMR spectra of **C1**.

(400 MHz, $\text{CD}_2\text{Cl}_2/\text{methanol-}d_4$ with a small amount of L-ascorbic acid)

Synthesis of $[\text{Ru}(\text{bda})(\text{cbz-py})_2]$ (**C2**).

$[\text{Ru}(\text{bda})(\text{DMSO})_2]$ (102.7 mg, 0.21 mmol, 1 eq.), cbz-py (100.1 mg, 0.41 mmol, 2 eq.) and methanol (10 mL) were added to a two-necked round-bottom flask and bubbled with N_2 for 15 min. The resultant dark-red solution was refluxed under N_2 for 8 h. After cooling to 293 K, the reaction mixture was filtered and washed with acetone several times until the filtrate became colorless. The obtained dark-red powder was dried in air and then extracted twice with chloroform/L-ascorbic acid aqueous solution. Subsequently, the organic phase was washed with water and dried with Na_2SO_4 , and the solvent was evaporated. The resulting dark-red powder was recrystallized by the gas-liquid diffusion method with diethyl ether- $\text{CH}_2\text{Cl}_2/\text{methanol}$ and dried in vacuo to afford dark-red needle-like crystals. Yield: 78.0 mg (0.080 mmol, 38%). ^1H NMR (Fig. 3, 400 MHz, $\text{CD}_2\text{Cl}_2/\text{methanol-}d_4$ with a small amount of L-ascorbic acid): δ = 8.38 (d, J = 7.8 Hz, 2H), 8.17 (dd, J = 0.9, 7.8 Hz 2H), 8.09 (d, J = 7.8 Hz, 4H), 8.01 (dd, J = 1.4, 5.5 Hz, 4H), 7.87 (t, J = 7.8 Hz, 2H), 7.52 (d, 4H, J = 8.2 Hz), 7.49 (4H, dd, J = 1.4, 5.5 Hz), 7.41 (4H, td, J = 1.4, 7.8 Hz), 7.32 (4H, td, J = 0.9, 7.8 Hz). MALDI-TOF MS (positive mode, $\text{CH}_2\text{Cl}_2/\text{methanol}$) m/z^+ = 832.13. (**C2**+ H^+) calcd. 832.84. Elemental analysis. calcd. for $\text{C}_{46.5}\text{ClH}_{31}\text{N}_6\text{O}_4\text{Ru}$ (**[C2]** $\cdot 0.5\text{CH}_2\text{Cl}_2$): C, 63.88; H, 3.57; N, 9.61. Found: C, 63.88; H, 3.51; N, 9.61. IR (KBr pellets, cm^{-1}): 3059, 1634, 1605, 1507, 1477, 1448, 1368, 1344, 1220, 1183, 831, 777, 748, 722. Single crystals of **C2** were obtained by the gas-liquid diffusion method with diethyl ether- $\text{CH}_2\text{Cl}_2/\text{methanol}$. The ORTEP figure and crystallographic data were attached in Fig. 4 and Table. 1, respectively.

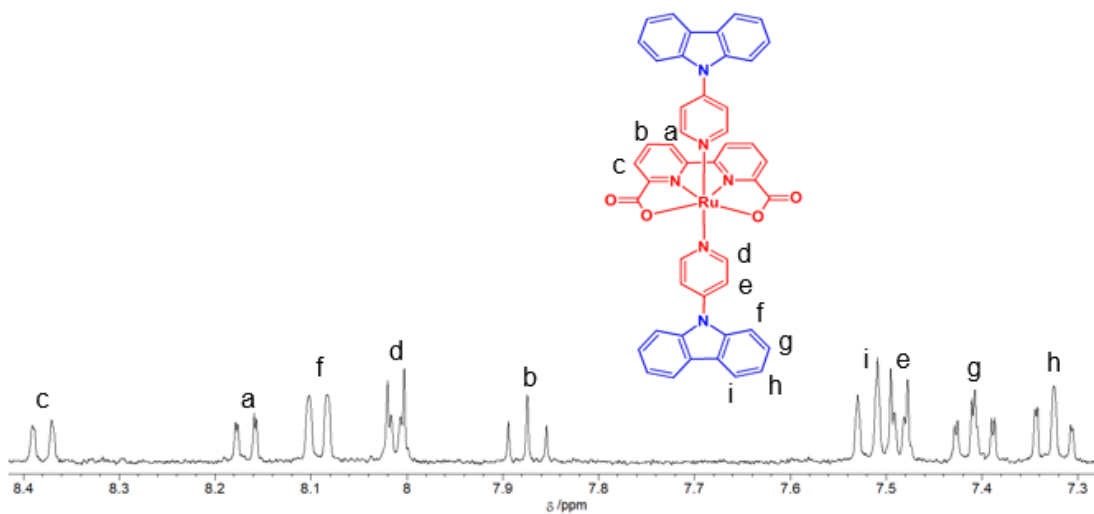


Figure 3. The aromatic region of ^1H NMR spectra of **C2**.
(400 MHz, $\text{CD}_2\text{Cl}_2/\text{methanol-}d_4$ with a small amount of L-ascorbic acid)

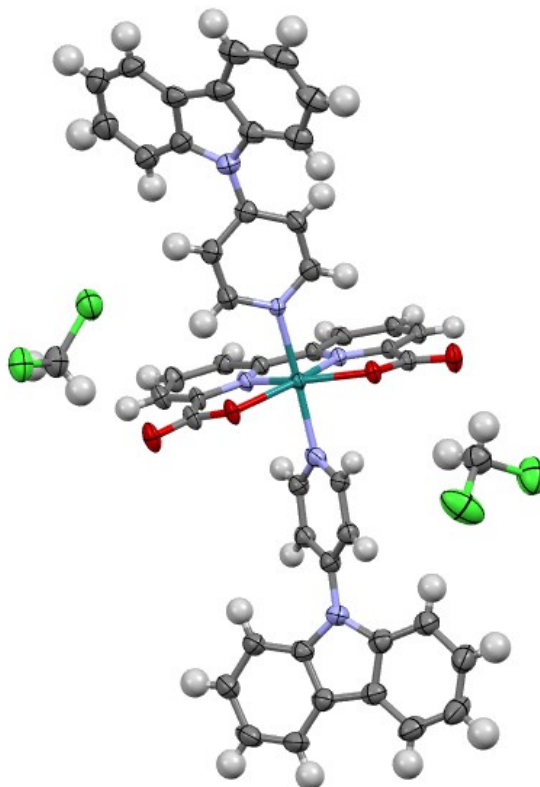


Figure 4. ORTEP drawings of **C2**· $2\text{CH}_2\text{Cl}_2$. Thermal ellipsoids are shown at the 50% probability level.

Color chart: grey: C, yellow green: Cl, white: H, purple: N, red: O, Green: Ru.

Table 1. Crystallographic parameters of. **C2·2CH₂Cl₂**.

Complex	C2·2CH ₂ Cl ₂
<i>T</i> / K	150
Formula	C ₄₆ H ₃₀ N ₆ O ₄ Ru·2CH ₂ Cl ₂
Formula weight	1001.68
Crystal system	<i>monoclinic</i>
Space group	<i>P2₁/n</i>
<i>a</i> / Å	8.08230(10)
<i>b</i> / Å	25.8123(5)
<i>c</i> / Å	20.3078(3)
<i>α</i> / deg.	90
<i>β</i> / deg.	93.8950(10)
<i>γ</i> / deg.	90
<i>V</i> / Å ³	4226.88(12)
<i>Z</i>	4
<i>D</i> _{cal} / g×cm ⁻³	1.574
Reflections collected	32223
Unique reflections	8639
GOF	1.100
<i>R</i> _{int}	0.0570
<i>R</i> (<i>I</i> > 2.00σ(<i>I</i>))	0.0648
<i>R</i> _w ^a	0.1679

$$^a R_w = [\Sigma(w(F_o^2 - F_c^2)^2) / \Sigma w(F_o^2)^2]^{1/2}.$$

3-3 Results and discussion

3-3-1 UV-Vis absorption spectra

The photophysical and electrochemical properties of **C1** and **C2** were investigated to elucidate the effect of cbz functionalization on the molecular catalyst **C0**. The UV-vis absorption spectra in dichloromethane/2, 2, 2-trifluoromethanol (TFE) are shown in Fig. 5a. The cbz-functionalized complexes **C1** and **C2** exhibited similar spectra to that of **C0**, but with new sharp absorption peaks at 286 and 334 nm. Similar absorption peaks, at near-identical positions, were observed for the cbz-py ligand. Thus, these two absorption bands were assigned to the intra-ligand transition (^1LC) of the cbz-py ligand. In the wavelength range above 350 nm, two contrasting trends were observed: the band at ~ 370 nm was more strongly observed in **C1** and **C2** than in **C0**, while the absorbances of two bands at 475 and 531 nm were near-identical to those of **C0**. In the case of **C0**, the absorption band at 370 nm was assigned as the $^1\text{MLCT}$ transition to the pyridine ligand, while those at 475 and 531 nm are other $^1\text{MLCT}$ transitions to the bda ligand.^{5, 7, 18} The molecular structures of **C1** and **C2** are near-identical to that of **C0**, except for the cbz group(s), and thus, the same MLCT transitions to py or the bda ligands were also observed for these cbz-functionalized complexes. These assignments are validated because the absorbances of the lower-energy MLCT transitions to the bda ligands are near-identical in these three complexes. A higher absorbance of the MLCT transition to the py ligand, with a slight red shift in **C1** and **C2** compared to that in **C0**, was observed. This was ascribed to the π -extension of the py ligand by cbz functionalization, which leads to an increase in the transition dipole moment. In the mixture containing water, these absorption bands were shifted to shorter wavelengths by ~ 40 nm (Fig. 5b). This solvatochromic behavior is further evidence of the CT nature of these absorption bands. These higher energy MLCT absorption bands with large ϵ were observed below 425 nm, so that the contribution of these strong absorption should be negligible in the photochemical OER with blue-light excitation (~ 470 nm).

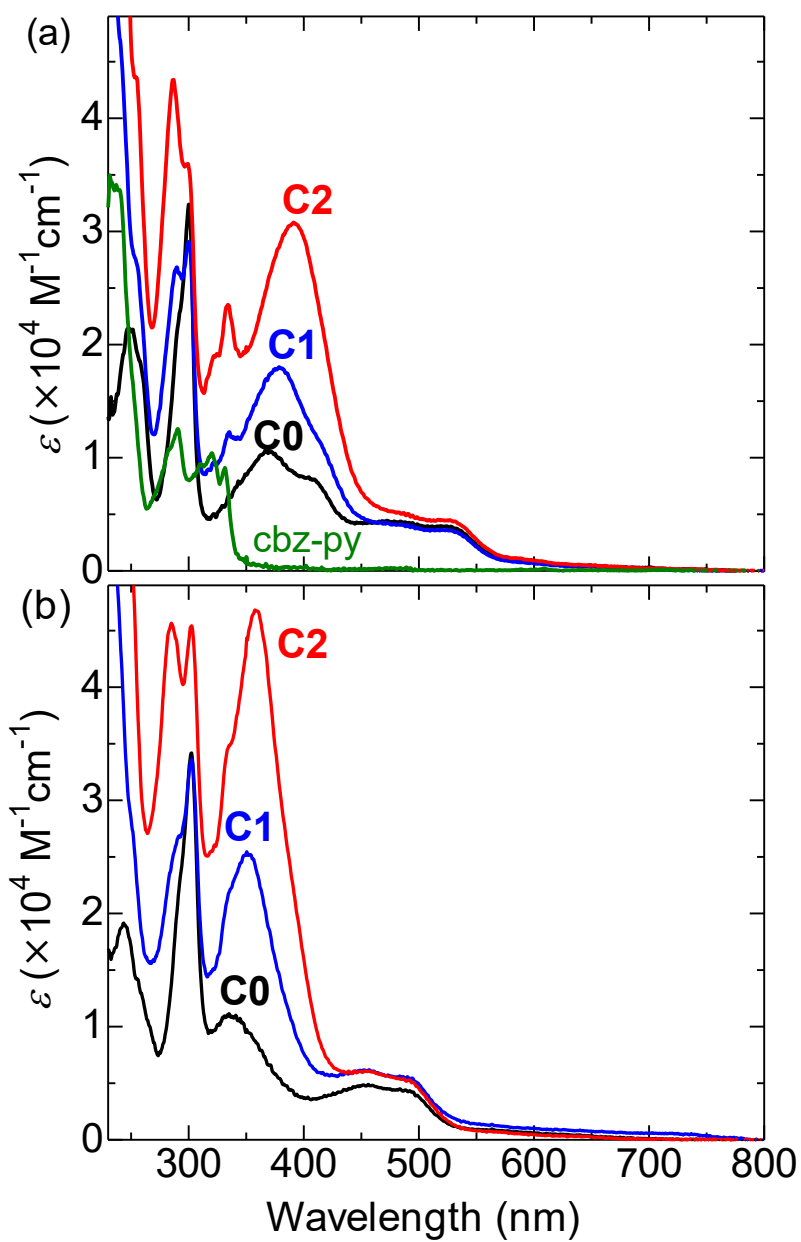


Figure 5. UV-vis absorption spectra of the C0 (black), C1 (blue), C2 (red) complexes and cbz-py (green) ligand (10 μM) in (a) dichloromethane/TFE (v/v = 9/1) and (b) HClO₄ aq. (pH = 1.0)/TFE/acetonitrile (v/v/v=3/2/1).

3-3-2 Electrochemical property

Differential pulse voltammetry (DPV) was performed to evaluate the effect of the introduced cbz group on the redox properties. As shown in Fig. 6, two oxidation peaks attributed to the redox couples, Ru^{III/II} and Ru^{IV/III}, were observed in both complexes, as reported for **C0** (Table 2). A peak assigned to Ru^{III/II} was observed at 0.8–0.9 V vs NHE, similar to that reported for **C0** in acetonitrile. This suggests that these complexes mainly exist as a structure in which the acetonitrile solvent is coordinated to the Ru center under this solvent condition.^{18a, 22} The redox potential of Ru^{III/II} was slightly shifted to positive in the order **C0** (0.85 V vs NHE) < **C1** (0.87 V) < **C2** (0.90 V). These results were attributed to the substituent effect of the cbz group introduced in **C1** and **C2**, as reported for the electron-withdrawing-group-functionalized [Ru(bda)(py)₂] series.^{7, 18, 24} This is supported by the fact that **C0-Br** with more electron-withdrawing Br groups showed a more positive Ru^{III/II} redox potential (0.92 V) than the others.

On the other hand, the oxidation peaks of Ru^{IV/III}, observed on the more positive side of the redox potential, were all similar at 1.13–1.14 V (Table 2). This is consistent with a previous report that the substituent effect is negligible in the redox potential of Ru^{IV/III}.^{7, 18} In addition to the redox couples of the Ru center, **C1** and **C2** showed marked oxidation peaks in the more positive potential region (1.4–1.5 V vs NHE), in which **C0** did not present any peaks. Because the cbz-py ligand also exhibited a similar oxidation wave (Fig. 7a), the oxidation wave at ~1.4 V should include the oxidation current of the cbz groups in **C1** and **C2**. Although similar redox behavior was observed in the CV of the water-containing mixtures (Fig. 7b), the oxidation waves of the cbz group gradually disappeared by repeating the potential sweep of the CV cycles. In fact, the large cbz oxidation peak of **C2** almost disappeared after only three potential sweep cycles (Fig. 8b), while the cbz oxidation current decay of **C1** was significantly slower (~50 cycles) than that of **C2** (Fig. 8a). This difference indicates that the number of cbz groups in one molecule is a crucial factor in the redox behavior. A similar trend was reported for the electrode bearing Ru-bda complexes connected to the cbz moiety by a long alkoxy chain^{3b} and CV of cbz under DMF²⁵, in which less polycarbazole is generated. Thus, the rapid current decrease of the cbz oxidation for **C2** in aqueous solvent suggests that an irreversible conversion to an oxidized species would be triggered by the cbz oxidation.

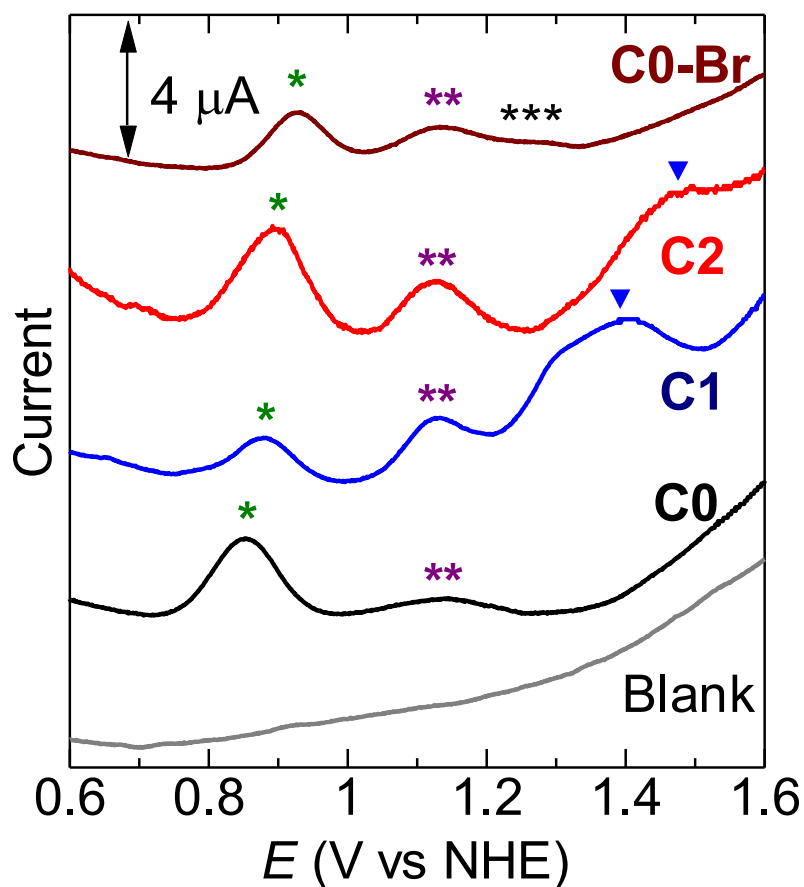


Figure 6. DPV curves of the complexes **C0** (black), **C1** (blue), **C2** (red) and **C0-Br** (Brown) in pH = 1.0 HClO₄ aq./TFE/acetonitrile (v/v/v = 3/2/1) containing 0.1 M NaClO₄; scan rate = 10 mVs⁻¹. Single (*), double (**), and triple asterisks (***) denote a redox couple of Ru^{III/II}, Ru^{IV/III}, and Ru^{V/IV}, respectively. A cascade of Ru^{V/IV} and (cbz^{ox}/cbz) on C1 and C2 are denoted as inverted triangle (▼). A redox peak of **C0-Br** assigned as Ru^{V/IV} observed at 1.29 V_{vs NHE} was denoted as black triple asterisks.

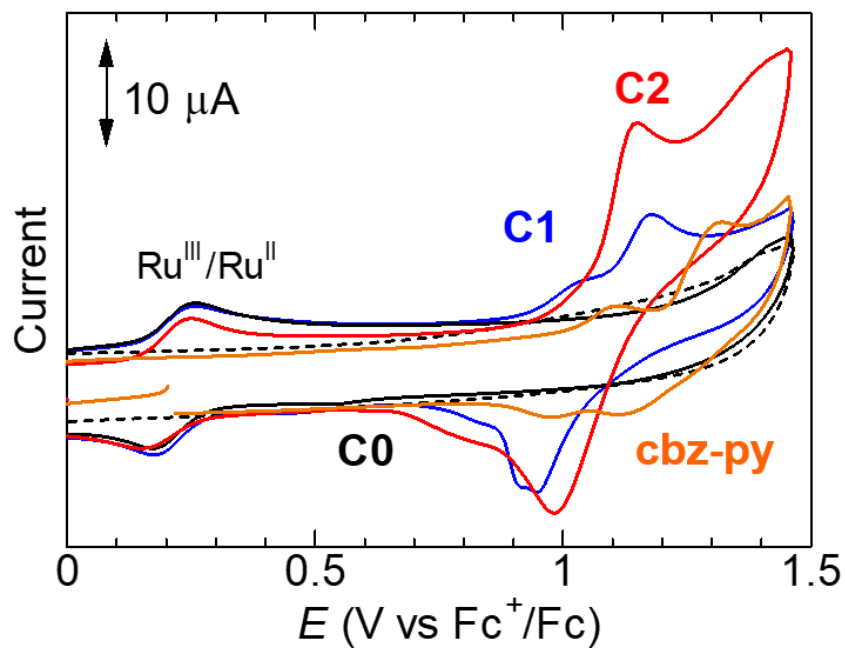
Table 2. Redox potentials of **C0**, **C1**, and **C2** estimated by DPV measurement.

Complex	$E(\text{Ru}^{\text{III/II}})$ (V _{vs NHE})	$E(\text{Ru}^{\text{IV/III}})$ (V _{vs NHE})	$E(\text{cbz}^{\text{ox}}/\text{cbz})^a$ (V _{vs NHE})
C0	0.85	1.14	n.d.
C1	0.87	1.13	1.41
C2	0.90	1.13	1.48
C0-Br ^b	0.92	1.14	n.d.

^a Irreversible in aqueous mixture.

^b A redox peak assigned as Ru^{V/IV} was observed at 1.29 V_{vs NHE}.

(a)



(b)

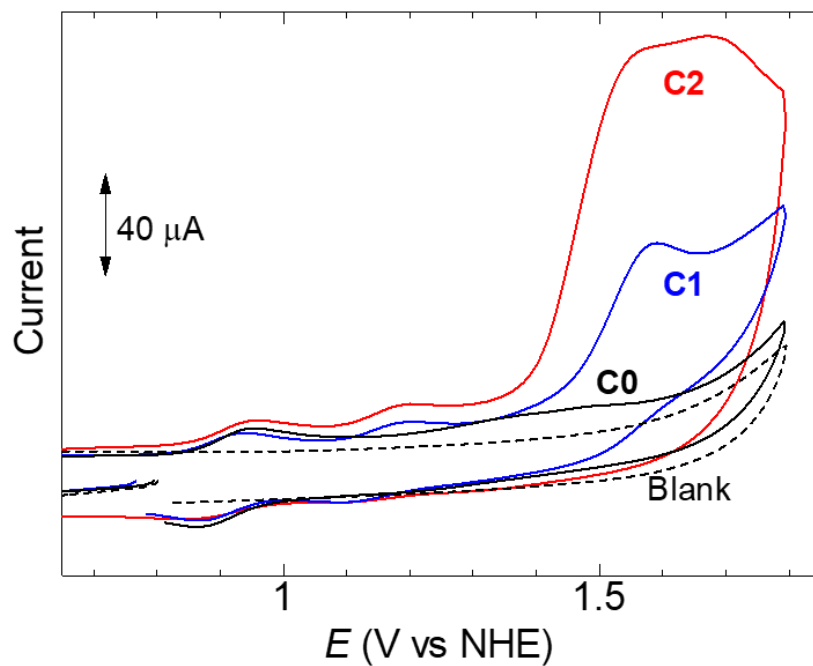


Figure 7. Cyclic voltammograms of **C0**, **C1**, **C2**, and **cbz-py** in (a) dichloromethane/TFE(v/v=9/1) (200 μM , scan rate 100 mVs^{-1}) and (b) HClO_4 aq. (pH = 1.0)/TFE/acetonitrile (v/v/v=1/2/1) (200 μM , scan rate 100 mVs^{-1}).

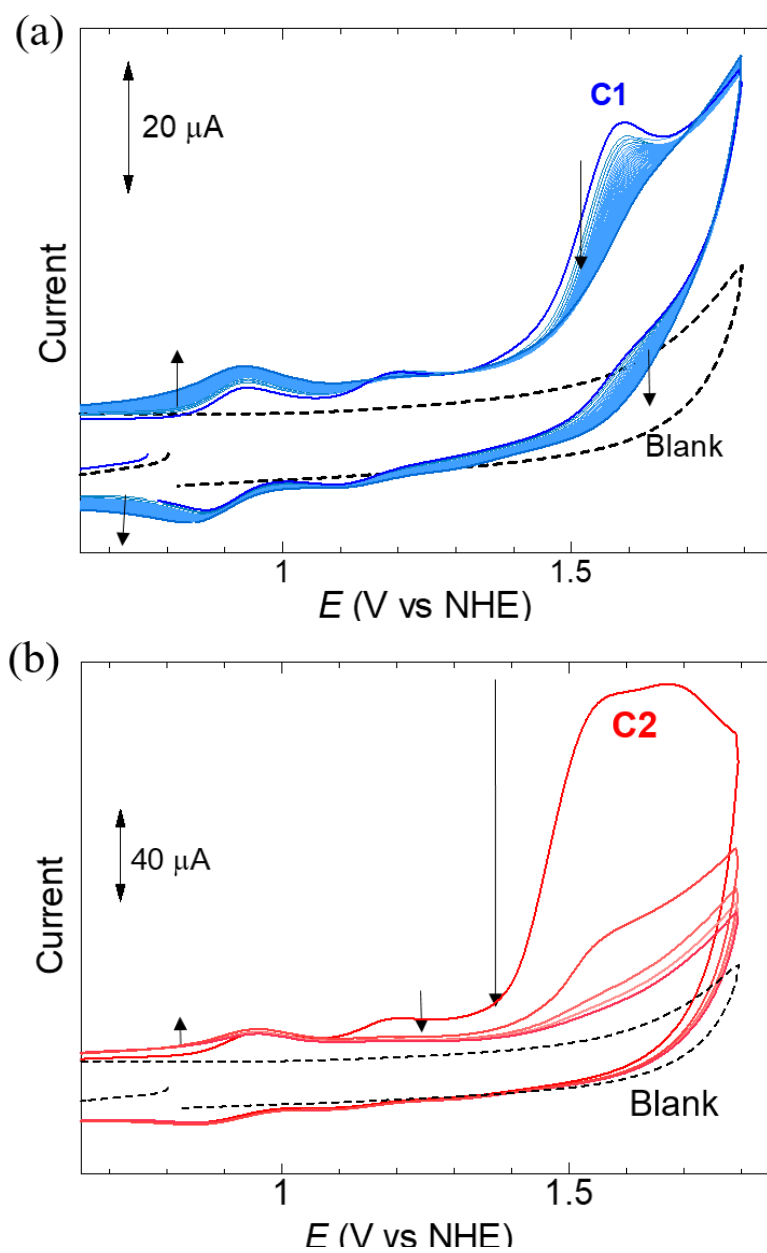


Figure 8. Changes of cyclic voltammograms during potential sweep cycles of (a) C1 (1-50th cycles) and (b) C2 (1-5th cycles). (200 μM , 0.1 M NaClO_4 solution of HClO_4 aq(pH=1.0)/TFE/acetonitrile (v/v/v=1/2/1) mixture).

The results of DPV measurement under various pH were shown in Fig. 9 and pourbaix diagrams of **C1** and **C2** were in Fig. 10. In addition to the redox waves of $\text{Ru}^{\text{III/II}}$, $\text{Ru}^{\text{IV/III}}$ and $\text{Ru}^{\text{V/IV}}$, non-pH dependent peaks or cascades attributed as cbz oxidation were observed at > 1.4 V. At pH=8, both complexes showed low-potential $\text{Ru}^{\text{V/IV}}$ redox process (~ 1.0 V) and these results clearly show that they are enough available for photochemical OER similar as **C0** (Fig. 11). Redox processes on the Ru center resemble the reported Ru-bda results in acetonitrile-contained mixtures, and it is indicated that **C1** and **C2** exist as acetonitrile-coordinated and one-carboxylate dissociated species in acidic media.^{18b, 22} In the neutral~basic condition, 1 or $3n\text{H}^+/2ne^-$ PCET processes assigned as the redox by Ru μ -oxo dimer, often reported that generated on the electrode when the electrochemical oxidation of Ru-bda series²⁶.

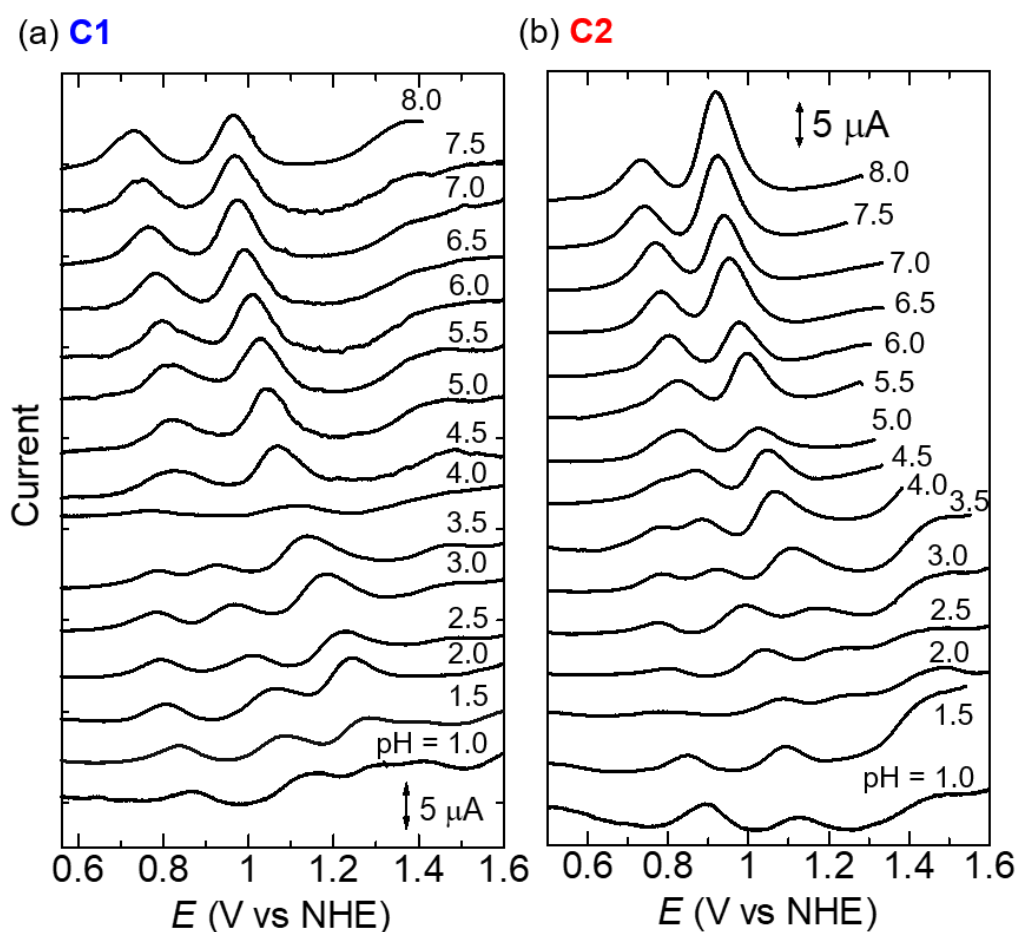


Figure 9. DPV curves of the (a) **C1** and (b) **C2** in the various pH.

Condition : Britton-Robinson buffer (40 mM, pH = 1-8)/TFE/acetonitrile (v/v/v = 3/2/1) containing 0.1 M NaClO_4 ; scan rate = 10 mVs^{-1} . On **C2**, DPV in > 1.3 V couldn't be measured well due to circumstances about the current range caused by large catalytic current.

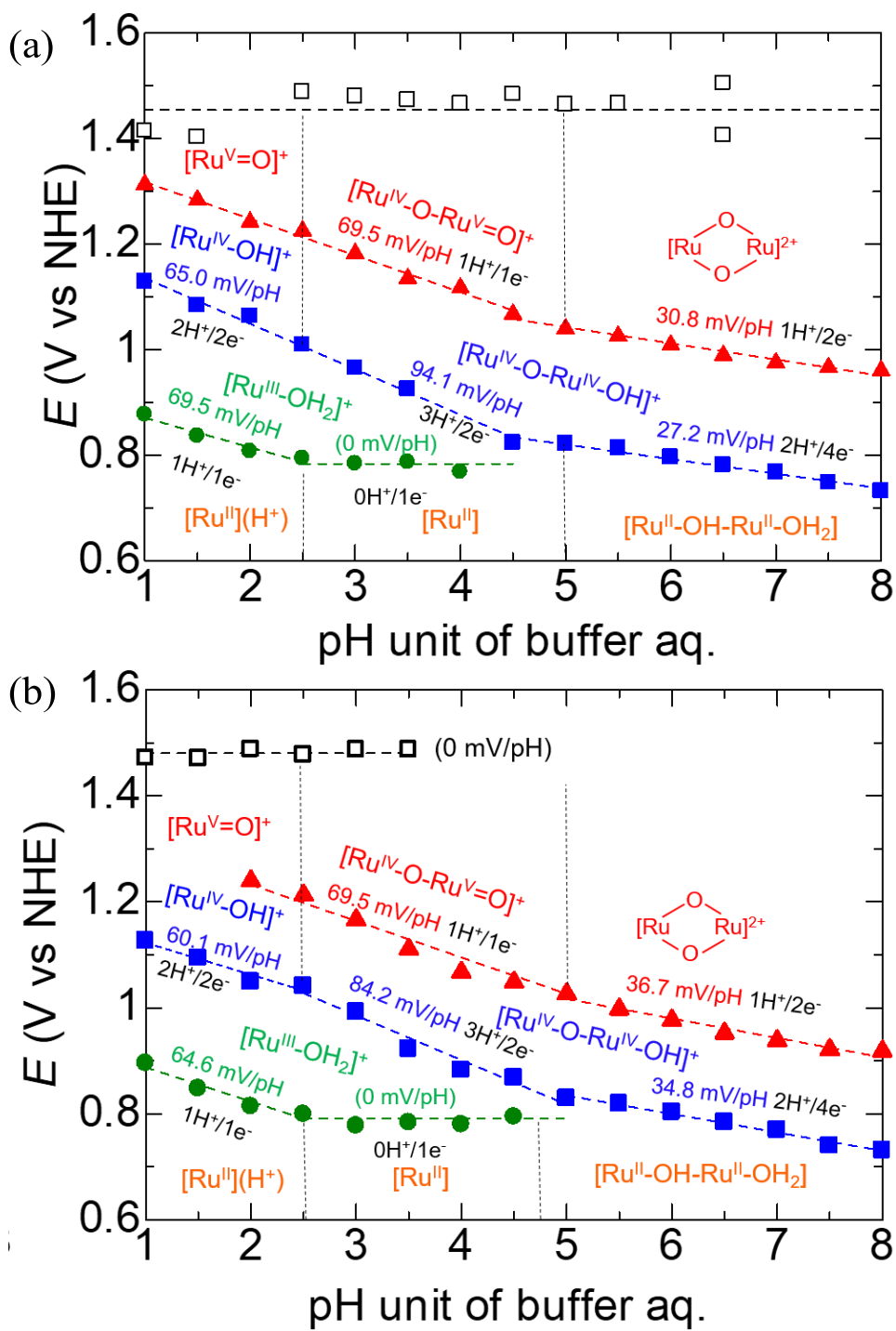


Figure 10. Pourbaix diagram of (a) C1 and (b) C2 plotted from the results of DPV measurements. (Fig. 10)

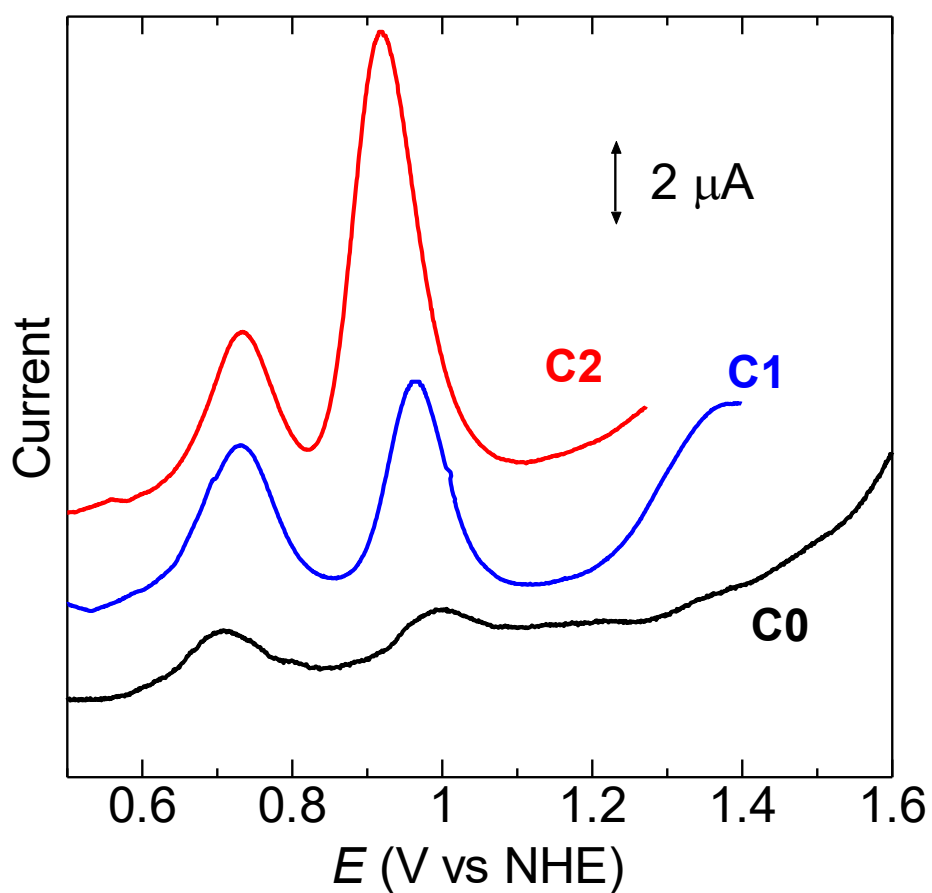


Figure 11. DPV curves of the complexes **C0** (black line), **C1** (blue) and **C2** (red) in buffer aq. (borate buffer on **C0**, Britton-Robinson buffer on the others, 40 mM, pH = 8.0) /TFE/acetonitrile (v/v/v = 3/2/1) containing 0.1 M NaClO₄; scan rate = 10 mVs⁻¹.

3-3-3 Theoretical calculation

In [Ru(bda)(py)₂]-type molecular catalysts, the electron-withdrawing functional group attached on the py ligand plays an important role on both the physical properties and catalytic activities.^{7, 18, 24} Our electrochemical measurements for **C1** and **C2** revealed that the shifts of the Ru^{III/II} redox couple of these cbz-functionalized complexes were more positive than that of **C0**, suggesting the electron-withdrawing nature of the cbz moiety.²⁷ To gain further insight into the effect of the cbz group, density functional theory (DFT) calculations were carried out using Gaussian 09 W. Fig. 12 shows the schematic molecular orbital (MO) energy diagrams for **C0**, **C1**, and **C2**, and the energy of each MO is listed in Table 3. In all three complexes, the highest occupied molecular orbital (HOMO) is localized in the *t*_{2g} orbital of the central Ru(II) ion (Fig. 13-15), and the orbital energy is stabilized in the order **C0** (-4.8747 eV) > **C1** (-4.9008 eV) > **C2** (-4.9247 eV), depending on the number of cbz moieties. Generally, a stronger π -accepting ligand generates a larger ligand field splitting of the central metal ion, resulting in more stabilized *t*_{2g} orbitals in the octahedral coordination geometry. These stabilized HOMO of **C1** and **C2** than **C0** indicate the electron-withdrawing nature of the cbz moiety. This well agrees with the positive shift of the Ru^{III/II} redox couple, as estimated from the DPV measurements (Fig. 6). Similar stabilization was also observed for the lowest unoccupied molecular orbital (LUMO) and LUMO+3, wherein the energies of these unoccupied orbitals also decreased with increasing number of cbz groups. The LUMO was stabilized because it comprises both the π^* orbital of the bda ligand and d orbital of the Ru(II) center (Table 3). Because LUMO+3 is localized on the π^* orbitals of the py ligand, the stabilized LUMO+3 for **C1** and **C2** over that of **C0** should originate from the electron-withdrawing nature of the cbz group. In addition, as previously discussed in § 3-3-2, the effect of the cbz moiety on the [Ru(bda)(py)₂] molecule is similar to that of the Br-functionalized complex (**C0-Br**). Thus, the cbz group attached to the py ligand should act as an electron-withdrawing substituent, as suggested by the electrochemical measurements in § 3-3-2.

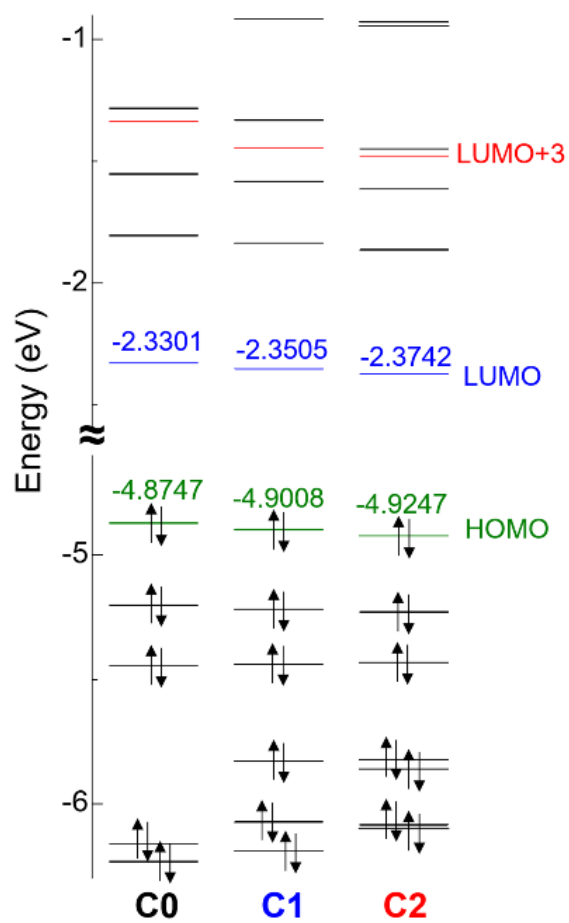


Figure 12. Schematic molecular orbital diagrams of CX in the ground state.

Table 3. MO energies of each complex estimated by DFT calculation.

	C0 (eV)	C1 (eV)	C2 (eV)
LUMO+6			-0.9293
LUMO+5	-0.7301	-0.9178	-0.9301
LUMO+4	-1.2849	-1.3331	-1.4504
LUMO+3	-1.3396	-1.4468	-1.4803
LUMO+2	-1.5543	-1.5856	-1.6172
LUMO+1	-1.8071	-1.8381	-1.8653
LUMO	-2.3301	-2.3535	-2.3742
HOMO	-4.8747	-4.9008	-4.9247
HOMO-1	-5.2055	-5.2211	-5.2311
HOMO-2	-5.4483	-5.4426	-5.4347
HOMO-3	-6.1620	-5.8314	-5.8249
HOMO-4	-6.2350	-6.0760	-5.8630
HOMO-5	-6.6034	-6.1933	-6.0875
HOMO-6	-6.7389		-6.0875

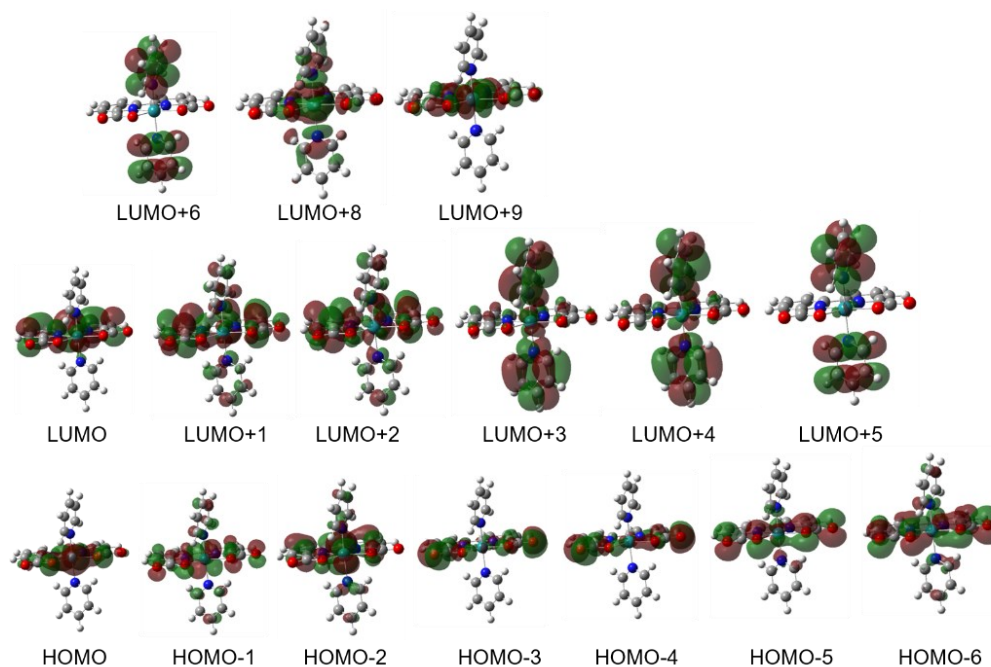


Figure 13. Selected molecular orbitals for the ground state of C0. (Isovalue = 0.02) The green and red color represent different phases.

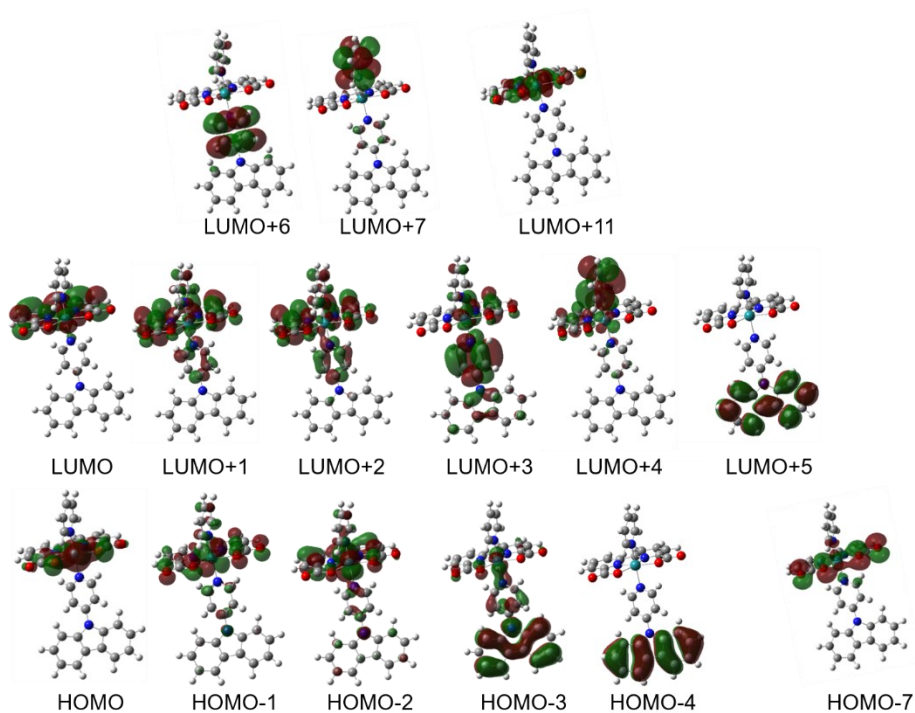


Figure 14. Selected molecular orbitals for the ground state of **C1**. (Isovalue = 0.02) The green and red color represent different phases.

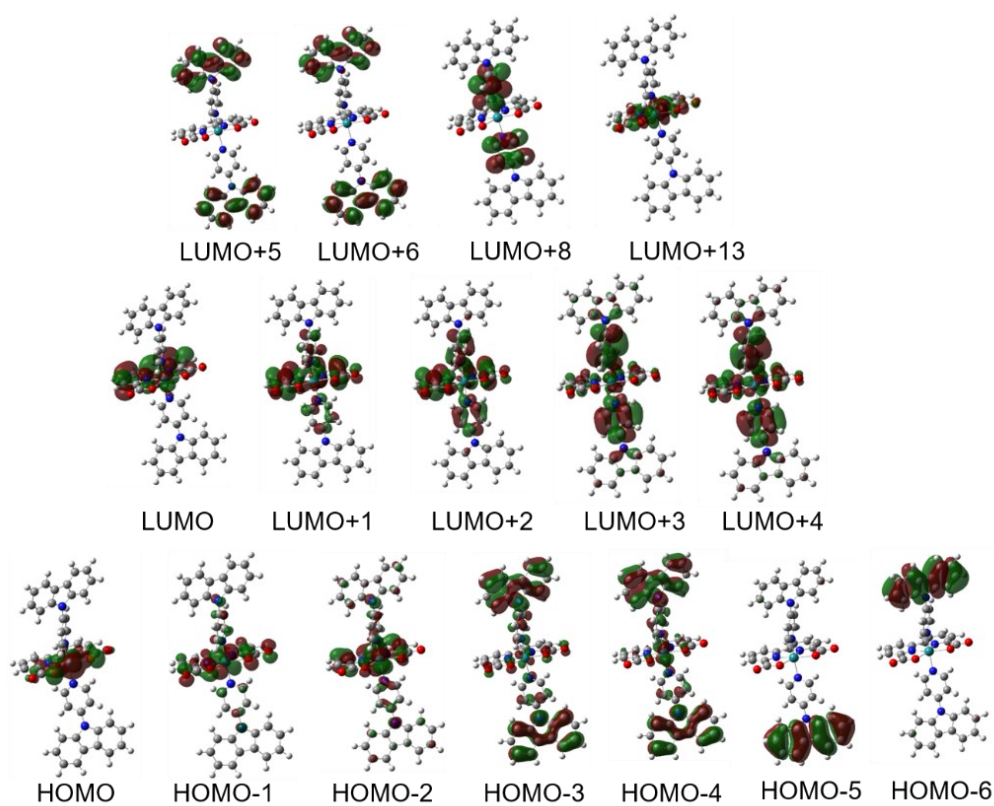


Figure 15. Selected molecular orbitals for the ground state of **C2**. (Isovalue = 0.02) The green and red color represent different phases.

Time-dependent density functional theory (TD-DFT) calculation was conducted to gain deeper insight into the photophysical property of **C1** and **C2**. The results are summarized in Tables 4-6. The simulated absorption spectra of all three complexes were well agreed to the experimental absorption spectra (Fig. 16). The two lowest-energy absorption bands at around 470 and 510 nm with comparable oscillator strength ($f = 0.03$ - 0.04) are basically assigned to the MLCT transition from the Ru 4d to π^* orbital of bda ligand with slight contribution of the π orbital of py ligand. Two remarkably intense bands ($f > 0.1$) were appeared in both the simulated spectra of **C1** and **C2** at ~ 400 nm as the CT transition from the Ru-bda unit to the cbz-py ligand. The orbital of cbz moiety was involved in these transitions (e.g. LUMO+3 of **C1** and **C2**), suggesting that the intense nature should originate from the electron withdrawing nature of cbz moiety, leading to the larger dipole moment of CT transition from Ru-bda to py ligand. On the other hand, the ligand-to-ligand charge transfer (1 LLCT) absorption from the π orbital of cbz-py to the bda π^* orbital was hardly found in the visible region ($\lambda > 400$ nm) of simulated spectra.

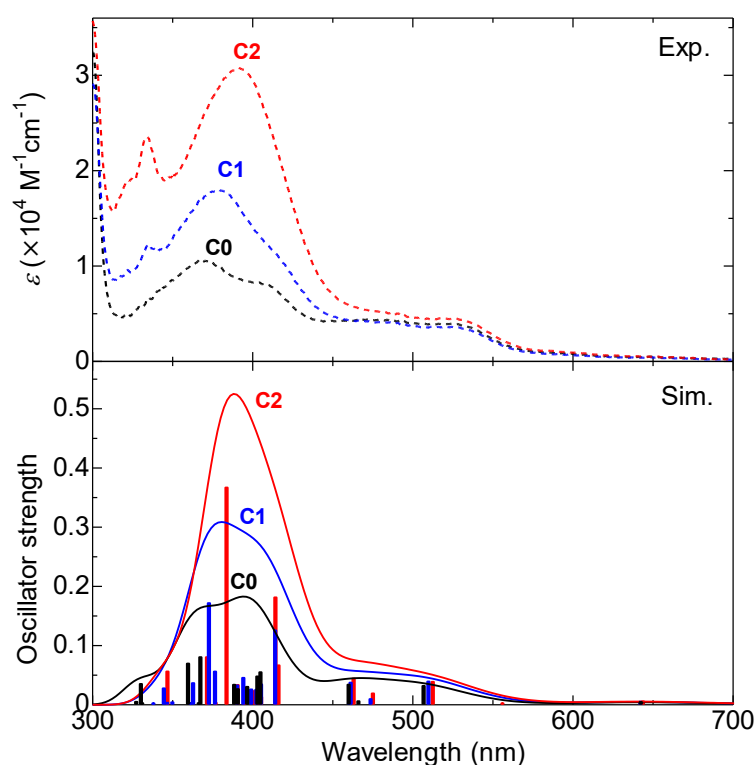


Figure 16. Comparison with (top) experimental spectra in dichloromethane/methanol ($v/v=9/1$) and (bottom) simulated absorption spectra by TD-DFT calculations of **C0** (black), **C1** (blue) and **C2** (red). The values of calculated oscillator strength are plotted as bar charts.

Table 4. Wavelength, oscillator strength (f), and contributions of major transitions ($f > 0.01$) of **C0**.

No.	λ (nm)	f	Major contributions	(%)	Assignment
1	507.05	0.0316	HOMO-2 ->LUMO	77	MLCT : Ru(d) -> bda(π^*)
			HOMO-1 ->LUMO+2	15	
2	460.21	0.0338	HOMO-1 ->LUMO+1	93	MLCT : Ru(d) -> bda(π^*)
3	405.18	0.0547	HOMO-2 ->LUMO+1	7	MLCT : Ru(d) -> bda(π^*) + py(π^*)
			HOMO-1 ->LUMO+2	55	
			HOMO-1 ->LUMO+4	30	
4	403.22	0.0476	HOMO-2 ->LUMO+2	14	MLCT : Ru(d) -> py(π^*)
			HOMO-2 ->LUMO+4	11	
			HOMO-1 ->LUMO+3	60	
			HOMO ->LUMO+9	11	
5	396.85	0.0300	HOMO-2 ->LUMO+2	47	MLCT : Ru(d) -> bda(π^*)
			HOMO-1 ->LUMO+3	27	
			HOMO ->LUMO+9	20	
6	390.99	0.0262	HOMO-2 ->LUMO	7	MLCT : Ru(d) -> py(π^*)
			HOMO-2 ->LUMO+1	6	
			HOMO-2 ->LUMO+3	48	
			HOMO-1 ->LUMO+2	10	
			HOMO-1 ->LUMO+4	20	
			HOMO ->LUMO+8	6	
7	388.7	0.0335	HOMO-2 ->LUMO+2	29	MC : Ru(d) -> Ru(d)
			HOMO ->LUMO+9	60	
8	367.63	0.0802	HOMO-2 ->LUMO+4	71	MLCT : Ru(d) -> py(π^*)
			HOMO-1 ->LUMO+3	8	
			HOMO ->LUMO+6	18	
9	359.95	0.0694	HOMO-2 ->LUMO+4	14	MLCT : Ru(d) -> py(π^*)
			HOMO ->LUMO+6	78	
10	330.48	0.0349	HOMO-6 ->LUMO	85	LC : bda(π) -> bda(π^*)
			HOMO-1 ->LUMO+6	8	

Table 5. Wavelength, oscillator strength (f), and contributions of major transitions ($f > 0.01$) of **C1**.

No.	λ (nm)	f	Major contributions ^a	(%)	Assignment
1	510.05	0.0390	HOMO-2 ->LUMO	76	MLCT : Ru(d) -> bda(π^*)
			HOMO-1 ->LUMO+2	12	
2	461.48	0.0371	HOMO-1 ->LUMO+1	93	MLCT : Ru(d) -> bda(π^*)
3	414.35	0.1253	HOMO-1 ->LUMO+2	45	MLCT : Ru(d) -> bda(π^*)+cbz-py(π^*)
			HOMO-1 ->LUMO+3	38	
4	405.51	0.0342	HOMO-3 ->LUMO	10	MLCT : Ru(d) -> cbz-py(π^*)
			HOMO-2 ->LUMO+3	10	
			HOMO-1 ->LUMO+2	17	
			HOMO-1 ->LUMO+3	21	
5	402.61	0.0252	HOMO-1 ->LUMO+4	23	LLCT : cbz-py(π) -> bda(π^*)
			HOMO-3 ->LUMO	48	
			HOMO-2 ->LUMO+2	10	
6	399.34	0.0257	HOMO-1 ->LUMO+4	21	MLCT : Ru(d)+ bda(π) -> bda(π^*)
			HOMO-3 ->LUMO	9	
			HOMO-2 ->LUMO+2	45	
			HOMO-1 ->LUMO+3	8	
			HOMO-1 ->LUMO+4	7	
7	394.44	0.0453	HOMO ->LUMO+11	23	MLCT : Ru(d) -> cbz-py(π^*)
			HOMO-3 ->LUMO	26	
			HOMO-2 ->LUMO+3	33	
			HOMO-1 ->LUMO+2	6	
8	390.55	0.0323	HOMO-1 ->LUMO+4	16	MC : Ru(d) -> Ru(d)
			HOMO-2 ->LUMO+2	27	
9	376.75	0.0559	HOMO ->LUMO+11	59	MLCT : Ru(d) -> cbz-py(π^*)
			HOMO-2 ->LUMO+3	15	
			HOMO-2 ->LUMO+4	16	
10	372.95	0.1714	HOMO ->LUMO+6	58	MLCT : Ru(d) -> py(π^*)+cbz-py(π^*)
			HOMO-2 ->LUMO+4	44	
			HOMO-1 ->LUMO+3	6	
11	363.07	0.0363	HOMO ->LUMO+6	36	MLCT : Ru(d) -> py(π^*)
12	344.82	0.0275	HOMO ->LUMO+7	90	LLCT : cbz-py(π) -> bda(π^*)
			HOMO-7 ->LUMO	8	
			HOMO-3 ->LUMO+1	77	

^aMinor contributions (< 5%) are omitted.

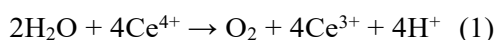
Table 6. Wavelength, oscillator strength (f), and contributions of major transitions ($f > 0.01$) of **C2**.

No.	λ (nm)	f	Major contributions ^a		(%)	Assignment
1	512.77	0.0385	HOMO-2	->LUMO	72	MLCT : Ru(d) -> bda(π^*)
			HOMO-1	->LUMO+2	10	
			HOMO-1	->LUMO+4	7	
			HOMO	->LUMO+2	6	
2	475.38	0.0189	HOMO	->LUMO+3	94	MLCT : Ru(d) -> cbz-py(π^*)
3	463.32	0.0441	HOMO-1	->LUMO+1	93	MLCT : Ru(d) -> cbz-py(π^*)
4	416.39	0.0664	HOMO-2	->LUMO+1	6	MLCT : Ru(d) -> bda(π^*)
			HOMO-1	->LUMO+2	68	
			HOMO-1	->LUMO+4	19	
5	414.49	0.1811	HOMO-2	->LUMO+4	8	MLCT : Ru(d) -> cbz-py(π^*)
			HOMO-1	->LUMO+3	81	
6	405.54	0.0130	HOMO-4	->LUMO	34	LLCT : cbz-py(π) -> bda(π^*) mixed with MLCT : Ru(d) -> cbz-py(π^*)
			HOMO-2	->LUMO	10	
			HOMO-2	->LUMO+3	20	
			HOMO-1	->LUMO+4	22	
7	403.66	0.0125	HOMO-3	->LUMO	92	LLCT : cbz-py(π) -> bda(π^*)
8	401.23	0.0229	HOMO-2	->LUMO+2	60	MLCT : Ru(d) -> bda(π^*)
			HOMO-1	->LUMO+3	6	
			HOMO	->LUMO+13	20	
9	395.52	0.0236	HOMO-4	->LUMO	57	LLCT : cbz-py(π) -> bda(π^*)
			HOMO-2	->LUMO+3	28	
10	390.88	0.0332	HOMO-2	->LUMO+2	19	MC : Ru(d) -> Ru(d)
			HOMO	->LUMO+13	65	
11	383.99	0.3667	HOMO-2	->LUMO+2	6	MLCT : Ru(d) -> cbz-py(π^*)
			HOMO-2	->LUMO+4	82	
			HOMO-1	->LUMO+3	6	
12	371.75	0.0802	HOMO	->LUMO+8	96	MLCT : Ru(d) -> cbz-py(π^*)
13	347.08	0.0560	HOMO-3	->LUMO+1	90	LLCT : cbz-py(π) -> bda(π^*)

^aMinor contributions (< 5%) are omitted.

3-3-4 Chemical water oxidation

OER with the Ce^{IV} sacrificial oxidant $(\text{NH}_4)_2[\text{Ce}(\text{NO}_3)_6]$ (CAN) was carried out to evaluate the effect of cbz functionalization on the catalytic activity. Fig. 17 shows the results of the OER in the presence of 100 μM **CX** WOC catalyst ($\text{X} = \mathbf{0}, \mathbf{1}, \mathbf{2}$) and 120 mM CAN at room temperature. The estimated turn-over frequency for the initial 30 s of reaction (TOF_i) and maximum TOF (TOF_{max}) are listed in Table 2. All three complexes catalytically evolved O_2 , whereas no O_2 evolved in the absence of a WOC. The amounts after 2 min of reaction almost reached a value (150 μmol) corresponding to the complete consumption of CAN when the following reaction occurred:



The OER activity (TOF_i and TOF_{max}) of **C2** was higher than those of **C1** and **C0**. This occurs because the electron-withdrawing cbz moieties in **C2** enhance the catalytic activity by destabilizing the $[\text{Ru}^{\text{V}}=\text{O}]^+$ species, thereby leading to the formation of radical couplings ($\text{Ru}^{\text{IV}}-\text{O}-\text{O}-\text{Ru}^{\text{IV}}$ species) as reported in the literature.^{5c} On the other hand, the OER activity of **C1** started to decrease after ~ 45 s, suggesting the presence of deactivation processes.

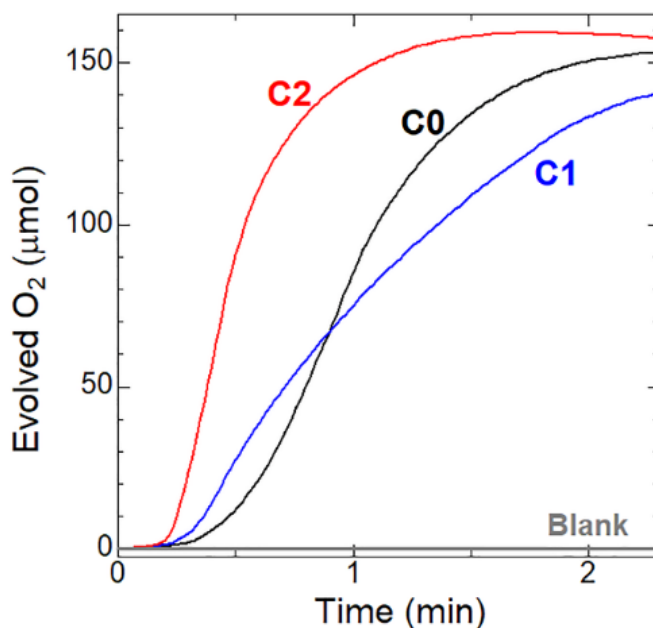


Figure 17. Chemical OER plots of the complexes **C0** (black), **C1** (blue), and **C2** (red) in pH = 1.0 HClO_4 aq./TFE/acetonitrile (v/v/v = 3/2/1), $[\text{CAN}] = 120$ mM, and $[\text{Cat.}] = 100$ μM .

Gray line shows the result in the absence of a WOC.

To obtain more detailed information on the reaction mechanism, the catalyst concentration ([Cat.]) dependence of the OER was next investigated (Fig. 18a-c, Table 7). The OER rate (mM s^{-1}) of all the three complexes decreased with decreasing [Cat.]. Moreover, the linear proportional correlation between the OER rate and square of the catalyst concentration ($[\text{Cat.}]^2$) (Fig. 19), suggests that the OER proceeds as a second-order reaction. These results are in good agreement with the proposed reaction mechanism for the Ru-bda catalyst via the $\text{Ru}^{\text{IV}}\text{-O-O-Ru}^{\text{IV}}$ species^{5, 7, 18, 24} and previous reports on related kinetic analysis.^{18a, 23} The O_2 evolved for **C0** and **C1** under $[\text{Cat.}] = 25 \mu\text{M}$ conditions approximated $70 \mu\text{mol}$ after 25 min of reaction. On the other hand, **C2** evolved $\sim 140 \mu\text{mol}$ O_2 after 12 min reaction, because of the almost complete consumption of CAN as the one-electron oxidant. These results indicate the superior performance of **C2** even at low CAN concentrations. Notably, remarkable changes in the OER rate before the complete consumption of CAN were observed for **C1** and **C2** under low [Cat.] conditions. In particular, at $25 \mu\text{M}$ for **C2** and below $50 \mu\text{M}$ for **C1**, the OER rate decreased once within the initial 3 min reaction and then increased again (Fig. 18b and 18c for **C1** and **C2**, respectively). This unique behavior was not observed for **C0**, indicating that the oxidation reaction of the cbz moieties in **C1** and **C2** are key to this unique behavior.

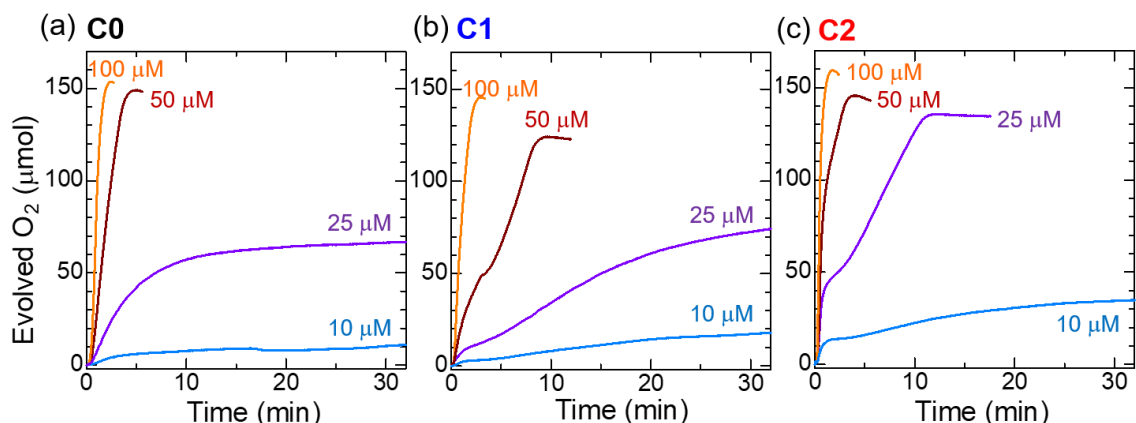


Figure 18. Catalyst concentration dependence of the chemical OERs of (a) **C0**, (b) **C1**, and (c) **C2**. $[\text{CAN}] = 120 \text{ mM}$, $[\text{Cat.}] = 10 \mu\text{M}$ (light blue), $25 \mu\text{M}$ (purple), $50 \mu\text{M}$ (brown), and $100 \mu\text{M}$ (orange) in $\text{pH} = 1.0 \text{ HClO}_4 \text{ aq./TFE/acetonitrile}$ ($v/v/v = 3/2/1$).

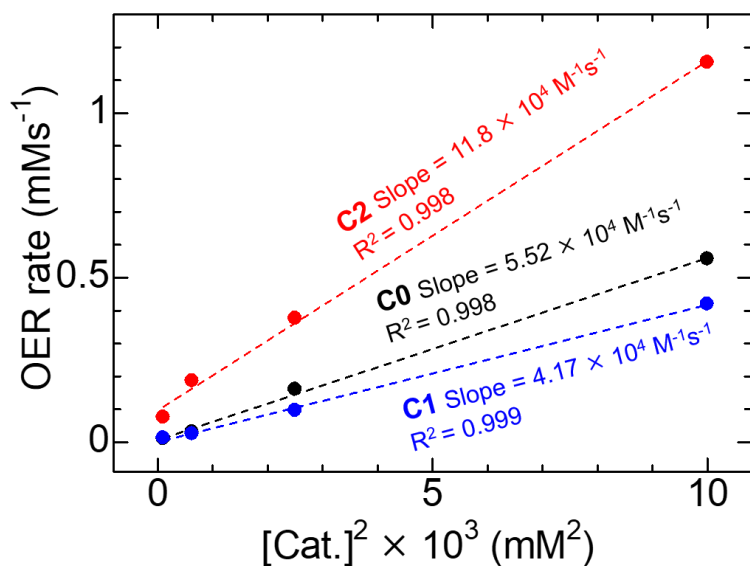


Figure 19. [Cat.] dependence of OER rate (= Evolved O₂ amount / Time) (Estimated from TOF_{max}).

Table 7. O₂ evolution catalytic activity of each WOC.^a

Catalyst	[Cat.] (μM)	[CAN] (mM)	TOF _i (s ⁻¹) ^b	TOF _{max} (s ⁻¹) ^c
C0	100	120	0.84	5.6
	50	120	0.51	3.2
	25	120	0.46	1.3
	10	120	0.26	1.0
	50	90	0.28	3.7
	50	60	0.25	3.9
C1	100	120	1.7	4.2
	50	120	1.1	1.9
	25	120	1.0	1.0
	10	120	0.43	1.3
	50	90	3.0	7.3
	50	60	4.0	10
C2	100	120	6.0	11
	50	120	5.1	7.5
	25	120	5.5	7.5
	10	120	4.3	7.6
	50	90	4.0	8.4
	50	60	4.2	7.1

^a pH = 1.0 HClO₄ aq./TFE/acetonitrile (v/v/v = 3/2/1).

^b Estimated from the values obtained for the initial 30 s after mixing.

^c Estimated from the values obtained for the 9 s which TOF value is highest.

To examine the effect of cbz oxidation, OER of **C0** in the presence of two equivalents of unsubstituted carbazole was investigated (cbz-H, Fig. 20). Only a small amount of oxygen ($\sim 5.5 \mu\text{mol}$) was produced in the initial 2 min of reaction, after which the OER was paused for 5 min. Subsequently, the OER restarted to generate O_2 ($\sim 130 \mu\text{mol}$). The oxidation potential of cbz (1.4–1.5 V) in the above-mentioned electrochemical measurements was estimated to be more negative than that of the $\text{Ce}^{\text{IV/III}}$ redox potential of CAN (1.70 V vs NHE).²⁸ This suggests that both the Ru centre and the cbz-py ligand can be oxidized by the excess amount of CAN, and thus, that the cbz-oxidized species can be involved in the catalytic OER.

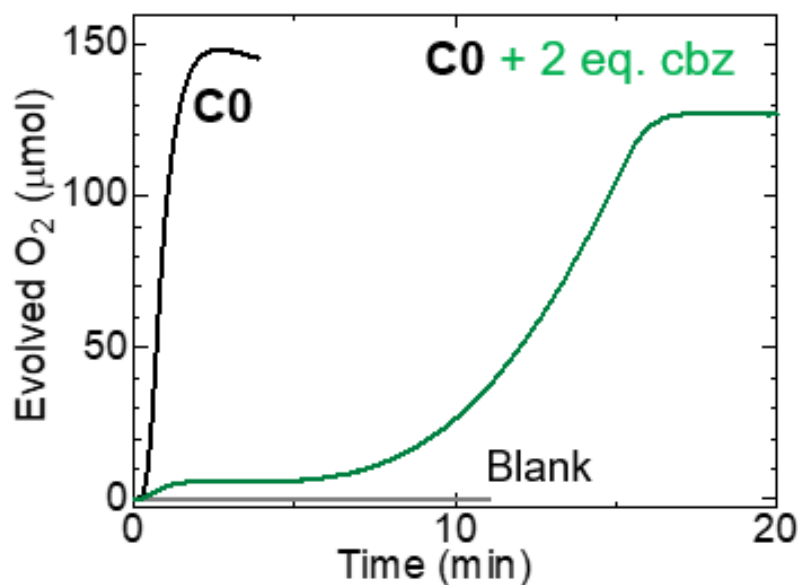


Figure 20. The chemical OER plots of **C0** in the presence of 2 eq. of cbz-H with $[\text{Cat.}] = 100 \mu\text{M}$ and $[\text{CAN}] = 120 \text{ mM}$.

Because the oxidation of the cbz moieties in **C1** and **C2** is expected to occur more easily in the presence of a large excess of CAN, the CAN concentration dependence was next investigated with $[\text{Cat.}] = 50 \mu\text{M}$ (Fig. 21). No significant change in the TOF_{max} of **C0** was observed by decreasing $[\text{CAN}]$; however, the value for **C1** increased at least threefold when $[\text{CAN}]$ was decreased from 120 mM to 90 or 60 mM (Table 7). Notably, this unique behavior, in which the OER rate changed before the complete consumption of CAN, was hardly observed at lower $[\text{CAN}]$. For **C2**, a decrease in the OER rate was observed after approximately 1 min when $[\text{CAN}]$ equaled 120 mM but not with lower concentrations. This infers that the large excess of CAN oxidizes the cbz group(s) of **C1** and **C2**, leading to a change in the OER mechanism.

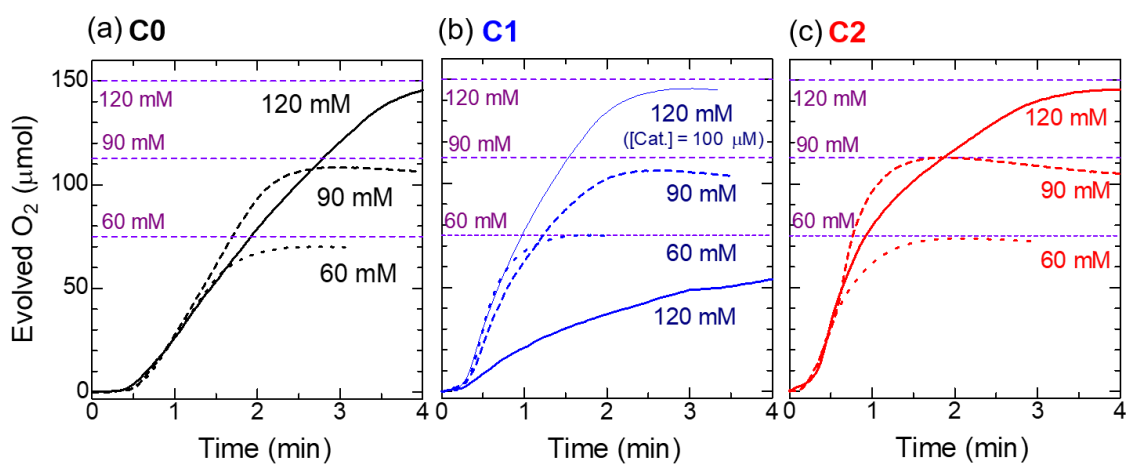
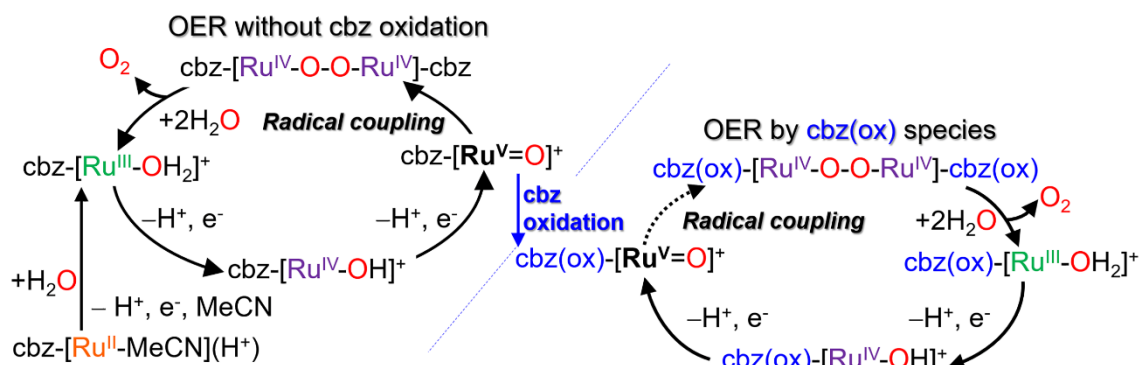


Figure 21. Chemical OER plots of (a) **C0** (b) **C1** (c) **C2**(50 μM) under [CAN] = 60-120 mM. [CAN] = 120 mM (bold lines), 90 mM (dashed lines) and 60 mM (dotted lines). Purple dashed lines in each panel show the calculated O₂ amounts based on the amount of one-electron oxidant CAN.

Scheme 2 shows the possible OER mechanism of the cbz-modified catalysts, **C1** and **C2**. The key step for the OER of **C0** is the radical coupling reaction of two $\text{Ru}^{\text{V}}=\text{O}$ species to form the $\text{Ru}^{\text{IV}}-\text{O}-\text{O}-\text{Ru}^{\text{IV}}$ species. For **C1** and **C2**, comprising cbz moieties, in the presence of a large excess of CAN, the oxidation of the cbz group(s) competes with the formation of the $\text{Ru}^{\text{IV}}-\text{O}-\text{O}-\text{Ru}^{\text{IV}}$ species through radical coupling and the subsequent reaction to produce oxygen.



Scheme 2. OER mechanism of **C1** and **C2** involving the oxidation of the cbz moiety.

Although the characterization of cbz-oxidized species was not succeeded, the formation of nitrocarbazole derivatives resulted from an oxidative nitration by CAN has been reported.²⁹ In order to obtain more detail information about these oxidized species, mass spectroscopy measurements for the extracts of the OER-ceased reaction mixture with **C1** (50 μ M) or **C2** (25 μ M) by CH_2Cl_2 were carried out (Fig. 22). On the MS spectra of them, the peak with Ru isotopic pattern was observed at $m/z^+ = 541.97$ (**C1**) or 789.29 (**C2**). A dissociation of py ligands is reported to be main decomposition/deactivation pathway for Ru-bda series.^{5c} Additionally, considering the values of octanol-water partition coefficient, $\log P_{\text{OW}}$ of the solvents for the reaction (Acetonitrile : -0.34 ³⁰, TFE : 0.36 ³¹), TFE should be mainly distributed to organic layer on the extraction. Since these knowledge, decomposed **C1** and **C2** can exist as $[\text{Ru}(\text{bda})(\text{H}_2\text{O})(\text{TFE})(\text{py}\text{-ligand})]$ species in the extract, assuming that Ru-bda backbone exists as $[\text{Ru}(\text{bda})(\text{H}_2\text{O})]^+$, similar as in acidic mixture. From these consideration, $[\text{Ru}(\text{bda})(\text{H}_2\text{O})(\text{TFE})(\text{py})]^+\text{H}^+$ ($m/z^+ = 541.27$) is the plausible species on **C1**. (Fig. 22a) On the other hand, the small peak was also observed at $m/z^+ = 307.13$. Considering the m/z^+ of the nitrated cbz-py + O + H⁺ ($=307.30$), this peak can be assigned as dissociated 4-(nitrocarbazolyl-hydroxide or N-oxide) pyridine. (Fig. 22a, inset) Assuming carbazole moieties were converted to such oxidized species (cbz(ox)-py), the strongest peak observed for the extract from the **C2** reaction solution could be assigned to $[\text{Ru}(\text{bda})(\text{H}_2\text{O})(\text{TFE})(\text{cbz}(\text{ox})\text{-py})]^+\text{Na}^+$ ($m/z^+ = 790.60$, Fig. 22b). If such the irreversible oxidation processes of the cbz moiety occurs, the radical coupling of $[\text{Ru}^{\text{V}}=\text{O}]^+$ complexes to form $\text{Ru}^{\text{IV}}\text{-O-O-Ru}^{\text{IV}}$ species can be suppressed by steric hindrance and/or electrostatic repulsion between the cbz-oxidized complexes $\text{cbz}(\text{ox})\text{-}[\text{Ru}^{\text{V}}=\text{O}]^+$, resulting in a slower OER. Although the OER activity of the cbz-oxidized species was lower than that of the species without cbz oxidation, these results suggest that the cbz-functionalization of the **C0** molecular catalyst is a promising approach for the integration of the hole-mediator function near the WOC center.

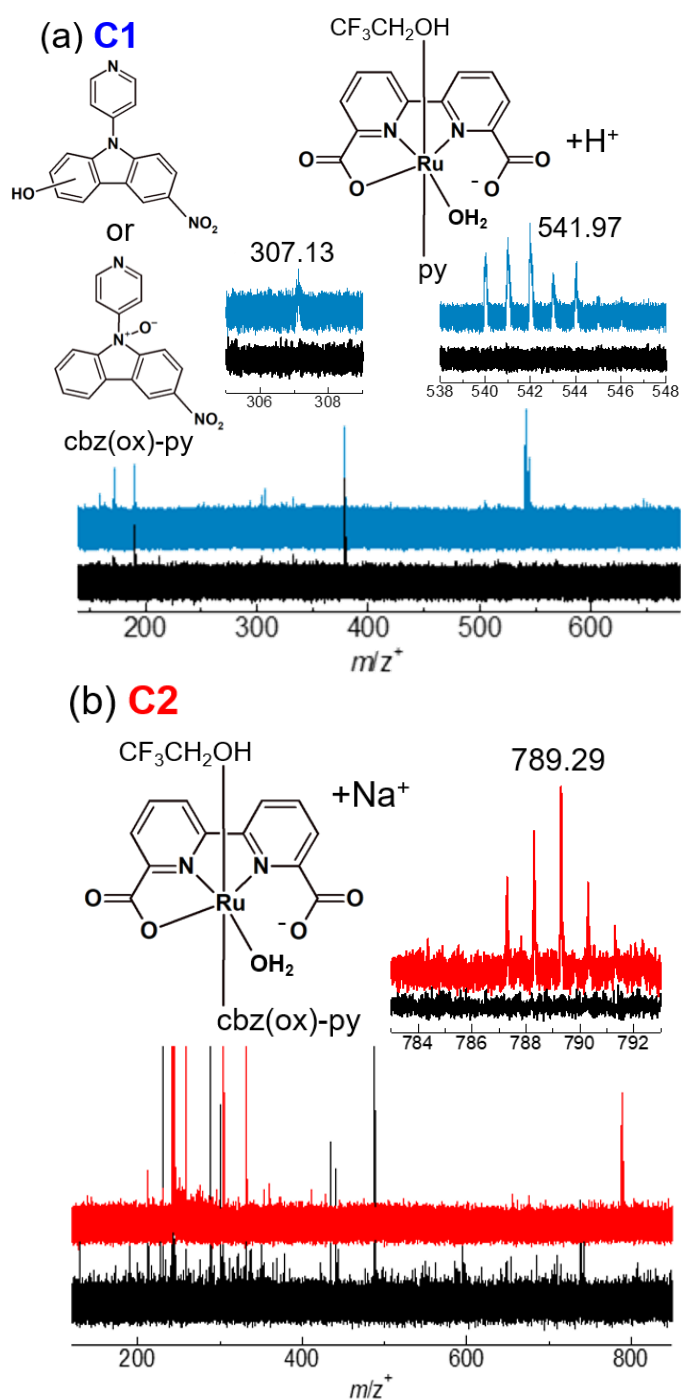


Figure 22. MALDI-MS spectra of the extract from the reaction mixture after chemical OER of (a) **C1** (CH_2Cl_2 soln.) and (b) **C2** (sodium trifluoroacetate/ CH_2Cl_2 /MeOH soln.).

Reaction mixture [**C2**] = 25 μM , [**C1**] = 50 μM , [CAN] = 120 mM, in pH = 1.0 HClO_4 aq./TFE/acetonitrile (v/v/v = 3/2/1) stirred for 30 min was extracted by CH_2Cl_2 and solvent was removed. Matrix : CHCA, reflection-positive mode.

The spectrum without the extract was shown as black solid line. The insets are the magnification of the peaks assignable to a Ru-derived species and cbz (ox)-py.

3-3-5 Photochemical water oxidation

Photochemical OER was conducted in the presence of $[\text{Ru}(\text{bpy})_3]^{2+}$ (bpy = 2, 2'-bipyridine) as the PS and $\text{Na}_2\text{S}_2\text{O}_8$ as the sacrificial oxidant. The estimated TOF_{max} and turnover number (TON) for 60 min of reaction are listed in Table 8. As shown in Fig. 23, the photochemical OER activities of **C1** and **C2** in the initial 10 min of reaction were higher than that of **C0**.

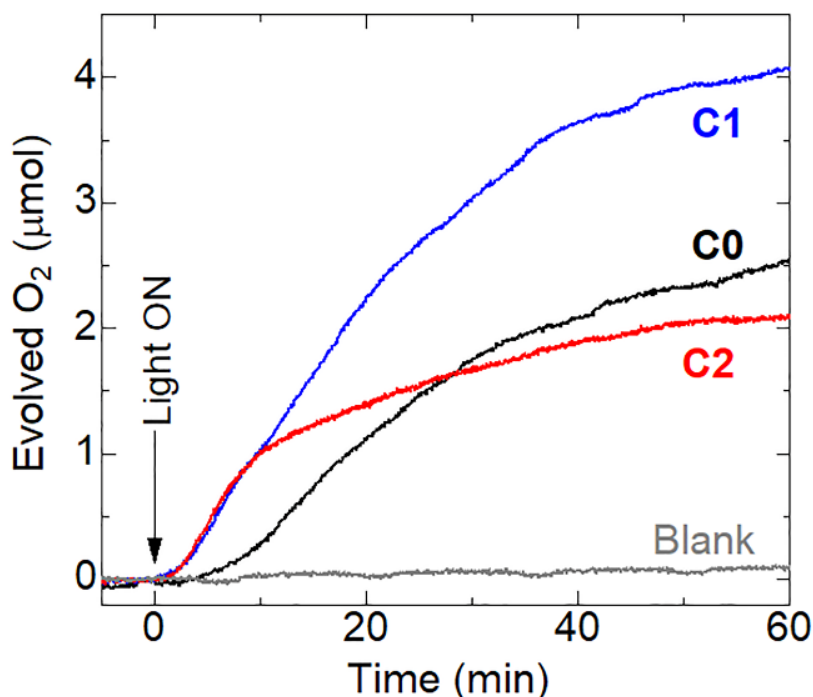


Fig. 23. Photochemical OER plots of the complexes **C0** (black), **C1** (blue), and **C2** (red) in borate buffer (10 mM, pH = 8.0) aq./TFE /acetonitrile (v/v/v = 3/2/1). [Cat.] = 10 μM , $[\text{Ru}(\text{bpy})_3]^{2+}$ = 200 μM , $[\text{Na}_2\text{S}_2\text{O}_8]$ = 5 mM, λ = 470 nm, 30 mWcm^{-2} .

Table 8. Photocatalytic O_2 evolution activity of each WOC. ^a

Catalyst	$\text{TOF}_{\text{max}}(\text{min}^{-1})$ ^b	TON ^c
C0	1.5	49
C1	2.7	79
C2	2.7	40

^a Borate buffer (10 mM, pH8.0) aq./TFE/acetonitrile (v/v/v = 3/2/1) [Cat.] = 10 μM , $[\text{Ru}(\text{bpy})_3]^{2+}$ = 200 μM , $[\text{Na}_2\text{S}_2\text{O}_8]$ = 5 mM, λ = 470 \pm 10 nm, 30 mWcm^{-2} .

^b Estimated from the values at 15–20 min (**C0**) and 3–8 min (others) after light irradiation.

^c Estimated from the values at 60 min after light irradiation.

Since no O₂ evolution was detected in the absence of [Ru(bpy)₃]²⁺ PS (Fig. 24), these photochemical OER reactions weren't driven only by catalyst itself, such as a cbz-photoexcited process.

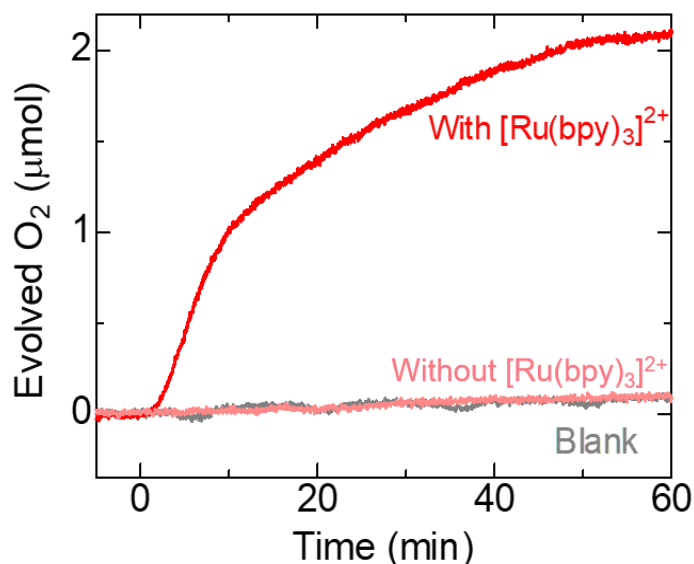


Figure 24. Photochemical OER plots of **C2** (10 μM) without [Ru(bpy)₃]²⁺ in borate buffer (10 mM, pH = 8.0) aq./TFE /acetonitrile (v/v/v = 3/2/1). [Cat.] = 10 μM, [Na₂S₂O₈] = 5 mM, λ = 470 nm, 30 mWcm⁻².

The TOF_{max} values of **C1** and **C2** were also 1.8 times higher than that of **C0**. These better catalytic activities are ascribed to the contribution of the electron-withdrawing cbz moiety, as discussed in § 3-3-2. The photochemical OER rate of **C2** decreased after 10 min of irradiation, and the TON after 1 h of irradiation was less than that of **C0**. However, such a decrease in photochemical OER activity was not observed for **C1**, wherein the TON was approximately 1.6 times higher than that of **C0**. Next the photochemical OER of **C0** in the presence of two equivalents of cbz-H were examined in order to determine the contribution of the cbz moiety (Fig. 25). In contrast to the chemical OER (Fig. 6a), the addition of cbz-H hardly affected the photochemical OER of **C0**, suggesting that the oxidation of cbz does not significantly affect the photo-oxygenation reaction. Considering the redox potentials of [Ru(bpy)₃]-type PSs (ground state Ru^{III/II}, ~1.27 V and ³MLCT excited Ru^{II*/I}, ~0.96 V),³² the Ru centers of **C1** and **C2** can be oxidized by these PS species, while the cbz moiety cannot be oxidized. However, in the photolysis using a [Ru(bpy)₃]²⁺ PS and Na₂S₂O₈ sacrificial oxidant, the sulfate radical, generated by the one-electron reduction of the persulfate anion was reported to be a sufficiently strong oxidant (>2.4 V vs NHE³³) to decompose the [Ru(bpy)₃]²⁺ oxidatively.³⁴ The UV-vis absorption spectra after 1 h of photochemical OER were obtained to evaluate the stability of the [Ru(bpy)₃]²⁺ photosensitizer (Fig. 26).

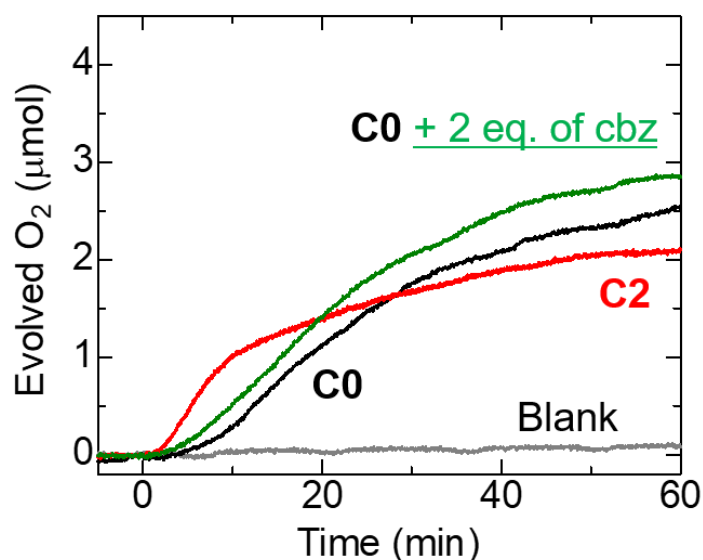


Figure 25. Photochemical OER plots of C0 (10 μM) with cbz-H (20 μM) adduct.

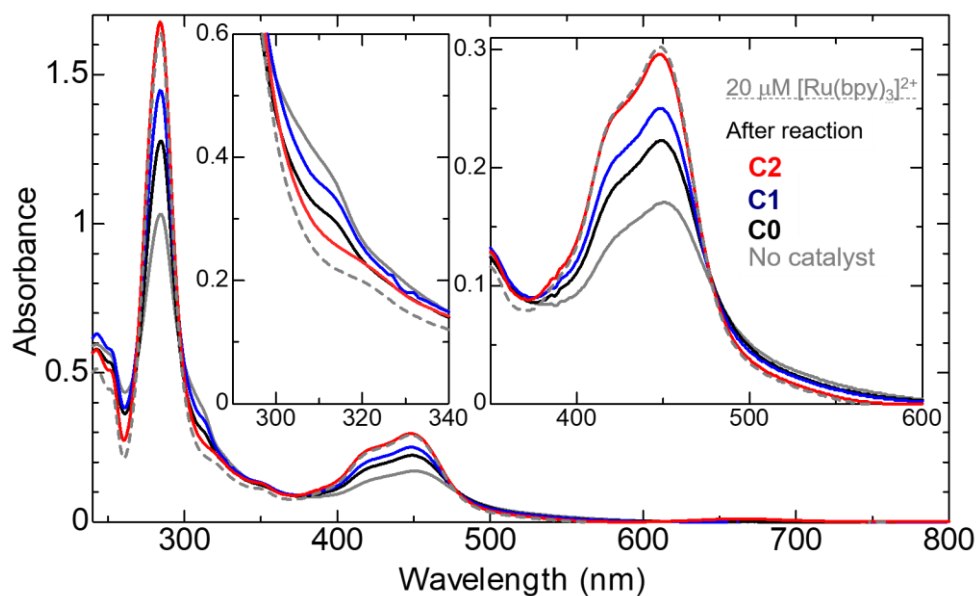


Figure 26. UV-Vis absorption spectra of reaction mixture after 1 h photolysis (solid line, red : C2, blue : C1, black : C0 and no catalyst : gray. Diluted 10th fold.) and 20 μM [Ru(bpy)₃]²⁺ soln. (gray, dashed line, pH=8.0, bubbled for 30 min and stated in the dark for 1 h).

The ¹MLCT absorption band at ~450 nm decreased to almost half in the absence of a catalyst after 1 h of reaction, while the decrease in ¹MLCT absorption was effectively suppressed in the order C0 < C1 < C2. Notably, in the reaction with C2, hardly any changes were observed in both the absorbance and width of the ¹MLCT band after 1 h of photochemical OER, indicating the negligible decomposition of [Ru(bpy)₃]²⁺ PS. In addition, the absorption peak at 316 nm was assigned to the oxidative decomposed species of the Ru photosensitizer.^{34a} Thus,

the decreasing photochemical OER activity of **C2** within 10 min of reaction should not be due to the decomposition of the $[\text{Ru}(\text{bpy})_3]^{2+}$ PS. Considering that the cbz oxidation wave of **C2** in the CV measurement decreased more rapidly by only a few potential sweeps than that of **C1** (Fig. 7), the decreasing photochemical OER activity of **C2** can be associated with the oxidative decomposition of the cbz moiety by sulfate radicals to form a less active species. This is also supported by the photochemical OER reaction in the presence of one-electron sacrificial oxidant $[\text{Co}^{\text{III}}\text{Cl}(\text{NH}_3)_5]^{2+}$ ³⁵; the decrease of photochemical OER rate of **C2** within 10 min irradiation was hardly observed and the evolved O_2 amount of **C2** after 60 min irradiation was comparable to that of **C1** (Fig. 27). The TON values of **C1** and **C2** (9.1) are also higher than that of **C0** (6.2) under this condition.

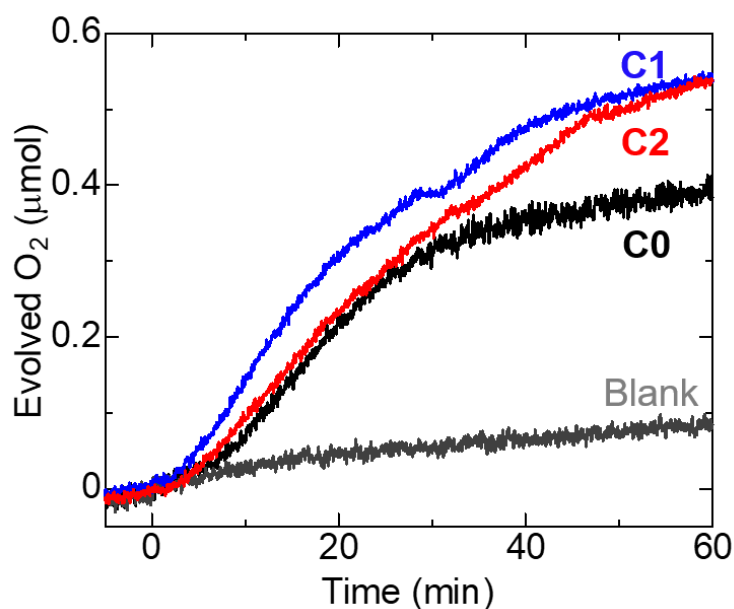


Figure 27. Photochemical OER plots of complexes **C0** (black), **C1** (blue) and **C2** (red) with Co^{III} oxidant in acetate buffer (40 mM, pH=5.0) aq. / TFE / acetonitrile (v/v/v = 3/2/1). $[\text{Cat.}] = 10 \mu\text{M}$, $[\text{Ru}(\text{bpy})_3]^{2+} = 200 \mu\text{M}$, $[\text{CoCl}(\text{NH}_3)_5]^{2+} = 4 \text{ mM}$, $\lambda = 470 \text{ nm}$, 30 mWcm^{-2} .

Finally, [Cat.] dependency of photochemical OER activity has been checked to investigate the reaction mechanism (Figure 28). As Figure 28d, linear correlation was observed between $[\text{Cat.}]^2$ and OER rate for all the three cases. This result indicates that photochemical OER process is also a 2nd-order reaction similar as chemical OER (Fig.28d). In other words, mononuclear species dominantly drive the catalysis, not by μ -oxo dimer²⁶ or trimer species,³⁶ that catalyzes in the 1st-order reaction.

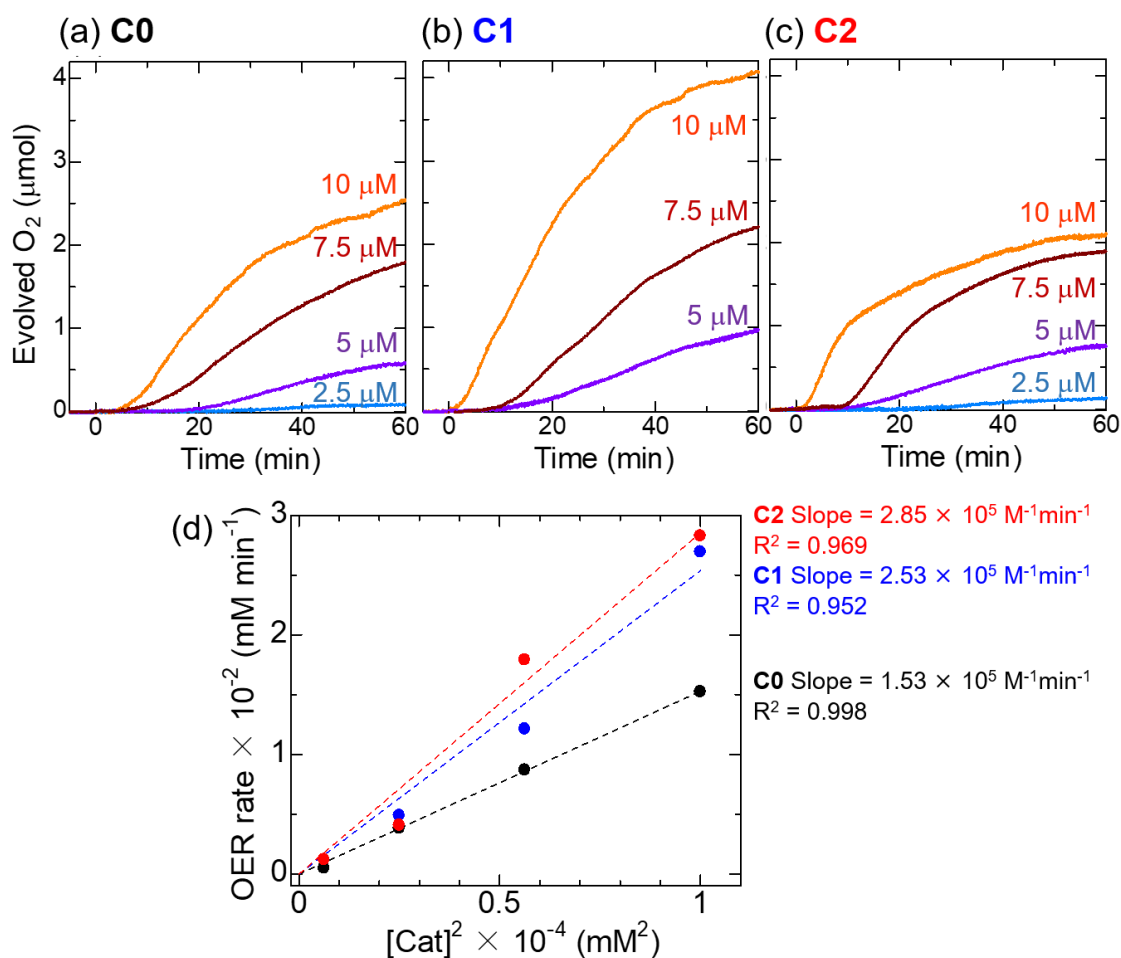
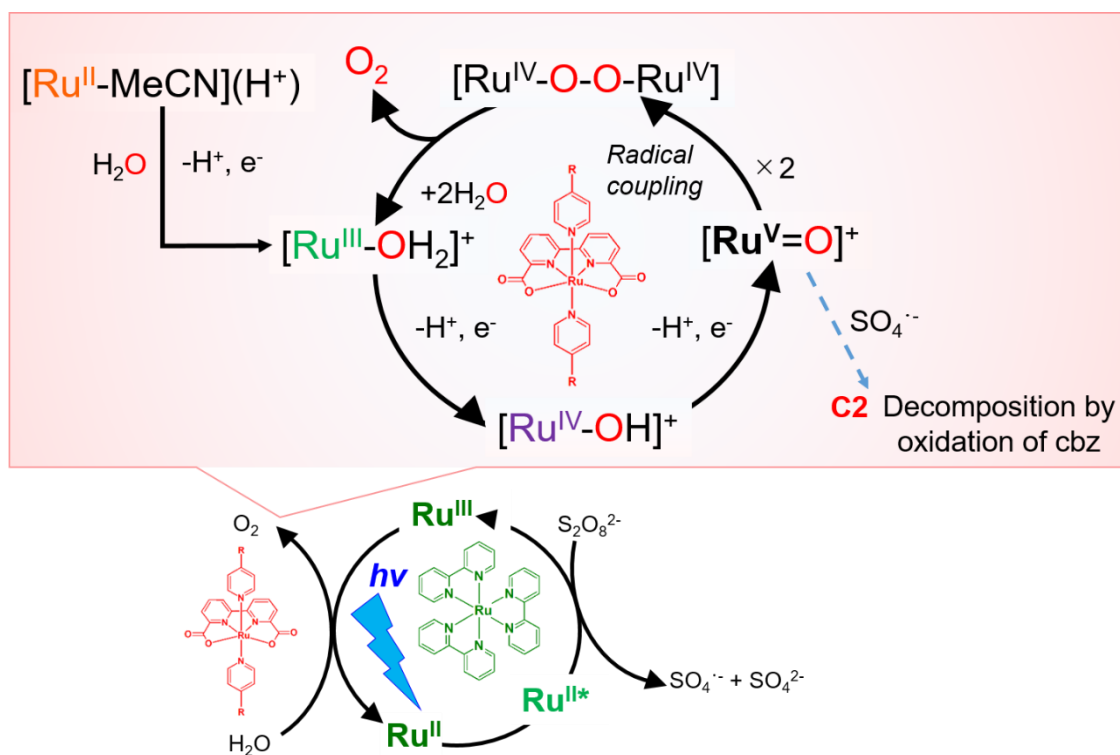


Figure 28. Photochemical OER plots of (a) C0, (b) C1 and (c) C2 under $[\text{Cat}] = 2.5\text{-}10 \mu\text{M}$, in borate buffer (10 mM, pH=8.0) aq. / TFE / acetonitrile (v/v/v = 3/2/1), $[\text{Ru}(\text{bpy})_3]^{2+} = 200 \mu\text{M}$, $[\text{Na}_2\text{S}_2\text{O}_8] = 5 \text{ mM}$, $\lambda = 470 \text{ nm}$, 30 mWcm^{-2} . (d) Photochemical OER dependency on $[\text{Cat.}]$ of C0 (black), C1 (blue) and C2 (red).

Scheme 3 shows the plausible OER mechanism of each catalyst. Four-electron oxidation of Ru center of the catalyst follows oxidation of Ru PS by sacrificial oxidant. The key step of OER is the radical coupling reaction of two $\text{Ru}^{\text{V}}=\text{O}$ species similar as chemical OER on all the catalysts. On **C2**, oxidative decomposition would be also induced by sulfate radical produced by a reduction of persulfate oxidant.



Scheme 3. Photochemical OER mechanism.

2-4 Conclusion

It was synthesized that the [Ru(bda)(py)₂]-type OER molecular catalysts **C1** and **C2**, with one and two carbazole (cbz) group(s), respectively, as precursors of hole-mediators and investigated the effect of cbz functionalization on the photophysical and OER activity as compared to that of the unsubstituted **C0**. Theoretical calculations, spectroscopic and electrochemical measurements revealed the cbz moiety functions as electron-withdrawing groups that improve the OER activity in both chemical OER in the presence of CAN and photochemical OERs comprising a [Ru(bpy)₃]²⁺ photosensitizer and Na₂S₂O₈. Even at a low catalyst concentration (25 μM), **C2** completely consumed CAN to generate O₂. In the chemical OER with a large excess of CAN, both **C1** and **C2** exhibited unique behavior, in which the OER activity changed during the reaction. This indicated competition between the oxidation of the cbz moiety and OER at the Ru center. In the photochemical OER, both **C1** and **C2** exhibited high initial OER activities. A rapid deactivation behavior was observed for **C2**, while **C1** showed higher OER activity and durability comparable to that of the unsubstituted **C0**. This suggested that the number of cbz groups in the catalyst molecule is key to this behavior.

3-5 References

- 1 (a) K. Karon, M. Lapkowski, *J. Solid State Electrochem.*, 2015, **19**, 2601. (b) L. Kortekaas, F. Lancia, J. D. Steen, W. R. Browne, *J. Phys. Chem. C*, 2017, **121**, 14688. (c) M. Li, *Chem. - A Eur. J.*, 2019, **25**, 1142.
- 2 Z. Singh, P. R. Donnarumma, M. B. Majewski, *Inorg. Chem.*, 2020, **59**, 12994.
- 3 (a) H. Iwami, M. Okamura, M. Kondo, S. Masaoka, *Angew. Chem. Int. Ed.*, 2021, **60**, 5965. (b) J. Zhang, J. Du, J. Wang, Y. Wang, C. Wei, M. Li, *Angew. Chem. Int. Ed.*, 2018, **57**, 16698.
- 4 J. Zhang, J. Wang, C. Wei, Y. Wang, G. Xie, Y. Li, M. Li, *Nat. Commun.* 2020, **11**.
- 5 (a) B. Zhang, L. Sun, *J. Am. Chem. Soc.* 2019, **141**, 5565. (b) L. Duan, A. Fischer, Y. Xu and L. Sun, *J. Am. Chem. Soc.* 2009, **131**, 10397. (c) L. Duan, F. Bozoglian, S. Mandal, B. Stewart, T. Privalov, A. Llobet, L. Sun, *Nat. Chem.*, 2012, **4**, 418.
- 6 S. Berardi, G. La Ganga, M. Natali, I. Bazzan, F. Puntoriero, A. Sartorel, F. Scandola, S. Campagna, M. Bonchio, *J. Am. Chem. Soc.*, 2012, **134**, 11104.
- 7 Y. Sato, S. Takizawa and S. Murata, *Eur. J. Inorg. Chem.*, 2015, 5495.
- 8 *CrysAlisPro*, version 1.171.39.45h, Rigaku Corporation, Oxford, UK, 2018.
- 9 G. M. Sheldrick, *Acta Crystallogr., Sect. A: Found. Adv.*, 2015, **71**, 3.
- 10 G. M. Sheldrick, *Acta Crystallogr., Sect. C: Struct. Chem.*, 2015, **71**, 3.
- 11 O. V. Dolomanov, L. J. Bourhis, R. J. Gildea, J. A. K. Howard and H. Pushmann, *Olex2, J. Appl. Crystallogr.*, 2009, **42**, 339.
- 12 *Gaussian 09, Revision E.01*, M. J. Frisch, G. W. Trucks, H. B. Schlegel, G. E. Scuseria, M. A. Robb, J. R. Cheeseman, G. Scalmani, V. Barone, B. Mennucci, G. A. Petersson, H. Nakatsuji, M. Caricato, X. Li, H. P. Hratchian, A. F. Izmaylov, J. Bloino, G. Zheng, J. L. Sonnenberg, M. Hada, M. Ehara, K. Toyota, R. Fukuda, J. Hasegawa, M. Ishida, T. Nakajima, Y. Honda, O. Kitao, H. Nakai, T. Vreven, J. A. Montgomery, Jr., J. E. Peralta, F. Ogliaro, M. Bearpark, J. J. Heyd, E. Brothers, K. N. Kudin, V. N. Staroverov, R. Kobayashi, J. Normand, K. Raghavachari, A. Rendell, J. C. Burant, S. S. Iyengar, J. Tomasi, M. Cossi, N. Rega, J. M. Millam, M. Klene, J. E. Knox, J. B. Cross, V. Bakken, C. Adamo, J. Jaramillo, R. Gomperts, R. E. Stratmann, O. Yazyev, A. J. Austin, R. Cammi, C. Pomelli, J. W. Ochterski, R. L. Martin, K. Morokuma, V. G. Zakrzewski, G. A. Voth, P. Salvador, J. J. Dannenberg, S. Dapprich, A. D. Daniels, Ö. Farkas, J. B. Foresman, J. V. Ortiz, J. Cioslowski, D. J. Fox, Gaussian, Inc., Wallingford CT, 2009.
- 13 (a) A. D. Becke, *J. Chem. Phys.*, 1993, **98**, 5648. (b) C. Lee, W. Yang, R. G. Parr, *Phys. Rev. B*, 1988, **37**, 785.
- 14 (a) D. Andrae, U. Haussermann, M. Dolg, H. Stoll, H. Preuss, *Theor. Chem. Acta.*, 1990, **77**, 123. (b) W. Küechle, M. Dolg, H. Stoll, H. Preuss, *J. Chem. Phys.*, 1994, **100**, 7535.

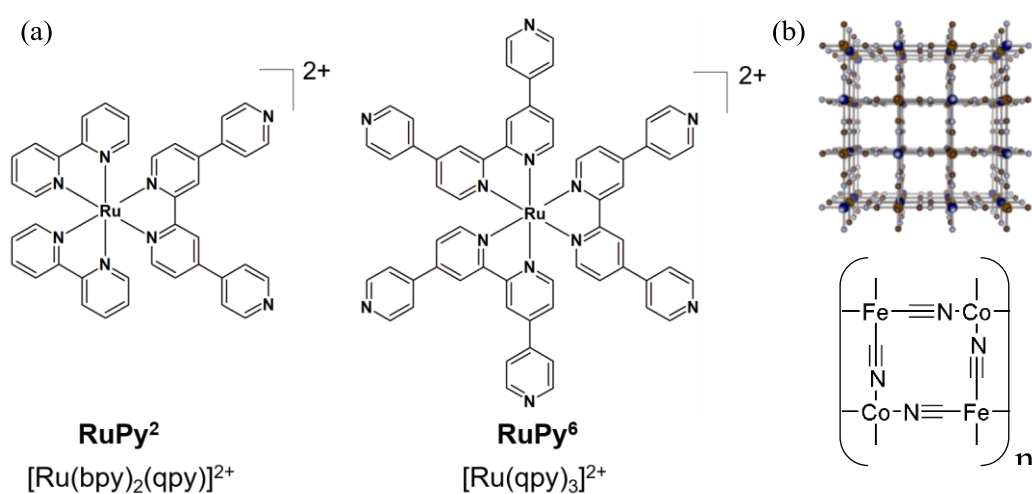
- 15 (a) P. J. Hay, W. R. Wadt, *J. Chem. Phys.* 1985, **82**, 270. (b) W. R. Wadt, P. J. Hay, *J. Chem. Phys.* 1985, **82**, 284. (c) P. J. Hay, W. R. Wadt, *J. Chem. Phys.* 1985, **82**, 299.
- 16 C. L. Donnici, D. H. M. Filho, L. L. C. Moreira, G. T. dos Reis, E. S. Cordeiro, I. M. F. de Oliveira, S. Carvalho and E. B. Paniago, *J. Braz. Chem. Soc.*, 1998, **9**, 455.
- 17 T. Morofuji, H. Kinoshita and N. Kano, *Chem. Commun.*, 2019, **55**, 8575.
- 18 (a) Y. Xie, D. W. Shaffer and J. J. Concepcion, *Inorg. Chem.*, 2018, **57**, 10533. (b) L. Duan, L. Wang, A. K. Inge, A. Fischer, X. Zou and L. Sun, *Inorg. Chem.*, 2013, **52**, 7844.
- 19 E. Dulière, M. Devillers and J. Marchand-Brynaert, *Organometallics*, 2003, **22**, 804.
- 20 L. Wang, K. Fan, Q. Daniel, L. Duan, F. Li, B. Philippe, H. Rensmo, H. Chen, J. Sun and L. Sun, *Chem. Commun.*, 2015, **51**, 7883.
- 21 D. Hong, S. Mandal, Y. Yamada, Y. M. Lee, W. Nam, A. Llobet and S. Fukuzumi, *Inorg. Chem.*, 2013, **52**, 9522.
- 22 N. Song, J. J. Concepcion, R. A. Binstead, J. A. Rudd, A. K. Vannucci, C. J. Dares, M. K. Coggins and T. J. Meyer, *Proc. Natl. Acad. Sci.*, 2015, **112**, 4935.
- 23 D. W. Shaffer, Y. Xie, D. J. Szalda and J. J. Concepcion, *Inorg. Chem.*, 2016, **55**, 12024.
- 24 B. J. J. Timmer, O. Kravchenko, T. Liu, B. Zhang and L. Sun, *Angew. Chem.*, 2021, **133**, 14625.
- 25 E. Contal, C. M. Souguez, S. Lakard, A. E. Taouil, C. Magnenet, B. Lakard, *Front. Mater.*, 2019, **6**, 131.
- 26 J. J. Concepcion, D. K. Zhong, D. J. Szalda, J. T. Muckerman, E. Fujita, *Chem. Commun.*, 2015, **51**, 4105.
- 27 E. T. Veiga, A. V. Müller, L. D. Ramos, K. P. M. Frin and A. S. Polo, *Eur. J. Inorg. Chem.*, 2018, 2680.
- 28 E. Wadsworth, F. R. Duke and C. A. Goetz, *Anal. Chem.*, 1957, **29**, 1824.
- 29 (a) M. A. Ponce and R. Erra-Balsellsnitro, *J. Heterocycl. Chem.*, 2001, **38**, 1071. (b) M. Chakrabarty and A. Batabyal, *Synth. Commun.*, 1994, **24**, 1.
- 30 K. Verschueren, *Handbook of environmental data on organic chemicals*. Van Nostrand Reinhold, New York, 1983.
- 31 M. Kurfířt, M. Dračínský, Š. Červenková, C. Lucie, P. Cuřínová, V. Hamala, M. Hovorková, P. Bojarová, J. Karban, *Chem- Eur. J.*, 2021, **27**, , 13040.
- 32 C. R. Bock, J. A. Connor, A. R. Gutierrez, T. J. Meyer, D. G. Whitten, B. P. Sullivan and J. K. Nagle, *J. Am. Chem. Soc.*, 1979, **101**, 4815.
- 33 D. M. Stanbury, *Adv. Inorg. Chem.*, 1989, **33**, 69.
- 34 (a) U. S. Akhtar, E. L. Tae, Y. S. Chun, I. C. Hwang and K. B. Yoon, *ACS Catal.*, 2016, **6**, 8361. (b) B. Limburg, E. Bouwman and S. Bonnet, *ACS Catal.*, 2016, **6**, 5273.
- 35 N. Curtis, G. Lawrance, A. Sargeson, *Aust. J. Chem.* 1983, **36**, 1327.

36 Y. Tsubonouchi, S. Lin, A. R. Parent, G. W. Brudvig, K. Sakai, *Chem. Commun.*, 2016, **52**, 8018.

Chapter 4
Photochemical Oxygen Evolution
Reaction with Pyridyl-Anchor Modified
Ru(II) Photosensitizers and
Sensitizer-Loaded Nanoparticles

4-1. Introduction

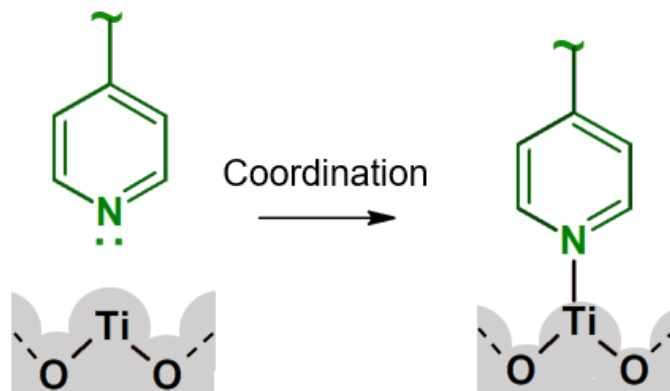
As mentioned in Chapter 1, several recent progresses toward supramolecular photocatalysts for water oxidation suggest that photocatalytic OER activity is improved by the coordination-bond assembly of a molecular PS and a WOC.¹ However, to achieve high charge-separation efficiency, it remains unclear whether direct-bonding interactions between the PS and WOC are necessary or not. Therefore, in order to investigate the effect of direct coordination bonding between the PS and the WOC, two Ru(II)-polypyridine complexes, $[\text{Ru}(\text{bpy})_2(\text{qpy})]^{2+}$ and $[\text{Ru}(\text{qpy})_3]^{2+}$ (**RuPy²** and **RuPy⁶**; Scheme 1a, $\text{qpy} = 2,2'-4,4''-4',4'''$ -quaterpyridine), were selected as the PS for water oxidation in this work.



Scheme 1. The molecular structures of (a) the Ru(II) photosensitizers and (b) CoFe-PBA WOC used in this study.

Although **RuPy⁶** has been reported by Hanan *et al.* to be a highly efficient PS for H₂ production,^{2,3} to the best of author's knowledge, there is no report on the photocatalytic water-oxidation reaction driven by these pyridyl-functionalized $[\text{Ru}(\text{bpy})_3]^{2+}$ analogues. In addition, highly positive Ru(III/II) redox potential was known because of the electron-withdrawing ability of pyridyl groups,²⁻⁴ which is expected to be advantageous for water oxidation reaction.

Furthermore, the effect of **RuPyⁿ** (n= 2, 6, Scheme 2.) immobilization on the surfaces of TiO₂ nanoparticles on the photocatalytic O₂-evolution reaction was also interesting because several pyridyl-anchor-modified dyes have been reported^{3, 5}. Sakai and Ozawa firstly demonstrated that a [Ru(bpy)₃]²⁺-type photosensitizer can be more stably immobilized on the surface of TiO₂ using the pyridyl anchoring group (Scheme 2) compared to the widely used carboxylate or phosphonate-anchoring group, because of its Lewis acid-base bonding manner avoids hydrolysis.^{3a}



Scheme 2. Modification on TiO₂ surface by a pyridyl anchor.

The K_{2x}Co_(3-x)[Fe(CN)₆]₂·nH₂O Prussian-blue analogue (hereafter CoFe-PBA, Scheme 1b)⁶ was selected as the WOC, because the labile Co(II) sites on the surface of CoFe-PBA are expected to easily form coordination bonds with the pyridyl anchors of **RuPyⁿ**. In this chapter, it was demonstrated that the pyridyl groups of the **RuPyⁿ** photosensitizers suppress reactivity with the Na₂S₂O₈ sacrificial electron acceptor, and that such a detrimental effect is overcome by the immobilization of **RuPy²** on the surface of TiO₂ nanoparticles.

4-2 Materials and Methods

4-2-1 Synthesis and Materials

2,2'-4,4''-4'''-Quaterpyridine (qpy) ⁷, [Ru(bpy)₂(qpy)](PF₆)₂ (**RuPy**²) ^{2a}, [Ru(bpy)₂(qpy)](PF₆)₂ (**RuPy**⁶) ^{2b}, and [Ru(bpy)₃](SO₄) ⁸ were synthesized as previously reported. TiO₂ nanoparticles (SSP-M, $\sim\phi = 15$ nm) were purchased from the Sakai Chemical Industry Co. Ltd. The CoFe-PBA water-oxidation catalyst, was synthesized by a previously reported method ^{6a}.

4-2-2 Preparation of **RuPy**ⁿ-immobilized TiO₂ nanoparticles (**RuPy**ⁿ@TiO₂)

The TiO₂-nanoparticle powder (120.4 mg) was dispersed in a solution of **RuPy**ⁿ (1.25 mM, 24 mL) in acetonitrile/toluene (2:3 v/v for **RuPy**², and 11:9 v/v for **RuPy**⁶). The solution was stirred in the dark, overnight, at room temperature. The **RuPy**ⁿ-immobilized TiO₂ nanoparticles obtained in this manner were isolated by ultracentrifugation (50000 rpm, 15 min), and the supernatant was removed. After washing twice with the reaction solvent, the isolated **RuPy**ⁿ@TiO₂ was dried under vacuo. The amount of immobilized **RuPy**ⁿ on the TiO₂ nanoparticles was determined by UV-vis absorption spectroscopy of the supernatant.

4-2-3 Preparation of **RuPy**ⁿ-immobilized TiO₂ electrodes.

The TiO₂-modified Fluorine-doped tin oxide (FTO) electrode (apparent area of TiO₂ film is 1 × 1 cm²) was immersed in a solution of **RuPy**ⁿ (0.15 mM, 9 mL) in acetonitrile/toluene (2:3 v/v for **RuPy**², and 11:9 v/v for **RuPy**⁶). The solution was stirred in the dark, overnight, at room temperature. After washing twice with the reaction solvent, the isolated **RuPy**ⁿ@TiO₂ electrodes were dried under vacuo.

4-2-4 Measurements

UV-vis absorption spectra and diffuse-reflectance spectra were recorded on a Shimadzu UV-2400PC spectrophotometer. The obtained reflectance spectra were converted to absorption spectra using the Kubelka-Munk function $F(R_{\infty})$. Luminescence spectra were recorded on a JASCO FP-6600 spectrofluorometer at 298 K. Emission quantum yields (Φ_{em}) were measured using a Hamamatsu C9920-02 absolute photoluminescence quantum-yield-measurement system equipped with an integrating sphere apparatus and a 150-W continuous-wave xenon light source. Emission lifetime (τ) measurements were conducted using a Hamamatsu Photonics C4334 system equipped with a streak camera as the photodetector and a nitrogen laser as the excitation light source ($\lambda_{ex} = 470$ nm for **RuPy**² and 474 nm for **RuPy**⁶). Each sample solution was deoxygenated by bubbling with N₂ for 30 min at 298 K. Cyclic voltammetry (CV) was conducted using a Hokuto Denko HZ-3000 electrochemical measurement system equipped with glassy carbon, Pt wire, and Ag/Ag⁺ electrodes as the working, counter, and reference electrodes, respectively. Ferrocene was used the internal standard. An acetonitrile solution containing 0.1 M of tetrabutylammonium hexafluorophosphate

(TBAPF₆), as the supporting electrolyte, and 1.0 mM of the Ru(II) complex, was used in the CV experiments. **RuPyⁿ**-immobilized TiO₂-modified FTO electrode were prepared by literature method.³⁴ All solutions were deaerated by bubbling N₂ for 15 min prior to any measurement. IR spectra were recorded on a Jasco FT-IR 4100 spectrophotometer with KBr pellets. Zeta potential measurement and dynamic light scattering (DLS) analysis were conducted using an OTSUKA ELSZ-1000SC1 analyzer.

4-2-5 Calculation of the amount of immobilized Ru(II) complexes on the TiO₂ nanoparticles

To estimate the amount of immobilized Ru(II) complexes on TiO₂ nanoparticle, UV-Vis absorption spectra of each supernatant solution used for the immobilization reaction was measured (Figure 1 shown below). The Ru(II) complex concentration used for the UV-Vis absorption spectral measurement (C_A) is estimated by Equation (1-1) based on the Lambert-Beer law.

$$A = C_A \cdot l \cdot \varepsilon \quad (1-1)$$

A = absorbance, C_A = concentration of the Ru(II) complex, l = cell path length (1 cm), ε = molar absorption coefficient The absorbance at the ¹MLCT absorption band of each complex in each the solvent (**RuPy⁶**: 475 nm, **RuPy²**: 465 nm) and their corresponding molar absorption coefficients (**RuPy²**: $1.7 \times 10^4 \text{ M}^{-1} \text{ cm}^{-1}$; **RuPy⁶**: $2.6 \times 10^4 \text{ M}^{-1} \text{ cm}^{-1}$) enable us to estimate the concentration of the Ru(II) complex that was not immobilized in the reaction. Since a 125- fold diluted solution was used in each measurement, the concentration of the original supernatant solution (C_B) is calculated by $C_B = C_A \times 125$. The total volume of the supernatant solution is 24 mL. Thus, the amount of Ru(II) complexes in the supernatant solution (M_S) is estimated by Equation (1-2).

$$M_S = C_B \times 24 / 1000 \text{ (mol)} \quad (1-2)$$

Finally, the molar amount of the Ru(II) complex immobilized on the TiO₂ surface (M_i) can be estimated by Equation (1-3).

$$M_i = M_0 - M_S \text{ (mol)} \quad (1-3)$$

where M_0 denotes the molar amount of the Ru(II) complex in the 1.25 mM Ru(II) solution used for the immobilization reaction. The results are summarized in Table 1.

Table 1. Absorbance of each supernatant solution and the calculated C_B and M_i values.

	RuPy²@TiO₂	RuPy⁶@TiO₂
<i>A</i>	0.108	0.146
C_B (mM)	0.746	0.704
M_i (μmol)	12.0	13.6

4-2-6 Calculation of the surface coverage of Ru(II) complexes per unit area of TiO₂

Assuming that the TiO₂ nanoparticles are spherical, the surface area on the TiO₂ nanoparticle (S_m) was calculated by using Equation (1-4).

$$S_m = 4 \cdot \pi \cdot \left(\frac{a}{2} \times 10^{-7}\right)^2 \text{ (cm}^2 \text{ per one particle)} \quad (1-4)$$

a = Averaged particle diameter of TiO₂ nanoparticle (15 nm)

Since the calculated surface area (S_m) based on Equation (1-4) corresponds to only one TiO₂ nanoparticle, it is necessary to determine the number of TiO₂ nanoparticles (P_t) contained in 120 mg to estimate the total surface area of TiO₂ (S_t) used in the immobilization reaction of the Ru(II) complexes. The total volume of 120 mg of TiO₂ nanoparticles (V_t) can be calculated using Equation (1-5) based on the density of TiO₂ (anatase TiO₂ = 3.90 g/cm³).

$$V_t = \frac{120 \times 10^{-3} \text{ (g)}}{3.90 \text{ (g/cm}^3\text{)}} \text{ (cm}^3\text{)} \quad (1-5)$$

The number of TiO₂ nanoparticles (P_t) in 120 mg is also estimated using Equations (1-6) and (1-7) based on the volume of one TiO₂ nanoparticle (V_m) and the total volume (V_t).

$$V_m = \frac{4}{3} \cdot \pi \cdot \left(\frac{a}{2} \times 10^{-7}\right)^3 \text{ (cm}^3 \text{ per one particle)} \quad (1-6)$$

$$P_t = \frac{V_t}{V_m} \quad (1-7)$$

Then, the total surface area of 120 mg of TiO₂ (S_t) can be estimated by Equation (1-8).

$$S_t = S_m \times P_t \text{ (cm}^2\text{)} \quad (1-8)$$

The amount of immobilized Ru(II) complexes per unit area of TiO₂ (Surface coverage: N) is estimated by Equation (1-9) based on the amount of immobilized Ru(II) complex (M_i) and the total

surface area of 120 mg of TiO₂ (S_t). The estimated N and M_i values are summarized in Table 2 in the § 4-3-1.

$$N = \frac{M_i}{S_t} \text{ (mol/cm}^2\text{)} \quad (1-9)$$

4-2-7 Photochemical O₂-evolution Reaction

A phosphate-buffer-water/acetonitrile (2:1 v/v) solution (18 mM, pH = 7.2) containing the Ru(II) photosensitizer (100 μM of the Ru(II) complex) and the water-oxidation catalyst (1 mg CoFe-PBA) was placed, in the dark, in a Pyrex vial (~15 mL volume) with a small magnetic stirring bar and covered with a rubber septum. A Na₂S₂O₈ solution (5, 10 mM) was injected into this mixed solution or dispersion by a syringe and the resultant solution (total 5 mL) was deoxygenated by bubbling with Ar gas for 30 min. A robust O₂ sensor probe (Pyro Science, FireSting O₂ oxygen meter) was fitted to the top of the septum to detect the oxygen concentration within the headspace of the vial. The vial was irradiated with a blue LED lamp ($\lambda = 470 \pm 10$ nm; 210 mW; OptoDevice Lab. Ltd., OP6-4710HP2) from underneath. The temperature was set to 293 K with a homemade aluminum water-cooling jacket and a temperature circulator (EYELA CCA-1111). Turnover numbers (TONs) and turnover frequencies (TOFs) were determined from the amount of evolved O₂; four photoredox cycles of the Ru(II) photosensitizer are required to oxidize one water molecule. The apparent quantum yield (Φ_{Ox}) was calculated using the following equation:

$$\Phi_{Ox} = N_e/N_p = 4N_{O_2}/N_p \quad (2)$$

where N_e is the number of reacted electrons, N_{O_2} is the number of evolved O₂ molecules, and N_p is the number of incident photons.

4-3 Results and Discussion

4-3-1 Fabrication and Characterization of RuPyⁿ@TiO₂

As mentioned in § 4-1, the pyridyl group has been reported to be a useful organic anchor for immobilizing various functional molecules on TiO₂ electrodes. In order to investigate the differences in the immobilization behavior of RuPy² and RuPy⁶, the UV-vis absorption spectra of the supernatant solutions obtained following their immobilization reactions were measured (Figure 1 and Table 2). The amounts of immobilized RuPyⁿ on the TiO₂ nanoparticles are summarized in Table 2 and are compared with that of the previously reported RuCP² phosphonate-functionalized Ru(II) photosensitizer⁹. The amounts of immobilized RuPy² and RuPy⁶ are comparable with that of RuCP², indicating that the pyridyl groups of RuPyⁿ (n = 2, 6) act as effective anchors. It is interesting to note that the amount of immobilized RuPy⁶ was moderately higher than that of RuPy² in spite of its bulkier molecular structure.^{2, 4} The slightly larger amount of immobilized RuPy⁶ over RuPy² implies that uncoordinated pyridyl groups contribute to arranging the molecular orientations of the immobilized molecules so as to form a more tightly packed structure on the surface.

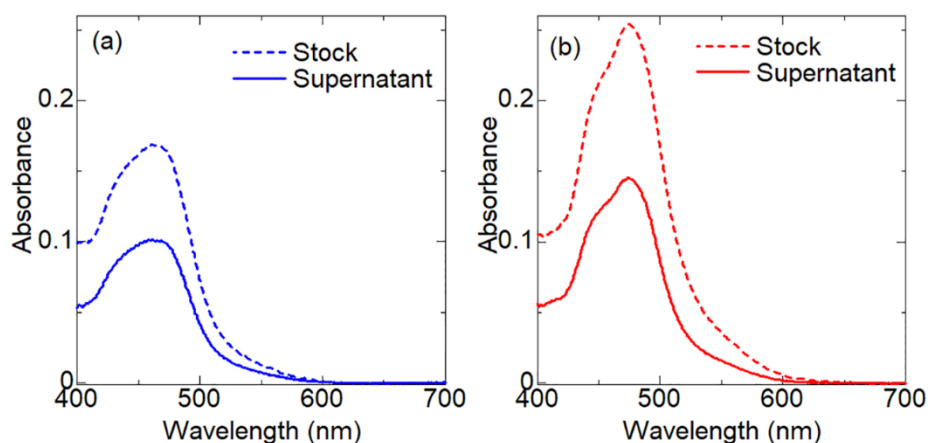


Figure 1. UV-Vis absorption spectra of the stock and supernatant solutions of (a) RuPy² and (b) RuPy⁶. These solutions were diluted 125 times by the solvent of each reaction.

Table 2. Amounts of immobilized Ru(II) complexes on TiO₂ nanoparticle surfaces.

Complex	Amount of immobilized Ru(II) complex	
	(nmol/mg TiO ₂)	Surface coverage (nmol/cm ²)
RuPy ²	99.6	0.0971
RuPy ⁶	113	0.110
RuCP ² ^a	116	0.113

^a Ref. 9.

4-3-2 Photochemical properties

As shown in Figure 2a, characteristic ¹MLCT absorptions were clearly observed at around 470 nm in the UV-vis diffuse reflectance spectra of the **RuPyⁿ**-immobilized TiO₂ nanoparticles (**RuPyⁿ@TiO₂**) similar to the absorption spectra of each **RuPyⁿ** solution (Figure 2b and Table 3), indicating that the **RuPyⁿ** photosensitizing molecules were successfully immobilized on the TiO₂ surface. The slightly larger absorption band observed for **RuPy⁶@TiO₂** compared to **RuPy²@TiO₂** is ascribable to the larger molar absorption coefficient of the ¹MLCT band of **RuPy⁶** than that of **RuPy²**.

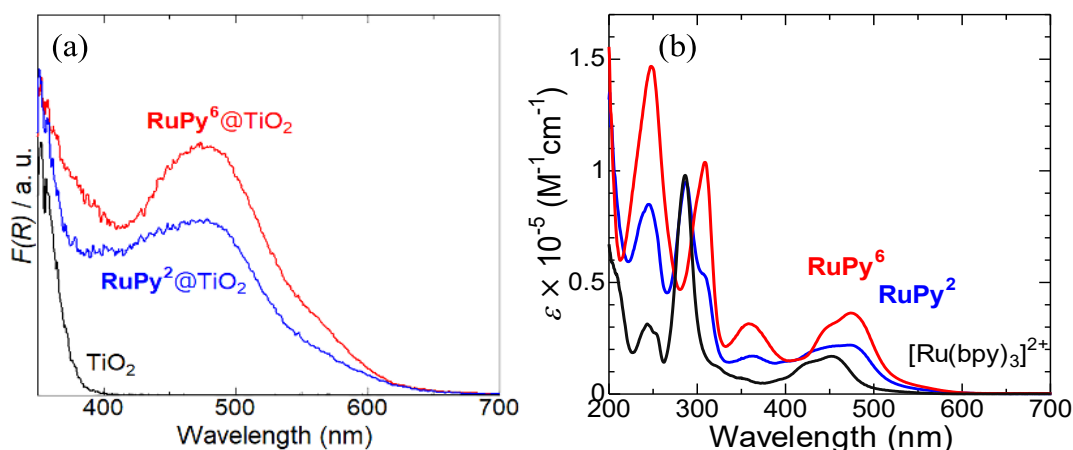


Figure 2. (a) UV-vis diffuse reflectance spectra of **RuPyⁿ@TiO₂** ($n = 2, 6$) in the solid state at room temperature. (b) UV-vis absorption spectra of **RuPyⁿ** ($n = 2$ or 6) and $[\text{Ru}(\text{bpy})_3]^{2+}$ (12.5 mM) in the phosphate buffer aq. (18 mM, pH = 7.2)/MeCN (2:1 v/v) at room temperature.

Table 3. Photophysical properties of **RuPyⁿ** and $[\text{Ru}(\text{bpy})_3]^{2+}$ in solution (298 K) and frozen glass (77 K) states.

	RuPy²	RuPy⁶	$[\text{Ru}(\text{bpy})_3]^{2+}$
λ_{abs} (nm) ^a	470	474	452
ϵ ($\text{M}^{-1}\text{cm}^{-1}$) ^a	2.2×10^4	3.6×10^4	1.7×10^4
λ_{em} (nm at 298 K) ^{a, b}	671	654	622
λ_{em} (nm at 77 K) ^{b, c}	617	618	585
Φ_{em} ^{a, b} (%)	6.8	18	9.6
τ_{em} (ns) ^{a, d}	480	778	706

^a 12.5 μM , phosphate buffer water/acetonitrile ($v/v = 2:1$) solution (18 mM, pH = 7.2)

^b Excited by the light of each maximum absorption wavelength.

^c 12.5 μM MeOH/EtOH ($v/v=1:1$) solution and the results are shown in Figure 4.

^d Excited by the 470 nm light.

It is well known that the $^3\text{MLCT}$ emission of the $[\text{Ru}(\text{bpy})_3]^{2+}$ molecular photosensitizer is strongly quenched by immobilization on TiO_2 ¹⁰. In contrast, the each RuPy^n clearly exhibited a $^3\text{MLCT}$ emission band from the corresponding $\text{RuPy}^n@ \text{TiO}_2$ nanoparticles (Figure 3), although the intensities of the emissions from $\text{RuPy}^n@ \text{TiO}_2$ were weaker than those of their non-immobilized solution states, which is ascribable to excitation light scattering of the TiO_2 nanoparticles. Indeed, the emission quantum yield of $\text{RuPy}^2@ \text{TiO}_2$ was determined to be comparable ($\Phi = 0.07$) to that observed in the solution state ($\Phi = 0.068$, Table 3)

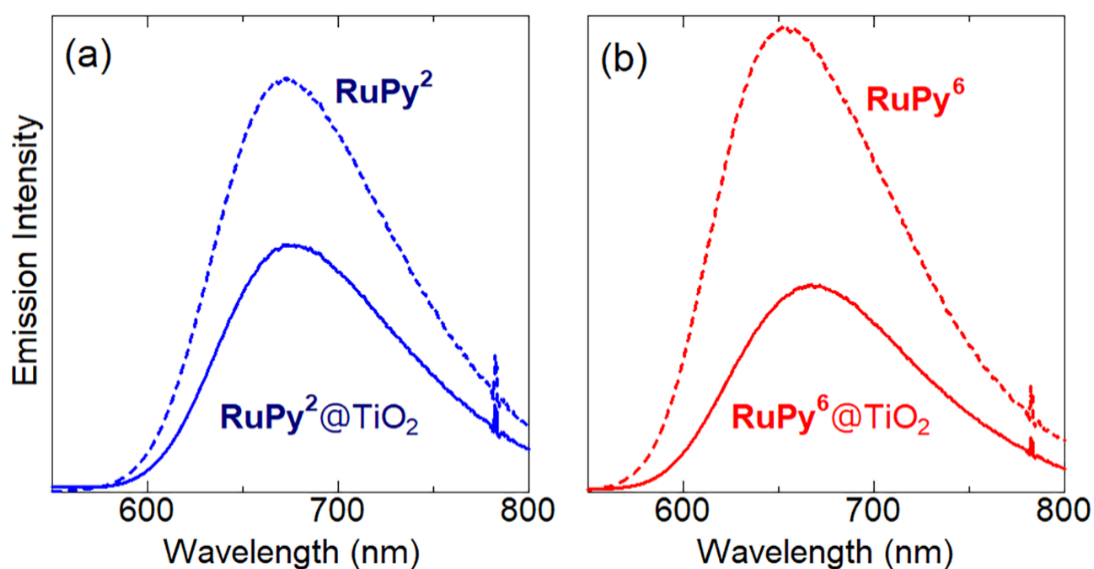


Figure 3. Emission spectra of (a) $\text{RuPy}^2@ \text{TiO}_2$ and (b) $\text{RuPy}^6@ \text{TiO}_2$ in the dispersed solution (12.5 μM , water/acetonitrile (v/v = 2:1) solution). Dotted lines are the solution-state emission spectra of RuPy^n in the same solvent and concentration.

As shown in Figure 4, the $^3\text{MLCT}$ emission wavelengths of **RuPy²** and **RuPy⁶** at both 298 and 77 K are red-shifted (> 30 nm) with respect to the emission of $[\text{Ru}(\text{bpy})_3]^{2+}$. Such a tendency is possibly caused by the introduction of electron-withdrawing pyridyl ligands. In 298 K, **RuPy²** showed emission with longer wavelength than the others. This behaviour is resembled reported wide p-conjugated substituents¹² and possibly caused by the larger $S_1\text{-}T_1$ energy gap by easier molecular distortion of helteleptic complexes, suggested from larger $E_{\text{abs}}-E_{\text{em}}$ ($=1240/\lambda_{\text{abs}}-1240/\lambda_{\text{em}}$) of **RuPy²** (0.79 eV) than that of $[\text{Ru}(\text{bpy})_3]^{2+}$ (0.74 eV) and **RuPy⁶** (0.72 eV).

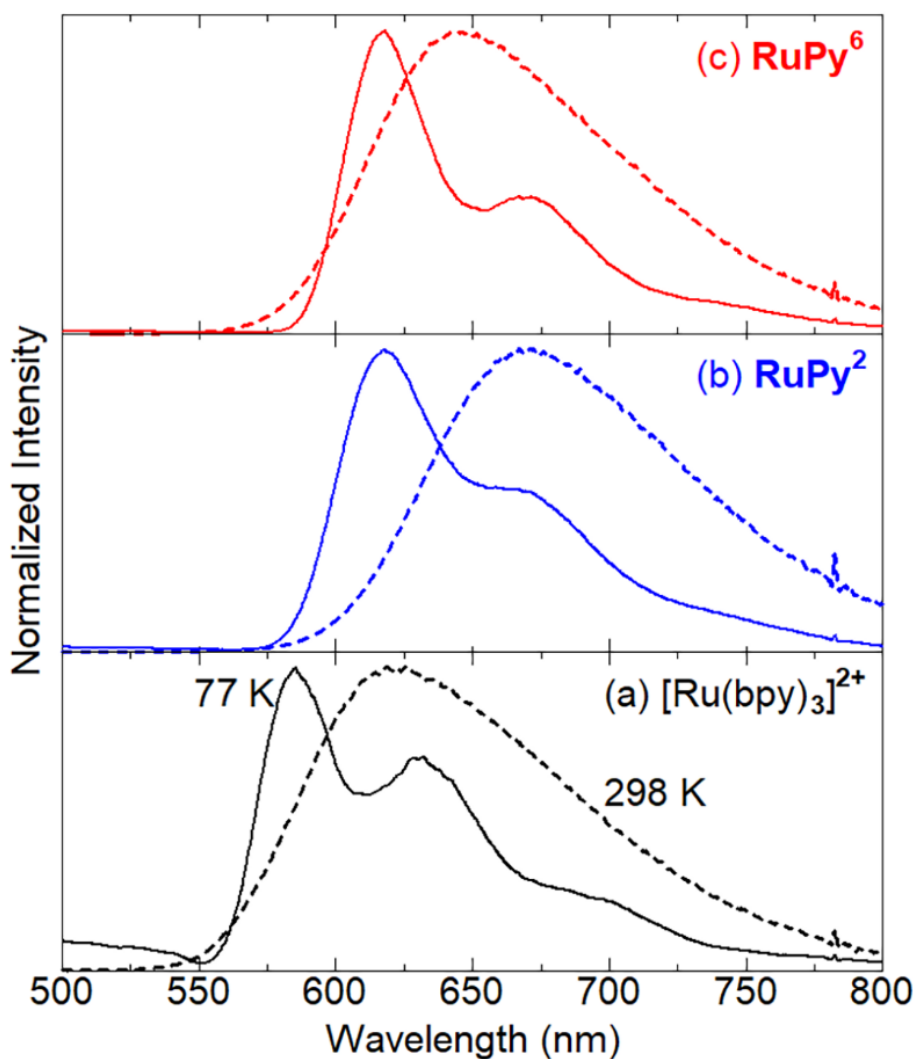


Figure 4. Emission spectra of (a) $[\text{Ru}(\text{bpy})_3]^{2+}$, (b) **RuPy²** and (c) **RuPy⁶** in the solution state. Solid and dotted lines show the spectra at 298 K (in MeCN/H₂O =1:2) and 77 K (in MeOH/EtOH =1:1), respectively.

4-3-3 Dispersion properties of RuPyⁿ@TiO₂

The particle diameters of RuPyⁿ@TiO₂ estimated by the dynamic light scattering method were distributed from sub-micron to several tens micron range, different from pristine TiO₂ (Figure 5). This result indicates that dispersibility of RuPyⁿ@TiO₂ were improved after immobilization, possibly due to the positive charge of PS molecules.

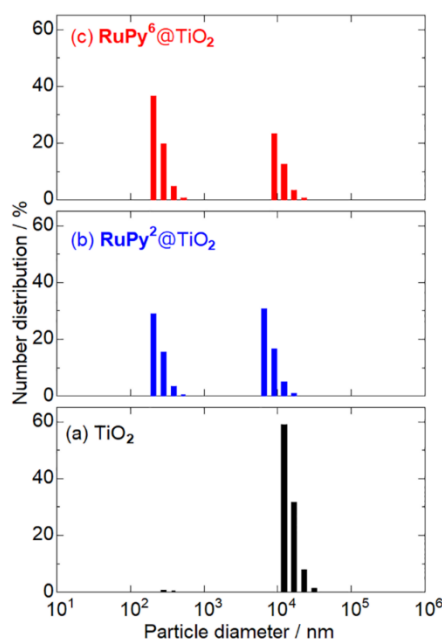


Figure 5. Particle diameter distributions estimated by the dynamic light scattering method for (a) TiO₂, (b) RuPy²@TiO₂ and (c) RuPy⁶@TiO₂ nanoparticles dispersed in water.

The immobilization of positively-charged RuPyⁿ at the surface of TiO₂ nanoparticle was also confirmed by the zeta potential measurements (Table 4); both RuPy²@TiO₂ and RuPy⁶@TiO₂ exhibited positive zeta potential ranging from 11 to 28 mV, whereas the potential of non-modified TiO₂ nanoparticle was negative (-27 mV) because OH⁻ anions were thought to be coordinated to Ti(IV) ion at the TiO₂ surface.¹⁰ The larger positive zeta potential of RuPy⁶@TiO₂ than RuPy²@TiO₂ is probably because the ratio of pyridyl-coordinated Ti(IV) sites to uncoordinated (or OH-coordinated) Ti(IV) sites is larger for RuPy⁶@TiO₂ than RuPy²@TiO₂ even in the comparable amount of the immobilized RuPyⁿ dye on the TiO₂ surface.

Table 4. Zeta potentials of RuPyⁿ@TiO₂ dispersed in H₂O/CH₃CN mixed solvent (v/v = 1/2).

Zeta potential (mV)	
RuPy ² @TiO ₂	+11.11
RuPy ⁶ @TiO ₂	+27.69
TiO ₂	-20.63

4-3-4 Electrochemical property

The cyclic voltammograms of each complex were shown in Fig. 6. The more pyridyl groups were introduced, the more positive redox potential of Ru(III/II) (E_{ox}) was observed. (Table 5) The E_{ox} value positively shifted in the order of $[Ru(bpy)_3]^{2+} < RuPy^2 < RuPy^6$. On the other hand, cyclic voltammetry experiments using the $RuPy^n$ immobilized TiO_2/FTO working electrode exhibited similar redox behavior to that of each complex in the solution state, clearly indicating that the Ru(III)/Ru(II) redox potential were negligibly affected by the immobilization to the TiO_2 surface probably due to the localization of the HOMO at the central Ru(II) ion (Figure 6). As a result, the excited electron in the 3MLCT state of $RuPy^n$ does not have sufficient negative potential (Table 5) to be injected to the conduction band of TiO_2 (-0.59 V in pH 7.2¹³) in neutral media.

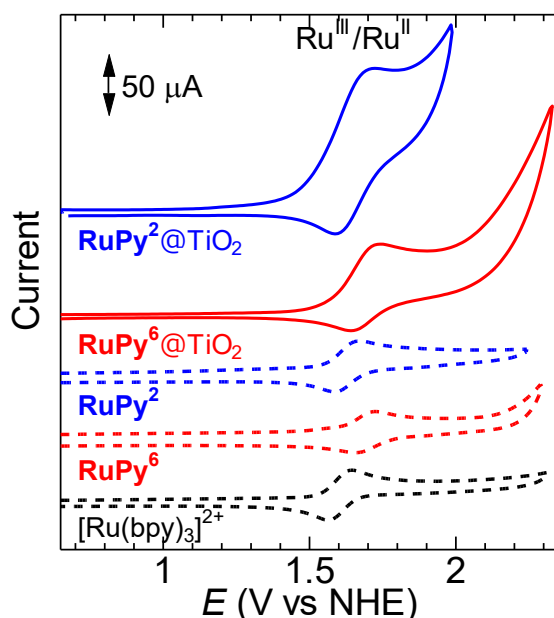


Figure 6. Cyclic voltammograms of $RuPy^2$ and $RuPy^6$ immobilized on the TiO_2/FTO working electrode (blue and red solid lines) containing 0.1 M TBAPF₆ as the supporting electrolyte and Pt coil, Ag/Ag^+ as the counter and reference electrode, respectively. Blue, red and black dotted lines are the voltammograms of 1.0 mM $RuPy^2$, $RuPy^6$ and $[Ru(bpy)_3]^{2+}$ anhydrous CH_3CN solution with the glassy carbon working electrode.

Table 5. Photochemical and electrochemical properties of $RuPy^n$ and $[Ru(bpy)_3]^{2+}$.

	$RuPy^2$	$RuPy^6$	$[Ru(bpy)_3]^{2+}$
E_{00} (eV) ^a	+2.01	+2.01	+2.11
E_{ox} (V vs NHE) ^b	+1.66	+1.69	+1.53
E_{ox}^* (V vs NHE) ^c	-0.35	-0.32	-0.59

^a Estimated from λ_{em} at 77 K (Table 3) with the formula that $E_{00} = 1240/\lambda_{em}$

^b Estimated by CV measurements in CH_3CN solution and the results are shown in Figure 6.

^c E_{ox}^* was estimated using the following equations $E_{ox}^* = E_{ox} - E_{00}$, where E_{00} was approximated as λ_{em} at 77 K.

4-3-5 Photochemical O₂-evolution Reactions

Although several groups have reported photocatalytic hydrogen-evolution reactions driven by pyridyl-functionalized Ru(II) photosensitizers, such as **RuPy**⁶, photocatalytic O₂-evolution catalyzed by such a pyridyl-functionalized Ru(II) PS has not been reported. Photocatalytic O₂-evolution experiments were performed in the presence of molecular **RuPy**ⁿ or the TiO₂-immobilized photosensitizers, with Na₂S₂O₈ as the sacrificial electron acceptor. The results are displayed in Figure 7, while TONs, TOFs, and Φ_{O_x} values are summarized in Table 6. Oxygen evolution was observed upon irradiation of each **RuPy**ⁿ-containing sample with light, and the TONs of these reactions after 60 min of irradiation were above unity. Hence, O₂ was evolved through photocatalytic processes involving the **RuPy**ⁿ photosensitizers. However, as shown in Figure 7(a), the TONs and TOFs of **RuPy**² and **RuPy**⁶ were less than half and a quarter of those of [Ru(bpy)₃]²⁺, respectively, in the presence of 5 mM Na₂S₂O₈ sacrificial electron acceptor. In contrast, it is noteworthy that both the TON and TOF of **RuPy**² increased remarkably when immobilized on the surfaces of TiO₂ nanoparticles (**RuPy**²@TiO₂), whereas such the improvement by immobilization was hardly observed for **RuPy**⁶@TiO₂. Considering that both pyridyl groups of **RuPy**² are coordinated to Ti⁴⁺ ions on the surfaces of the TiO₂ nanoparticles, the uncoordinated pyridyl groups of **RuPy**ⁿ may suppress photoinduced charge separation between the photosensitizer, the sacrificial electron acceptor, and the water-oxidation catalyst. The photosensitizing efficiency of **RuPy**ⁿ dyes in homogeneous system was improved by increasing the concentration (10 mM) of Na₂S₂O₈ sacrificial electron acceptor, indicating that the oxidative quenching of the photoexcited [**RuPy**ⁿ]^{*} by S₂O₈²⁻ anion could be the rate determining step of photocatalytic O₂ evolution reaction. In contrast, completely different behaviors were observed for the heterogeneous systems, **RuPy**²@TiO₂ and **RuPy**⁶@TiO₂ (see Figures 7(b) and 7(c)); the efficiency of **RuPy**²@TiO₂ strongly depended on the S₂O₈²⁻ concentration whereas **RuPy**⁶@TiO₂ exhibited negligible dependence on the S₂O₈²⁻ concentration. These remarkably different behaviors between **RuPy**²@TiO₂ and **RuPy**⁶@TiO₂ indicate that the surface condition of the **RuPy**ⁿ immobilized TiO₂ nanoparticle greatly influenced on the photocatalytic O₂ evolution activity.

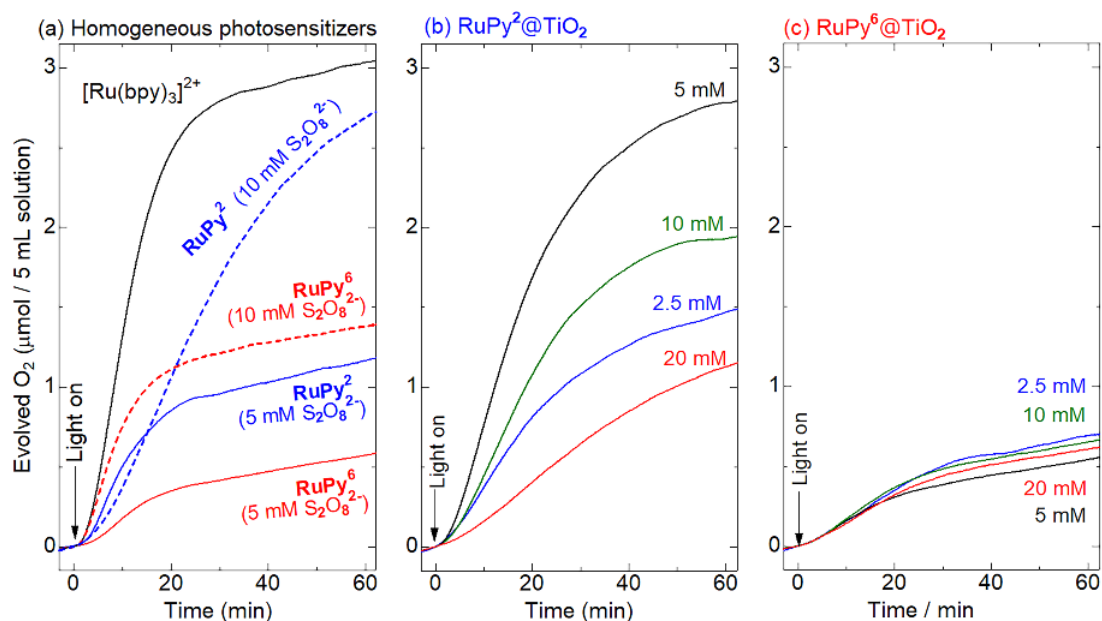


Figure 7. Photocatalytic O₂-evolution reactions driven by (a) homogeneous photosensitizer [Ru(bpy)₃]²⁺ (black), **RuPy²** (blue) and **RuPy⁶** (red) or (b) heterogeneous photosensitizer **RuPy²@TiO₂** and (c) **RuPy⁶@TiO₂** (red) (100 μM of the Ru(II) complex) with CoFe-PBA (1 mg) in Na₂S₂O₈ sacrificial electron acceptor (2.5 to 20 mM) and 18 mM phosphate-buffer-water/acetonitrile (2:1 v/v) solution (pH 7.2) under an atmosphere of Ar.

A blue LED ($\lambda = 470 \pm 10$ nm) was used as the light source.

Table 6. Photocatalytic O₂-evolution-reaction results.

Photosensitizer	[Na ₂ S ₂ O ₈]	O ₂ (μmol) ^a	TON ^a	TOF (min ⁻¹) ^b	Φ _{Ox} (%) ^a
[Ru(bpy) ₃] ²⁺	5 mM	3.03	24.3	1.04	0.409
RuPy²	5 mM	1.17	9.32	0.400	0.157
	10 mM	2.69	21.6	0.339	0.362
RuPy⁶	5 mM	0.572	4.57	0.141	0.0771
	10 mM	1.38	11.1	0.597	0.186
RuPy²@TiO₂	2.5 mM	1.47	11.8	0.299	0.198
	5 mM	2.78	22.3	0.611	0.375
	10 mM	1.59	12.7	0.249	0.214
	20 mM	1.13	9.02	0.128	0.152
RuPy⁶@TiO₂	2.5 mM	0.693	5.54	0.126	0.0933
	5 mM	0.541	4.32	0.127	0.0729
	10 mM	0.651	5.20	0.136	0.0877
	20 mM	0.606	4.85	0.113	0.0817

^a After irradiation for 60 min. ^b After irradiation for 10 min.

To clarify the origin of the differences in the photosensitizing efficiencies of the three molecular photosensitizers, emission-quenching experiments using $\text{Na}_2\text{S}_2\text{O}_8$ as a sacrificial electron acceptor was conducted. Stern-Volmer plots of **RuPy**⁶, **RuPy**², and $[\text{Ru}(\text{bpy})_3]^{2+}$ in the presence of various concentrations of $\text{Na}_2\text{S}_2\text{O}_8$ are shown in Figure 8. The calculated Stern-Volmer constant (K_{sv}), emission lifetime (τ_{em}), and quenching rate constant (k_{q}) of each complex are listed in Table 7. The quenching efficiencies of **RuPy**⁶, and **RuPy**² by $\text{S}_2\text{O}_8^{2-}$ were significantly lower than that of $[\text{Ru}(\text{bpy})_3]^{2+}$ over the entire concentration range. The k_{q} value decreased in the order: $[\text{Ru}(\text{bpy})_3]^{2+} \gg \text{RuPy}^2 > \text{RuPy}^6$, suggesting that greater numbers of pyridyl-anchor-modified bpy ligands result in less-efficient quenching of the Ru(II) complex by $\text{S}_2\text{O}_8^{2-}$. Considering that $[\text{Ru}(\text{bpy})_3]^{2+}$ has previously been reported to form an ion-pair intermediate with $\text{S}_2\text{O}_8^{2-}$ during electron-transfer¹⁴, the lower quenching efficiencies of **RuPy**ⁿ ($n = 2, 6$) compared to that of $[\text{Ru}(\text{bpy})_3]^{2+}$ are ascribable to suppression of ion-pair formation by the sterically bulky pyridyl groups of the qpy ligand(s).

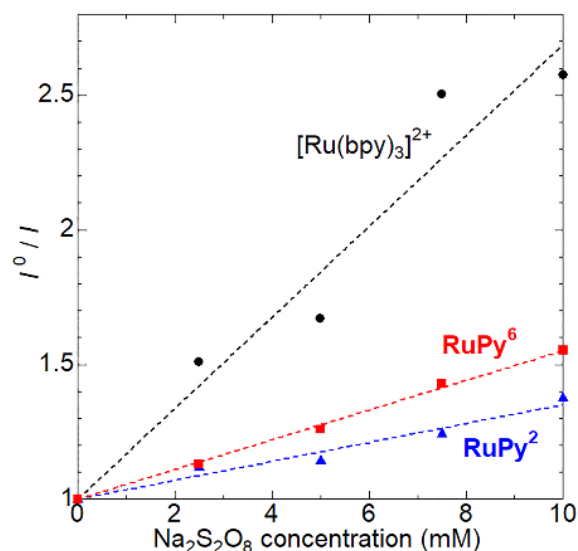


Figure 8. Stern–Volmer plots of 100 μM solutions of $[\text{Ru}(\text{bpy})_3]^{2+}$ (black closed circles), **RuPy**² (blue closed triangles), and **RuPy**⁶ (red closed triangles) in the presence of various concentrations of $\text{Na}_2\text{S}_2\text{O}_8$ at room temperature. A 2:1 (v/v) mixture of $\text{H}_2\text{O}/\text{CH}_3\text{CN}$ was used as the solvent during these experiments.

Table 7. Stern-Volmer and quenching rate constants for $[\text{Ru}(\text{bpy})_3]^{2+}$, **RuPy**², and **RuPy**⁶.

Photosensitizer	K_{sv} (mM^{-1}) ^a	k_{q} ($\text{M}^{-1}\text{s}^{-1}$) ^b
RuPy ⁶	0.0552	7.10×10^7
RuPy ²	0.0351	7.31×10^7
$[\text{Ru}(\text{bpy})_3]^{2+}$	0.168	2.38×10^8

^a Estimated from the slope of the Stern–Volmer plot displayed in Figure 8.

^b Estimated using the equation: $k_{\text{q}} = K_{\text{sv}}/\tau_{\text{em}}$; the τ_{em} of each complex is listed in Table 3.

In contrast, comparable emission quenching ($I^0/I \sim 1.5$) using CoFe-PBA was observed for all three molecular photosensitizers (Figure 9), whereas the adsorption of these **RuPyⁿ** dyes to the surface of CoFe-PBA were confirmed by UV-Vis absorption spectral changes (Figure 10 and Table 7). These results suggest that the pyridyl groups of **RuPyⁿ** hardly affect their reactivities with the CoFe-PBA catalyst at the photoexcited state. Hence, the lower photosensitizing efficiencies of the **RuPyⁿ** ($n = 2, 6$) molecular photosensitizers toward the water-oxidation reaction compared to $[\text{Ru}(\text{bpy})_3]^{2+}$ are due to the poorer reactivity of the sacrificial electron-accepting $\text{S}_2\text{O}_8^{2-}$ ion when sterically bulky pyridyl groups are present.

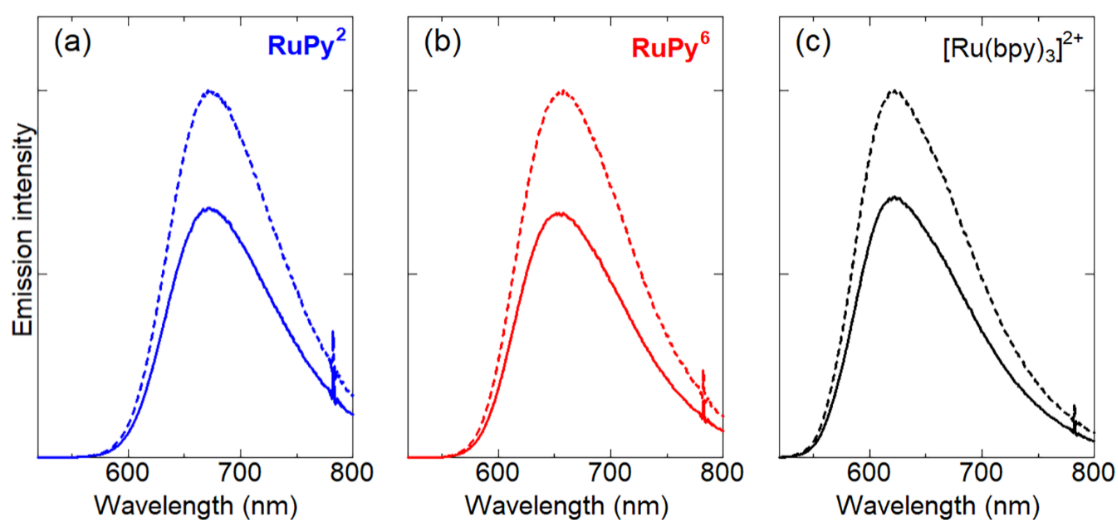


Figure 9. The emission spectra of each Ru(II) photosensitizer in the presence (solid line) or absence (dotted line) of 1 mg CoFe-PBA. (In phosphate buffer $\text{H}_2\text{O}/\text{CH}_3\text{CN}$ ($v/v = 2:1$) solution (18 mM, $\text{pH} = 7.2$), 12.5 μM). Each decrement of maximum emission intensity was (a) **RuPy²** : 32%, (b) **RuPy⁶** : 33%, (c) $[\text{Ru}(\text{bpy})_3]^{2+}$: 29%, respectively.

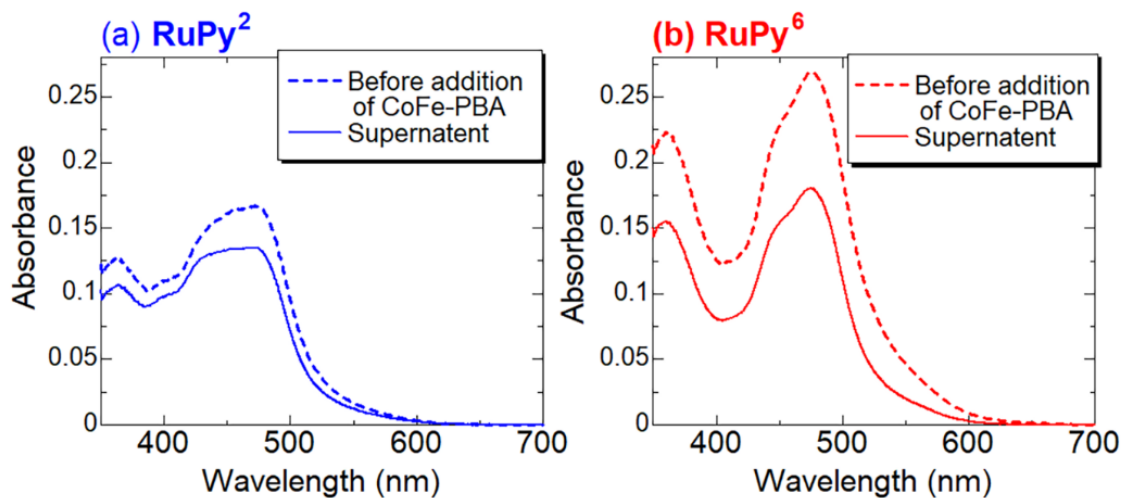


Figure 10. UV-Vis absorption spectral change of 0.8 mM (a) **RuPy²** and (b) **RuPy⁶** in 18 mM phosphate buffer H₂O/CH₃CN (v/v = 2:1) solutions by the immobilization reaction with 10 mg of CoFe-PBA powder. Dotted lines show the spectra before addition of CoFe-PBA and the solid lines are the spectra of the supernatant solutions obtained by the ultracentrifugation of the reaction mixture of **RuPyⁿ** solutions and CoFe-PBA (the reaction time was 1 day at room temperature).

Table 7. Estimated adsorption amounts of **RuPyⁿ** dyes on the CoFe-PBA catalyst.

	Abs. of before addition. ^a	Abs of supernatant solution ^a	Adsorption amount (nmol/mg)
RuPy²	0.167	0.135	76
RuPy⁶	0.269	0.180	131

^a λ_{abs} = 470 nm for **RuPy²** and 474 nm for **RuPy⁶**.

The immobilization of molecular photosensitizers onto the surfaces of TiO₂ nanoparticles generally tends to suppress their reaction efficiencies with sacrificial reagents and catalysts because of the slower diffusions of larger nanoparticles compared to those of single molecules. Nevertheless, the photosensitization efficiency of the immobilized **RuPy²@TiO₂** was higher than that of its molecular equivalent, **RuPy²** in the optimized condition (5 mM Na₂S₂O₈ solution). This result suggests that the immobilization of **RuPy²** onto the TiO₂ nanoparticles provides benefits that compensate for slower nanoparticle diffusion, which is a plausible reason for the observed improvement in reactivity of the TiO₂-immobilized **RuPy²** with the sacrificial S₂O₈²⁻ acceptor. In contrast, such the enhancement by immobilization was hardly observed for **RuPy⁶**. As discussed above, the uncoordinated pyridyl anchoring groups of the **RuPyⁿ** certainly suppress their reactivities with S₂O₈²⁻, probably due to steric hindrance (Figure 8). In the case of **RuPy²@TiO₂**, the bulky qpy ligands of the **RuPy²** coordinate to the Ti⁴⁺ ions on the surfaces of the TiO₂ nanoparticles. Such a molecular arrangement of molecular **RuPy²** on the surface may negate the detrimental effects associated with the bulkiness of the uncoordinated pyridyl groups of the qpy ligand, resulting in higher photosensitization efficiency of the heterogeneous **RuPy²@TiO₂** photosensitizer compared to that of homogeneous **RuPy²**. Indeed, the **RuPy²@TiO₂** emission was more effectively quenched by S₂O₈²⁻ than that of **RuPy²** (Figure 11).

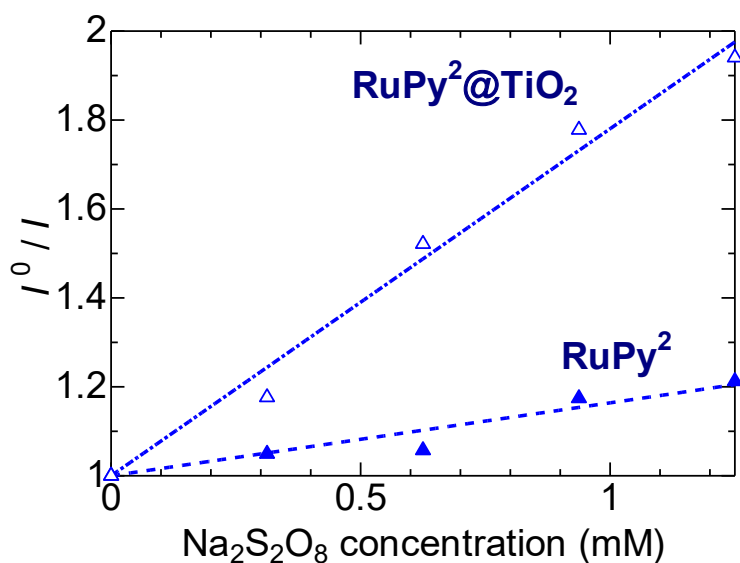
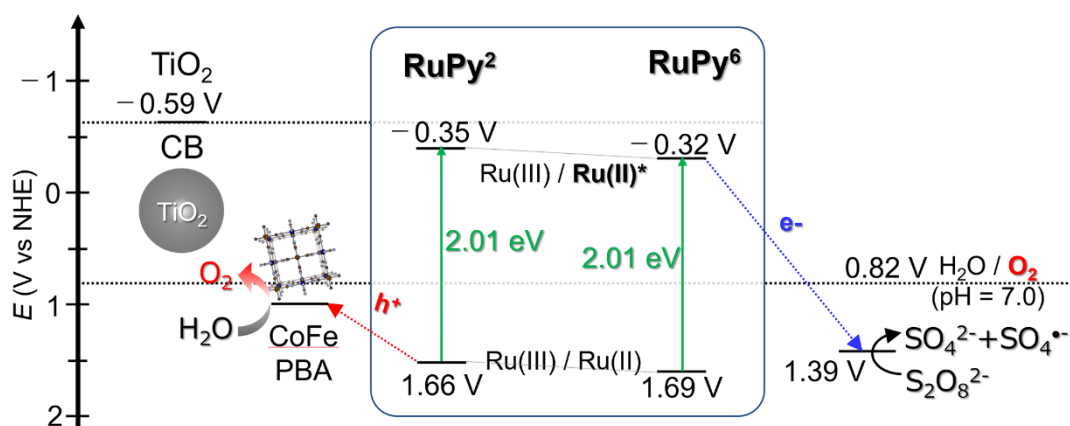


Figure 11. Stern–Volmer plots of **RuPy²** (closed triangle), or **RuPy²@TiO₂** (open triangle) in the presence of various concentrations of Na₂S₂O₈ at room temperature. A mixture of H₂O/CH₃CN (v/v = 2:1) was used for these measurements. [**RuPy²**] = 12.5 μM.

This assumption is also reasonable when considering the **RuPy⁶@TiO₂** results, that is, more than half of the pyridyl groups of **RuPy⁶** remain uncoordinated in **RuPy⁶@TiO₂**, and these groups face the outer edges of the **RuPy⁶@TiO₂** nanoparticles, resulting in low efficiency compared to that of **RuPy⁶**. In addition, the positively charged surface of **RuPyⁿ@TiO₂** nanoparticle may promote the electron transfer quenching process by the S₂O₈²⁻ anionic sacrificial electron acceptor. In fact, the zeta potentials of both **RuPyⁿ@TiO₂** was negatively shifted in the presence of S₂O₈²⁻ (Table 8). Note that the contribution of photoinduced interfacial electron transfer from **RuPyⁿ*** to the TiO₂ nanoparticles would be negligible due to the lack of a Ru(III)/Ru(II)* redox potential (Scheme 3).

Table 8. Zeta potentials of **RuPyⁿ@TiO₂** dispersed in H₂O/CH₃CN mixed solvent (v/v = 1/2) with/without of Na₂S₂O₈ sacrificial electron acceptor.

	Zeta potential (mV)			
	Without Na ₂ S ₂ O ₈	1.1 eq Na ₂ S ₂ O ₈	5 mM Na ₂ S ₂ O ₈	10 mM Na ₂ S ₂ O ₈
RuPy²@TiO₂	11.11	10.13	8.89	-3.13
RuPy⁶@TiO₂	27.69	20.39	10.08	-4.06



Scheme 3. Depicting a plausible electron-transfer mechanism for **RuPyⁿ@TiO₂** (n = 2, 6) during the photocatalytic O₂-evolution reaction. The redox potential of S₂O₈²⁻ and the conduction-band minimum of TiO₂ are taken from the literature^{13, 15}.

Although the photosensitizing efficiency of **RuPy²@TiO₂** decreased by increasing S₂O₈²⁻ concentration above 5 mM (Figure 2(b)), it would be due to the particle aggregation induced by the charge neutralization by surrounding S₂O₈²⁻ anions around the positively charged **RuPy²@TiO₂** nanoparticles as suggested by zeta potential shift (Table 8) and particle diameter changes estimated by dynamic light scattering (DLS) method (Figure 12). Such the aggregation of nanoparticles should

suppress the reaction with both $S_2O_8^{2-}$ sacrificial acceptor and the CoFe-PBA catalyst because of the slower diffusion of aggregated nanoparticles. On the other hand, the photosensitizing efficiency of **RuPy⁶@TiO₂** hardly depended on the $S_2O_8^{2-}$ concentration. Although the reason isn't well-revealed yet, the pyridyl groups at the outer surface of **RuPy⁶@TiO₂** might bind to the CoFe-PBA catalyst, resulting in the lower efficiency of photo-induced electron transfer reaction from the surface-immobilized **RuPy^{6*}** to $S_2O_8^{2-}$ sacrificial acceptor.

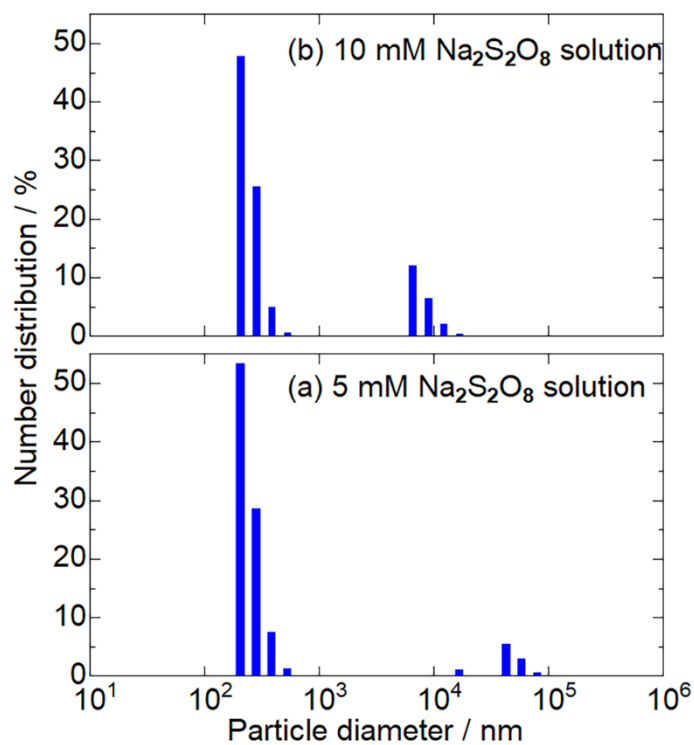
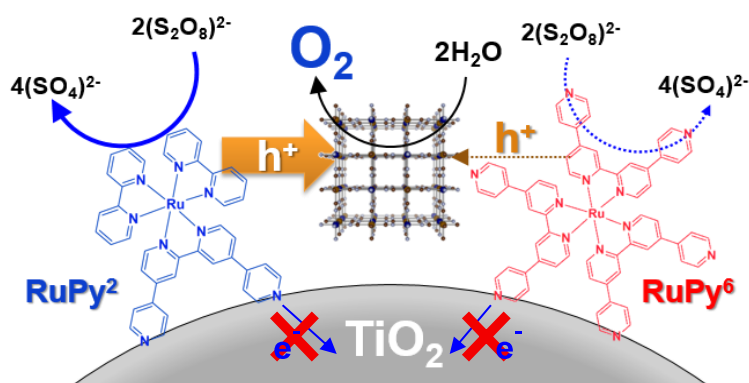


Figure 12. Particle diameter distributions of **RuPy²@TiO₂** in (a) 5 mM and (b) 10 mM $Na_2S_2O_8$ solution estimated by the dynamic light scattering method.

4-4 Conclusions

In this study, we immobilized pyridyl-anchor-functionalized Ru(II) photosensitizers (**RuPyⁿ**; n = 2, 6) on the surfaces of TiO₂ nanoparticles in order to investigate the effects of the pyridyl anchoring groups on the photocatalytic O₂-evolution reaction driven by the CoFe-PBA Prussian blue analogue catalyst. Emission quenching experiments clearly indicate that the pyridyl groups of the **RuPyⁿ** molecular photosensitizers suppress their reactivities with the S₂O₈²⁻ sacrificial electron acceptor, resulting in lower photocatalytic O₂-evolution activities in the presence of the CoFe-PBA catalyst than that of the unmodified [Ru(bpy)₃]²⁺ complex. A catalyst-adsorption ability was also observed, even though it didn't provide positive effect on photocatalytic OER activity. Although the ³MLCT emission of the **RuPyⁿ** photosensitizers were hardly quenched by immobilization on the TiO₂ nanoparticles under neutral condition, the **RuPy²**-loaded TiO₂ nanoparticles (**RuPy²@TiO₂**) exhibited higher photocatalytic O₂-evolution activity under the same experimental condition than that of free **RuPy²**, while the immobilization of **RuPy⁶** on the TiO₂ nanoparticles hardly improved its activity. These contrasting results clearly indicate that the surfaces of the **RuPyⁿ@TiO₂** nanoparticles have a dominating influence over the photocatalytic O₂-evolution reaction. (Scheme 4) On a more positive note, under the condition without a reaction process with sacrificial oxidant, for example on the photoelectrode with tuning of their redox potential or the kind of semiconductor, pyridyl anchor-modified sensitizers can become a more promising candidate.



Scheme 4. Photochemical OER of **RuPyⁿ@TiO₂**.

4-5 References

- 1 (a) F. Li, Y. Jiang, B. Zhang, F. Huang and Y. Gao, L. Sun, *Angew. Chem. Int. Ed.*, 2012, **51**, 2417. (b) L. Wang, M. Mirmohades, A. Brown, L. Duan, F. Li, Q. Daniel, R. Lomoth, L. Sun and L. Hammarström, *Inorg. Chem.*, 2015, **54**, 2742.
- 2 (a) E. Rousset, D. Chartrand, I. Ciofini, V. Marvaud, G.S. Hanan, *Chem. Commun.* 2015, **51**, 9261. (b) E. Rousset, D. Chartrand, I. Ciofini, V. Marvaud, G.S. Hanan, *Inorg. Chem.* 2017, **56**, 9515.
- 3 (a) K. Takijiri, K. Morita, T. Nakazono, K. Sakai, H. Ozawa, *Chem. Commun.*, 2017, **53**, 3042. (b) K. Morita, K. Takijiri, K. Sakai, H. Ozawa, *Dalton Trans.*, 2017, **46**, 15181.
- 4 P. Shi, B. J. Coe, S. Sánchez, D. Wang, Y. Tian, M. Nyk, and M. Samoc, *Inorg. Chem.* 2015, **54**, 11450.
- 5 (a) Y. Ooyama, S. Inoue, T. Nagano, K. Kushimoto, J. Ohshita, I. Imae, K. Komaguchi, Y. Harima, *Angew. Chem. Int. Ed.*, 2011, **50**, 7429. (b) C. -L. Mai, T. Moehl, C. -H. Hsieh, J. -D. Décoppet, S. M. Zakeeruddin, M. Grätzel, C. -Y. Yeh, *ACS Appl. Mater. Interfaces*, 2015, **7**, 14975
- 6 (a) S. Goberna-Ferrón, W. Y. Hernández, B. Rodríguez-García, J. R. Galán-Mascarós, *ACS Catal.* 2014, **4**, 1637. (b) S. Pintado, S. Goberna-Ferrón, E. C. Escudero-Adán, J. R. Galán-Mascarós, *J. Am. Chem. Soc.*, 2013, **135**, 13270.
- 7 R.J. Morgan, A.D. Baker, *J. Org. Chem.* 1990, **55**, 1986.
- 8 D. Hong, S. Mandal, Y. Yamada, Y. M. Lee, W. Nam, A. Llobet and S. Fukuzumi, *Inorg. Chem.*, 2013, **52**, 9522.
- 9 A. Kobayashi, S. Furugori, M. Yoshida, M. Kato, *Chem. Lett.*, 2016, **45**, 619.
- 10 J. Zhao, H. Hidaka, A. Takamura, E. Pelizzetti, N. Serpone, *Langmuir* 1993, **9**, 1646.
- 11 W. D. K. Clark, N. Sutin, *J. Am. Chem. Soc.* 1977, **99**, 4676.
- 12 A. Nakagawa, E. Sakuda, A. Ito, N. Kitamura, *Inorg. Chem.* 2015, **54**, 10287.
- 13 G. Rothenberger, D. Fitzmaurice, M. Grätzel, *J. Phys. Chem.* 1992, **96**, 5983.
- 14 (a) H.S. White, W.G. Becker, A.J. Bard, *J. Phys. Chem.* 1984, **88**, 1840. (b) A. L. Kaledin, Z. Huang, Y. V. Geletii, T. Lian, C. L. Hill, D. G. Musaev, *J. Phys. Chem. A* 2010, **114**, 73.
- 15 U. Fürholz, A. Haim, *Inorg. Chem.* 1987, **26**, 3243.

Chapter 5
Synthesis and Properties of
Pyridyl-anchor and Carbazole
Modified Ru(II) Complexes

5-1 Introduction

As discussed in Chapter 4, the pyridyl-anchor modified Ru(II) PSs were found to show a highly positive Ru(III/II) redox potential suitable for O₂ evolution via hole-transfer (HM) moiety and their pyridyl anchors are valuable for a stable immobilization on TiO₂-modified electrodes.¹ However, there are still a problem to apply for OER photoanodes, difficulty for a connection with catalysts, unlikely to carboxyl or phosphonate group, for which bridging-metal methods are applicable. This aspect restricts the application of pyridyl-anchor sensitizers only for co-adsorption with catalysts.² The solution for this problem is required for application of the pyridyl-anchor sensitizer for through-bond conjugated photo(electro)chemical OER devices, especially for a HM-integrated system.

On the other hand, as discussed in Chapter 3, the introduction of carbazole (cbz) groups to the Ru-bda molecular water oxidation catalyst (WOC) can be a promising direction to improve the photochemical OER. In addition, the polymerization ability of cbz and following species, polycarbazole, can be utilized to construct a good hole-mediated connector.³

From this viewpoint, cbz-electropolymerization is expected as a promising method to connect PSs and catalysts with introducing a mediator part. In this context, Ru(II) dyes having both pyridyl anchors and cbz hole-mediator precursors, **S_{C2}** and **S_{C4}** (Fig. 1), were synthesized and their photochemical property was evaluated to elucidate the effect of these functionalization. Although an introduction of cbz substituents to [Ru(bpy)₃]²⁺ moiety has been already reported,⁴ co-introduction of other functional groups including pyridyl anchor has never been reported yet.

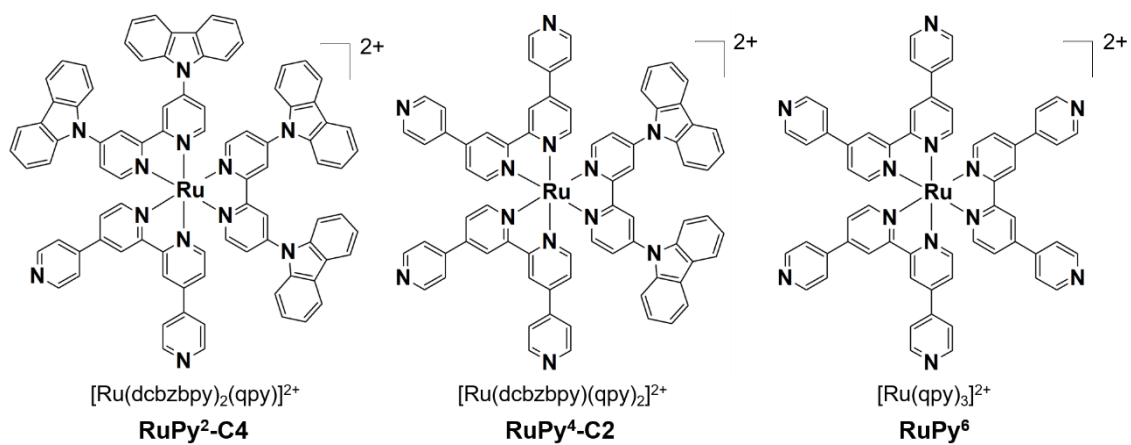


Figure 1. Molecular structures of the complexes **RuPy²-C4**, **RuPy⁴-C2** and **RuPy⁶**.

5-2 Experimental

5-2-1 Instruments and measurement

Synthetic experiments with microwave irradiation were carried out by a Biotage Initiator+ with 20 mL glass vials. ^1H NMR spectra were recorded using a JEOL ECZ-400S spectrometer. MALDI-TOF MS measurements were carried out using a Bruker Autoflex Speed spectrometer, with α -cyano-4-hydroxycinnamic acid as the matrix. UV-vis absorption spectra were recorded on Hitachi U-3000 spectrophotometers. Luminescence spectra were recorded on a JASCO FP-6600 spectrofluorometer at 298 K or 77 K. Emission quantum yields (Φ_{em}) were measured using a Hamamatsu C9920-02 absolute photoluminescence quantum-yield-measurement system equipped with an integrating sphere apparatus and a 150-W continuous-wave xenon light source. Emission lifetime (τ) measurements were conducted using a Hamamatsu Quantaurus Tau ($\lambda_{\text{ex}} = 280$ nm). Each sample solution was deoxygenated by bubbling with N_2 for 30 min at 298 K. Electrochemical measurements (CV) were recorded using a HOKUTO DENKO HZ-3000 electrochemical measurement system equipped with glassy carbon, Pt wire, and Ag/Ag $^+$ (in acetonitrile) or Ag/AgCl (in aq.) electrodes as the working, counter, and reference electrodes, respectively. 0.1 M tetrabutylammonium hexafluorophosphate (TBAPF $_6$) or sodium perchlorate were used as the supporting electrolyte in the electrochemical measurements in acetonitrile or aqueous solution, respectively. Ferrocene was used as internal reference. All solutions were deaerated by N_2 bubbling for 15 min before measurement.

5-2-2 Franck–Condon Analysis of Emission Spectra

Emission spectra under 77 K were fit by a two-mode Franck–Condon analysis, eq. 1.⁵

$$I(\tilde{\nu}) = \sum_{v_M=0}^{\infty} \sum_{v_L=0}^{\infty} \left(\frac{E_{00} - v_M \hbar \omega_M - v_L \hbar \omega_L}{E_{00}} \right)^4 \left(\frac{S_M^{v_M}}{v_M!} \right) \left(\frac{S_L^{v_L}}{v_L!} \right) \exp \left[-4 \ln 2 \left(\frac{\tilde{\nu} - E_0 + v_M \hbar \omega_M + v_L \hbar \omega_L}{\Delta \tilde{\nu}_{1/2}} \right)^2 \right] \quad (1)$$

$I(\tilde{\nu})$ (cm^{-1}) is the emission intensity at a given wavenumber relative to that of the 0 \rightarrow 0 emission transition. E_{00} is the energy gap between the zeroth vibrational levels in the ground and emitting excited states, $\hbar \omega_M$ and $\hbar \omega_L$ are the quantum spacing for the averaged medium- and low-frequency vibrational mode, respectively. S_M and S_L are the electron-vibrational coupling constant or S-factor⁶ reflecting the extent of change along the normal coordinate of the average medium- and low-frequency modes. $\Delta \tilde{\nu}_{1/2}$ is the full width at half-maximum (fwhm) for an individual vibronic line in the emission spectrum. The photon numbers of the emission spectrum were corrected to a wavenumber scale by using the eq. 2.⁷

$$I(\tilde{\nu}) = I(\lambda) \times \lambda^2 \quad (2)$$

The parameters E_{00} , $\hbar\omega_{M\text{ or }L}$, $S_{M\text{ or }L}$ and $\Delta\tilde{\nu}_{1/2}$ were optimized with a least-squares minimization routine by using a Generalized Reduced Gradient (GRG2) algorithm.⁸ The summation was carried out over 11 vibrational levels ($\nu_M: 0 \rightarrow 10$).

5-2-3 Single crystal X-ray diffraction measurement

Single-crystal X-ray diffraction data were collected using a Rigaku XtaLAB Synergy diffractometer equipped with Cu K α radiation (PhotonJet (Cu)). Each crystal was mounted on a MicroMount using paraffin oil. The crystal was then cooled using a N₂-flow-type temperature controller. The diffraction data were processed using CrysAlisPRO software.⁹ The structures were solved by direct methods using SHELXT¹⁰ and refined by full-matrix least-squares refinement using SHELXL.¹¹ Non-hydrogen atoms were refined anisotropically, while the hydrogen atoms were refined using the riding model. All calculations were performed using the Olex2 software package.¹² The crystallographic data obtained for **RuPy⁴-C2** are listed in Table 1.

5-2-4 Theoretical calculation

Calculations were performed using the Gaussian 09 software package.¹³ Geometry optimizations and TD-DFT calculation were performed in the ground state using the PBE0 functional¹⁴ together with the LANL2DZ effective core potentials and associated basis set.¹⁵ Solvent (MeCN) was modelled by a conductor-like polarizable continuum model (cpcm)¹⁶, according to a reported method for pyridyl-modified Ru(II) complexes.¹⁷ Although the results of DFT and TD-DFT studies on **RuPy⁶** have been already reported, re-calculation of this complex was carried out to obtain information of its molecular orbital energy, which wasn't reported. All orbitals are visualized by Gaussview 0.5 software package.¹⁸

5-2-5 Materials

4,4'-dibromo-2,2'-bipyridine,¹⁹ 2,2'-4,4''-4',4'''-quaterpyridine (qpy),²⁰ and [RuCl₂(DMSO)₄]²¹ were synthesized according to previously reported methods. [Ru(qpy)₃]²⁺ (**RuPy**⁶) was obtained as a PF₆ salt as reported.¹⁷ High-purity water was obtained by passing house-distilled water through a Millipore Milli-Q Simplicity® UV system. All other reagents and solvents were purchased from commercial sources and used as received unless otherwise noted.

5-2-6 Synthesis

Synthesis of 4,4'-di(9*H*-carbazol-9-yl)-2,2'-bipyridine (dcbzbpy)

4,4'-di(9*H*-carbazol-9-yl)-2,2'-bipyridine was synthesized according to the literature method for 5,5'-di(9*H*-carbazol-9-yl)-2,2'-bipyridine²² with some modifications as follows; carbazole (2.22 g, 13.2 mmol, 3 eq.), 5,5'-dibromo-2,2'-bipyridine (1.41 g, 4.5 mmol, 3 eq.), CuI (180 mg, .087 mmol), K₂CO₃ (3.66 g, 25.4 mmol), 18-crown-6 (99.8 mg, 0.3 mmol), and N,N'-dimethylpropyleneurea (DMPU) (0.6 mL) were charged in a schlenk tube and sealed under the Ar atmosphere. The reaction mixture was heated to 210 °C by mantle heater for 3 days. After cooling to room temperature, the obtained brownish-black solid was rigorously stirred in 2 M HCl aq. (20 mL). The precipitate was filtered, washed with ammonia aq. (28%) and water, and dissolved in dichloromethane. The organic solution was dried over MgSO₄, and filtered. The solvent was evaporated under vacuum and then the obtained grey solid was recrystallized from dichloromethane/acetone. The resultant precipitates were washed with acetone. The brown powder was subject to silica-gel chromatography with dichloromethane/methanol (v/v = 9/1) as eluent, and after washing with acetone, dcbzbpy was obtained as off-white solid (119.5 mg, 4%). ¹H NMR (Fig. 2, 400 MHz, CDCl₃) δ = 8.82-8.80 (4H, m), 8.10 (4H, d), 7.62 (4H, d), 7.58 (2H, dd), 7.42 (4H, td), 7.30 (4H, t).

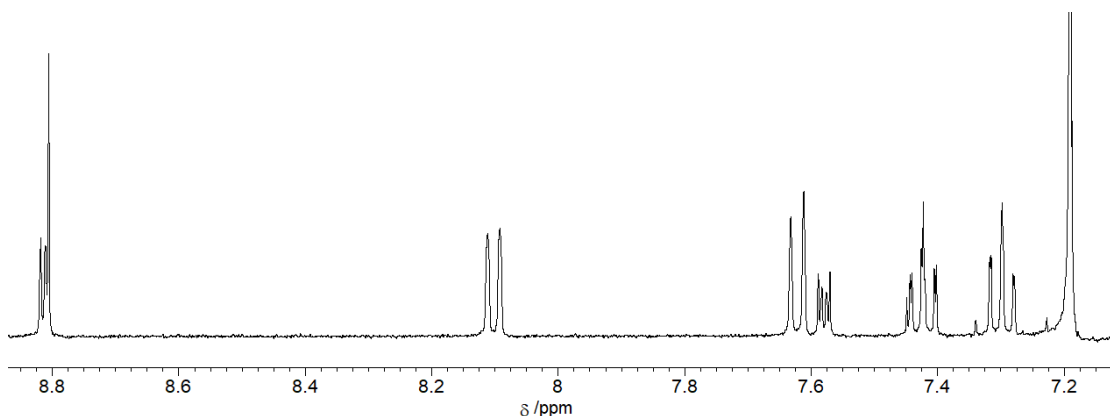


Figure 2. The aromatic region of ¹H NMR spectrum of dcbzbpy.

Synthesis of $[\text{Ru}(\text{dcbzbp})_2(\text{qpy})_2](\text{PF}_6)_2$ (= $\text{RuPy}^4\text{-C2}(\text{PF}_6)_2$).

$[\text{RuCl}_2(\text{DMSO})_4]$ (58.8 mg, 121 μmol , 1 eq.), qpy (74.9 mg, 241 μmol , 2 eq.) and dcbzbp (59.0 mg, 121 μmol , 1 eq.) were dispersed in 20 mL of ethylene glycol, and this mixture was heated at 240°C by the microwave reactor for 1 h. After the solution was cooled to room temperature, 80 mL of H_2O and 20 mL of aqueous saturated KPF_6 solution were added to afford a dark-red precipitation, which was collected by celite filtration, washed with water and diethyl ether, and redissolved to acetonitrile. This crude product was purified by an alumina gel column chromatography with 0.1wt% KPF_6 of acetone/MeOH (v/v = 95/5) as eluent. The second reddish-orange band was collected, and the solvent was removed by evaporation, which was recrystallized from acetone/diethyl ether, and dried in vacuo. Yield: 49.0 mg (33 μmol , 27%). ^1H NMR (Fig. 3, 400 MHz, CD_3CN) δ = 9.09 (4 H, dd, J = 1.7, 8.2 Hz), 8.92 (2 H, d, J = 2.2 Hz), 8.83 (8 H, ddd, J = 1.6, 4.2, 9.6 Hz), 8.28 (2 H, d, J = 6.1 Hz), 8.19 (4 H, d, J = 7.0 Hz), 8.03 (4 H, t, J = 5.2 Hz), 7.94-7.87 (10 H, m), 7.83-7.78 (8 H, m), 7.50 (4 H, td, J = 1.3, 8.3 Hz), 7.38 (4 H, dd, J = 7.7 Hz). MALDI-TOF MS (positive mode, CH_3CN) m/z^+ = 1208.2 ($[\text{M}]^+$), 1353.2($[\text{M}](\text{PF}_6)^+$). calcd. 1208.33 ($[\text{M}]^+$), 1353.30($[\text{M}](\text{PF}_6)^+$). Single crystals were obtained by the natural-evaporation method with acetonitrile/toluene (v/v = 1/1). The ORTEP figure and crystallographic data were attached in Fig. 4 and Table. 1, respectively.

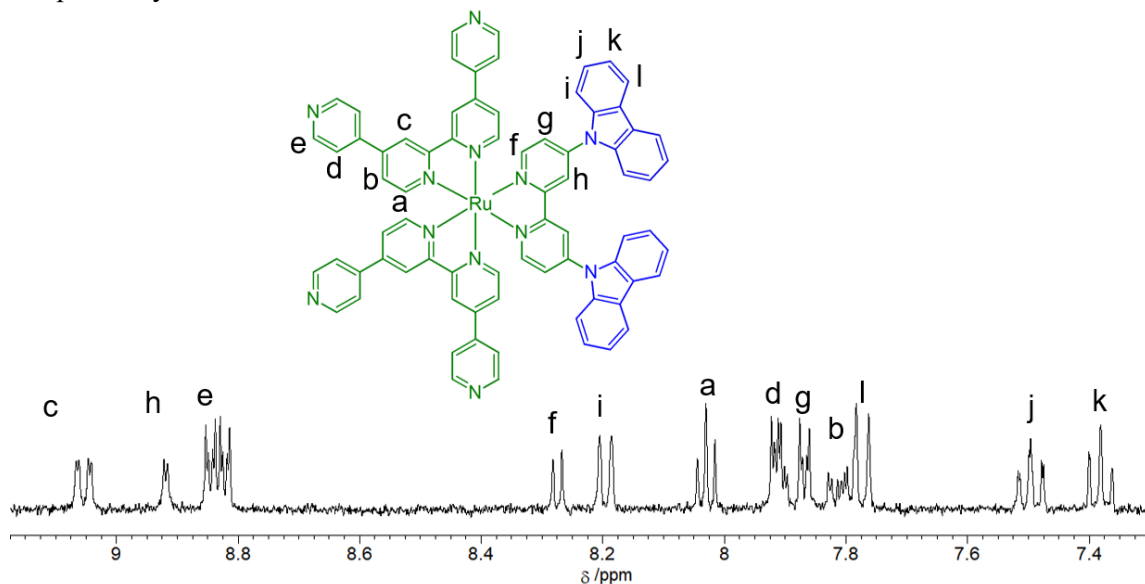


Figure 3. The aromatic region of ^1H NMR spectrum of $[\text{RuPy}^4\text{-C2}](\text{PF}_6)_2$. (400 MHz, CD_3CN)

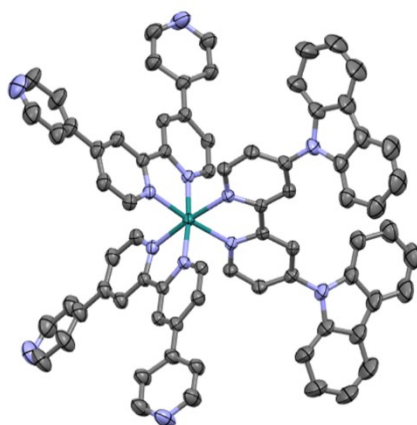


Figure 4. ORTEP drawing of **RuPy⁴-C2**. Thermal ellipsoids are shown at the 50% probability level.

All counter anions, solvent molecules and hydrogen atoms are omitted for clarity.

Color chart: grey: C, purple: N, red: O, green: Ru.

Table 1. Crystallographic parameters of **RuPy⁴-C2** (PF₆)₂ · 4MeCN · 1 acetone.

Complex	[RuPy ⁴ -C2](PF ₆) ₂ · 4MeCN · 1 acetone
<i>T</i> / K	93
Formula	C ₈₂ H ₆₂ F ₁₂ N ₁₆ P ₂ Ru
Formula weight	1662.48
Crystal system	<i>Monoclinic</i>
Space group	<i>C2/c</i>
<i>a</i> / Å	19.8262(3)
<i>b</i> / Å	19.0188(2)
<i>c</i> / Å	24.1535(3)
<i>a</i> / deg.	90
<i>b</i> / deg.	113.795(2)
<i>g</i> / deg.	90
<i>V</i> / Å ³	8333.4(2)
<i>Z</i>	4
<i>D</i> _{cal} / g×cm ⁻³	1.325
Reflections collected	29635
Unique reflections	8478
GOF	1.075
<i>R</i> _{int}	0.0344
<i>R</i> (<i>I</i> > 2.00σ(<i>I</i>))	0.0486
<i>R</i> _w ^a	0.1420

$$^a R_w = [\Sigma(w(F_o^2 - F_c^2)^2) / \Sigma w(F_o^2)^2]^{1/2}.$$

Synthesis of $[\text{Ru}(\text{dcbzbp})_2(\text{qpy})](\text{PF}_6)_2$ (= **RuPy²-C4** (PF_6)₂).

$[\text{RuCl}_2(\text{DMSO})_4]$ (58.4 mg, 120 μmol , 1 eq.), qpy (37.5 mg, 121 μmol , 1 eq.) and dcbzbp (117.3 mg, 240 μmol , 2 eq.) were dispersed in 20 mL of ethylene glycol, and this mixture was heated at 240°C by the microwave reactor for 1 h. After the solution was cooled to room temperature, 80 mL of H_2O and 20 mL of aqueous saturated KPF_6 solution were added to afford a dark-red powder, which was collected by celite filtration, washed with water and diethyl ether, and redissolved to acetonitrile. This crude product was purified by an alumina gel column chromatography with 0.1 wt% KPF_6 of acetone/MeOH (v/v = 99/1) as eluent. The second reddish-orange band was collected and then the solvent was removed by evaporation. The resultant solid was recrystallized from acetone/diethyl ether and dried in vacuo. Yield: 48.3 mg (29 μmol , 24%). ^1H NMR (Fig. 5, 400 MHz, CD_3CN) δ = 9.11 (2 H, s), 8.97 (4 H, dd), 8.85 (4 H, dd), 8.34 (4 H, dd), 8.21 (8 H, t), 8.10 (2 H, d), 7.97-7.92 (8 H, m), 7.83-7.78 (10 H, m), 7.50 (8 H, dd), 7.38 (8 H, dd). MALDI-TOF MS (positive mode, CH_3CN) m/z^+ = 1384.4 ($[\text{M}]^+$), 1529.3($[\text{M}](\text{PF}_6)^+$). calcd. 1384.55 ($[\text{M}]^+$), 1529.52($[\text{M}](\text{PF}_6)^+$).

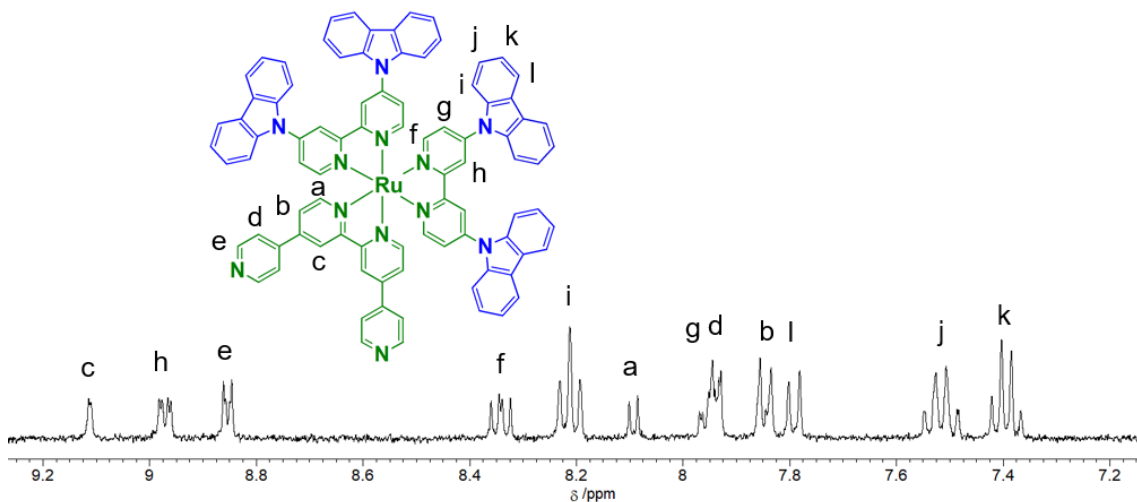


Figure 5. The aromatic region of ^1H NMR spectrum of $[\text{RuPy}^2\text{-C4}](\text{PF}_6)_2$.
(400 MHz, CD_3CN)

5-3 Results and discussion

5-3-1 Photophysical property

UV-Vis absorption and emission spectra of **RuPy²-C4**, **RuPy⁴-C2** and **RuPy⁶** in acetonitrile at 298 K are shown in Fig. 6. Photophysical properties are summarized in Table 2. The broad absorption bands assignable to ¹MLCT-based transition to qpy or dczbpy ligand were observed around 425-600 nm and 320-400 nm. The intense absorption bands at shorter wavelength below 310 nm are basically assigned to the ¹LC absorption of qpy ligand (310 nm) and the dczbpy ligand (286 nm). The wavelength of MLCT absorption band at around 480 nm (λ_{abs}) was shifted to the lower energy by increasing the number of cbz groups. This longer wavelength shift should be caused by cbz functionalization to the bpy ligand (*vide infra*, § 5-3-2). The absorption coefficient ε of each complex in visible region above 400 nm were similar, and the MLCT absorption edge was found to be close to 600 nm, suggesting that **RuPy⁴-C2** and **RuPy²-C4** are good visible-light absorber as **RuPy⁶**.

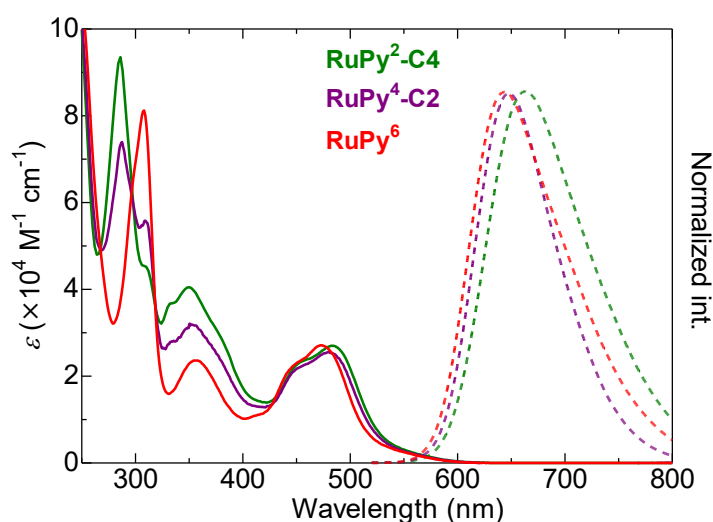


Figure 6. UV-Vis absorption spectra (solid line, 10 μM) and emission spectra (dashed line, $\lambda_{\text{ex}} = 482$ nm on **RuPy²-C4** and 480 nm on **RuPy⁴-C2**) of **RuPy⁴-C2** (green) and **RuPy²-C4** (purple) and **RuPy⁶** (red). (CH_3CN , 298 K)

Table 2. Photophysical properties of Ru complexes.

	λ_{abs} (nm) ^{a, b}	ε ($\times 10^4 \text{ M}^{-1} \text{ cm}^{-1}$) @ λ_{abs} ^b	$\lambda_{\text{em, 298 K}}$ (nm) ^{a, b}	$\lambda_{\text{em, 77 K}}$ ^{a, c} (nm)
RuPy²-C4	484 (2.56)	2.70	664 (1.87)	629 (1.97)
RuPy⁴-C2	480 (2.58)	2.55	648 (1.91)	626 (1.98)
RuPy⁶	473 (2.62)	2.71	643 (1.93)	617 (2.01)

^a Absorption energy (E_{abs} or E_{em} , = 1240 / λ) are noted in parentheses.

^b In MeCN, 298 K.

^c In MeOH/EtOH (v/v = 1/1), 77 K.

All the three complexes showed the broad emission band without vibronic structure in acetonitrile at 298 K, suggesting the $^3\text{MLCT}$ phosphorescence as well observed for Ru(II) polypyridyl complexes. This emission band ($\lambda_{\text{em}, 298 \text{ K}}$) was also red-shifted by increasing the number of cbz group. Similar red-shift behaviours are often reported in similar Ru(II) heteroleptic complexes with bulky substituents.^{17b, 23} To get deeper insight on the emission property, emission spectra of these complexes at 77 K were measured (Fig. 7). All the three emission spectra were evaluated by Franck-Condon analysis (Fig. 8). The estimated parameters are listed in Table 3. At 77 K, all the complexes exhibited the spectra with vibronic structure. The wavelength of emission maximum ($\lambda_{\text{em}, 77 \text{ K}}$) were located at the shorter wavelength than that at 298 K. The E_{00} values estimated by Franck-Condon analysis were also lower-energy shifted by the increasing number of cbz groups as $\lambda_{\text{em}, 298 \text{ K}}$. On the other hand, the values of $E_{\text{abs}} - E_{\text{em}, 293 \text{ K}}$, reflected the excited singlet-triplet splitting energy, shows a comparable value in each complex (0.67-0.69 eV), suggested that small contribution by the difference of singlet-triplet splitting. Therefore, these spectral shifts observed in both the absorption and emission spectra can be due to the effect to HOMO by mixing cbz (π), same as the absorption behavior (*vide infra* § 5-3-2). The weaker solvation induced by the bulky functional group was another possible origin of the redshift of MLCT transition. However, in **RuPy^{6-x}-CX** series, $\Delta\tilde{\nu}_{1/2}$, which reflected the solvation structural change, was increased by modification of cbz, in order of **RuPy²-C4** > **RuPy⁴-C2** > **RuPy⁶**, so that the solvation effect can hardly influence on this redshift, similar to reported Ru(II) heteroleptic complexes with bulky substituents.²³

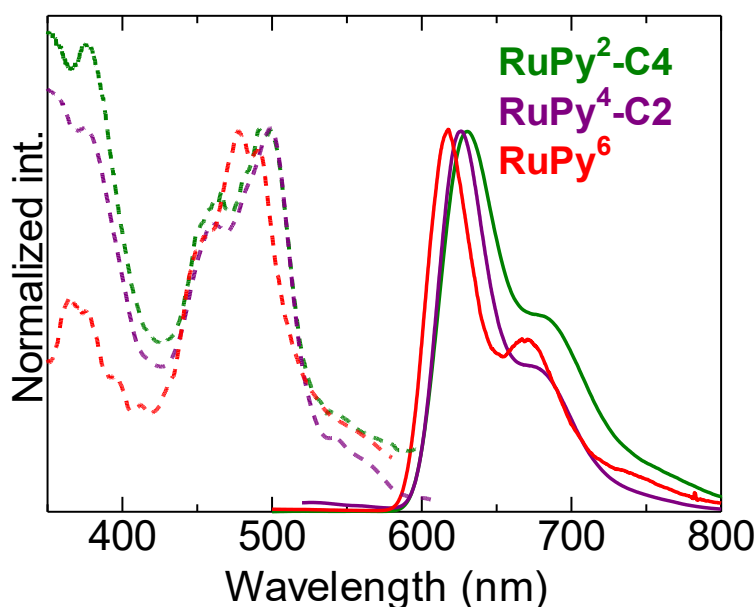


Figure 7. Emission (solid line $\lambda_{\text{ex}} = 470 \text{ nm}$ on **RuPy⁶** 480 nm on **RuPy⁴-C2** and **RuPy²-C4**) and excitation spectra (dashed line, $\lambda_{\text{em}} = 617$ (**RuPy⁶**), 630 (**RuPy⁴-C2**) and 631 nm (**RuPy²-C4**)) of **RuPy²-C4** (green) and **RuPy⁴-C2** (purple) and **RuPy⁶** (red). (MeOH/EtOH ($v/v = 1/1$), 77 K)

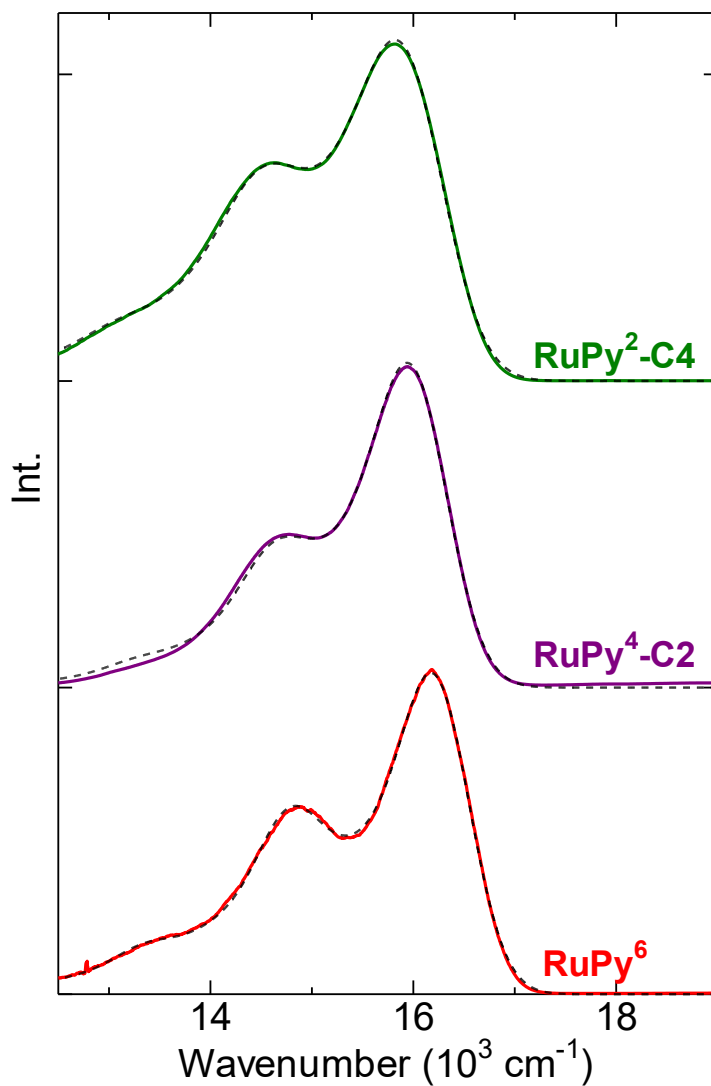


Figure. 8. Corrected emission spectra (solid lines) and theoretical fits (black dashed lines).

Table 3. Photophysical properties of Ru complexes (MeOH/EtOH ($\nu/\nu = 1/1$), 77 K).

	E_{00} (eV)	E_{00} (10^3 cm^{-1})	$\Delta\tilde{\nu}_{1/2}$ (cm^{-1})	$\hbar\omega_M$ (cm^{-1})	S_M	$\hbar\omega_L$ (cm^{-1})	S_L
RuPy²-C4	1.97	15.9	944	1399	0.69	686	0.48
RuPy⁴-C2	1.98	16.0	843	1338	0.50	675	0.37
RuPy⁶	2.01	16.2	819	1420	0.70	713	0.42

Emission decay curves and quantum yields of **RuPy⁴-C2** and **RuPy²-C4** were evaluated. Estimated emission quantum yield (Φ_{em}), emission lifetime (τ), radiative and nonradiative constants (k_r and k_{nr}) are listed in Table 4. Both **RuPy⁴-C2** and **RuPy²-C4** exhibited comparable Φ_{em} to that of **RuPy⁶**. The lifetimes τ of both **RuPy⁴-C2** and **RuPy²-C4** were estimated to be about 1 μ s that is long enough for photoredox sensitization (Fig. 9). Such a long emission lifetime can be caused by the prolonged π -system suppress the ³MC activation.^{17,23} The τ values of **RuPy⁴-C2** and **RuPy²-C4** were slightly shorter than **RuPy⁶**. As a result, the k_r and k_{nr} values of **RuPy⁴-C2** and **RuPy²-C4** were larger than those of **RuPy⁶**. The larger k_r of **RuPy^X-CY** is possibly due to the π -extension by cbz functionalization. Increasing k_{nr} by increasing the number of cbz group is plausibly explained by Energy-gap law, because the linear correlation with $\ln(k_{nr})$ and E_{00} was found as shown in Fig. 10.

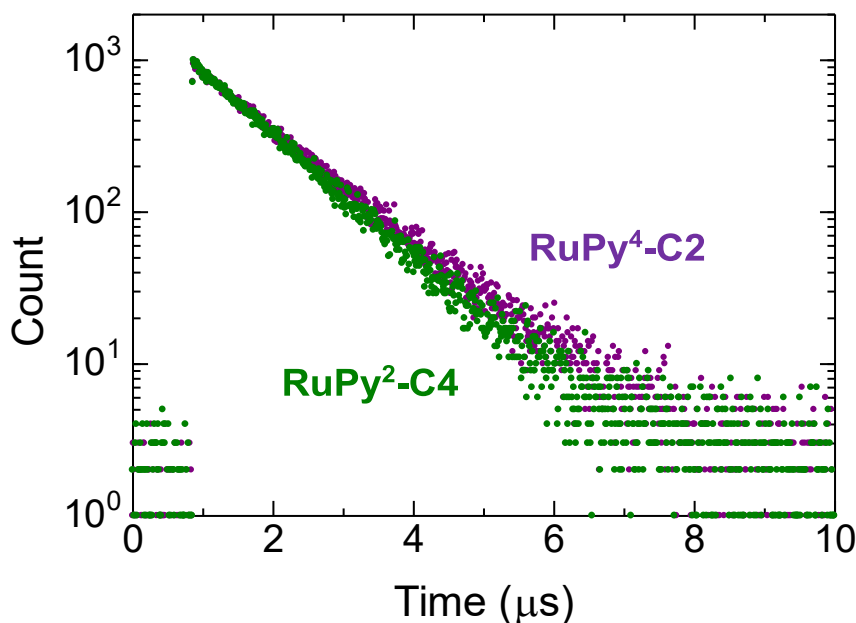


Figure 9. Emission decay curves of [S_{C2}] (purple) and [S_{C4}] (green). (1 μ M, CH₃CN, 298 K, λ_{ex} = 280 nm)

Table 4. Luminescence data of Ru complexes (CH₃CN, 298 K).

Complex	Φ_{em}	τ (μ s)	k_r (s^{-1})	k_{nr} (s^{-1})
RuPy²-C4	0.21	1.05	2.00×10^5	7.52×10^5
RuPy⁴-C2	0.24	1.15	2.09×10^5	6.61×10^5
RuPy⁶	0.23 ^a	1.78 ^a	1.29×10^{5b}	4.32×10^{5b}

^a Ref. 17a. ^b Estimated from the data in ref. 17a.

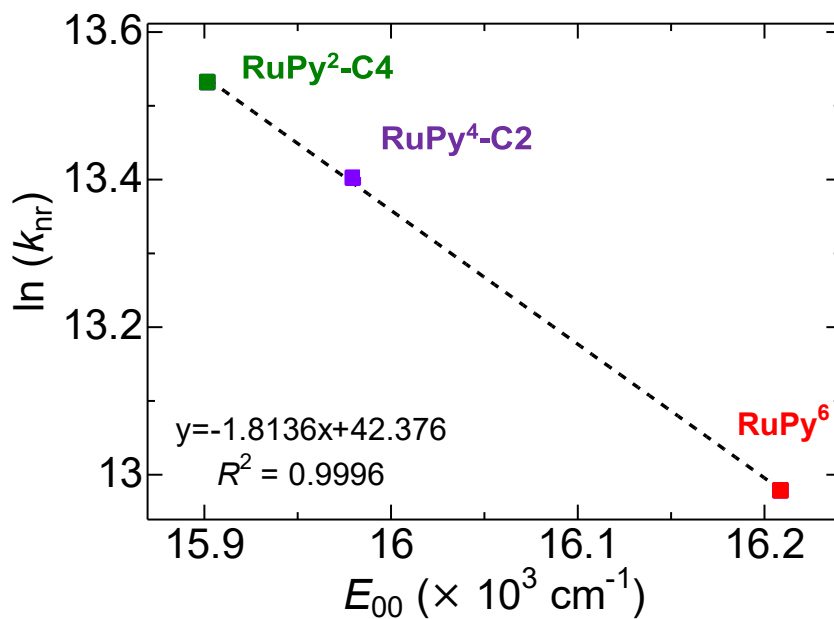


Figure 10. Energy gap plot of three complexes.
(E_{00} values were estimated from the Franck-Condon analysis of emission spectra at 77 K.)

5-3-2 Theoretical calculation

DFT calculation was carried out to reveal the photophysical properties of **RuPy²-C4** and **RuPy⁴-C2**. Molecular-orbital energy diagrams and molecular orbital contours are shown in Figures 11-14. As shown in Fig. 11, the more cbz substituents were introduced the more HOMO and LUMO are destabilized. HOMO and most of HOMO-*x* (*x* < 4) of **RuPy²-C4** and **RuPy⁴-C2** are delocalized not only on the metal center as **RuPy⁶** but also on the cbz moieties. The destabilization of HOMO level will be caused by decreasing electron density of Ru center by modifying cbz. HOMO-1 and HOMO-2 energy values of each complex were 2.7-2.9 eV, and the orbitals localized on qpy ligand(s) was relatively stabilized in comparison with those on dcbzbpq (Fig. 11b). The LUMO of each complex is mainly localized on qpy ligands (80%), even though a couple of ligands were substituted to dcbzbpq. However, by increasing number of introduced dcbzbpq, the population on qpy (100% > 88% > 81%) was decreased and LUMO was slightly destabilized. (~1.0 eV, Fig. 11). This tendency should result from the weaker electron-withdrawing ability of cbz than pyridyl groups. The populations of HOMO and LUMO implies that the lowest-energy transition of **RuPy²-C4** and **RuPy⁴-C2** at the visible region may have the metal-mixed ligand-to-ligand charge transfer (¹MMLLCT) character from the mixed MO composed of the Ru(d) and cbz(π) orbitals.

The remarkable destabilization of HOMO can be a main reason of the red-shifted absorption and emission wavelength for **RuPy²-C4** and **RuPy⁴-C2**. In fact, the HOMO-LUMO energy gap decreased in the following order, **RuPy⁶** (3.53 eV) > **RuPy⁴-C2** (3.34 eV) > **RuPy²-C4** (3.31 eV), similar order to the trends found for experimental E_{abs} and E_{em} (Table 2).|

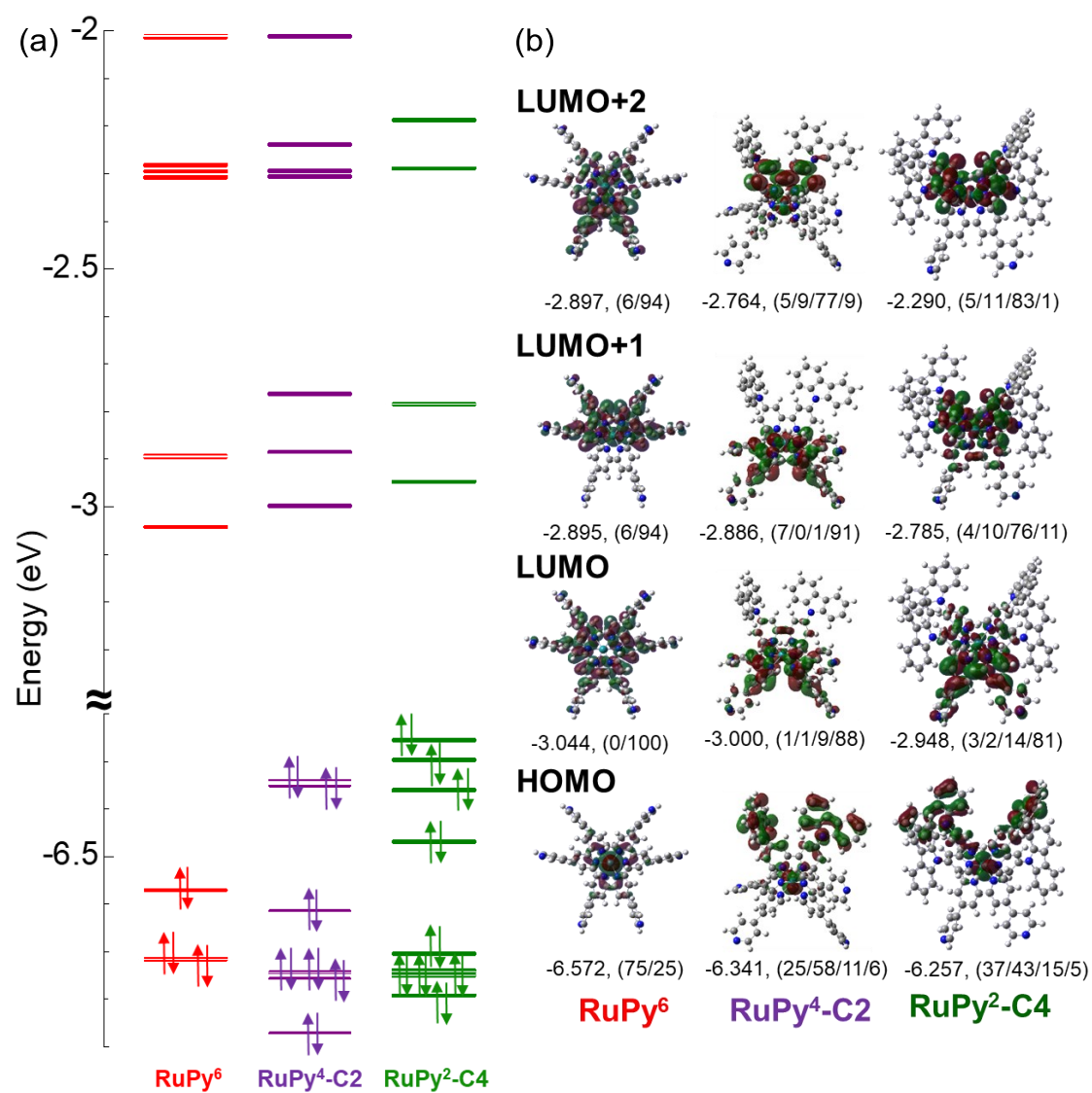


Figure 11. (a) Schematic molecular orbital energy diagrams of Ru(II) complexes in the ground state in acetonitrile. (b) HOMO, LUMO, LUMO+1 and LUMO+2 of each complex combined with energy (eV) and composition of orbitals (Ru/cbz/bpy_{dcz}bpy/qpy, %).

TD-DFT calculation in acetonitrile was also investigated. The simulation spectra and the lists of major transitions are shown in Fig. 15 and Tables 5-7, respectively. The simulated absorption spectra were qualitatively agreed to the experimental ones with two absorption bands around 425-600 nm and 320-400 nm. As the list of main transitions shown in Tables 5-7, these two bands of **RuPy**⁶ are assigned to the ¹MLCT transition from the Ru (d) orbital to the π^* orbital of bpy moieties of qpy ligand (bpy_{qpy}) and to π^* orbital delocalizing in the whole qpy ligand including the terminal pyridyl groups, respectively (Table 5 and Fig. 12). In contrast, these absorption bands of **RuPy**^{4-C2} could be assigned to the charge-transfer transitions from the Ru(d) orbital effectively mixed with the π orbital of cbz moiety to mainly the π^* orbital of qpy ligand, that is ¹MMLLCT transition (see Table 6 and Fig. 13). The similar trend was found for the **RuPy**^{2-C4} (Table 7 and Fig.14), and the larger contribution of the transition to dcbzbpy π^* orbital was observed. In addition, on the simulated absorption spectra, (Fig. 15) the peak corresponding on the lowest-energy absorption bands are red-shifted by increasing number of cbz parts with similar oscillator strength f , similar as the experimental ones. These results also suggest that mixing of cbz(π) can only contribute to on the redshift of λ_{abs} but not on the increasing molar absorptivity in the transitions corresponded to the visible absorption band.

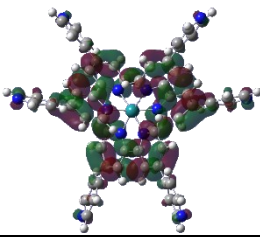
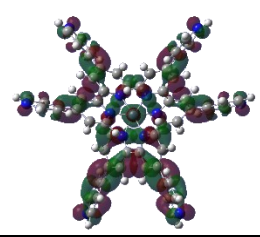
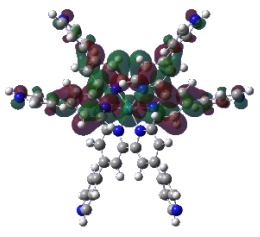
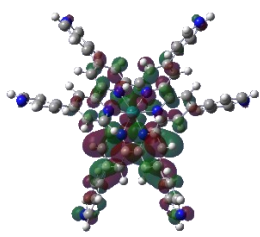
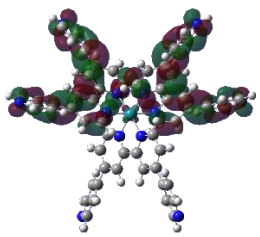
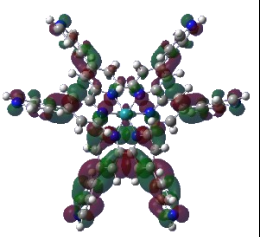
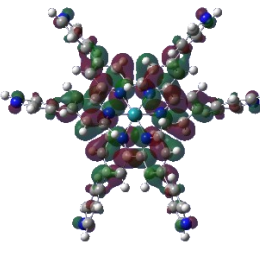
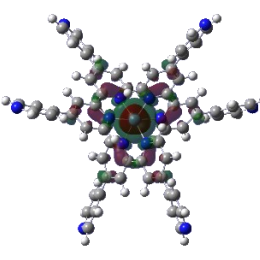
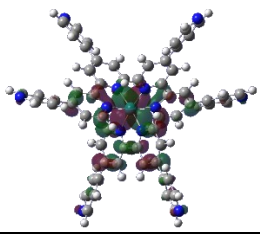
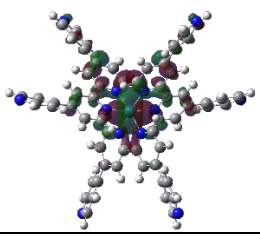
				
	LUMO+5 -2.283, (0/100)	LUMO+6 -2.240, (2/98)		
				
LUMO+1 -2.897, (6/94)	LUMO+2 -2.895, (6/94)	LUMO+3 -2.309, (1/99)	LUMO+4 -2.296, (1/99)	
				
	LUMO -3.044, (0/100)	HOMO -6.572, (75/25)		
				
	HOMO-1 -6.715, (71/29)	HOMO-2 -6.719, (71/29)		

Figure 12. Selected molecular orbitals for the ground state of **RuPy**⁶ (Isovalue = 0.02) combined with energy (eV) and composition of orbitals (Ru/qpy, %).

Table 5. Wavelength, oscillator strength (f), and contributions of major transitions ($f > 0.05$) of **RuPy**⁶.

λ (nm)	f	Major contributions	(%)	Assignment
452.05	0.0516	HOMO-1 ->LUMO	88	MLCT : Ru(d) -> bpy _{qpy} (π^*)
451.12	0.0553	HOMO-2 ->LUMO	87	MLCT : Ru(d) -> bpy _{qpy} (π^*)
		HOMO-2 ->LUMO+2	8	
434.08	0.308	HOMO-2 ->LUMO	10	MLCT : Ru(d) -> bpy _{qpy} (π^*)
		HOMO-2 ->LUMO+2	44	
433.95	0.3108	HOMO-1 ->LUMO+1	42	MLCT : Ru(d) -> bpy _{qpy} (π^*)
		HOMO-2 ->LUMO+1	43	
357.44	0.1305	HOMO-1 ->LUMO	10	MLCT : Ru(d) -> bpy _{qpy} (π^*)
357.11	0.1347	HOMO-1 ->LUMO+2	44	
357.11	0.1347	HOMO	94	MLCT : Ru(d) -> qpy(π^*)
345.34	0.0809	HOMO ->LUMO+3	93	MLCT : Ru(d) -> qpy(π^*)
		HOMO ->LUMO+4	93	
345.28	0.1503	HOMO-2 ->LUMO+5	18	MLCT : Ru(d) -> bpy _{qpy} (π^*)
		HOMO-1 ->LUMO+6	79	
344.5	0.108	HOMO-2 ->LUMO+6	45	MLCT : Ru(d) -> qpy(π^*)
		HOMO-1 ->LUMO+5	45	
340.68	0.214	HOMO-2 ->LUMO+5	72	MLCT : Ru(d) -> qpy(π^*)
		HOMO-1 ->LUMO+6	18	
340.68	0.214	HOMO-2 ->LUMO+3	66	MLCT : Ru(d) -> qpy(π^*)
		HOMO-1 ->LUMO+4	27	

^aMinor contributions (< 5%) are omitted.

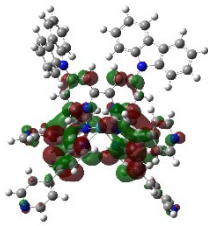
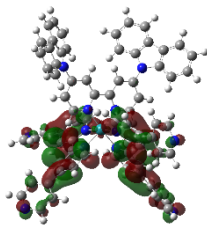
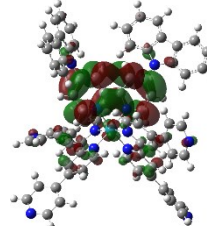
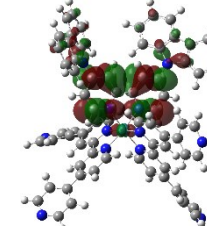
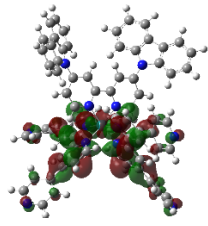
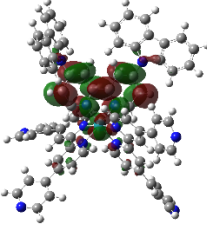
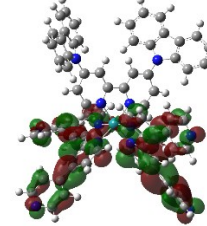
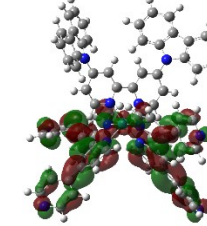
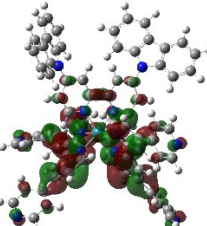
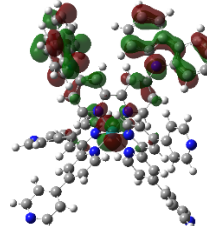
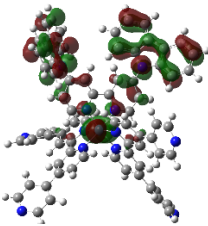
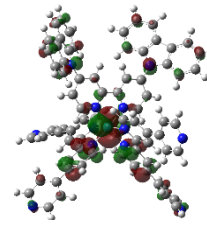
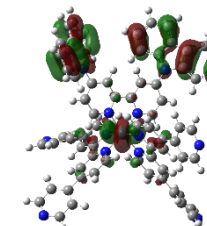
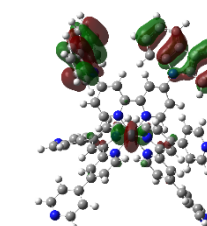
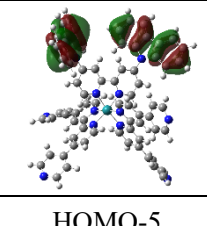
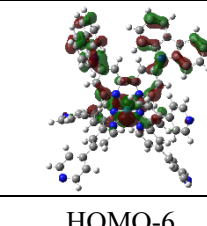
			
LUMO+5 -2.240, (0/2/15/82)	LUMO+6 -2.013, (1/0/3/95)	LUMO+7 -1.846, (2/13/69/17)	LUMO+8 -1.754, (1/22/72/5)
			
LUMO+1 -2.886, (7/0/1/91)	LUMO+2 -2.764, (5/9/77/9)	LUMO+3 -2.308, (5/0/1/99)	LUMO+4 -2.295, (2/0/1/97)
			
	LUMO -3.000, (1/1/9/88)	HOMO -6.341, (25/58/11/6)	
			
HOMO-1 -6.353, (30/51/11/6)	HOMO-2 -6.615, (63/11/8/18)	HOMO-3 -6.743, (37/46/4/13)	HOMO-4 -6.746, (24/65/3/8)
			
	HOMO-5 -6.757, (0/99/0/0)	HOMO-6 -6.872, (50/26/9/15)	

Figure 13. Selected molecular orbitals for the ground state of **RuPy⁴-C2** (Isovalue = 0.02) combined with energy (eV) and composition of orbitals (Ru/cbz/bpy_{dc}zbp_y/qp_y, %).

Table 6. Wavelength, oscillator strength (f), and contributions of major transitions ($f > 0.05$) of **RuPy⁴-C2**.

λ (nm)	f	Major contributions	(%)	Assignment
473.47	0.0794	HOMO-6 ->LUMO	20	MMLLCT : Ru(d)+cbz(π) -> qpy(π^*)
		HOMO ->LUMO	75	
449.48	0.2485	HOMO-4 ->LUMO	10	MLCT : Ru(d) -> qpy(π^*) MMLLCT : Ru(d)+cbz(π) -> qpy(π^*)
		HOMO-3 ->LUMO	17	
		HOMO-2 ->LUMO	48	
		HOMO-1 ->LUMO	7	
		HOMO ->LUMO+1	9	
446.84	0.3525	HOMO-6 ->LUMO+2	6	MMLLCT : Ru(d)+cbz(π) -> bpy _{dczbpy} (π^*)
		HOMO-3 ->LUMO+1	7	
		HOMO-2 ->LUMO+1	18	
		HOMO ->LUMO+2	59	
435.59	0.0722	HOMO-4 ->LUMO+2	10	MLCT : Ru(d) -> bpy _{dczbpy} (π^*) MMLLCT : Ru(d)+cbz(π) -> bpy _{dczbpy} (π^*)
		HOMO-3 ->LUMO+2	17	
		HOMO-2 ->LUMO+2	52	
		HOMO-1 ->LUMO+2	12	
404.34	0.0809	HOMO-4 ->LUMO	13	MMLLCT : Ru(d)+cbz(π) -> bpy(π^*)
		HOMO-4 ->LUMO+2	11	
		HOMO-3 ->LUMO	21	
		HOMO-3 ->LUMO+2	18	
		HOMO-2 ->LUMO	8	
		HOMO-1 ->LUMO	14	
		HOMO-1 ->LUMO+2	8	

368.23	0.0662	HOMO-2	->LUMO+5	19	MMLLCT : Ru(d)+cbz(π) -> bpy _{qpy} (π^*)
		HOMO-1	->LUMO+5	65	
365.57	0.0964	HOMO-2	->LUMO+3	19	MMLLCT : Ru(d)+cbz(π) -> qpy(π^*)
		HOMO-1	->LUMO+3	63	
361.27	0.1148	HOMO-6	->LUMO+5	10	MMLLCT : Ru(d)+cbz(π) -> bpy _{qpy} (π^*)
		HOMO	->LUMO+5	71	
359.9	0.142	HOMO-6	->LUMO+4	12	MMLLCT : Ru(d)+cbz(π) -> bpy(π^*)
		HOMO	->LUMO+3	8	
		HOMO	->LUMO+4	63	
345.81	0.1584	HOMO-4	->LUMO+3	8	MLCT : Ru(d)+cbz(π) -> qpy(π^*)
		HOMO-3	->LUMO+3	14	
		HOMO-2	->LUMO+3	55	
		HOMO-2	->LUMO+5	9	
345.43	0.2314	HOMO-3	->LUMO+4	9	MMLLCT : Ru(d)+cbz(π) -> bpy(π^*)
		HOMO-2	->LUMO+4	44	
		HOMO-2	->LUMO+6	6	
		HOMO-1	->LUMO+6	9	
		HOMO-1	->LUMO+8	7	
		HOMO	->LUMO+7	6	

^aMinor contributions (< 5%) are omitted.

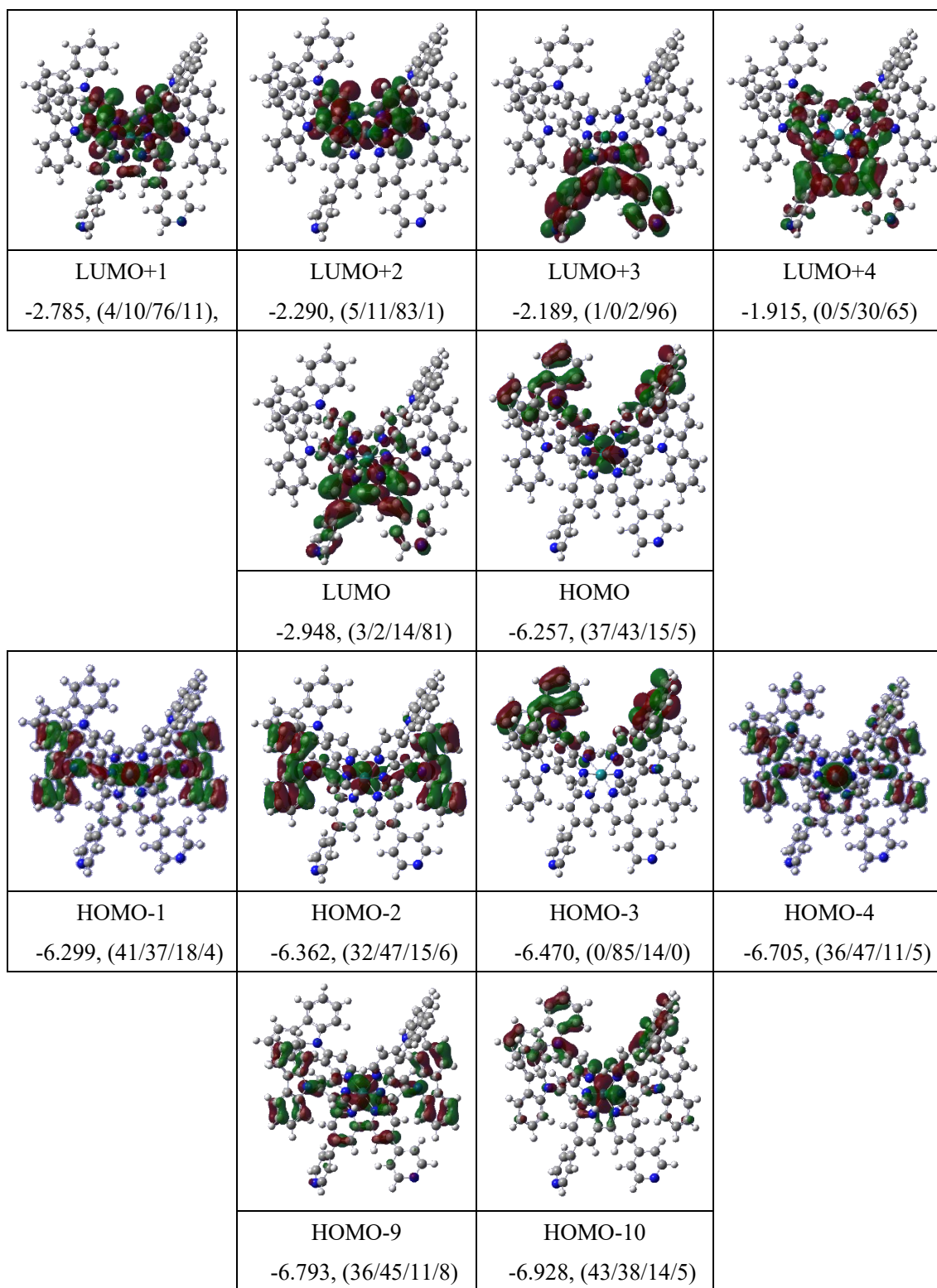


Figure 14. Selected molecular orbitals for the ground state of **RuPy²-C4** (Isovalue = 0.02) combined with energy (eV) and composition of orbitals (Ru/cbz/bpy_{dc}zbp_y/qpy, %).

Table 7. Wavelength, oscillator strength (f), and contributions of major transitions ($f > 0.05$) of **RuPy²-C4**.

λ (nm)	f	Major contributions	(%)	Assignment
465.34	0.2509	HOMO-10 -> LUMO+1	10	MMLLCT : Ru(d)+cbz(π) -> bpy _{dczbpy} (π^*)
		HOMO-1 -> LUMO+1	32	
		HOMO -> LUMO+1	42	
460.18	0.2476	HOMO-9 -> LUMO	20	MMLLCT : Ru(d)+cbz(π) -> qpy(π^*)
		HOMO-2 -> LUMO	65	
		HOMO -> LUMO+2	6	
448.53	0.0802	HOMO-10 -> LUMO+2	7	MMLLCT : Ru(d)+cbz(π) -> bpy _{dczbpy} (π^*)
		HOMO-9 -> LUMO+1	16	
		HOMO-2 -> LUMO+1	27	
		HOMO-1 -> LUMO+2	11	
		HOMO -> LUMO+2	34	
446.78	0.2104	HOMO-9 -> LUMO+2	23	MMLLCT :
		HOMO-2 -> LUMO+2	67	Ru(d)+cbz(π) -> bpy _{dczbpy} (π^*)
408.95	0.0586	HOMO-4 -> LUMO+2	10	LLCT : cbz(π) -> bpy(π^*)
		HOMO-3 -> LUMO	46	
		HOMO-3 -> LUMO+1	32	
402.84	0.0858	HOMO-4 -> LUMO	26	MMLLCT : Ru(d)+cbz(π) -> bpy(π^*)
		HOMO-4 -> LUMO+1	20	
		HOMO-3 -> LUMO+2	33	
372.28	0.0847	HOMO-10 -> LUMO	9	MMLLCT : Ru(d)+cbz(π) -> bpy(π^*)
		HOMO-4 -> LUMO+4	10	
		HOMO-1 -> LUMO+4	34	
		HOMO -> LUMO+4	34	
365.57	0.1215	HOMO-10 -> LUMO+4	6	MMLLCT : Ru(d)+cbz(π) -> bpy(π^*)
		HOMO-1 -> LUMO+4	34	
361.68	0.1983	HOMO -> LUMO+4	40	
		HOMO-9 -> LUMO+1	17	MMLLCT :
357.55	0.0838	HOMO-1 -> LUMO+3	44	Ru(d)+cbz(π) -> bpy _{dczbpy} (π^*)+qpy(π^*)
		HOMO-9 -> LUMO+3	17	MMLLCT : Ru(d)+cbz(π) -> qpy(π^*)
		HOMO-2 -> LUMO+3	68	

^aMinor contributions (< 5%) are omitted.

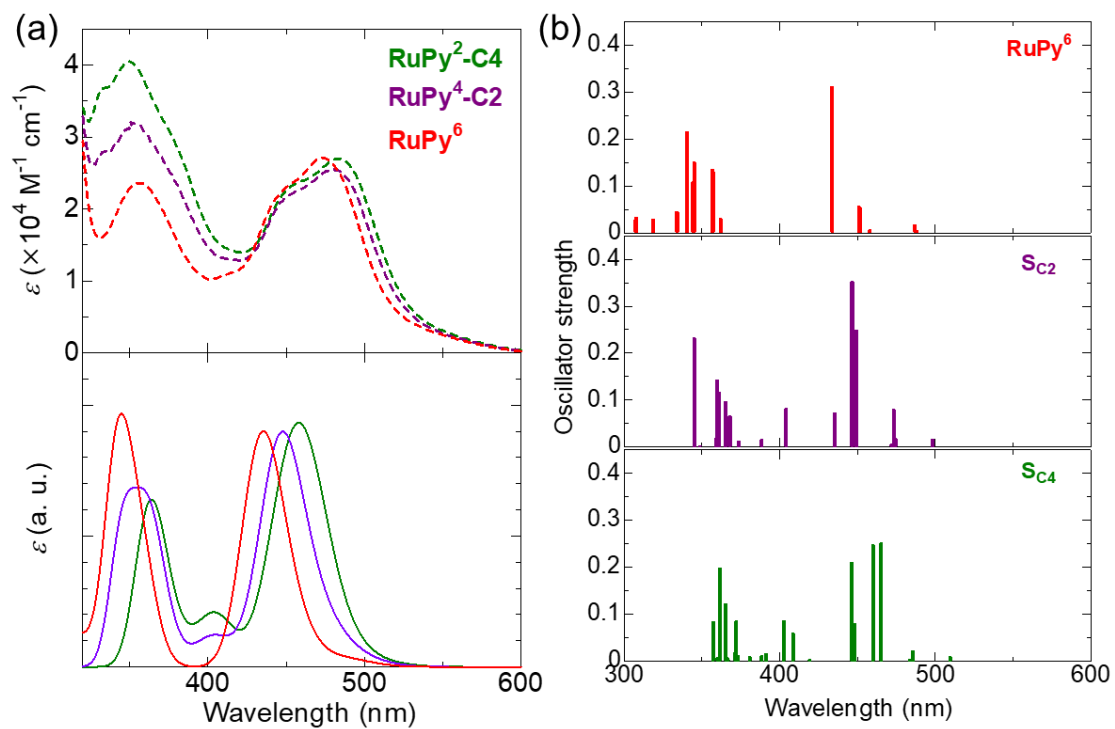


Figure 15 (a) Comparison with experimental spectra in acetonitrile (upper, dotted line) and simulated absorption spectra in acetonitrile by TD-DFT calculations (bottom, solid line, nstate =20) and (b) the bar chart of oscillator strength of **RuPy⁴-C2** (green) and **RuPy²-C4** (purple) and **RuPy⁶** (red).

5-3-3 Electrochemical property

Considering the lower electron-withdrawing ability of cbz groups than pyridyl groups^{24, 25} and destabilization of HOMO as suggested by DFT calculations (§ 5-3-2), the redox potential of Ru(III/II) on **RuPy⁴-C2** and **RuPy²-C4** was suggested to appear at more negative region than that of **RuPy⁶**. Unfortunately, the quantitative estimation of Ru(III/II) redox potential of these complexes from the cyclic voltammograms was difficult, because of the overlap with the one-oxidation and two-reduction redox waves of cbz, characteristic behavior on producing bicarbazole.²⁶ (Fig. 16) However, the anodic peak observed at ~1.6 V, slightly lower than that of **RuPy⁶** (1.72 V), on **RuPy²-C4** was plausibly assigned as the Ru(III/II) oxidation wave. The positive shift of oxidation wave on **RuPy²-C4** was more obviously observed, possibly because the larger number of cbz groups reduce the stabilization of cbz radical by the electron deficiency Ru(III). Additionally, the redox peaks assigned as polycarbazole derivatives became more intense by the repeated cycles of CV (Fig.17). On **RuPy²-C4**, the redox waves of cbz were observed more clearly and the polymerization peaks were more obvious than **RuPy⁴-C2**, plausibly because of the larger number of modified cbz. These results suggest the polymerization ability and an applicability for the electropolymerization with WOC of **RuPy⁴-C2** and **RuPy²-C4**.

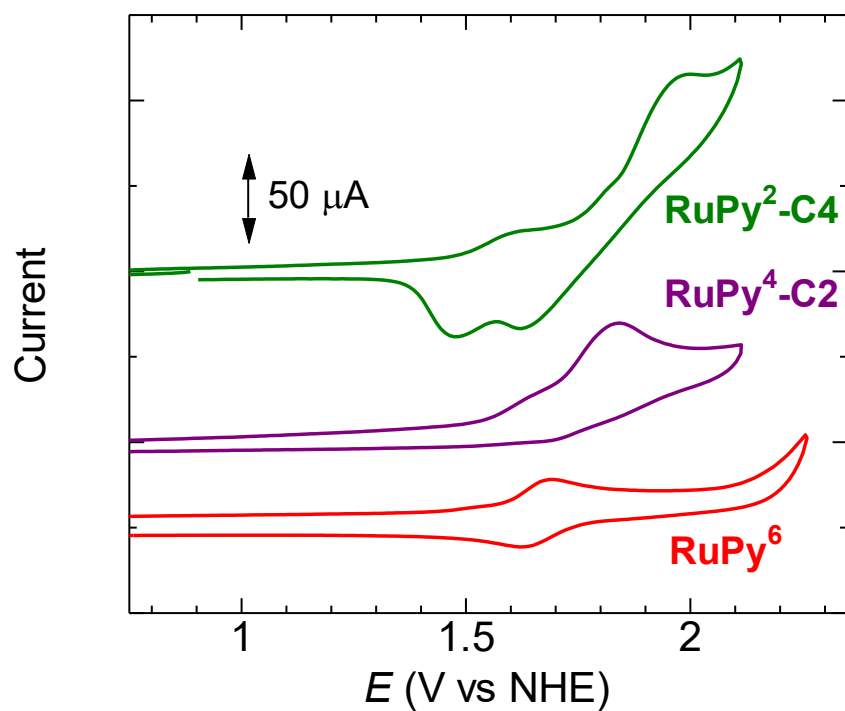


Figure 16. The first scan in cyclic voltammograms of **RuPy⁴-C2** (green), **RuPy²-C4** (purple) and **RuPy⁶** (red) in acetonitrile containing 0.1 M TBAPF₆. Scan rate: 100 mVs⁻¹.

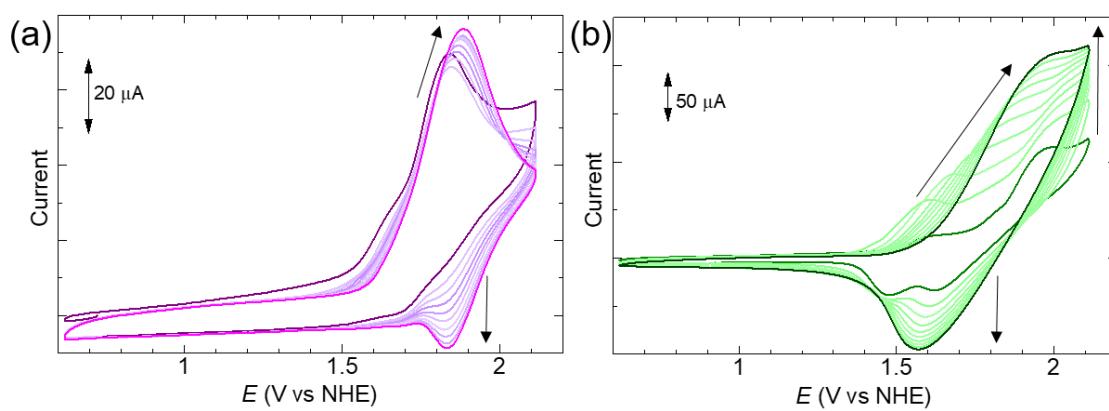


Figure 17. Repeated cyclic voltammograms of (a) **RuPy²-C4** and (b) **RuPy⁴-C2**.

Assuming the Ru(III/II) redox potential of **RuPy²-C4** and **RuPy⁴-C2** are similar to that of **RuPy⁶**, the redox potential in excited state Ru(III/II*) of them are to be ~ -0.3 V vs NHE, and it is apparently difficult to use them as sensitizers on TiO₂ electrodes. However, under a pure-aqueous condition, Ru(III/II) redox potential tends to shift negatively.²⁷ In the same way, as shown in Fig. 18, a cyclic voltammogram of **RuPy⁶**-modified TiO₂ electrode in the aqueous solution (pH=5), a reversible redox couple was observed at 1.45 V vs NHE, assigned as Ru(III/II) redox of **RuPy⁶**, 0.24 V shifted to negative side. Similar tendency was shown in that of **RuPy²-C4**-modified one, with slightly negative shift of anodic peaktop from **RuPy⁶**. (1.56 V \rightarrow 1.55 V) Considering the conduction-band edge of TiO₂ increases > -0.5 V in an acidic condition,²⁸ these complexes can inject electrons to a conduction-band of TiO₂ under acidic media. An application of the semiconductors with more positive conduction-band edge, such as ZnO,²⁹ can also be promising.

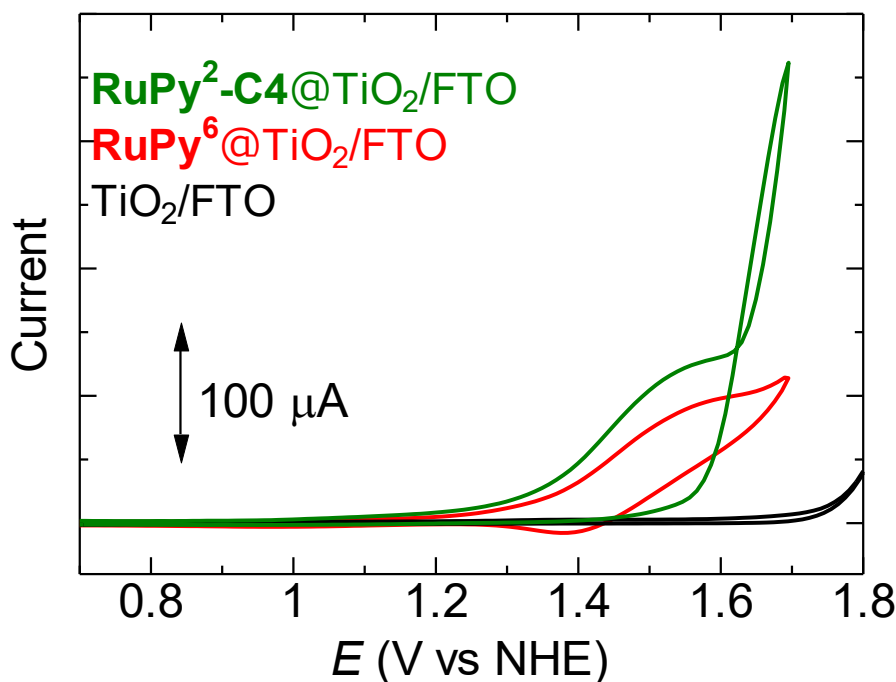


Figure 18. Cyclic voltammograms of **RuPy⁶** or **RuPy²-C4**-modified TiO₂/FTO electrode under pH =5.0 acetate buffer (0.1 M). Scan rate : 100 mVs⁻¹.

5-4 Conclusion

In this chapter, newly synthesized luminescent Ru(II) complexes having both the cbz hole-mediating precursors and the pyridyl anchors, **RuPy²-C4** and **RuPy⁴-C2** were characterized aiming to apply for polycarbazole-integrated water oxidation photoanodes. Obtained two complexes exhibited high molar absorptivity in visible region, long excitation lifetime and high k_r based on cbz-mixed CT transition. Furthermore, positive redox potential close to cbz oxidation was implied. In addition, these complexes were suggested to be electropolymerized in the CV measurement. However, in order to develop the desirable cbz-functionalized photoanodes, polymerization, further investigation with above-mentioned chromophores-modified semiconductor electrodes and WOCs discussed in Chapter 3.

Author hopes an intensive studies on HM polymer-conjugated photoanodes.

5-5 References

- 1 (a) K. Takijiri, K. Morita, T. Nakazono, K. Sakai, H. Ozawa, *Chem. Commun.*, 2017, **53**, 3042. (b) K. Morita, K. Takijiri, K. Sakai, H. Ozawa, *Dalton Trans.*, 2017, **46**, 15181. (c) K. Morita, K. Sakai, H. Ozawa, *ACS Appl. Energy Mater.* 2019, **2**, 987. (d) K. Akamine, K. Morita, K. Sakai, H. Ozawa, *ACS Appl. Energy Mater.* 2020, **3**, 4860.
- 2 (a) H. Iwami, M. Okamura, M. Kondo and S. Masaoka, *Angew. Chem. Int. Ed.*, 2021, **60**, 5965. (b) J. Zhang, J. Du, J. Wang, Y. Wang, C. Wei and M. Li, *Angew. Chem. Int. Ed.*, 2018, **57**, 16698.
- 3 Y. Zhu, D. Wang, Q. Huang, J. Du, L. Sun, F. Li, T. J. Meyer, *Nat. Commun.* 2020, **11**, 4610.
- 4 (a) J. Zhang, J. Du, J. Wang, Y. Wang, C. Wei, M. Li, *Angew. Chem. Int. Ed.*, 2018, **57**, 16698. (b) H. Iwami, M. Okamura, M. Kondo, S. Masaoka, *Angew. Chem. Int. Ed.*, 2021, **60**, 5965. (c) H. Iwami, M. Kondo, S. Masaoka, *ChemElectroChem.*, 2021, <https://doi.org/10.1002/celec.202101363>.
- 5 (a) H. Suzuki, T. Kanbara, T. Yamamoto, *Inorganica Chimica Acta* 2004, **357**, 4335. (b) H.-Y. Li, L.-X. Cheng, J. Xiong, L.-C. Kang, Q.-L. Xu, Y.-C. Zhu, Y.-M. Tao, Y.-X. Zheng, J.-L. Zuo, X.-Z. You, *Inorganica Chimica Acta*, 2011, **370**, 398.
- 6 J. V. Caspar, T. D. Westmoreland, G. H. Allen, P. G. Bradley, T. J. Meyer, W. H. Woodruff, *J. Am. Chem. Soc.* 1984, **106**, 3492.
- 7 K. Huang, A. Rhys, *Proc. R. Soc. London, Ser. A* 1950, **204**, 406.
- 8 G. H. Allen, R. P. White, D. P. Rillema, T. J. Meyer, *J. Am. Chem. Soc.* 1984, **106**, 2613.
- 9 D. Fylstra, L. Lasdon, J. Watson, A. Waren, *Interfaces*, 1998, **28**, 29.
- 10 *CrysAlisPro*, version 1.171.39.45h, Rigaku Corporation, Oxford, UK, 2018.
- 11 G. M. Sheldrick, *Acta Crystallogr., Sect. A: Found. Adv.*, 2015, **71**, 3.
- 12 G. M. Sheldrick, *Acta Crystallogr., Sect. C: Struct. Chem.*, 2015, **71**, 3.
- 13 O. V. Dolomanov, L. J. Bourhis, R. J. Gildea, J. A. K. Howard and H. Pushmann, *Olex2, J. Appl. Crystallogr.*, 2009, **42**, 339.
- 14 *Gaussian 09, Revision E.01*, M. J. Frisch, G. W. Trucks, H. B. Schlegel, G. E. Scuseria, M. A. Robb, J. R. Cheeseman, G. Scalmani, V. Barone, B. Mennucci, G. A. Petersson, H. Nakatsuji, M. Caricato, X. Li, H. P. Hratchian, A. F. Izmaylov, J. Bloino, G. Zheng, J. L. Sonnenberg, M. Hada, M. Ehara, K. Toyota, R. Fukuda, J. Hasegawa, M. Ishida, T. Nakajima, Y. Honda, O. Kitao, H. Nakai, T. Vreven, J. A. Montgomery, Jr., J. E. Peralta, F. Ogliaro, M. Bearpark, J. J. Heyd, E. Brothers, K. N. Kudin, V. N. Staroverov, R. Kobayashi, J. Normand, K. Raghavachari, A. Rendell, J. C. Burant, S. S. Iyengar, J. Tomasi, M. Cossi, N. Rega, J. M. Millam, M. Klene, J. E. Knox, J. B. Cross, V. Bakken, C. Adamo, J. Jaramillo, R. Gomperts, R. E. Stratmann, O. Yazyev, A. J. Austin, R. Cammi, C. Pomelli, J. W. Ochterski, R. L. Martin, K. Morokuma, V. G. Zakrzewski, G. A. Voth, P. Salvador, J. J.

- Dannenbergh, S. Dapprich, A. D. Daniels, Ö. Farkas, J. B. Foresman, J. V. Ortiz, J. Cioslowski, D. J. Fox, Gaussian, Inc., Wallingford CT, 2009.
- 15 C. Adamo and V. Barone, *J. Chem. Phys.*, 1999, **110**, 6158.
- 16 (a) P. J. Hay, W. R. Wadt, *J. Chem. Phys.*, 1985, **82**, 270. (b) P. J. Hay, W. R. Wadt, *J. Chem. Phys.*, 1985, **82**, 299. (c) W. R. Wadt, P. J. Hay, *J. Chem. Phys.*, 1985, **82**, 284.
- 17 M. Cossi, N. Rega, G. Scalmani and V. Barone, *J. Comput. Chem.*, 2003, **24**, 669.
- 18 (a) E. Rousset, D. Chartrand, I. Ciofini, V. Marvaud, G.S. Hanan, *Chem. Commun.* 2015, **51**, 9261. (b) E. Rousset, D. Chartrand, I. Ciofini, V. Marvaud, G.S. Hanan, *Inorg. Chem.* 2017, **56**, 9515.
- 19 R. Dennington, T. Keith, J. Millam, GaussView 05, Semichem Inc., Shawnee Mission, KS, 2009.
- 20 (a) D. Zhang, E. J. Dufek, E. L. Clennan, *J. Org. Chem.*, 2006, **71**, 315. (b) P. Kavanagh, D. Leech, *Tetrahedron Lett.*, 2004, **45**, 121. (c) W. Han, J. Han, H. Kim, M. J. Choi, Y. Kang, C. Pac, S. O. Kang, *Inorg. Chem.*, 2011, **50**, 3271.
- 21 C. Li, Y. Wang, Y. Lu, JingGuo, C. Zhu, H. He, X. Duan, M. Pan, C. Su, *Chin. Chem. Lett.*, **2020**, *31*, 1183
- 22 E. Dulière, M. Devillers and J. Marchand-Brynaert, *Organometallics*, 2003, **22**, 804.
- 23 H.-P. Liang, A. Acharjya, D. A. Anito, S. Vogl, T.-X. Wang, A. Thomas, B.-H. Han
- 24 A. Nakagawa, E. Sakuda, A. Ito, N. Kitamura, *Inorg. Chem.* 2015, **54**, 10287.
- 25 J. H. Blanch, *J. Chem. Soc. B*, 1966, **937**.
- 26 E. T. Veiga, A. V. Müller, L. D. Ramos, K. P. M. Frin and A. S. Polo, *Eur. J. Inorg. Chem.*, 2018, 2680.
- 27 (a) J. F. Ambrose, R. F. Nelson, *J. Electrochem. Soc.*, 1968, **115**, 1159. (b) S. -H. Hsiao, S. -W. Lin, *Polym. Chem.*, 2016, **7**, 198. (c) K. Karon, M. Lapkowski, *J. Solid State Electrochem.*, 2015, **19**, 2601. (d) L. Kortekaas, F. Lancia, J. D. Steen, W. R. Browne, *J. Phys. Chem. C*, 2017, **121**, 14688. (e) E. Contal, C. M. Souguez, S. Lakard, A. E. Taouil, C. Magnenet, B. Lakard, *Front. Mater.*, 2019,**6**,131.
- 28 (a) V. Balzani, P. Ceroni, A. Credi, M. Venturi, *Coord. Chem. Rev.*, 2021, **433**, 213758. (b) F. P. Dwyer, *Journal and Proceedings - Royal Society of New South Wales*, 1949, **83**, 134. (c) M. C. Elliot, E. J. Harshenhart, *J. Am. Chem. Soc.*, 1982, **104**, 7519.
- 29 (a) E. M. James, T. J. Barr, G. J. Meyer, *ACS Appl. Energy Mater.* 2018, **1**, 859. (b) D. F. Watson, A. Marton, A. M. Stux, G. J. Meyer, *J. Phys. Chem. B* 2003, **107**, 10971. (c) G. Rothenberger, D. Fitzmaurice, M. Grätzel, *J. Phys. Chem.* 1992, **96**, 5983.
- 30 A. G. Tamirat, J. Rick, A. A. Dubale, W.-N. Su, B.-J. Hwang, *Nanoscale Horiz.* 2016, **1**, 243.

Chapter 6

General Conclusion

In this thesis, the hole-transporter (HT) functionalized photochemical oxygen-evolution reaction (OER) system was focused aiming to integrate water oxidation catalyst (WOC), HT, and photosensitizer (PS).

In chapter 1, the background and the purpose of this thesis were described. The progress of light-driven OER systems as the half-reaction of artificial photosynthesis, various methods of WOC and PS for efficient electron transfer, and utilization of HT materials to suppress a charge recombination were briefly reviewed. The outline of this thesis about the integrations of WOC, PS and HT was summarized.

In chapter 2, stepwise growths of $K_{2x}Co^{III}_{(3-x)}[Fe^{II}(CN)_6]_2 \cdot nH_2O$ (**CoFe-PBA**) WOC and $K_2Cd^{II}[Ru^{II}(CN)_6]$ (**CdRu-PWA**) HT on a Ru(II) dye-immobilized TiO_2 electrode were investigated to utilize HT with high redox potential to conjugate WOC and PS. Obtained photoanodes **B^xW^yRu** exhibited electrochemical OER behavior and lower catalytic activity was shown on **CdRu-PWA**-loaded anodes than non-loaded one possibly due to the lower amount of WOC and insulation by **CdRu-PWA** layer. On the other hand, the comparable photocurrents assignable to OER were observed on **B³Ru** and **B³WRu**, suggesting the effectiveness of PWA as a HT layer. However, their low photoelectrocatalytic activities indicate that further progress is necessary to overcome the insulating nature.

In chapter 3, novel Ru(II) complexes WOCs, modified 1 or 2 eq. of carbazole(cbz)-HT precursor to Ru-bipyridine dicarboxylato complex WOC backbone (denoted as **C1** or **C2**) were synthesized. The introduction of electron-withdrawing cbz groups was found to improve the OER catalytic ability plausibly due to stabilize the μ -peroxo Ru(IV)-O-O-Ru(IV) species. Furthermore, multi-step OER behavior involving the cbz oxidation was observed in chemical OER by Ce(IV) strong oxidant. From this study, the efficacy for the homogeneous OER catalysis of cbz-functionalization to a molecular WOC was indicated and the origin of unique OER behavior was elucidated.

In chapter 4, an application of pyridyl-anchor modified Ru(II) complexes as the PS for OER were investigated with the attention to their positive Ru(III/II) redox potential and WOC-capturing ability. **RuPy²** and **RuPy⁶**, $[Ru(bpy)_3]^{2+}$ derivatives having two or six pyridyl anchors acted as sensitizers for photocatalytic OER in the presence of $Na_2S_2O_8$ sacrificial oxidant. Although these complexes were found to be adsorbed on the surface of **CoFe-PBA** WOC, photochemical OER activity decreased by increasing the number of pyridyl anchors, because the reactivity with sacrificial oxidant was suppressed by the bulky pyridyl group. The photo-induced electron injection from these surface-immobilized **RuPyⁿ** sensitizer to the conduction band of TiO_2 nanoparticle was hardly observed. Nevertheless, the reactivity with sacrificial oxidant and photochemical OER activity were improved by the immobilization of **RuPy²** on TiO_2 surface, probably because the detrimental effect of bulky pyridyl groups was cancelled by

immobilization. These results indicate the applicability of the Ru(II) sensitizers with pyridyl strong-electron withdrawing anchors for photochemical OER system. This work also suggests that the orientation of PS molecules on the surface of nanoparticles can contribute to the photochemical OER activity.

In chapter 5, novel cationic Ru(II) chromophores bearing both cbz HT-precursors and pyridyl anchors, **RuPy²-C4** and **RuPy⁴-C2** were synthesized aiming to apply PSs with pyridyl-anchors for HT-integrated photoanodes. The absorption and emission of these complexes can be assigned as metal-mixed ligand-to-ligand charge transfer (MMLLCT) transitions from the Ru ($d\pi$) mixed with cbz(π) moiety to the bpy ligands (π^*), and the introduction of cbz leads to destabilization of HOMO and redshift of absorption or emission wavelength. Additionally they exhibited strong visible absorption, long emission lifetime and higher k_r values suitable for PS on OER. Polymerization ability of these complexes was also suggested. These results implied the possibility to application on the WOC-PS integration via polycarbazole HT.

Among these results, suppressing the electron-insulation should be cared for HT-integrated photochemical OER system. In this context, cbz derivatives can be promising materials. Through the elucidation of cbz-introduction to Ru(II) complex chromophores and catalysts, efficacy of hole-donating nature of cbz HT-precursors for molecular-based photocatalytic OER was suggested. Additionally, electron-withdrawing pyridyl groups were proposed as promising anchors for OER systems combined HT. Although the construction of hole-mediator integrated efficient OER photoanodes with proper potential gradient is in progress yet, the knowledge gained from these studies will provide a fundamental knowledge to investigate HT-integrated photochemical OER system.

Appendix

Table 1. Cartesian coordinates for optimized ground state structure of **C2** by theoretical calculation.

Number	X	Y	Z
Ru	0.000061	-0.000440	0.315213
O	0.050653	1.958639	-0.726056
O	-0.050276	-1.959276	-0.726525
O	-0.066289	-4.202909	-0.196918
O	0.067024	4.202133	-0.195847
N	-0.027556	-1.281512	1.818198
N	0.027394	1.280226	1.818520
N	-6.221939	0.031257	-0.873248
N	-2.105788	0.074997	0.081314
N	6.221931	-0.030562	-0.873283
N	2.105860	-0.075698	0.081543
C	-0.040244	-2.615523	1.586483
C	-0.005840	-0.737964	3.086641
C	0.005397	0.736368	3.086819
C	-4.848987	0.046395	-0.556662
C	-0.001824	1.606637	4.184153
C	0.040174	2.614303	1.587149
C	-0.012670	-2.993477	3.964694
C	-0.033105	-3.506781	2.657274
C	3.933527	-0.797856	-1.313812
C	0.032795	3.505292	2.658154
C	2.987476	0.653816	0.813089
C	4.347959	0.688419	0.533028
C	0.001125	-1.608507	4.183757
C	0.012029	2.991660	3.965445
C	-0.057914	-2.989122	0.109111
C	7.047382	1.120636	-0.930588
C	7.016863	-1.163915	-1.179771
C	-7.016605	1.164947	-1.179214
C	4.849009	-0.046199	-0.556559
C	-7.047658	-1.119724	-0.931153
C	2.586707	-0.796829	-0.970629
C	6.716379	2.470043	-0.769250

C	0.058293	2.988284	0.109894
C	8.347706	-0.729702	-1.423572
C	-4.348019	-0.688916	0.532511
C	8.365838	0.715086	-1.271256
C	-9.372637	-1.676987	-1.416092
C	-9.054738	-3.024038	-1.232116
C	-8.365991	-0.713710	-1.271729
C	-9.339626	1.672843	-1.724978
C	-8.347521	0.731150	-1.423349
C	-3.933384	0.798199	-1.313604
C	9.372277	1.678663	-1.415075
C	-6.716975	-2.469279	-0.770422
C	-2.987526	-0.654736	0.812519
C	-6.674779	2.521043	-1.200638
C	6.675332	-2.520073	-1.201957
C	9.340038	-1.671018	-1.725628
C	-7.682026	3.442273	-1.503978
C	7.737575	3.413477	-0.918475
C	-7.738374	-3.412413	-0.920186
C	-9.000010	3.026338	-1.769908
C	9.054057	3.025551	-1.230481
C	-2.586537	0.796714	-0.970502
C	7.682802	-3.440921	-1.505708
C	9.000719	-3.024563	-1.771312
H	-0.019109	1.212669	5.193824
H	-0.005847	-3.669093	4.812626
H	-0.042813	-4.569293	2.447706
H	4.261220	-1.358065	-2.179615
H	0.042602	4.567859	2.448867
H	2.581329	1.217066	1.641143
H	5.013007	1.263102	1.164321
H	0.018196	-1.214793	5.193529
H	0.004989	3.667063	4.813545
H	1.848274	-1.369999	-1.517366
H	5.703347	2.788115	-0.555354
H	-5.013164	-1.263815	1.163513

H	-10.383820	-1.380853	-1.676552
H	-9.824705	-3.780441	-1.340927
H	-10.359785	1.354756	-1.914972
H	-4.260995	1.358899	-2.179122
H	10.383546	1.382883	-1.675607
H	-5.704036	-2.787687	-0.556593
H	-2.581430	-1.218497	1.640252
H	-5.669712	2.860753	-0.982778
H	5.670330	-2.860121	-0.984328
H	10.360142	-1.352602	-1.915371
H	-7.438370	4.499260	-1.531060
H	7.503934	4.466235	-0.798319
H	-7.504980	-4.465283	-0.800521
H	-9.757881	3.765966	-2.005246
H	9.823861	3.782183	-1.338860
H	-1.847971	1.369990	-1.516996
H	7.439374	-4.497945	-1.533372
H	9.758766	-3.763904	-2.006994

Table 2. Cartesian coordinates for optimized ground state structure of **C1** by theoretical calculation.

Number	X	Y	Z
Ru	-1.957772	-0.026687	-0.481986
O	-1.641020	1.887456	-1.559343
O	-1.761900	-2.028984	-1.420635
O	-1.911372	-4.248076	-0.813927
O	-1.741393	4.151445	-1.134574
N	-2.354983	-1.243653	1.022478
N	-2.292464	1.315889	0.927792
N	-3.946363	0.031989	-1.213884
N	4.369148	-0.033640	-0.160786
N	0.143879	-0.096328	-0.199775
C	-2.317913	-2.586162	0.851382
C	-2.640538	-0.647323	2.233961
C	-2.624484	0.825731	2.174292
C	-6.452542	-0.015541	-2.462625
C	-2.896265	1.740990	3.198991
C	-2.219166	2.639195	0.650234
C	-2.871307	-2.863769	3.178749
C	-2.575991	-3.431511	1.928331
C	2.251862	-0.873358	-1.073118
C	-2.484827	3.574176	1.648363
C	0.825890	0.695065	0.668074
C	2.213834	0.736415	0.714952
C	-2.904623	-1.470695	3.335713
C	-2.825389	3.115681	2.931826
C	-1.976375	-3.022396	-0.568320
C	5.179164	1.128243	-0.098996
C	5.219613	-1.167341	-0.199864
C	2.960432	-0.057075	-0.174309
C	0.862031	-0.874959	-1.057758
C	4.812568	2.478105	-0.106691
C	-1.834991	2.951101	-0.791714
C	6.568363	-0.722295	-0.155400
C	-6.250985	-0.668276	-1.242328

C	6.542796	0.729270	-0.096887
C	-5.377573	0.664787	-3.043003
C	7.549892	1.702356	-0.064815
C	-4.991108	-0.626425	-0.648710
C	4.899518	-2.528886	-0.212317
C	7.608512	-1.660467	-0.156914
C	5.835418	3.430991	-0.075683
C	7.190417	3.051404	-0.047298
C	-4.141157	0.674975	-2.399275
C	5.954693	-3.446367	-0.212750
C	7.296044	-3.020858	-0.191629
H	-3.159903	1.389156	4.189815
H	-3.074004	-3.503056	4.030641
H	-2.540124	-4.501876	1.767165
H	2.776041	-1.481229	-1.798742
H	-2.420316	4.626966	1.402578
H	0.234094	1.304037	1.336384
H	2.709137	1.362914	1.445142
H	-3.131612	-1.034357	4.301706
H	-3.036707	3.825939	3.723278
H	0.274850	-1.492439	-1.726221
H	3.775907	2.788623	-0.154172
H	-7.053271	-1.210022	-0.755255
H	-5.486429	1.186172	-3.986443
H	8.595537	1.411360	-0.063051
H	-4.795910	-1.132314	0.286195
H	3.873145	-2.874834	-0.212681
H	8.643149	-1.334005	-0.125137
H	5.574438	4.484178	-0.081557
H	7.960255	3.815315	-0.022621
H	-3.280225	1.204380	-2.787483
H	5.729863	-4.507774	-0.227258
H	8.091930	-3.757991	-0.196073
H	-7.421785	-0.038111	-2.948555

Table 3. Cartesian coordinates for optimized ground state structure of **C0** by theoretical calculation.

Number	X	Y	Z
Ru	-0.000018	-0.000029	-0.550067
O	-0.067786	-1.955754	-1.593609
O	0.067924	1.955808	-1.593558
O	0.101806	4.199647	-1.065226
O	-0.101787	-4.199617	-1.065373
N	0.036983	1.280483	0.952451
N	-0.037057	-1.280525	0.952423
N	2.107201	-0.096437	-0.776662
N	-2.107194	0.096411	-0.776656
C	0.061533	2.613920	0.719336
C	0.011060	0.737281	2.220933
C	-0.011164	-0.737358	2.220914
C	4.841457	-0.107830	-1.382608
C	-0.011456	-1.608581	3.317527
C	-0.061542	-2.613966	0.719266
C	0.037006	2.993204	3.097378
C	0.062079	3.505755	1.789713
C	-3.931686	0.820776	-2.169809
C	-0.062058	-3.505823	1.789615
C	-2.991028	-0.593965	-0.010759
C	-4.357439	-0.607968	-0.283242
C	0.011386	1.608470	3.317567
C	-0.037011	-2.993304	3.097301
C	0.083175	2.986156	-0.758829
C	-4.841420	0.107981	-1.382708
C	-2.576206	0.800283	-1.844963
C	-0.083135	-2.986155	-0.758904
C	4.357395	0.608021	-0.283103
C	3.931785	-0.820563	-2.169821
C	2.990983	0.593940	-0.010680
C	2.576281	-0.800150	-1.845035
H	0.008727	-1.215718	4.327614
H	0.036031	3.669400	3.944920

H	0.081316	4.568013	1.579532
H	-4.260184	1.390782	-3.030629
H	-0.081273	-4.568082	1.579429
H	-2.580906	-1.148299	0.821471
H	-5.023528	-1.177017	0.354636
H	-0.008816	1.215587	4.327647
H	-0.035997	-3.669529	3.944820
H	-1.829199	1.351263	-2.402523
H	5.023436	1.177069	0.354828
H	4.260319	-1.390472	-3.030692
H	2.580775	1.148234	0.821535
H	1.829306	-1.351106	-2.402676
H	5.899629	-0.108388	-1.620034
H	-5.899579	0.108606	-1.620193

Table 4. Cartesian coordinates for optimized ground state structure of **RuPy²-C4** by theoretical calculation.

Atom	X	Y	Z
Ru	0.095453	0.852266	-0.017372
N	0.740432	-0.755712	-1.147533
N	0.891711	2.329050	-1.220208
N	-0.885940	-0.485647	1.218309
N	-0.346673	2.545150	1.077610
N	1.991986	0.547580	0.750438
N	-1.823904	0.923029	-0.783203
N	3.640623	7.788970	-4.902507
N	-1.776187	8.711192	4.374988
N	-3.147451	-3.225704	3.488277
N	-5.841766	0.888843	-2.060874
N	2.311712	-4.073191	-3.220259
N	5.930290	-0.257059	2.019357
C	1.784281	-2.972242	-2.526910
C	2.001179	-1.216186	-0.869832
C	2.537001	-2.319159	-1.536679
C	0.490580	-2.489998	-2.802391
C	-1.311737	3.749639	2.926073
C	-0.909737	4.983680	2.379544
C	2.711237	-0.471930	0.182709
C	1.973879	4.489210	-2.675259
C	4.619426	0.014719	1.596636
C	4.019707	-0.749023	0.581285
C	-2.217466	-0.676482	0.955259
C	1.302024	4.693823	-1.458478
C	-0.315239	-1.194710	2.223084
C	-2.748794	0.131011	-0.154268
C	-1.205248	6.263389	3.063005
C	0.054207	3.735022	0.527191
C	-1.017671	2.566389	2.255166
C	3.868909	1.056770	2.173721
C	0.771414	3.611544	-0.751050

C	3.032677	6.773254	-2.787290
C	0.009563	-1.394936	-2.093772
C	-4.085730	0.114610	-0.553320
C	1.538161	2.122730	-2.393569
C	2.082526	3.164071	-3.139314
C	-0.216909	4.952472	1.157610
C	2.544785	5.622829	-3.437559
C	-1.023798	-2.108797	2.994762
C	-2.231283	1.699017	-1.817701
C	-2.986531	-1.571242	1.700520
C	2.575226	1.291825	1.722008
C	-2.392852	-2.311325	2.736546
C	3.566037	7.818528	-3.550489
C	-3.544554	1.715154	-2.273871
C	-0.345745	7.373205	2.947013
C	-4.504847	0.907902	-1.634368
C	-0.666404	8.562032	3.613033
C	-2.358633	6.416166	3.856902
C	2.623356	5.589712	-4.843459
C	-2.601671	7.643081	4.485375
C	3.170887	6.682272	-5.526162
C	-4.083636	-4.153329	2.970522
C	-4.431863	-4.430607	1.641893
C	-4.633793	-4.892000	4.051357
C	-5.372688	-5.444242	1.412737
C	-5.574195	-5.903483	3.802306
C	-5.946070	-6.170687	2.478925
C	-3.105824	-3.374944	4.895639
C	-2.382791	-2.651725	5.853227
C	-4.019802	-4.395116	5.269876
C	-2.567278	-2.990161	7.201002
C	-4.190969	-4.720225	6.624306
C	-3.455488	-4.017641	7.586818
C	-6.648090	-0.265894	-2.212726
C	-7.931857	0.135672	-2.667836
C	-6.322308	-1.618105	-2.042339

C	-8.917763	-0.829048	-2.925933
C	-7.319920	-2.567315	-2.304647
C	-8.607840	-2.181282	-2.735170
C	-6.615344	2.020457	-2.416262
C	-6.285406	3.381363	-2.374900
C	-7.912981	1.582392	-2.790707
C	-7.273086	4.302851	-2.749658
C	-8.889038	2.519603	-3.162552
C	-8.560430	3.880711	-3.147153
C	3.617859	-4.166254	-3.758622
C	1.622921	-5.274312	-3.514413
C	4.649267	-3.218314	-3.779183
C	3.754984	-5.427141	-4.397408
C	0.334142	-5.681200	-3.145695
C	2.494973	-6.131152	-4.236726
C	5.841952	-3.567300	-4.427875
C	4.956689	-5.758623	-5.042005
C	-0.083405	-6.959078	-3.542618
C	2.059162	-7.407321	-4.625450
C	6.000984	-4.825663	-5.048222
C	0.764164	-7.813736	-4.280800
C	6.472754	-1.541156	2.268040
C	6.938148	0.706362	2.265767
C	5.857281	-2.799142	2.224030
C	7.825212	-1.390358	2.673623
C	6.906547	2.098033	2.107336
C	8.121379	0.031233	2.666591
C	6.633363	-3.916493	2.561959
C	8.586559	-2.520836	3.007989
C	8.079007	2.812539	2.389957
C	9.285631	0.763640	2.945413
C	7.986358	-3.784359	2.943219
C	9.256407	2.157272	2.811718
H	3.516222	-2.697417	-1.274489
H	-0.123538	-2.934383	-3.575274
H	-1.831666	3.695020	3.875077

H	4.589974	-1.526726	0.091212
H	1.179291	5.699126	-1.076146
H	0.738551	-1.027637	2.399393
H	-1.310147	1.610036	2.666382
H	4.266655	1.657282	2.981714
H	3.027562	6.857904	-1.705969
H	-0.975999	-0.998628	-2.296726
H	-4.810275	-0.482180	-0.015958
H	1.616817	1.098698	-2.732102
H	2.604950	2.929406	-4.059123
H	0.088150	5.879560	0.689330
H	-0.504589	-2.673754	3.758380
H	-1.475011	2.302673	-2.300899
H	-4.044842	-1.679524	1.504559
H	1.975414	2.080019	2.156513
H	3.951965	8.709846	-3.066335
H	-3.800253	2.322816	-3.132466
H	0.572775	7.319982	2.372877
H	-0.012867	9.425392	3.539856
H	-3.075461	5.610753	3.972691
H	2.246599	4.745531	-5.410561
H	-3.488503	7.780786	5.095597
H	3.233660	6.676828	-6.609598
H	-3.989880	-3.903584	0.803833
H	-5.660354	-5.676071	0.391478
H	-6.001695	-6.475057	4.620683
H	-6.673345	-6.948184	2.266794
H	-1.709603	-1.845625	5.584316
H	-2.016562	-2.445419	7.962055
H	-4.886816	-5.498593	6.922899
H	-3.573231	-4.256127	8.639289
H	-5.335123	-1.943790	-1.734511
H	-9.902902	-0.533556	-3.274406
H	-7.091532	-3.621423	-2.177680
H	-9.358262	-2.941690	-2.927742
H	-5.311617	3.732581	-2.053340

H	-7.040714	5.363404	-2.728363
H	-9.884862	2.196403	-3.450780
H	-9.301681	4.620399	-3.433233
H	4.544652	-2.237862	-3.328300
H	-0.327498	-5.050837	-2.562517
H	6.657040	-2.850301	-4.455594
H	5.073855	-6.719404	-5.534325
H	-1.078963	-7.297306	-3.271081
H	2.716401	-8.072448	-5.177552
H	6.938402	-5.064983	-5.540566
H	0.408846	-8.796746	-4.573944
H	4.814421	-2.925887	1.955986
H	6.021420	2.622961	1.766488
H	6.179463	-4.902563	2.533124
H	9.621867	-2.418434	3.319070
H	8.078981	3.892586	2.277197
H	10.196732	0.259101	3.252901
H	8.560046	-4.670404	3.196677
H	10.146752	2.740770	3.024536

Table 5. Cartesian coordinates for optimized ground state structure of **RuPy⁴-C2** by theoretical calculation.

Number	X	Y	Z
Ru	0.991923	-0.069421	-0.040775
N	0.995418	-1.432638	-1.590668
N	2.516074	1.120318	-0.766138
N	-0.642479	-1.054572	0.760193
N	1.212445	1.291711	1.498992
N	2.420774	-1.410434	0.607014
N	-0.572751	1.090505	-0.745481
N	7.835516	5.445609	-2.746934
N	2.209335	6.377306	6.405773
N	1.328630	-6.486368	-6.618736
N	7.335573	-6.288234	2.328182
N	-4.170498	-2.851089	2.209071
N	-3.965431	3.292196	-1.936217
C	1.128770	-3.432395	-3.575496
C	1.857951	-2.489296	-1.454703
C	1.938522	-3.488299	-2.428569
C	0.249390	-2.338662	-3.693008
C	0.647463	2.290515	3.616155
C	1.612877	3.300142	3.438974
C	2.669213	-2.468679	-0.228126
C	4.616806	2.832356	-1.548405
C	4.365069	-3.337083	1.284259
C	3.629139	-3.432866	0.091111
C	1.198616	-4.481291	-4.618200
C	-1.868253	-0.511562	0.475783
C	3.948517	3.009919	-0.325312
C	-0.590953	-2.181045	1.512788
C	-1.827918	0.702585	-0.355018
C	1.820258	4.356143	4.455824
C	2.161176	2.262580	1.307579
C	0.476716	1.316324	2.637008
C	4.095995	-2.239266	2.124544
C	2.910331	2.151421	0.046590

C	6.570997	4.328182	-1.007048
C	0.209968	-1.371138	-2.693369
C	-2.962468	1.423289	-0.729639
C	3.155227	0.941885	-1.947945
C	4.194392	1.767311	-2.367103
C	2.371648	3.266136	2.257016
C	5.721157	3.729550	-1.957619
C	-1.729108	-2.807383	2.007970
C	1.522923	-5.814181	-4.298115
C	-0.447248	2.198130	-1.517021
C	-3.047150	-1.084273	0.954697
C	5.383251	-4.350789	1.641538
C	0.940023	-4.183434	-5.970412
C	3.130187	-1.306925	1.757188
C	-2.993949	-2.254884	1.729803
C	7.602731	5.168408	-1.441854
C	-1.538658	2.950975	-1.935820
C	3.083814	4.945484	4.656339
C	5.247388	-5.696759	1.249269
C	1.016695	-5.204471	-6.924949
C	-2.833152	2.564634	-1.538710
C	1.575080	-6.771698	-5.317929
C	3.230327	5.939701	5.630931
C	6.235564	-6.619876	1.611105
C	6.525158	-4.004815	2.389923
C	0.758013	4.808621	5.262530
C	5.963502	4.014861	-3.315422
C	7.464403	-4.993746	2.705090
C	0.995101	5.809459	6.212002
C	7.017944	4.868772	-3.659721
C	-5.364792	-3.041872	1.471681
C	-5.647001	-2.757327	0.128850
C	-6.316828	-3.679725	2.310246
C	-6.918914	-3.093362	-0.355287
C	-7.584847	-4.009117	1.807688
C	-7.883484	-3.706401	0.473451

C	-4.367152	-3.365025	3.513855
C	-3.508056	-3.356781	4.620427
C	-5.687820	-3.878539	3.603771
C	-3.984773	-3.904432	5.819600
C	-6.147517	-4.423265	4.812598
C	-5.287396	-4.439925	5.917448
C	-5.188673	2.741079	-2.390393
C	-6.081960	3.804516	-2.686167
C	-5.542356	1.404135	-2.616043
C	-7.364516	3.525093	-3.182511
C	-6.827516	1.144441	-3.111894
C	-7.735181	2.190225	-3.386647
C	-4.084491	4.703279	-1.942785
C	-3.172627	5.682622	-1.528057
C	-5.385212	5.045635	-2.397986
C	-3.575058	7.023065	-1.607732
C	-5.770125	6.393148	-2.471431
C	-4.856495	7.379853	-2.080840
H	2.643938	-4.300704	-2.308596
H	-0.420461	-2.241108	-4.538993
H	0.041380	2.239791	4.512844
H	3.823139	-4.246844	-0.595794
H	4.227184	3.829372	0.325098
H	0.390320	-2.590219	1.710863
H	-0.253958	0.529099	2.762085
H	4.611264	-2.112543	3.069267
H	6.460313	4.133175	0.054122
H	-0.460575	-0.525911	-2.766094
H	-3.941165	1.127029	-0.376964
H	2.821421	0.117139	-2.562592
H	4.676895	1.557046	-3.314183
H	3.108819	4.036316	2.069550
H	-1.626230	-3.726225	2.570974
H	1.709146	-6.121986	-3.274911
H	0.554937	2.468512	-1.820840
H	-4.002656	-0.616913	0.758710

H	0.705894	-3.174734	-6.292702
H	2.903364	-0.462744	2.394157
H	8.270624	5.633909	-0.724186
H	-1.378150	3.801121	-2.586396
H	3.952917	4.629299	4.089744
H	4.381264	-6.039985	0.693988
H	0.826627	-4.992040	-7.972136
H	1.817711	-7.804482	-5.089102
H	4.197480	6.400975	5.803210
H	6.145061	-7.662170	1.322556
H	6.704434	-2.983339	2.707047
H	-0.245971	4.414983	5.148101
H	5.335838	3.605777	-4.099462
H	8.353641	-4.744473	3.275141
H	0.187231	6.174625	6.837929
H	7.215600	5.104806	-4.700437
H	-4.917963	-2.307546	-0.535821
H	-7.161805	-2.880400	-1.392155
H	-8.320770	-4.496970	2.439859
H	-8.859828	-3.951879	0.067407
H	-2.510808	-2.934036	4.577512
H	-3.336628	-3.911500	6.690835
H	-7.155635	-4.818731	4.893184
H	-5.624609	-4.858575	6.860546
H	-4.857209	0.583396	-2.436225
H	-8.056644	4.329975	-3.411151
H	-7.125620	0.115783	-3.291977
H	-8.723910	1.954609	-3.767829
H	-2.190399	5.434640	-1.142380
H	-2.884868	7.800670	-1.294398
H	-6.761815	6.667385	-2.818621
H	-5.135548	8.427664	-2.132121

Acknowledgements

The study on this thesis has been carried out at the Department of Chemistry, Faculty of Science, Hokkaido University during April 2016-March 2022.

The author would like to express greatest profound appreciation to Professor Masako Kato for the earnest guidance and proper suggestions.

The author would like to express greatest deepest gratitude to Professor Kazuki Sada for the earnest guidance and proper suggestions as the author's supervisor in FY2021.

The author would like to express deepest appreciation to Associate Professor Atsushi Kobayashi for his numerous discussions and wide-ranging guidance.

The author would like to acknowledge gratefully to Assistant Professor Masaki Yoshida for his helpful discussions and supports with matured experimental techniques.

Furthermore, the author is deeply grateful to Assistant Professor Sun Yu and Assistant Professor W. M. C. Sameera for their helpful discussions and comments.

The author would like to express deepest appreciation to Professor Kei Murakoshi, Professor Yasuchika Hasegawa and Professor Kosei Ueno for reviewing this thesis.

The author also express gratitude to Professor Roland A. Fischer, Dr. Julien Warnan, Dr. Weijin Li, Dr. Zheng Wang, Mr. Zhenyu Zhou, Ms. Xiaoxin Ma and Mr. Shujin Hou for helpful discussions and warm hospitality during the short visit to their research group (December 2019). The author also appreciates deeply to Professor Shin-ichiro Noro for providing the opportunity of this visit.

The author would like to acknowledge to Mr. Daisuke Saito for helpful discussion and valuable supports, including some photophysical measurements in Chapter 5.

The author would also like to acknowledge to Dr. Tomohiro Ogawa, Dr. Yasuhiro Shigeta, and Mr. Sogo Furugori for helpful advice and valuable comments as well as numerous words of encouragements.

The author is deeply grateful to Mr. Nobutaka Yoshimura for valuable discussion.

The author is also deeply grateful to Dr. Paramita Kar, Dr. Kana Sato (Sawaguchi), Dr. Erika Saito, and Dr. Panyi Liang as well as all members of the Kato Group for helpful cooperation in the laboratory.

The author is also grateful to many researchers and students talked with the author in some congresses, symposiums and meetings for helpful comments and fruitful discussions.

This work was financially supported by Hokkaido University DX Doctoral Fellowship Grant Number JPMJSP2119.

Finally, I would like to express special thanks to my family, (Mr. Masayasu Otsuka, Ms. Sachiko Iwakuma, Ms. Mika Iwakuma and my sainted mother Ms. Yumi Otsuka) and friends for their supports and encouragements.

Hiroki Otsuka
Graduate School of Chemical Sciences and Engineering
Hokkaido University